SPIM

Thèse de Doctorat

école doctorale **sciences pour l'ingénieur et microtechniques**

UNIVERSITÉ DE TECHNOLOGIE BELFORT-MONTBÉLIARD

Modeling, simulation and control of the air-path of an internal combustion engine

Modélisation, simulation et commande de la boucle d'air d'un moteur à combustion interne

Fayez Shakil AHMED

SPIM

Thèse de Doctorat

école doctorale **sciences pour l'ingénieur et microtechniques**

UNIVERSITÉ DE TECHNOLOGIE BELFORT-MONTBÉLIARD

N° 2 0 3

THÈSE présentée par

Fayez Shakil AHMED

pour obtenir le

Grade de Docteur de
l'Université de Technologie de Belfort-Montbéliard

Spécialité : **Automatique**

Modeling, simulation and control of the air-path of an internal combustion engine

Modélisation, simulation et commande de la boucle d'air d'un moteur à combustion interne

Soutenue le 04 Juillet 2013 devant le Jury :

Pr. Didier MAQUIN	Président	Université de Lorraine
Pr. Eric BIDEAUX	Rapporteur	Université INSA de Lyon
Pr. Rachid OUTBIB	Rapporteur	Université d'Aix-Marseille
M. David GUYON	Examinateur	SOGEFI systèmes moteur SAS
Pr. Maurizio CIRRINCIONE	Examinateur	Université de Technologie de Belfort-Montbéliard
Pr. Mohammed EL BAGDOURI	Directeur de thèse	Université de Technologie de Belfort-Montbéliard
Dr. Salah LAGHROUCHE	Co-Directeur	Université de Technologie de Belfort-Montbéliard

List of publications

Peer-reviewed journal papers

F.S. Ahmed, S. Laghrouche, M. El Bagdouri *Overview of the modelling techniques of actuator non-linearities in the engine air path* Proceedings of the Institution of Mechanical Engineers, Part D: Journal of Automobile Engineering , Vol 227 Number 3, pp 443-454, 2012.

M. Harmouche, S. Laghrouche, F.S. Ahmed, M. El Bagdouri *Second-order sliding mode controllers: an experimental comparative study on a mechatronic actuator* Proceedings of the Institution of Mechanical Engineers, Part I: Journal of Systems and Control Engineering, Vol 226, Number 9, pp 1231-1248, 2012.

F. S. Ahmed, S. Laghrouche, M. El Bagdouri *Analysis, modeling, identification and control of pancake DC torque motors: Application to automobile air path actuators*, Mechatronics, Vol 22, Issue 2, pp 195-212, 2012.

Peer-reviewed international conference papers

F. S. Ahmed, S. Laghrouche, M. El Bagdouri. *Cascaded Second order sliding mode observer for state and friction dynamics of a control valve*, The 12th International Workshop on Variable Structure Systems 2012, Mumbai India, pp. 94-99.

F. S. Ahmed, S. Laghrouche, M. El Bagdouri. *State observation and friction estimation in engine air path actuator using higher order sliding mode observers*, 18th IFAC World Congress 2011, Milan Italy, Vol. 18, Issue 1, pp. 7480-7485.

F. S. Ahmed, S. Laghrouche, M. El Bagdouri. *An experimental comparative study of different second order sliding mode algorithms on a mechatronic actuator*, American Control Conference 2011, San Francisco USA, pp. 5286-5291.

F. S. Ahmed, S. Laghrouche, M. El Bagdouri. *Second-Order Sliding Mode based Output-Feedback Control of an Engine Air Path Actuator in presence of uncertainties*, Conference on Control and Fault-Tolerant Systems 2010, Nice France, pp. 50-56.

F. S. Ahmed, S. Laghrouche, M. El Bagdouri. *Pancake Type DC Limited Angle Torque Motor: Modeling and Identification, Application to Automobile Air Path Actuators*, 6th IFAC Symposium: Advances in Automotive Control 2010, Munich Germany, pp. 431-436.

S. Laghrouche, F.S. Ahmed, M. El Bagdouri. *Modeling and Identification of a Mechatronic Exhaust Gas Recirculation Actuator of an Internal Combustion Engine*, American Control Conference 2010, Baltimore USA, pp. 2242-2247.

F. S. Ahmed, S. Laghrouche, M. El Bagdouri. *Nonlinear modeling of Pancake DC Limited Angle Torque Motor based on LuGre friction mode*, IEEE Vehicle Power and Propulsion Conference 2010, Lille France, pp. 1-6.

Contents

List of publications **i**

Contents **iii**

List of Figures **ix**

Acknowledgement **xv**

Introduction **1**

0.1 Diesel Engine Air-path 3

0.1.1 Pressure Boosting (Turbocharging) 4

0.1.2 Exhaust Gas Recirculation 5

0.2 Air-path Subsystems 6

0.2.1 Variable Geometry Turbocharger (VGT) 6

0.2.1.1 VGT actuator 6

0.2.2 EGR Valve 7

0.2.3 Cooling Systems 7

0.2.4 Swirl actuators 7

0.3 Problems and contributions 8

0.3.1 System Modeling 11

0.3.2 Actuator Modeling 11

0.3.3 Actuator control 11

0.4 Thesis Structure 12

1 Airpath Modeling **15**

1.1 Introduction to Engine and Air-path Modeling 15
1.1.1 Mean Value Models 16
1.1.2 Discrete Event Models 16
1.1.3 Chapter Objectives and Goals 17
1.2 Engine Combustion 18
1.2.1 State of the art 19
1.2.1.1 Zero-dimensional model 19
1.2.1.2 Models based on fluid dynamics 19
1.2.1.3 Phenomenological models 19
1.2.2 Lebas' Phenomenological Model 20
1.3 Engine Intake 21
1.4 Engine Exhaust 21
1.5 Exhaust Gas Recirculation 21
1.6 Variable Geometry Turbocharger 23
1.6.1 Turbocharger mass-flow maps and correction 23
1.6.2 Compressor Power 25
1.6.3 Turbine Power 26
1.6.4 Turbocharger Speed 26
1.7 Simulator Implementation in AMESim 27
1.7.1 Cylinder and Combustion 27
1.7.2 Intake and Exhaust Manifolds 29
1.7.3 Exhaust Gas Recirculation 29
1.7.4 Variable Geometry Turbine 29
1.7.4.1 Turbine 30
1.7.4.2 Compressor 31
1.7.4.3 Inertial shaft 31
1.7.5 Fuel Injection 31
1.7.6 Auxiliary components 32
1.8 Summary 32

2 Actuator Modeling **33**
2.1 Actuator Terminology 34
2.2 Major Actuator Families 36
2.2.1 DC Motor based actuators 37

2.2.2 Torque Motor based actuators . . . 38
2.2.2.1 Working Principle . . . 39
2.3 Actuator Modeling . . . 43
2.3.1 PMDC Motor-Spring Systems . . . 47
2.3.2 Torque Motor . . . 50
2.3.3 Friction . . . 51
2.3.3.1 Effects of friction . . . 52
2.3.3.2 Friction Modeling . . . 56
2.3.3.3 Comparison . . . 57
2.3.4 Temperature variation . . . 58
2.3.5 Complete Model . . . 58
2.3.5.1 Extension to Double Action Actuators . . . 60
2.3.6 Actuator Implementation in AMESim . . . 60
2.4 Experimental Validation . . . 61
2.4.1 Parameter Identification . . . 62
2.4.2 Validation . . . 64
2.5 Aging . . . 64
2.5.1 Wear . . . 65
2.5.2 Clogging (Surface deterioration) . . . 65
2.5.3 Torque deterioration (Degradation of motor electrical characteristics) 66
2.6 Summary . . . 67

3 Simulation and Validation 69
3.1 Industrial Test Bench . . . 70
3.2 Air-path Controller . . . 72
3.2.1 Torque Reference Unit . . . 72
3.2.2 Fuel Injection Unit . . . 74
3.2.3 VGT Control Unit . . . 74
3.2.4 EGR Control Unit . . . 76
3.3 Simulation and Validation Results . . . 78
3.3.1 Boost Simulation . . . 79
3.3.1.1 Validation . . . 80
3.3.2 EGR Simulation and Validation . . . 82
3.4 Summary . . . 83

4 Specialized Actuator Control **85**
4.1 Introduction . . . 85
4.2 Experimental Setup . . . 87
4.3 Sliding Mode based Robust Control . . . 87
4.3.1 Actuator Model with Parametric and Load uncertainty . . . 88
4.3.2 Sliding Mode Control . . . 89
4.3.2.1 Twisting Algorithm . . . 91
4.3.2.2 Super twisting Algorithm . . . 92
4.3.2.3 Quasi-Continuous Algorithm . . . 93
4.3.2.4 Robust Differentiator . . . 94
4.3.3 Control Design . . . 95
4.3.3.1 Sliding Variables . . . 96
4.3.3.2 Feedback Linearization . . . 97
4.3.3.3 Controller Parameters . . . 98
4.3.4 Simulation . . . 99
4.3.4.1 Test Trajectory . . . 100
4.3.4.2 Simulation Results . . . 100
4.3.5 Experimental results . . . 102
4.3.5.1 Nominal Conditions . . . 102
4.3.5.2 Temperature tests . . . 103
4.3.5.3 Sinusoid tests . . . 107
4.3.6 Conclusion on sliding mode controllers . . . 107
4.4 Backstepping Based Adaptive Output Feedback Controller . . . 107
4.4.1 Problem Formulation . . . 109
4.4.1.1 Control problem formulation . . . 110
4.4.2 State Estimation . . . 111
4.4.2.1 Velocity Estimator . . . 112
4.4.2.2 Current observer . . . 112
4.4.3 Controller Design . . . 113
4.4.4 Lyapunov Analysis . . . 115
4.4.5 Simulation and Experiments . . . 119
4.4.5.1 Simulation results . . . 119
4.4.5.2 Experimental results . . . 120
4.5 Summary . . . 133

5 VGT Aerodynamic Force Modeling 135
5.1 Mechanism and Notations . . . 136
5.2 One dimensional CFD model . . . 138
5.2.1 Hypothesis and problem formulation with Navier-Stokes equations . 138
5.2.2 Model derivation . . . 140
5.2.3 Source terms . . . 144
5.2.3.1 Geometry of the flow-path . . . 144
5.2.3.2 Evaluation of the output angle . . . 145
5.2.3.3 Blade source terms . . . 146
5.2.3.4 Pressure losses . . . 148
5.2.3.5 Friction source terms . . . 150
5.3 Numeric resolution of 1D Navier Stokes Equations . . . 151
5.3.1 Numerical Resolution . . . 153
5.3.1.1 Explicit method . . . 154
5.3.1.2 Implicit method . . . 154
5.4 Calculation of aerodynamic force on the actuator . . . 156
5.4.1 Relation between crank handle angle and actuator position . . . 157
5.4.2 Relation between crank handle angle and lever direction . . . 159
5.4.3 Relation between the levers and unison ring . . . 159
5.4.3.1 Total torque on the rim . . . 159
5.4.3.2 Net torque on the crank handle . . . 160
5.4.4 Angle between the Crank Handle and Actuator Shaft . . . 161
5.5 Model validation . . . 161
5.6 Summary . . . 163

Conclusion and Perspectives 167

Appendices 173
A Tables . . . 173
B Torque and friction characteristics comparison . . . 174
C Sensors and transmission protocol in actuators . . . 176
D LaSalle Yoshizawa Theorem . . . 178
E Calculation of upper time bound of URED . . . 179

Bibliography 181

List of Figures

Figure 0.1. Evolution of European Emission standards 2
Figure 0.2. Engine air-path 4
Figure 0.3. Mechanical diagram of a variable geometry turbocharger 7
Figure 0.4. VGT with an electro-pneumatic actuator system 8
Figure 0.5. EGR actuator 9
Figure 0.6. Double air mixer 9
Figure 0.7. Inlet swirl actuator 10

Figure 1.1. Air-path variables and airflow. Variables: p =pressure, T =temperature, $\dot{m}$ =mass flow. Subscripts: i =intake manifold, e =exhaust manifold, T =Turbine, c =compressor, f=fuel, α =cylinder, atm =atmosphere, egr =EGR 18
Figure 1.2. Mass flow and pressure difference of EGR Valve at different openings 22
Figure 1.3. Mechanical diagram of a variable geometry turbocharger 23
Figure 1.4. Compressor performance curves for VGT installed on DV6TED4 . . 24
Figure 1.5. Turbine performance curves for VGT installed on DV6TED4 25
Figure 1.6. Overview of simulator implementation in AMESim 28
Figure 1.7. Cylinder Model 29
Figure 1.8. EGR Model 30
Figure 1.9. VGT Model 30
Figure 1.10. Fuel Injector Model 32

Figure 2.1. Different control valves and actuators in an air-path 34
Figure 2.2. DC Motor based actuators a: Bosch GPA-S b: Pierburg EAMi . . . 37
Figure 2.3. 3D Cutaway 38

Figure 2.4. Torque Motor based actuators (a)Valeo EGR Actuator (b)DELPHI Double Air Mixer . . . 39
Figure 2.5. Simplified working principle of torque motors . . . 40
Figure 2.6. Multi-coil torque motor . . . 41
Figure 2.7. Valeo torque motor . . . 42
Figure 2.8. Torque Motor Characteristics . . . 42
Figure 2.9. Expected characteristic of a Single Action Mechatronic Actuator . . . 43
Figure 2.10. Experimentally obtained characteristics of two Single Action Mechatronic Actuators . . . 44
Figure 2.11. Deadband . . . 45
Figure 2.12. Hysteresis . . . 46
Figure 2.13. Dead Zone . . . 46
Figure 2.14. Block diagram of Motor-Spring system . . . 47
Figure 2.15. Actuator Characteristics w.r.t. Duty Cycle . . . 49
Figure 2.16. Friction: a: Static and Coulomb b: Static, Coulomb and Viscous c: With Stribeck Effect . . . 52
Figure 2.17. Stribeck Stick-Slip observed in Single Action PMDC Actuator . . . 54
Figure 2.18. Hunting Effect in Single Action PMDC Actuator . . . 55
Figure 2.19. Karnopp Model . . . 56
Figure 2.20. Experimentally obtained characteristics of two Single Action Mechatronic Actuators at different temperatures . . . 59
Figure 2.21. AMESim Model of Single Action Mechatronic Actuator . . . 60
Figure 2.22. AMESim Model of Double Action Mechatronic Actuator . . . 60
Figure 2.23. Actuator Test Bench . . . 61
Figure 2.24. Actuator Test Bench Block Diagram . . . 62
Figure 2.25. Static Validation . . . 64
Figure 2.26. Dynamic Validation . . . 65
Figure 2.27. Worn out actuator parts . . . 66
Figure 2.28. Torque deterioration with age . . . 67

Figure 3.1. DV6TED4 Test bench (Faurecia) . . . 70
Figure 3.2. Controller Structure . . . 71
Figure 3.3. Torque Maps . . . 73
Figure 3.4. References and constraints (CMI - Qi Block) . . . 73

Figure 3.5. Fuel Injection Unit 74
Figure 3.6. VGT Control Unit 75
Figure 3.7. EGR Controller 77
Figure 3.8. EGR coefficient and inhibition 78
Figure 3.9. EGR Local-Loop Controller 78
Figure 3.10. Intake Manifold Pressure at 1500RPM, 40Nm 79
Figure 3.11. Intake Mass Flow (g/s) at 1500RPM, 40Nm 79
Figure 3.12. Exhaust Manifold Pressure at 1500RPM, 40Nm 80
Figure 3.13. Comparison at 1500RPM, 40Nm 81
Figure 3.14. Comparison at transition 1500RPM-2000RPM, 40Nm-70Nm 81
Figure 3.15. EGR Mass Flow at 1500RPM, 40Nm 82
Figure 3.16. EGR Mass Flow at 1500RPM, 40Nm 82

Figure 4.1. Actuator under PID control in Temperature Variations 86
Figure 4.2. Convergence of the sliding variable under Twisting algorithm 92
Figure 4.3. Convergence of the sliding variable under Super Twisting algorithm 93
Figure 4.4. Differentiator Simulation 95
Figure 4.5. Reference Trajectory 100
Figure 4.6. Simulation Results 101
Figure 4.7. Comparison: Desired and Actual Trajectories (Nominal Conditions) 104
Figure 4.8. Quasi Continuous Controller under Temperature Variation 105
Figure 4.9. Super Twisting Controller under Temperature Variation 106
Figure 4.10. Tracking a sinusoidal trajectory 108
Figure 4.11. Position Convergence, low-speed (Simulation) 120
Figure 4.12. Position Convergence, high-speed (Simulation) 121
Figure 4.13. Velocity Observer low-speed (Simulation) 121
Figure 4.14. Velocity Observer high-speed (Simulation) 122
Figure 4.15. Current Observer low-speed (Simulation) 122
Figure 4.16. Current Observer high-speed (Simulation) 123
Figure 4.17. Friction State Observer low-speed (Simulation) 123
Figure 4.18. Friction State Observer high-speed (Simulation) 124
Figure 4.19. Parameter Adaptation low-speed (Simulation) 124
Figure 4.20. Parameter Adaptation high-speed (Simulation) 125
Figure 4.21. Position Convergence, low-speed (Experimental) 125

Figure 4.22. Position Convergence, high-speed (Experimental) 126
Figure 4.23. Observer Convergence (x_1), low-speed (Experimental) 126
Figure 4.24. Observer Convergence (x_1), high-speed (Experimental) 127
Figure 4.25. Observed Velocity and Current, low-speed (Experimental) 127
Figure 4.26. Observed Velocity and Current, high-speed (Experimental) 128
Figure 4.27. Observed Friction State, low-speed (Experimental) 128
Figure 4.28. Observed Friction State, high-speed (Experimental) 129
Figure 4.29. Worst case condition (600mN.m Load Torque) 129
Figure 4.30. Temperature Variation 130
Figure 4.31. Positioning Response (Exhaust Pressure: 2 bar) 131
Figure 4.32. Tracking Response (Exhaust Pressure: 2 bar) 131
Figure 4.33. Positioning Response (Exhaust Pressure: 3 bar) 132
Figure 4.34. Tracking Response (Exhaust Pressure: 3 bar) 132

Figure 5.1. VGT with vane actuation mechanism 136
Figure 5.2. VGT Vanes, closed and open 138
Figure 5.3. VGT mechanical diagram 139
Figure 5.4. Velocity components of air-flow through a vane 139
Figure 5.5. Exhaust gas flow through VGT 142
Figure 5.6. Velocity triangle 145
Figure 5.7. Blade geometry 146
Figure 5.8. Gas outlet angles vs. $cos^{-1}(o/s)$ (straight back blades operating at low mach numbers) 147
Figure 5.9. Finite element division of VGT vane 147
Figure 5.10. Forces on the vane 157
Figure 5.11. Physical positions of primary lever pivot point (A), crank rotation axis (C) actuator position (B) 158
Figure 5.12. Turbocharger geometry with all dimensions 160
Figure 5.13. A Simulator based on C compiler code to solve 1D flow equations . . 162
Figure 5.14. Output results of the QtCreator simulator 163
Figure 5.15. Comparison of turbine inlet pressure, Engine: 2000RPM, 100Nm . . 164
Figure 5.16. Comparison of turbine inlet pressure, Engine: 2000RPM, 150Nm . . 164
Figure 5.17. Comparison of aerodynamic force on actuator, Engine: 2000RPM, 100Nm 165

Figure 5.18. Comparison of aerodynamic force on actuator, Engine: 2000RPM, 150Nm 165
Figure B.1. Electromagnetic coefficients of different actuators 175
Figure B.2. Static friction values of different actuators 175
Figure C.3. SENT Transmission Packet 178

Acknowledgement

There are a number of people without whom this thesis might not have been written and to whom I am greatly indebted. In the spirit of fairness, this work is dedicated to all of them:

To my parents, Nasreen Talat and Shakil Ahmed, who have been sources of encouragement and inspiration throughout my life in their own different ways and who taught me to question. Also to my more-like-parent brother and sisters (in-laws included), who have still not given up on the idea that they can make a disciplined person out of me. I should also mention my nieces and nephews, just for being there.

To my director M. El Bagdouri and my supervisor M. Laghrouche, for their valuable time, insightful advice and constructive criticism. They patiently (but mostly impatiently) provided the vision and guidance necessary for completion of this dissertation. Among the list of mentors, I would also like to mention Mr. Rais ul Hassan, who has spent the better part of his life in proving to adolescents that maths is our friend.

To my friends, colleagues and teammates Imad Matraji, Mohammed Harmouche and Adeel Mehmood. Together we turned the bleakest moments of research into memorable ones and are looking forward for more. Specially, to Nafisa M. R. Zaman, who actively supported me in my determination and, at times, kept me determined when I wasn't really so.

In the end, a special note of thanks to the industrial partners of project SIMBA, particulary David Guyon, Julien Peuch, Anita Grenier of SOGEFI SAS, Denis Ragot of Faurecia, Landry Saussol of LMS international and Guillaume Alix of IFP. Thank you for the time and effort expended in order to churn out a working simulator.

Introduction

The global competition in today's automobile market is a major challenge faced by the automobile industry. It is also associated with environmental and social issues such as sustainable development and anti-pollution campaigns. For example, in Europe, all vehicles equipped with a diesel engine will be required to substantially reduce their emissions of nitrogen oxides as soon as the Euro VI standard enters into force (see Figure 0.1). For example, emissions from cars and other transport vehicles will be capped at an additional reduction of more than 50% compared to the current Euro V standard [1]. Combined emissions of particulate matter and nitrogen oxides (NO_x) from diesel vehicles will also be reduced.

In order to meet these challenges and to offer products nearer to the clients' requirements, the industry needs to double its effort in research, development and innovation. Investments are required in high performance development tools that would reduce the time to market and the number of prototypes, and optimize their technical solutions. This also offers an opportunity for introducing new high performance products that are in conjunction with the social and environmental battle against air pollution caused by vehicle emissions. In order to avail this opportunity, the two key players of the automobile industry, namely the automobile manufacturers and Original Equipment Manufacturers (OEM or parts manufacturers), need to work in tandem. Their relationship is characterized by three major parameters:

- **Structure:** Both manufacturers are of different sizes and have different internal cultures, but they are confronted with similar competitive challenges.

- **Competition:** OEMs need to search ways for escaping the restrictive frame of unified parts, and to identify problems yet undiscovered, permitting them to extend their margins of competence.
- **Regulations:** The increasingly strict regulations on pollution have made the working modes more complex.

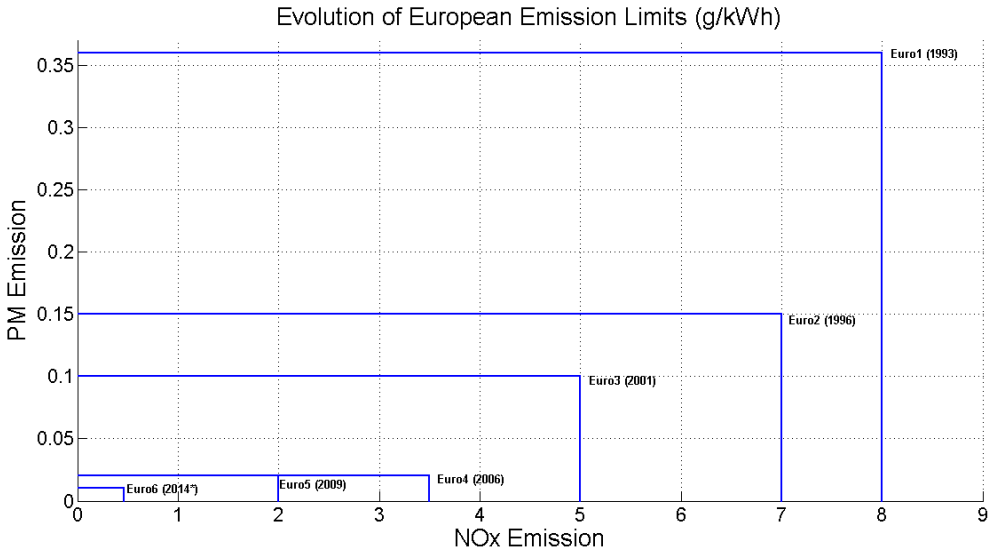


Figure 0.1. *Evolution of European Emission standards*

At present, automobile manufacturers develop the specification of individual parts separately for each OEM, while ignoring the mutual interaction between the parts. It is clear that this approach is not consistent with the actual challenges. Improvements in complex systems need to be introduced at the conception and design level with mutual interactions taken into account. For improving engine performance in terms of consumption and emission, a better understanding of the engine air-path is required, which demands in-depth knowledge related to the different physical phenomena related to it, as well as the interaction between its subsystems. Ambitious research is required around the internal combustion engine, concentrated towards the combustion process as well as the air-path dynamics. This is not possible without the *mutualization* of industrial competence, research and development skills manufacturers and experts. Fortunately, the OEMs are convinced that joint-research efforts in their domains related to engine air-path is the absolute need of the day. In this spirit, the project "Simulation de la boucle d'air" (SIMBA)

was conceived with the collaboration of industrial and academic partners, with the objectives of

- obtaining precise dynamic models of different parts of the engine air-path
- in-depth research of the mutual interaction between these parts and subsystems, including their effect on the global performance of the air-path
- developing a "predictive simulation tool" to improve product development in its conceptual phase, thereby reducing delays and techno-economical compromises

This thesis follows two major axes of research in the context of SIMBA. The first axis is oriented towards the problems related to the modeling of the global air-path system. This includes interlinkage of the subsystems of the air-path into a complete system, as well as consolidation of the efforts of different partners of the project into the above mentioned simulation tool. The second axis of research is focused on the modeling and control of mechatronic actuators. These actuators are basically motorized control valves used for regulating the air-mass flow in different sections of the air-path. In this chapter, we will explore the air-path and its subsections, and identify the problems that are addressed in the rest of this report.

0.1 Diesel Engine Air-path

The diesel engine, developed by Rudolf Diesel (March 18, 1858 – September 29, 1913), is a Compression Ignition (CI) internal combustion engine. In this engine, fuel is injected directly into the cylinder and ignited by the heat generated through the compression of the working fluid (air). The output torque is controlled by varying the quantity of injected fuel, thereby varying the air-fuel ratio. This principle contrasts with Spark-Ignition (SI) engines, in which an electric spark ignites a premixed air-fuel mixture of a fixed ratio. Diesel or CI engines generate ignition temperature by compressing air at much high compression ratios as compared to SI engines. The high cylinder temperature and pressure required for ignition in CI engines result in improved fuel efficiency, higher than any other internal or external combustion engine [2].

In diesel engines, air is compressed in the cylinder and fuel is injected at the exact moment at which ignition is required. This is done to avoid self-ignition of the fuel at lower

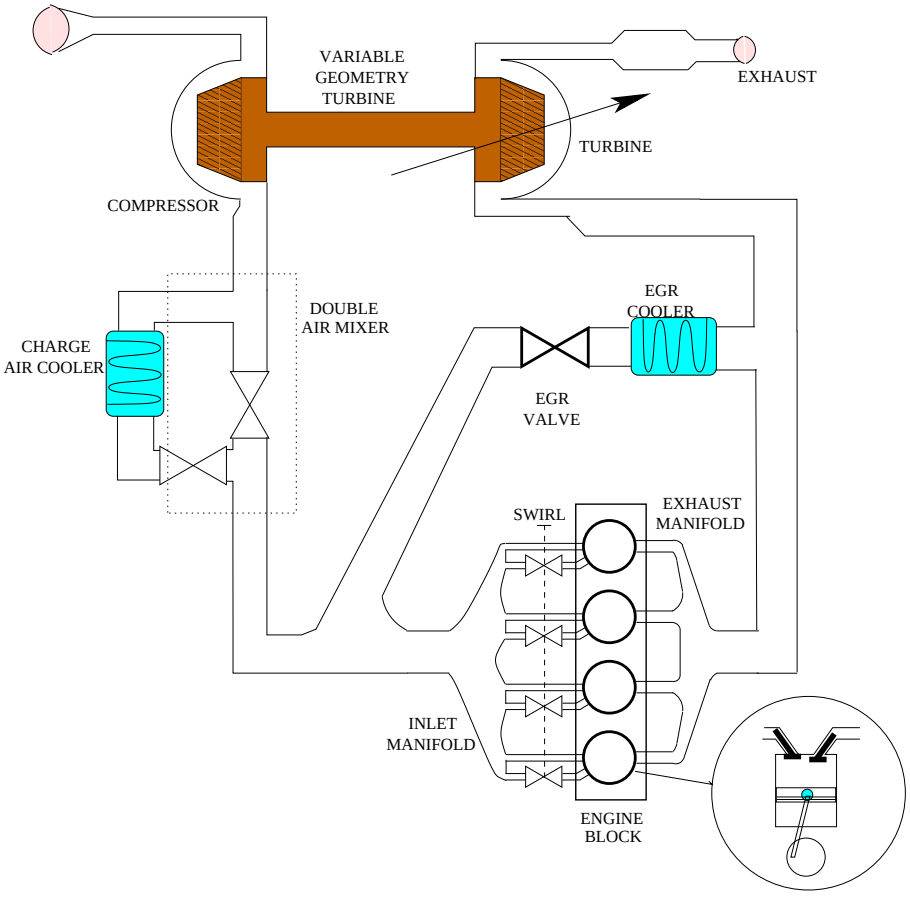


Figure 0.2. *Engine air-path*

pressures. The engine air-path maintains sufficient pressure in the intake manifold of the engine to ensure that the air mass-flow into the cylinder meets the combustion requirement [3]. It indirectly controls the cylinder temperature as well, in order to reduce NO_x formation. In this way the air-path is responsible for the management of the inlet and exhaust air quality and quantity for efficient combustion and pollution reduction [4, 5]. Let us now see how this management is achieved in modern diesel engine air-paths.

0.1.1 Pressure Boosting (Turbocharging)

The engine power or torque of a CI engine depends upon the the amount of fuel that can be burned efficiently inside it, i.e. the amount of air present in the cylinder. The power output can therefore be increased by forcing more air into the cylinder, achieving high Air to Fuel ratio (AFR) [6]. The air mass-flow is increased by increasing the pressure

in the intake manifold, which is why this process is called pressure boosting. This can also be interpreted as reduction in Brake Specific Fuel Consumption (BSFC), which is an immediate measure of increase in the engine's efficiency [2].

Mechanically driven air compressors, connected directly to the engine crankshaft, were initially introduced for this purpose. These *superchargers* had the major advantage of quick response to speed changes [7]. However, the power to drive the compressor was a parasitic load on the engine output. They also had higher cost, greater weight, more chances of mechanical failure and higher noise levels. The drawbacks of superchargers were overcome by exhaust gas turbochargers. Turbochargers use a turbine to run the compressor. The turbine itself is run by the exhaust gas, utilizing energy that would otherwise have been wasted. The compressor, running through the turbine forces air into the intake manifold, providing the pressure boost. Turbochargers are now a common feature in diesel engine automobiles [3]. The advantages of turbocharged engines are [7, 8, 9]:

- Due to the lower volumetric displacement required, the power-to-weight ratio of the engine is higher than naturally aspirated engines.
- The fuel consumption of a turbo engine is lower, as some of the normally wasted exhaust energy contributes to the engine's efficiency.
- The turbo engine's installation space requirement is smaller due to its smaller size.
- The high-altitude performance of a turbocharged engine is significantly better due to better performance of the turbine at low atmospheric pressures.

0.1.2 Exhaust Gas Recirculation

As discussed before, diesel engines are more fuel-efficient due to high compression and lean burning. However, they cannot use the pollutant reduction systems that are successful in gasoline engines [9]. While the air-fuel ration inside the cylinder of diesel engines can be as high as ten times the stoichiometric ratio, the fuel mixture is heterogeneous because combustion starts as soon as the fuel injection begins. The prevailing flame temperature therefore, is high at localized points in the cylinder. This increases the specific rate of NO_x generation [10].

EGR was proposed to alter combustion in spark ignition engines for knock suppression [11, 12]. This proved to be one of the most effective method for reducing NO_x emissions in diesel engines. In this method exhaust gas is added to the fresh air at the intake. The addition of inert gases to the intake mixture reduces peak burned gas temperatures and hence, reduces NO_x formation rates while improving fuel consumption [5]. Recently, EGR has been declared as a necessary means to meet the United States Environmental Protection Agency (EPA) NO_x regulations [11].

0.2 Air-path Subsystems

The functions of the air-path, mentioned in the previous section, require a certain number of subsystems to work together. As seen in Figure 0.2, the integral components of the engine air-path are the turbocharger, exhaust gas recirculation (EGR) valve [9, 4, 13] and some auxiliary systems such as heat exchanger, swirl system etc. Throttle valves are usually not required in CI engines, since engine speed can be controlled directly by controlling the fuel injection [14]. In this section, we will explore the major subsystems and their control mechanisms.

0.2.1 Variable Geometry Turbocharger (VGT)

As discussed above, the turbocharger turbine turns the compressor to provide pressure boost. In order to regulate the intake manifold pressure, the compressor and turbine speed needs to be controlled. In modern turbochargers, this is achieved by varying the geometry of the turbine inlet. A variable geometry turbocharger (see Figure 0.3) has moveable vanes located around the turbine. These vanes allows the turbine flow cross-section to be varied in accordance with the engine operating point.

0.2.1.1 VGT actuator

The position of the VGT vanes is controlled by a dedicated VGT actuator. The VGT actuator is a linear actuator, connected to the vanes through a rack and pinion crankshaft and a unison ring. The latter ensures that all the vanes move together. This actuator can be electro-mechanical or electro-pneumatic.

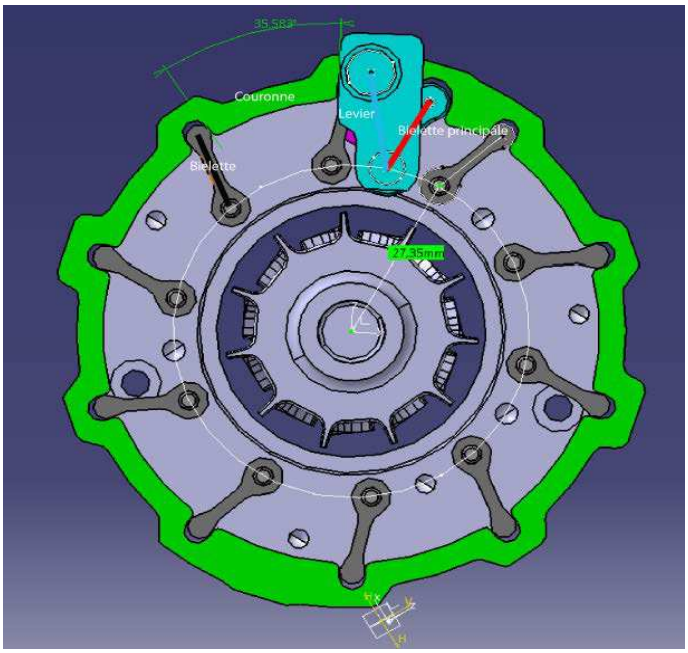


Figure 0.3. *Mechanical diagram of a variable geometry turbocharger*

0.2.2 EGR Valve

The flow of exhaust gas recirculated towards the intake manifold is regulated by a control valve between the intake and exhaust paths. This valve is a mechatronic actuator, which typically consists of a linear (globe) valve with a motor and a cam or screw drive to convert rotary motion to linear motion (Figure. 0.5).

0.2.3 Cooling Systems

Due to compression and combustion, gas temperature in different sections of the air-path can be very hot. Therefore, different means are employed for temperature regulation. One such method is the Double Air Mixer (Fig. 0.6), which maintains the temperature of the fresh air entering the intake manifold by mixing hot and cold air to maintain the air temperature. This mixer is actuated by two separate mechatronic butterfly valves.

0.2.4 Swirl actuators

Turbulent air mixes better with the fuel inside the cylinder. This mitigates some of the disadvantages of heterogeneous combustion (such as excessive NO_x). In some diesel engines, a swirl actuator is integrated in the air inlet manifold, the geometry of which

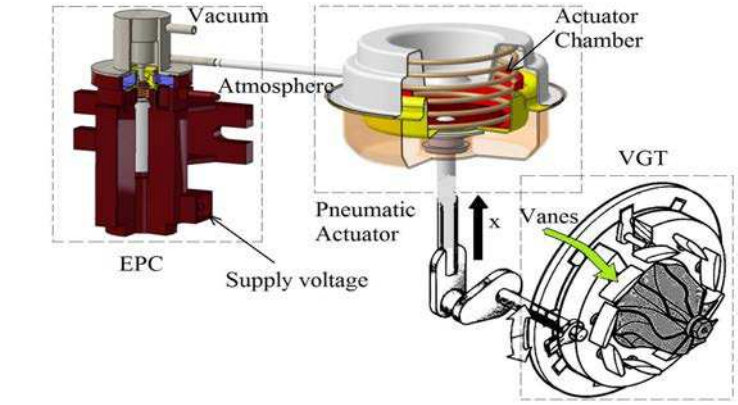




Figure 0.4. *VGT with an electro-pneumatic actuator system*

adds turbulence to the air flow (Figure 0.7). The flow of swirled air is controlled by a mechatronic actuator [15].

0.3 Problems and contributions

The discussion about the air-path and its subsystems brings forth some important points concerning its design and control. These are highlighted as follows:

- The coupling of the intake and exhaust paths, due to VGT and EGR, creates a significant interdependence between the subsystems. An air-path cannot provide the



Figure 0.5. *EGR actuator*



Figure 0.6. *Double air mixer*

performance expected according to the design specifications, if this interdependence is not taken into account at the design level. In other words, the dynamics and limitations of the air-path subsystems need to be studied together, in order to determine the behavior of the complete air-path.

- The performance of the air-path subsystems is dependent upon the performance of their actuation systems. Therefore, the mass-flow characteristics of the subsystems are not sufficient in order to determine the global behavior of the air-path. In such complicated systems, where the effect of variation of one actuator affects the global system, it is important to model the system response during actuator transition [13],

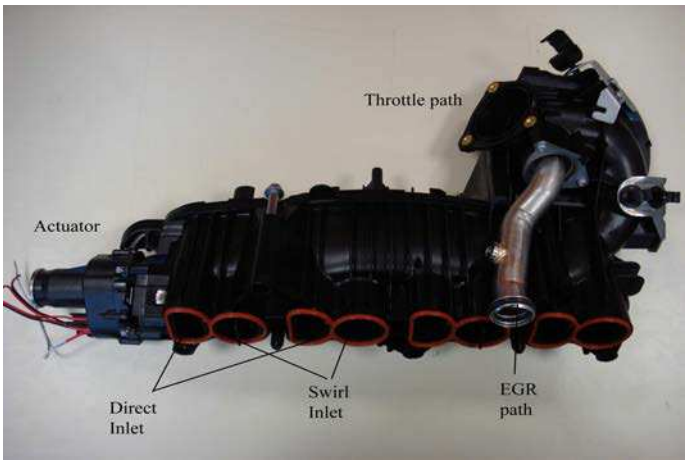


Figure 0.7. *Inlet swirl actuator*

and the characteristics and dynamics of the actuators also need to be taken into account.

In addition to these points, the discrete, cylinder-by-cylinder operation of the engine results in pulsations in the intake and exhaust air-flow. Therefore, the dynamics of air mass-flow are non-stationary at the turbine and intake manifold, even when the motor is in stationary regime (stable). On the other hand, the manifold air pressure sensors used in the intake manifold, do not have sufficient bandwidth to measure the pressure changes due to these pulsations, and their effect is generally disregarded in commercial engines. Improvements in the air-path design and control methods require that these pulsating dynamics and their influence on air-path subsystems be studied and robust control methods be developed to mitigate their negative effects.

These problems are at the core of the research work presented in this thesis. The goal is to develop a simulator that enables the industrial actors to study the these problems at design level, virtually realize scenarios that have not yet been considered practically, mark the areas of possible improvement in their system and control design and introduce new and better products (subsystems and complete systems) in the market. The overall work and contribution can be divided into three main segments, discussed below.

0.3.1 System Modeling

This part addresses the global air-path modeling, taking into account the pressure and air mass-flow dynamics in and between different subsystems of the engine air-path. This includes the addition of a discrete combustion model with the air-path model, in order to simulate the above-mentioned pulsating flow and problems related with it. As part of the Project SIMBA, the research and validation were performed using the commercial DV6TED4 4-cylinder, turbocharged engine. However, the model can be parameterized to the specification of any other engine and air-path.

0.3.2 Actuator Modeling

The modeling of the actuator dynamics in the engine environment is not only important from the air-path design point of view, but also from the control aspect, since the air-path can only meet its design specifications if its subsystems and their actuators work accurately. In this regard, the effect of flow characteristics, temperature, parametric variations and external forces also needs to be taken into account. On the other hand, the model also needs to be suitable for control design and implementation purposes. Therefore, actuator modeling has been given special attention in this thesis, taking into account their nonlinear dynamics and environmental influence.

One particular force worth mentioning here, is the aerodynamic force exerted on the VGT vanes by the exhaust gas flow. It is an important external force that has not received much attention in research, yet its influence on VGT control cannot be neglected. This force has also been studied and modeled in this work.

0.3.3 Actuator control

In practical application, the global air-path control task is facilitated by local-loop actuator controllers, which manage the actuator positioning tasks while the global controller generates positioning references in accordance with the engine's operating point. The third segment of this thesis is dedicated to the development of advanced robust controllers for local control of actuators. Using the actuator models, different control methods are developed, and then experimentally evaluated in terms of their response time and robustness to parametric variations, operating environment and external disturbances.

0.4 Thesis Structure

This report is divided as follows:

Chapter 1 deals with modeling of the air-path and its subsystems. The importance of both, Discrete Event Modeling (DEM) and Mean Value Modeling (MVM) are highlighted. Then, combustion modeling is discussed along with the intake and exhaust mass flows and EGR. The VGT is discussed in detail and modeling of mass-flow characteristics in the compressor and turbine are discussed. Power coupling between these stages is also modeled. In the end, simulation platforms are discussed and the implementation of the air-path simulator in AMESim is presented.

Chapter 2 is dedicated mechatronic actuator technologies that are commonly found in engine air-paths, and their modeling. The mechatronic actuation methods mostly found in commercial air-path valves are identified and a generic model is developed. This model takes into account the nonlinear characteristics of the actuators due to friction as well as the effects of temperature on their performance The parametric identification method for the model is described for its adaptation to different specific actuators. The model is experimentally validated using different commercial actuators. Integration of these models in the simulator is also discussed, and the actuators associated with the DV6TED4 engine are incorporated.

Chapter 3 contains the validation of the complete simulator. The results generated by the simulator are compared with the data obtained during experimental tests conducted during the project. As this required the simulator to be linked with the controller used in real tests, the open ECU controller was implemented in Matlab Simulink and an interface was developed between AMESim and Simulink. This controller is also described in this chapter. The results show that the simulator's outputs match the physical quantities of the real system.

Chapter 4 presents the development and experimental validation of different controller for local control of actuators. This study has been carried out, keeping in mind the present requirements and limitations of the automobile industry. The first part consists of a comparative study, in which various popular control methods were implemented on an air-path actuator. Their performance is compared in terms of response time and robustness against

parametric uncertainty (due to temperature changes) and load variation. In the next part, an advanced adaptive backstepping controller is developed, which dynamically adapts to variations in friction and external load. The performance of this controller is also demonstrated using simulation and experimental results.

Chapter 5 addresses an important problem in the air-path control, i.e. modeling of the aerodynamic force exerted on the VGT vanes by the exhaust gas flow. Modeling of this force is essential in the simulator as it affects the dynamics of the VGT actuator. In this chapter, a 1D exhaust gas flow model is obtained, which allows more accuracy in predicting the flow component acting on the VGT vanes. Using this model, the force exerted on the VGT vanes is estimated using finite element analysis of the vane geometry. The transfer of this force from the vane to the actuator is calculated, through geometric analysis of the linkage mechanism. Using these calculations, a simulation tool is developed which estimates the aerodynamic force using the turbine inlet states. The tool is experimentally validated using results obtained from engine test bench measurements.

Chapter 1

Airpath Modeling

1.1 Introduction to Engine and Air-path Modeling

The diesel engine is a complex physical machine, in which numerous chemical, thermal and mechanical processes occur at the same time. Therefore it is unrealistic to expect that a single simulator will match the specific requirements of each engine process [16]. For example, the mean engine torque is a nonlinear function of many variables, such as fuel quantity and injection timing, air-fuel ratio, speed, EGR etc, and accurate simulation using all these parameters is too time consuming for control purposes [9]. On the other hand, these processes are interdependent to such an extent that simplifying approaches may lead to completely inaccurate results. Therefore, research in a particular domain related to engines (e.g. fuel efficiency, pollution reduction..) still requires that processes with indirect influence be taken into consideration.

Certain processes in the engine are dependent upon time only. However, many other processes are discrete in nature and depend upon the engine's crankshaft position. The combustion process itself is highly transient, with large and rapid temperature and pressure variations [3]. These discrete processes are very fast (a few milliseconds for a full engine cycle) and usually are not accessible for control purposes [9]. Moreover, their models are complex and are not useful for the application in real-time feedback control systems [17]. Therefore, their behavior is often approximated with mean value models. However, their discrete nature cannot be ignored in *control design*, as they may have serious repercussions

on the overall performance of the engine system.

In this section, we will first look into the two modeling methods (mean and discrete) and classify important engine processes accordingly. In the light of this discussion, we will establish the objectives and goals of engine air-path modeling for this chapter.

1.1.1 Mean Value Models

Mean Value models (MVM) neglect the discrete cycles of the engine and assume that all processes and effects are spread out over the engine cycle [9]. All subsystems of the engine are modeled as lumped volume parameters. The reciprocating behavior of the engine is approximated by introducing delays between cylinder-in and cylinder-out effects. For example, the torque produced by the engine does not respond immediately to an increase in the manifold pressure. Therefore, in an MVM, it is updated after the induction-to-power-stroke (IPS) delay [18].

The complexity of Mean Value Engine Models is suitable for design of control and supervision systems [19].This modeling method is clearly insufficient for modeling the engine dynamics itself. However, other continuous time processes, which do not depend directly upon the crankshaft position, can be represented by MVMs satisfactorily. Examples of the continuous-time subsystems are the intake manifold dynamics, the acceleration of the crankshaft, the turbocharger speed dynamics. These models are commonly used in air-path control design, examples of which are [20, 21, 22, 23, 24]

1.1.2 Discrete Event Models

The term Discrete event models (DEM) is used as an abuse of terminology (as proposed in [9]), to refer to models that take into account the reciprocating behavior of the engine. This means that the independent variable in these models is not time, but the crankshaft angle. The discrete working principles of the subsystems must be considered in the following cases [9]:

- When the system representation and controller design are simpler in the crank-angle domain.

- When the control system has to achieve bandwidths that may raise synchronization problems.
- When cylinder-individual effects have to be analyzed

DEM are often formulated under the assumption that the engine speed is constant. In this case, their structure is simplified as they become equivalent to sampled data systems, for which a theoretical background exists [9]. Subsystems that often are modeled as discrete-event systems are the torque production, the gas exchange of the individual cylinders, the injection and the ignition processes, etc. [25, 16, 22].

1.1.3 Chapter Objectives and Goals

A major issue in the improvement of Diesel engines lies in the architecture and the control of the air-path. Fuel efficiency and pollution control regulations are forcing manufacturers to develop complex air-paths. For example, two-stage turbochargers are used to reduce the fuel/air equivalence ratio and variable actuation allows the reduction of the response time to high EGR demand, etc. [16]. Virtual simulation support allows manufacturers the facility of fast development (reducing time-to-market), while reducing prototyping costs. On the other hand, application expectations have to be accurately defined in order to adapt simulation with coherent models [22]. This is the motivation behind this work, in which we focus upon physical modeling and simulation of the diesel engine air-path at component level. This would allow manufacturers to study the behavior of the engine system virtually, with respect to changes in one or more components.

In this case, an air-path model cannot be attained without integrating a sufficiently accurate combustion model as well. The combustion model needs to reflect the effect of reciprocation on the mass-flow; therefore MVMs are not a choice. The physical nature of gaseous mass-flow itself is continuous in time. Therefore, if the engine model generates the discrete pressure and flow conditions on the crankshaft level, then the pulsating flow in the air-path can be accurately modeled using MVMs for air-path components.

In this chapter, we will study and model the physical dynamics of each part of the air-path, shown in Figure 1.1. Then, the models are implemented in a simulator, using AMESim platform. This software is one of the leading tools in the automotive industry for automotive and aerospace simulations. It was chosen for this study as it has abundant libraries for

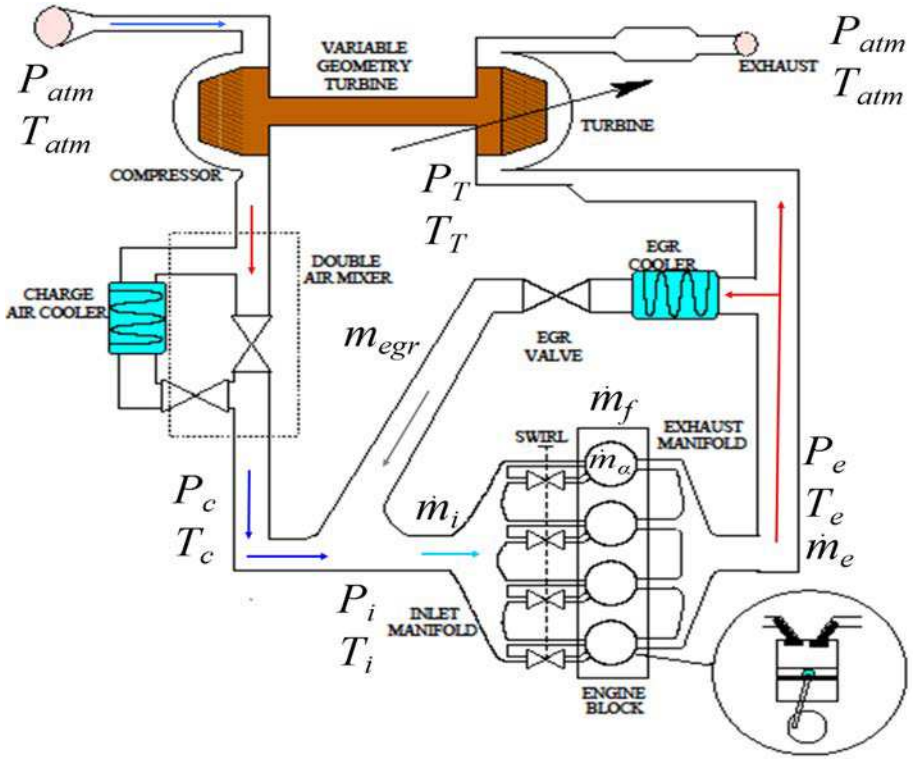


Figure 1.1. *Air-path variables and airflow. Variables:* p *=pressure,* T *=temperature,* $\dot{m}$ *=mass flow. Subscripts:* i *=intake manifold,* e *=exhaust manifold,* T *=Turbine,* c *=compressor,* f *=fuel,* α *=cylinder,* atm *=atmosphere,* egr *=EGR*

facilitating air-path design. In this chapter, the focus is on the air-flow dynamics and as an initial step, the scope is simulation is 0D, i.e. the lengths of transmission lines are not taken into account. The simulator will be further improved in the subsequent chapters, by adding actuator dynamics as well. The extension to 1D simulations will be considered in the future.

NB: In the rest of the paper, the notations and subscripts of Figure 1.1 will be used as reference.

1.2 Engine Combustion

Due to its reciprocating action, an internal combustion engine naturally discrete-event system. Engine models are primarily developed to study the combustion properties and torque generation. We are not interested in any of these processes directly; our focus

is to model the effects of reciprocation on the air-path. In this regard, the evolution of combustion is an important factor in the choice of model, as it defines the pressure dynamics inside the cylinder, which in turn, are the cause of pulsations in the air-path. Let us first briefly review some existing models based on this property.

1.2.1 State of the art

The shaft work by a diesel engine is the sum of work on the piston by the pressure produced by the heat released by combustion and the losses due to pumping, heat transfer and friction. The variety of combustion chambers and types of fuel injection equipments influence the heat release rate characteristically [9].

1.2.1.1 Zero-dimensional model

These models are attractive because they describe heat release rate by simple algebraic equations [26]. An important example of such a model is presented in[27], in which a strong relationship between fuel injection and heat release rates. However, this method is not accurate as there are no universal decay constants for elemental heat-release rates in different types of engines and their operating conditions.

1.2.1.2 Models based on fluid dynamics

These models are multidimensional models due to their inherent ability to provide detailed geometric information on the flow field based on the solution of the governing equations [26]. Several three-dimensional simulation models of injection, mixing and burning in diesel engines exist [28, 29], which describe the inner mechanism of diesel sprays and their influence on heat release. However, the volume of computation in multi-dimensional models is restrictive in carrying out detailed studies. In addition, their sub-models require a thorough validation with detailed experiments before employing them confidently in engine design work.

1.2.1.3 Phenomenological models

In phenomenological models, details of different phenomenon happening during combustion are added to basic equation of energy conservation [26]. In the simplest approach, [30] assumed the growth and motion of the spray within the chamber and [31] found that

the spray structure offered the clue to better heat release predictions.

The description of the thermodynamic conditions in the combustion chamber is based on a mathematical formulation of the conventional two-zone approach. It is assumed that at any time during the combustion process, the cylinder volume is divided into two zones, corresponding to burned and unburned gas regions [32]. In each zone the thermodynamic state is defined by the means of thermodynamic properties and the specific heat of each gas component changes according to the approximated formula from the JANAF thermodynamic properties table [33]. The quasi-dimensional thermodynamic model incorporates several sub-models to take into account several physical phenomena (turbulence, vaporization, spray and entrained gas mass flow rate). So far, this model provides the most accurate heat release approximations, while keeping low on computational requirements.

1.2.2 Lebas' Phenomenological Model

This phenomenological combustion and pollutant emissions model [34] is a recent development on Barba's approach [33]. In this model, the combustion process is divided in three parts:

- A cool flame, if Low Temperature Combustion conditions are met
- Pre-mixed burning with the hypothesis of flame propagation in the pre-mixed zone
- Oxidization the remaining fuel in a mixing controlled combustion mode.

The pressure evolution inside the combustion chamber is computed using the following equation:

$$\frac{dp}{dt} = \rho\left(\frac{dr}{dt}T + \frac{dT}{dt}r\right) + \frac{d\rho}{dt}rT, \tag{1.1}$$

where ρ is the density of the gas mixture inside the cylinder r is the perfect gas constant. For a mixture of N gases, r is determined by $r = \sum_{i=1}^{N} x_i r_i$, where x_i are the mass fractions of individual gases and r_i are their gas constants. T is the temperature, the evolution of which is determined by Barba's heat release model [33]. This model was chosen to be integrated in the simulator due to its accuracy and ease of implementation, as rich support for this model has been provided by IFP (France), in AMESim.

1.3 Engine Intake

From the air-path point of view, the engine works as a volumetric pump [9], i.e. the intake mass-flow is approximately proportional to its speed. Therefore, for a four stroke engine it can be modeled as

$$\dot{m}_i = \rho_i \dot{V} = \rho_i \eta_v \frac{V_d \omega_e}{4\pi}, \tag{1.2}$$

where ρ_i is the density of the gas at intake (dependent upon the intake manifold pressure and EGR ratio), η_v is the volumetric efficiency of the engine and V_d is the displaced volume.

1.4 Engine Exhaust

Since line losses are not taken into consideration, it is assumed that the exhaust conditions are the same throughout the path and pressure is undiminished from the engine up till the VGT turbine stage ($P_e = P_T$). The mass-flow is governed by the VGT position and the EGR.

1.5 Exhaust Gas Recirculation

Exhaust gas recirculation (EGR) redirects a portion of the cylinder exhaust gases into the intake manifold. As shown in Figure 1.1, the exhaust gas may be mixed directly with the intake flow or it may be cooled before mixing. As per the design of the DV6TED4 air-path, direct EGR is realized. The EGR mass-flow is regulated by a globe valve, conveniently referred to as the EGR valve. The flow dynamics are governed by the equations of orifice flow for compressible fluids, for an isothermal orifice with variable cross-sectional area.

$$\begin{aligned} \dot{m}_{egr} &= c_d A(x) \frac{p_e}{\sqrt{RT_e}} \Psi\left(\frac{p_e}{p_i}\right), \\ \Psi\left(\frac{p_e}{p_i}\right) &= \begin{cases} \sqrt{\gamma \left[\frac{2}{\gamma+1}\right]^{\frac{\gamma+1}{\gamma-1}}} & for\ p_i < p_{cr} \\ \left[\frac{p_e}{p_i}\right]^{1/\gamma} \sqrt{\frac{2\gamma}{\gamma+1}\left[1-\left(\frac{p_e}{p_i}\right)^{(\gamma-1)/\gamma}\right]} & for\ p_i > p_{cr} \end{cases} \end{aligned} \tag{1.3}$$

where c_d is the discharge coefficient of the valve, γ is the specific heat ratio, and R is the gas constant. The term $p_{cr} = \left[\frac{2}{\gamma+1}\right]^{\frac{\gamma}{\gamma-1}} p_e$ is the critical pressure, at which the flow reaches sonic conditions and velocity is choked [9]. The cross-sectional area function $A(x)$,

depends upon the valve opening position x. For the purpose of this study, this function was determined experimentally for the EGR Valve used in the DV6TED4 engine, using the gas-flow test bench at SOGEFI Motor Systems. As the globe wall maintains the same orifice shape throughout its opening range, its discharge coefficient is assumed to be constant for all openings. It was estimated at **0.85**, according to the geometry and channel specifications given in [35] and [36]. The valve was positioned at different opening percentages, determined by the percentage input voltage with respect to the voltage required for full opening. The actuator was mounted on the test bench and different mass flows were forced through it at different openings. The resulting pressure difference across the valve was recorded. The results are shown in Figure 1.2.

It can be noted that as the objective of these experiments was to calculate the effective area of the valve, these measurements were limited to mass flows, linear w.r.t. pressure differences. Based on these measurements, the area was calculated for each opening percentage, using Equation (1.3). The resultant area function was obtained through interpolation:

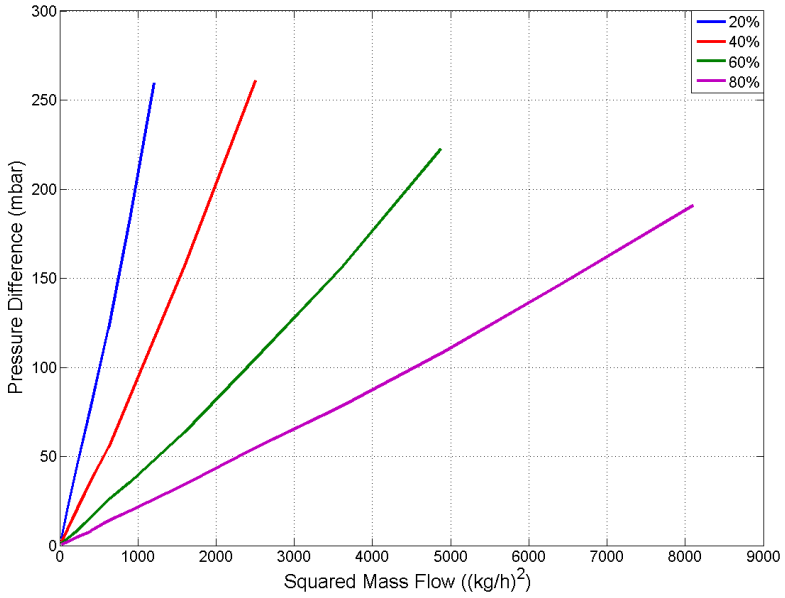


Figure 1.2. *Mass flow and pressure difference of EGR Valve at different openings*

$$A(x) = 0.0010251x^5 - 0.0031412x^4 + 0.00349001x^3 - 0.0016442x^2 + 0.0004x - (6.3816 \times 10^{-20}), \tag{1.4}$$

where the unit of $A(x)$ is m^2 and x varies from 0 (valve closed) to 1 (valve fully open). At $x = 1$, the full area is $1.6195e-004m^2$ or $161.95mm^2$.

1.6 Variable Geometry Turbocharger

The turbocharger, as introduced in the previous chapter, uses the energy of the exhaust gas passing through its turbine, to run the compressor and provide pressure boost in the intake manifold. The variable exhaust inlet of a VGT (Figure 1.3) allows the turbine flow cross-section to be varied in accordance with the engine operating point [37]. When the VGT vanes are closed, the exhaust gases speed up (since they are passing through a smaller orifice) and the turbine spins faster. When they open, the gases slows down but there is a larger amount of gasses to spin through turbine and give it more pumping power. Thus it effectively adapts the intake pressure to match the engine's needs during partial loads and transient running [38, 39]. As a result, the efficiency of the turbocharger and the engine is higher. Both intake and exhaust pressures are dependent upon VGT, the intake being regulated by the compressor and the exhaust by VGT vanes.

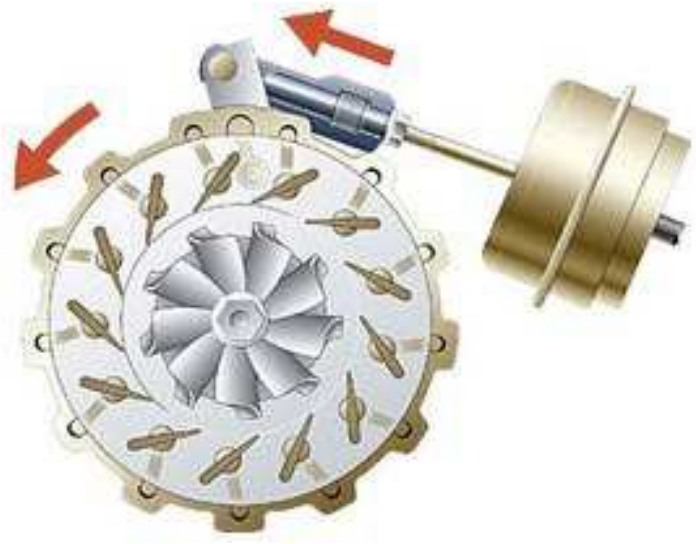


Figure 1.3. *Mechanical diagram of a variable geometry turbocharger*

1.6.1 Turbocharger mass-flow maps and correction

Manufacturers specify the performance characteristics of turbochargers in terms of the mass flow rate and isentropic efficiency for varying compressor speeds and pressure ratios

[40]. The flow performance curves of VGT used in the DV6TED4 engine are shown in Figures 1.4 and 1.5. The multiple data sets shown in Figure 1.5 correspond to flow characteristics at different VGT vane angles.

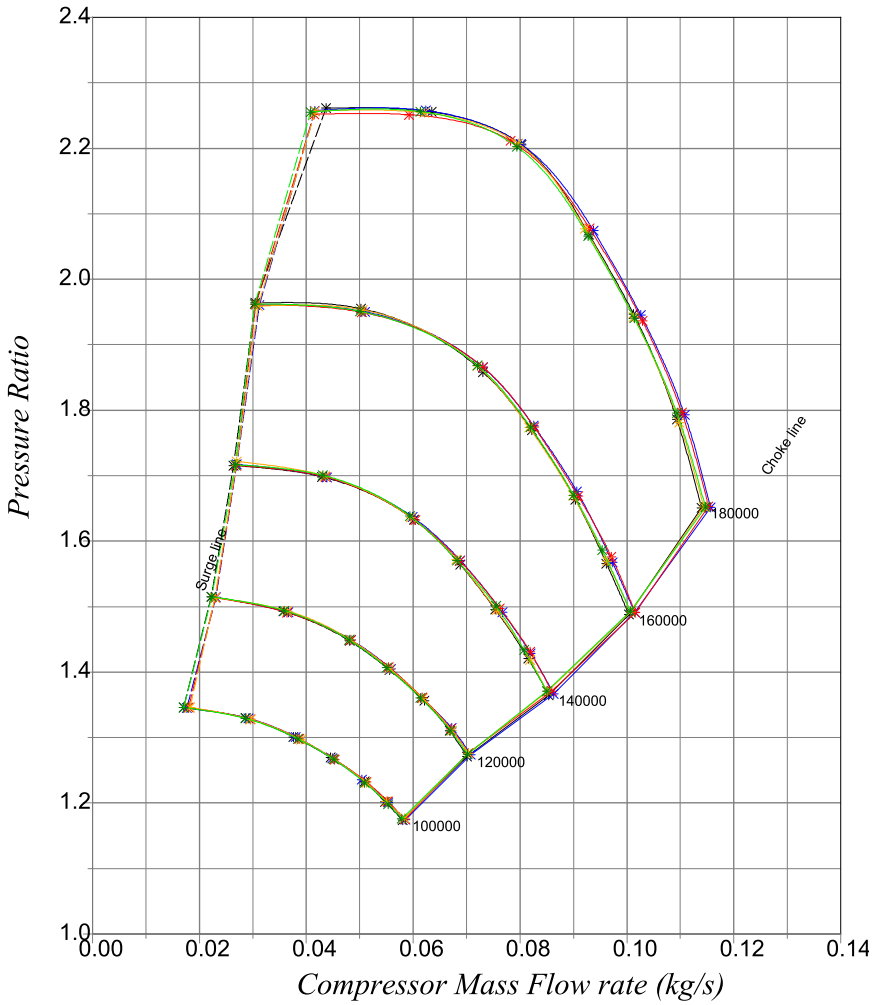


Figure 1.4. *Compressor performance curves for VGT installed on DV6TED4*

Conventionally, the performance maps are provided in terms of corrected mass flow rate $\dot{m}_{corr}$ and compressor rotational speed ω_{corr}, which eliminate the dependence of the maps on inlet conditions. These corrections make comparison possible between different compressors with different speed and mass flow characteristics. The corrected parameters are

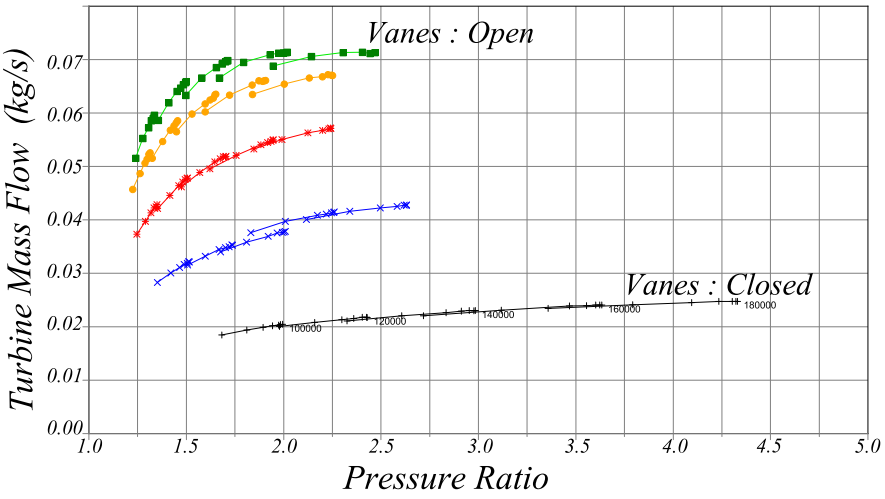


Figure 1.5. *Turbine performance curves for VGT installed on DV6TED4*

scaled according to standard temperature and pressure (STP) conditions, corresponding to 288.15K (15^oC) and 101.325 kPa (1.01325 bar) in Europe. For specific inlet conditions, the actual speed and mass-flow can be calculated by

$$\begin{aligned} \dot{m} &= \dot{m}_{corr}\frac{\delta}{\sqrt{\theta}}, \\ \omega &= \omega_{corr}\sqrt{\theta}, \end{aligned} \tag{1.5}$$

where

$$\theta = \frac{T_{inlet}}{288.15},\ \delta = \frac{P_{inlet}}{101.325}.$$

1.6.2 Compressor Power

Typically, the compressor stage of a turbocharger is of centrifugal type. The impeller rotation increases the velocity of the air, which is then decelerated in a diffuser. According to Bernoulli's principle, this results in increase in the static pressure. According to [41], the power P_c, required to drive the compressor to obtain a specific mass flow rate $\dot{m}_c$ is determined through the first law of thermodynamics:

$$P_c = \dot{m}_c\,(h_i - h_{atm}) = \dot{m}_c c_p\,(T_i - T_{atm}), \tag{1.6}$$

where h_x represent enthalpy and c_p is the specific heat coefficient of the air at constant pressure. For a general isentropic process, the pressure ratio is related to the temperature

ratio:

$$\frac{T_{1,is}}{T_2} = \left(\frac{p_1}{p_2}\right)^{\frac{\gamma-1}{\gamma}},$$

where γ is the ratio of the specific heat of the working fluid at constant pressure and constant volume (c_p/c_v) and the subscript is indicates isentropic process. In the case of compressor however, the process is not isentropic and the term isentropic efficiency $\eta_{c,is}$ needs to be defined, as

$$\eta_{c,is} = \frac{T_{i,is} - T_{atm}}{T_i - T_{atm}} \tag{1.7}$$

where $0 \leq \eta_{c,is} \leq 1$. Practically, $T_{i,is}$ represents the theoretical temperature rise (as predicted by the ideal gas law) and T_i is the actual temperature rise. From here, the temperature ratio for a turbocharger compressor can be related to the pressure ratio as

$$\frac{T_i}{T_{atm}} = 1 + \frac{1}{\eta_{c,is}}\left[\left(\frac{p_i}{p_{atm}}\right)^{\frac{\gamma-1}{\gamma}} - 1\right],$$

and Equation (1.6) becomes

$$P_c = \dot{m}_c c_p T_{atm} \frac{1}{\eta_{c,is}}\left[\left(\frac{p_i}{p_{atm}}\right)^{\frac{\gamma-1}{\gamma}} - 1\right]. \tag{1.8}$$

1.6.3 Turbine Power

The modeling of turbine is similar to that of the compressor, as given by Equations (1.6), (1.7) and (1.8). The power P_T input depends upon the exhaust gas flow $\dot{m}_T$ [41], calculated through the first law of thermodynamics:

$$P_T = \dot{m}_T c_p T_T \eta_{T,is}\left[\left(1 - \frac{p_T}{p_{atm}}\right)^{\frac{\gamma-1}{\gamma}}\right]. \tag{1.9}$$

where $\eta_{T,is}$ is the isentropic efficiency of the turbine.

1.6.4 Turbocharger Speed

Using the relationship between the net power and net torque ($P = \tau\omega$), the rotational speed of the turbocharger is calculated as follows:

$$\dot{\omega}_{tc} = \frac{P_T - P_c}{J_{tc}\omega_{tc}}, \tag{1.10}$$

where J_{tc} is the moment of inertia of the turbine-compressor linkage.

1.7 Simulator Implementation in AMESim

AMESim stands for **A**dvanced **M**odeling **E**nvironment for performing **Sim**ulations of engineering systems. It is a multi-domain software that allows interconnection between systems of different physical natures (hydraulic, pneumatic, mechanic, electrical, thermal, etc.). Modeling in AMESim is based on Bond graph theory, i.e. systems are modeled using a set of dynamic equations and power is transmitted between systems by a combination of generalized effort and flow notions [42]. However, AMESim uses graphic icons instead of traditional graphs, based on the standard symbols used in the engineering field or symbols which give an easily recognizable pictorial representation of the system. Interconnections are made through ports defined on the icons and causality is ensured by fixed input and output ports of each icon. AMESim comes with a large number of containing models for different physical domains. These libraries are written in C language

As mentioned in the introduction, this software was chosen because its libraries are adapted for automotive applications. The air-path was developed in the general form as shown in Figure 1.1. The implemented scheme is shown in Figure 1.6. The parameterization to the specifications of the engine and air-path of the DV6TED4 engine system was made possible by the collaborative effort of the partners of Project SIMBA. The details of the components of this model are presented in this section.

1.7.1 Cylinder and Combustion

The cylinder model in IFP library represents a combustion model in a thermal-pneumatic chamber with a variable volume, pressure dynamics and wall heat exchanges (Figure 1.7). This is a discrete event model, designed for direct injection diesel engines. The working fluid is a mixture of three gases: air, fuel and burned gas. The fuel $C_xH_yO_z$ is defined by 3 parameters: x, y, z and the heating value (Net Calorific Value). Combustion is simulated by Lebas' model [34, 43], which determines the heat release rate, and therefore the temperature evolution.

The additional important parameters required to configure this model are the cylinder geometry (bore, stroke, compression ratio), volume V_d, volumetric efficiency η_v, intake and exhaust valve characteristics, firing angle and number of injections. The pistons are connected to the crankshaft, upon which, the load torque is imposed through a rotary torque module (lower left of Figure 1.6).

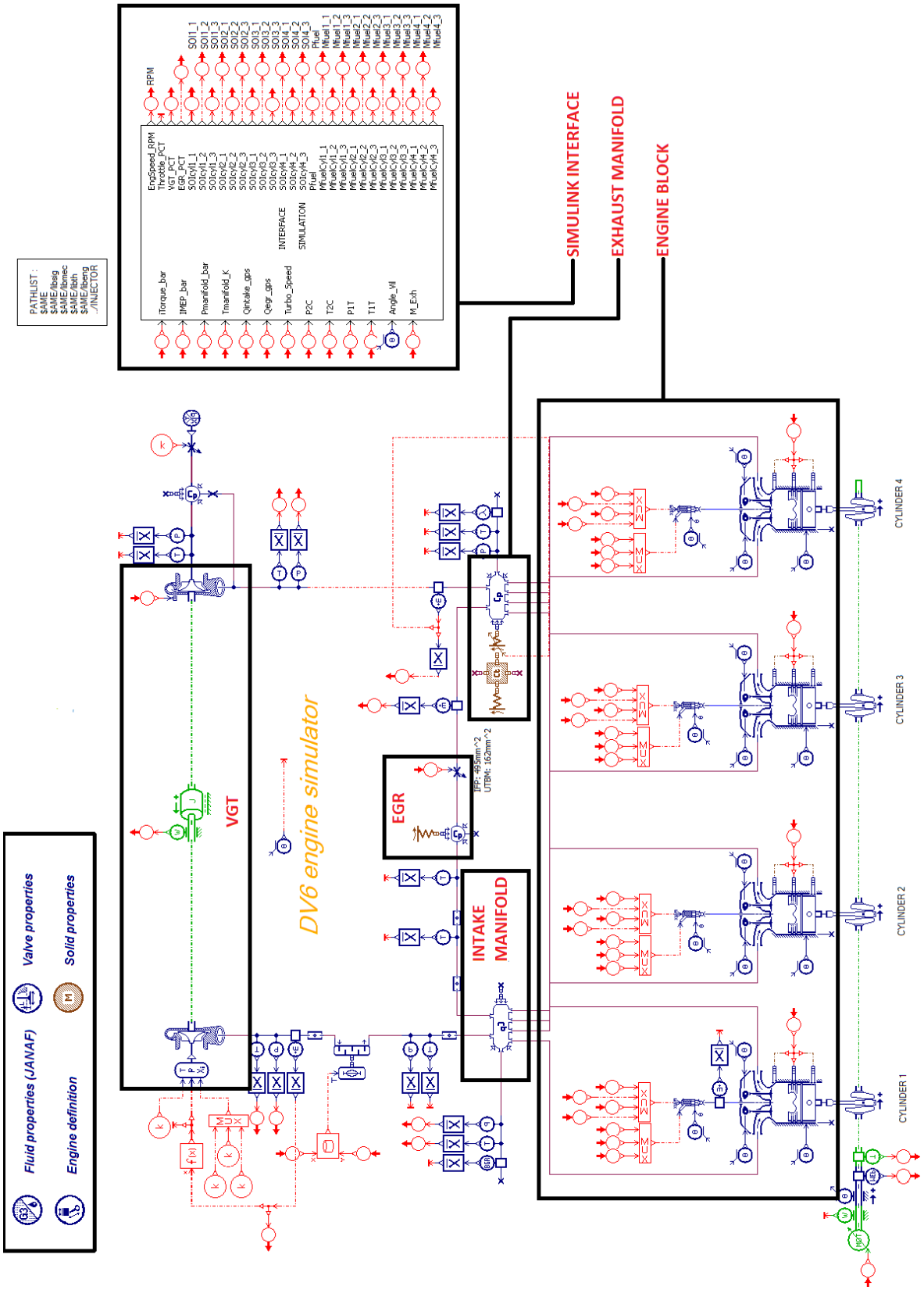


Figure 1.6. *Overview of simulator implementation in AMESim*

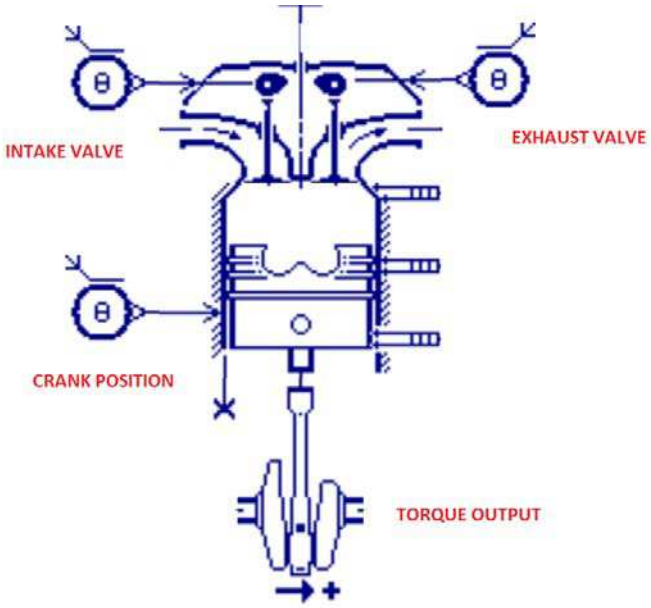


Figure 1.7. *Cylinder Model*

1.7.2 Intake and Exhaust Manifolds

As the air-path is modeled in 0D, the manifolds are modeled as constant volume chambers. The submodel provided in AMESim for this purpose can be configured to accommodate multiple gases, each with an associated mass flow rate and enthalpy flow rate. The model outputs are pressure and temperature, the latter being obtained using the ideal gas law. It can be seen in Figure 1.6 that the intake manifold is configured to receive fresh air from the turbocharger and burned gas from EGR. Air swirl is not taken into consideration, since the air-flow geometry is not studied in 0D models.

1.7.3 Exhaust Gas Recirculation

The EGR is implemented using a valve model based on equations of orifice flow with variable cross-sectional area (Figure 1.8), same as (1.3). A constant volume chamber is used to simulate the delay due to gas transmission lines.

1.7.4 Variable Geometry Turbine

The Variable Geometry Turbine (Figure 1.9) is modeled using three components: the turbine with variable flow area, the centrifugal compressor and an inertial component

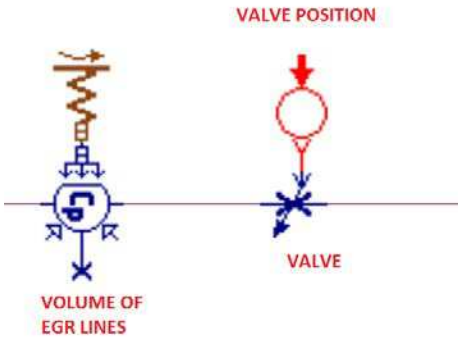


Figure 1.8. *EGR Model*

representing the connecting shaft.

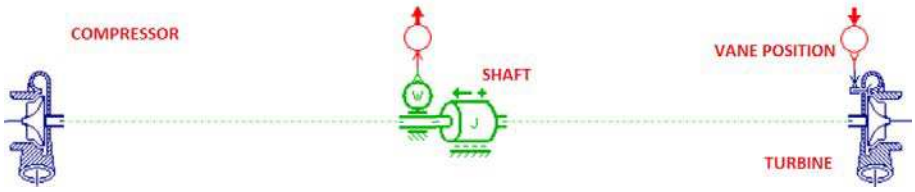


Figure 1.9. *VGT Model*

1.7.4.1 Turbine

The VGT vanes are defined in terms of percentage opening. The mass flow through the turbine is then determined using the manufacturer's characteristic curves. The flow characteristics of the turbine are provided to the model in form of table that contains the numeric values of the curve data points. Hence, for each tested vane opening, the number of iso lines are defined in the table. Then, for each iso line, the number of data points and their values (pressure ratio and mass flow) are defined, as follows

Vane POS0	Nb iso	
	RPM0	Nb Pr
	PR0	mass0
	PR1	mass1
	...	
Vane POS1	Nb iso	
	RPM0	Nb Pr
	PR0	mass0
	PR1	mass1
	...	

The turbine power is calculated in the same way as mentioned in Section 1.6, using Equation (1.9).

1.7.4.2 Compressor

The compressor receives input power from the turbine, and is modeled using the mass flow characteristics provided by the manufacturer. These characteristics are coded in the same manner as those of turbine, with the exception that vane position data sets are not present. The compressor dynamics are stabilized in the AMESim model by using smooth dissipation functions in cases where the rotational speed is very low. Power consumed by the compressor is calculated as mentioned in Section 1.6, using Equation (1.8).

1.7.4.3 Inertial shaft

This element adds the shaft inertia to the system. It is modeled simply as a mass rotating under an applied torque. The net speed of the turbocharger is calculated from the dynamic equation (1.10), using the turbine and compressor powers and the the moment of inertia of the shaft.

1.7.5 Fuel Injection

The fuel injection unit (Figure 1.10) is configured to provide a pilot injection and a main injection. The injection timing is configured in terms of crank angle position. Rail pressure and duration of injection are provided separately. More details of this unit are discussed in Chapter 3.

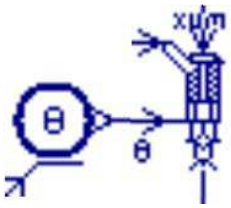


Figure 1.10. *Fuel Injector Model*

1.7.6 Auxiliary components

In addition to these major components, some minor additions were made in accordance with the specifications of DV6TED4. In the intake path, a pressure loss was introduced to simulate the effect of air filter and a heat exchanger was added between the compressor and the intake manifold. In order to validate the model, it was necessary to interface it with a controller already in use. Therefore, an interface block was also introduced to connect it to Simulink. The details of this interface and the controller are presented in Chapter 4.

1.8 Summary

In this chapter, the flow dynamics of the gases in the air-path were studied. The components were modeled and implemented to form a complete air-path simulator. In order to generate realistic pulsating flow and pressure, a cylinder by cylinder combustion model was used, in which injection and combustion are synchronized to the crankshaft angle.

The development in this chapter was focused on the gas flow inside the air-path. The flow dynamics depend on two important parameters; the position of the VGT vanes that governs the flow area through the turbine, and the position of the EGR valve that governs the flow area for EGR. In practice, these two are controlled using mechatronic actuators. The dynamics of these actuators play an important role in the overall performance of the air-path, as they have nonlinear characteristics. In the next chapter, a study is carried out on modeling of mechatronic actuator and their integration to complete the Simulator.

As a first step, the lengths of transmission lines were not considered in the model, keeping its level to 0D. In future, we intend to extend the models to obtain 1D simulations.

Chapter 2

Actuator Modeling

In the last chapter, we saw that control valves exist various parts of the air-path, to regulate the mass-flow of different gases (Figure 2.1). While the flow characteristics of these valves were modeled in the previous chapter, their dynamics can also not be ignored. The automobile engine is required to perform in a highly variable environment [44, 45, 46], where the load torque changes continuously with the changes in road conditions, engine load and weather [47] and these changes affect the valve actuation systems as well. In modern engines, the preferred method for valve actuation (positioning) is through electric motors. Therefore electro-mechanical models of these mechatronic (motor+valve) actuators need to be incorporated in the global air-path [47, 48, 49]. Actuators may be single action or double action. In the former, the motor drives the actuator in one direction and the return torque is provided by a spring. In the latter, the motor drives the actuator in both directions. Mechatronic actuators allow precise control over air flow dynamics under different operating conditions [44], however this is only possible if their control has been designed to accommodate their nonlinear behavior, as well as parametric variations and external disturbances [50, 51].

The focus of this study is the characteristics of different actuation methods (positioners) and their classification according to their construction and technology. A survey of commercial actuators showed that there exist two categories of mechatronic actuators in the market. The first category is of PMDC motor based single action actuators. These are characterized by return springs and gearing. The second category is of torque motor based

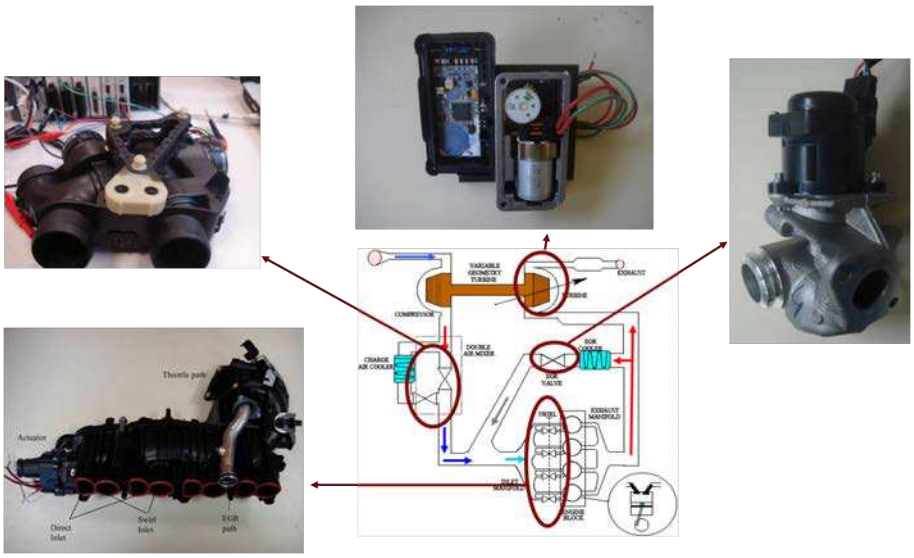


Figure 2.1. *Different control valves and actuators in an air-path*

single action actuators. Since torque motors can drive the actuator directly, due to their high torque, no gearing is required. Hence they are characterized by the presence of return springs. In this chapter, these classes of actuators have been modeled and a generic nonlinear model has been derived, which can be parameterized according to the specifications of a large number of actuators. The main causes of actuator nonlinearity are friction and temperature variation. The proposed model takes into account these factors, and is simple enough to be used for simulation and control.

2.1 Actuator Terminology

Air-path actuators, like all control valves, consist of three basic components, the working part or valve body, the positioner, which is a device that positions the throttling element inside the valve body, and position sensors to provide feedback to the controller that governs the positioner [52].

Valve Body

The valve body in air-path actuators is either of globe type in linear actuators or butterfly type in rotary actuators. Stick-slip can be a serious problem where high pressure build-up is expected when the valve is closed. Butterfly valves are hence, seldom used where the required flow might be less than 15% of the valve opening [52]. It has been seen that

butterfly valves are indeed used where continuous flow is required, while globe valves are used for measured or ”dosed” air flow. EGR valves are almost exclusively globe valves.

Positioner

An actuator with an electric motor as the prime mover comes to our minds whenever we discuss electronics based control systems. However, until recently, electric motors were not the movers of choice. Instead manufacturers preferred electro-pneumatic or vacuum actuators in the air-path [13], since they could provide a better size-to-torque ratio. Now, with recent advances in electric motor technology, older electro-pneumatic actuators are losing their popularity in favor of fast and efficient mechatronic actuators [45]. Normally, two types of motors are found as positioners in air-path actuators, the Permanent Magnet DC motor (PMDC motor) or limited angle torque motors [48]. PMDC motors are used mostly with a high gear reduction to provide enough application torque. Torque motors are a special breed of high torque electric motors, that can be used for direct drive of actuators. On the other hand, their rotation is limited. These motors allow actuators to have faster response time and accuracy in transient conditions[45, 50]. Apart from these, some variants of the conventional PMDC motor can also be found in application. The variations usually involve differences in construction. Stepper motors are also used in actuators found in very high power applications. Their use however is rare in the engine air-path control.

The positioner defines the action type of the actuator. Positioners are of either single action type or double action type. Single action positioners have combined motor-spring systems. The spring provides return force. Single action actuators always return to their original zero position when de-energized. Double action positioners have motors only, and the direction depends upon the motor power supply direction. These actuators maintain their position when de-energized. Geartrains are used for torque enhancement wherever necessary. PMDC motor based actuators almost always require gear reduction. In single action actuators, plain gears are used, while double action actuators use at least one worm-gear stage, to provide higher holding torque. Furthermore, positioner rotation can be converted into linear motion for linear actuators, using cams and screws. In this thesis, the term mechatronic actuator refers to actuators with electric motors as positioners.

Sensor

Position sensors are important in actuator control therefore it seems suitable to introduce

different common sensing technologies as well. Modern actuators use non-contact sensors exclusively as they are more accurate and last longer due to lesser wear [14, 53]. The common principles used in non-contact sensor technology are capacitive, optical, magnetic and inductive [14]. Capacitive sensors allow good accuracy at low range but they are highly sensitive to humidity, vibrations and other environmental factors. Optical sensors, such as incremental encoders are highly accurate in a large range, and are extensively used in industrial machine tools. However they are fragile, expensive and must be protected from dust and ambient light [53]. Hall effect based sensors are the most common type of position sensors found in automotive actuators. They are inexpensive and highly robust due to their practical insensitivity to nonmagnetic dust, humidity and vibrations.

2.2 Major Actuator Families

Mechatronic actuators are most commonly found as single action actuators, in which force is applied in only one direction. In order to open the actuator, the magnitude of force is increased, and in order to close, the magnitude is decreased. The return force is provided by a return spring. Double action actuators, though less common, are found where more precision is required and where a higher holding torque is required. The actuators considered in this study are presented below.

Actuator	**Motor Type**	**Manufacturer**
EGR	Torque	Valeo
Double Air Mixer	Torque	Delphi
Air Inlet Swirl	PMDC	Bosch
Air Inlet Swirl	PMDC	Pierburg

TABLE 2.1: *Actuators Under Study*

A description of all these actuators is presented in the following subsections. They have been categorized according to their mechanisms. As discussed above, the first category contains PMDC motor based single action actuators, the second category contains Torque motor based single action actuators.

2.2.1 DC Motor based actuators

Permanent magnet DC motors have been popular historically in the actuator business. Cheap and easily available, most manufacturers prefer using small DC motors to make actuators. However these motors do not provide enough torque for air-path applications, and hence, need sufficient gear reduction. A motor-spring system has the motor working against a spring. Hence it can move in one direction by increasing the motor voltage and in the other direction by decreasing the voltage. Supply polarity does not have to be switched since the spring pushes the shaft back to the original position. Hence these actuators can be used for position control in open loop, since they can maintain a certain position at a certain voltage.

In this study, we have taken actuators based on permanent magnet DC motors and spring, the Bosch GPA-S and the Pierburg EAM-i. These two simple rotary actuators (Figures 2.2 and 2.3) contain a motor-spring system for position control. The motor and output shafts are coupled with two stage simple gears. The return spring is pre-compressed to ensure that the valve returns to its initial position in case of electrical failure.

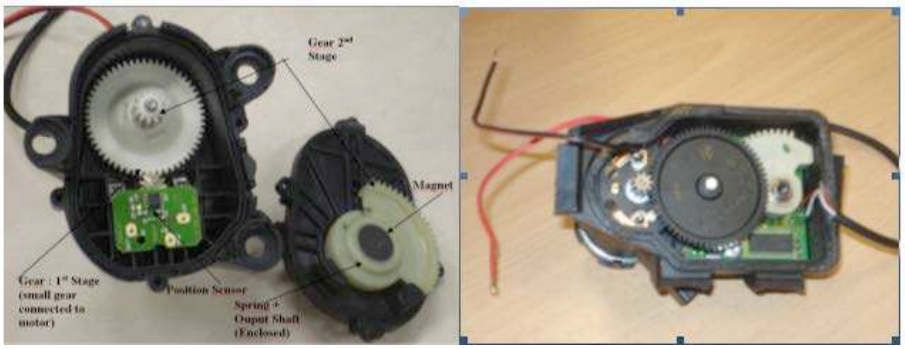
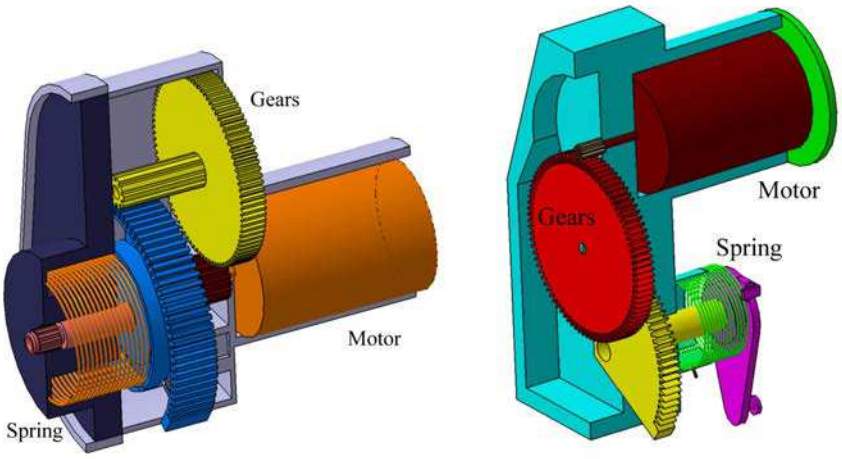


Figure 2.2. *DC Motor based actuators a: Bosch GPA-S b: Pierburg EAMi*

The issue of gearing PMDC motors to generate the desired size to torque ratio, and the resultant increase in friction and backlash problems [48, 54, 50, 55], has been addressed recently, with new advances in electric motor technology. New high torque direct drive motors, such as the Pancake DC torque motor [56, 57] produce enough torque to be connected directly to the load-bearing mechanical parts, without any reduction coupling required.



(a) Bosch (b) Pierburg

Figure 2.3. *3D Cutaway*

2.2.2 Torque Motor based actuators

"Size to torque ratio" is an important parameter that actuator designers search for in a motor [56]. Small DC motors require a substantial gear reduction to be able to provide enough torque. Not only does that add miniaturization problems for the designer, but gear trains are prone to mechanical non-linearities, such as gearbox friction and backlash.

Direct Drive motors, such as the limited angle torque motor, have been in use for a long time in the aerospace industry [56, 58]. These motors provide limited angular motion, suitable for actuator purposes, at a relatively high torque [59]. They can hence be coupled to the mechanical part of the actuator without any additional parts or reduction. This leads to better tracking and positioning control of actuators since the nonlinearities associated with gears are no longer present [60, 61]. Their improved size-to-torque ratio and fast response time are also an asset for the designer.

In the automobile industry, manufacturers have turned their attention towards axial flux torque motors [56, 59] for actuators. The torque motor develops a much higher torque internally, as compared to the DC motor. Hence it normally does not require gears and can be used directly to drive mechanical parts of actuators. However, by virtue of its construction, it does not provide continuous rotation. It can maintain certain positions,

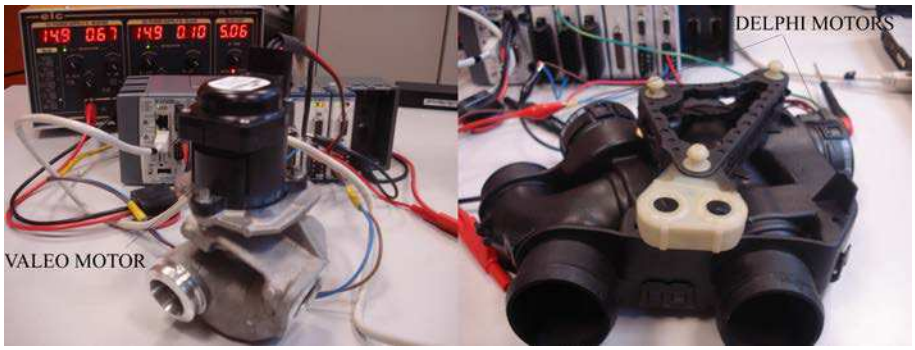


Figure 2.4. *Torque Motor based actuators (a)Valeo EGR Actuator (b)DELPHI Double Air Mixer*

and once energized, the rotor attains the position rapidly. Once positioned, further motion in any direction is no longer possible. Naturally a four pole torque motor is capable of maintaining positions at intervals of 90^o only. In order to achieve continuous motion, the torque motors are used exclusively as motor-spring single action systems (as described in the case of PMDC) for rotation of about 70^o between the poles.

2.2.2.1 Working Principle

The torque motor has a four-pole electromagnetic stator with axial flux. The rotor has a fixed four pole permanent magnet disk with alternating polarities. When energized, the rotor rotates to a position where the stator and rotor poles are aligned, and holds itself there. However, with a torsion spring, it can be used efficiently and effectively for continuous actuators [56]. Unfortunately, not much literature is present on this motor, to the best of our knowledge. Therefore they were studied in detail during this research work. The motor construction can be seen in Figure 2.5 and the working principle is described below:

- In general, this motor has a four-pole electromagnetic stator with axial flux. Four separate pole pieces, each wound with its own coil.
- In the stator design, the coils are wound in such a way that when the motor is energized, the pole faces develop alternate magnetic polarities (North-South-North-South).

- The rotor has a fixed disk of permanent magnet with alternating polarities (North-South-North-South).
- When the motor is energized, the stator magnetic field pulls the magnet to align rotor poles with stator poles (Stator North poles pull Rotor South poles and vice versa).
- Since the rotor is fixed to a bearing, this pull develops a torque about the rotor axis, rotating the rotor until rotor poles are aligned with stator poles.
- The torque motor rotates to the position of alignment as soon as it is powered, and holds itself there.
- Since no net torque can be present once the magnetic fields attain axial alignment, no rotation is possible after alignment.
- However, with a torsion spring, the motor can be used efficiently and effectively for positioning over the working range between poles.

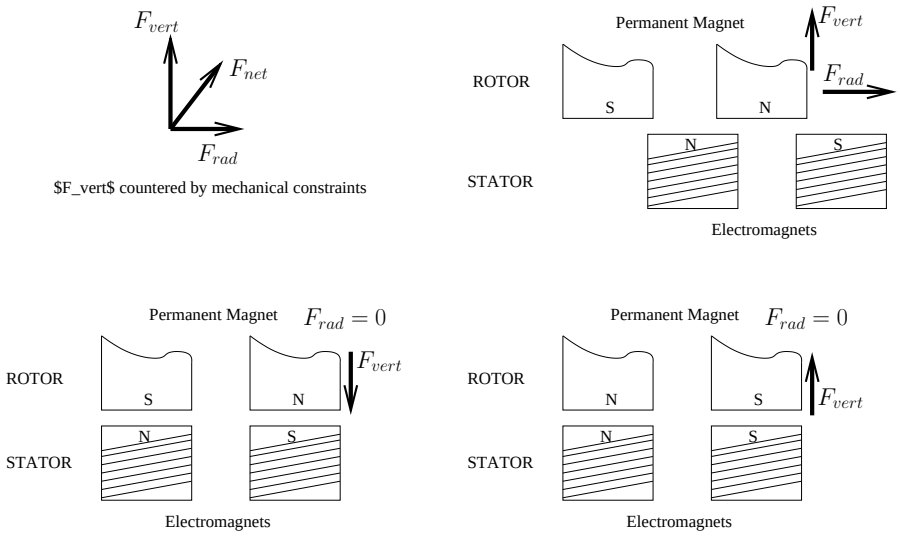


Figure 2.5. *Simplified working principle of torque motors*

Two actuators, using torque motors as positioner are shown in Figure 2.4. These actuators use torque motors of different constructions, but the principle is the same. The Delphi Double air mixer uses multi-coil torque motor and the Valeo EGR Actuator uses single

coil torque motor. The difference between these constructions is described below:

Multi-coil Torque Motor (Figure 2.6): In this type of construction, each stator pole has its separate set of windings.

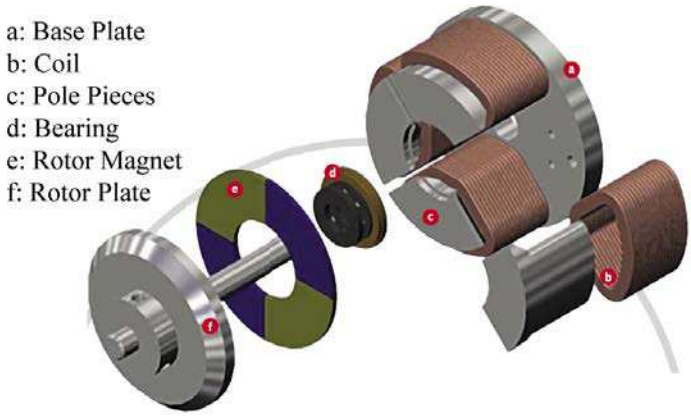


Figure 2.6. *Multi-coil torque motor*

Single Coil Torque Motor (Figure 2.7): In this type of construction, the stator poles are magnetized using a single coil. The coil energizes a central pole piece, which, according to the construction and rotor alignment, develops a magnetic Pole on the face that is towards the rotor. Through its elongated construction, this single piece is divided into two poles. The other two pole pieces are connected to the opposite side of the central pole piece, through the metal plate. This results in giving them opposite poles on the face that is towards the rotor. Thus, a single coil provides alternate N-S-N-S configuration.

Remark:

The construction not only restricts the motion of a torque motor to 90^o, but results in a torque characteristic very different from that of DC motors. While the torque of DC motors is proportional to the current only, the torque motor has a torque that is a function of the angular misalignment between stator and rotor poles. Hence the torque varies with respect to the rotor angle. This has been illustrated in Figure 2.8. It can be seen that that the effective working area of the torque motor is nearly 75^o, while as the poles reach alignment (0^o and 90^o), the torque reduces to 0. In practice, the torque can be modeled

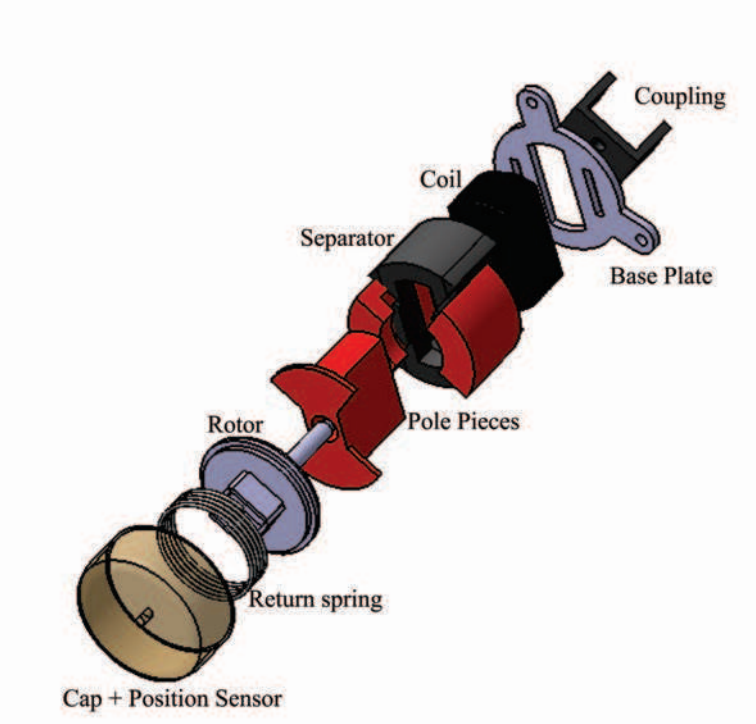


Figure 2.7. *Valeo torque motor*

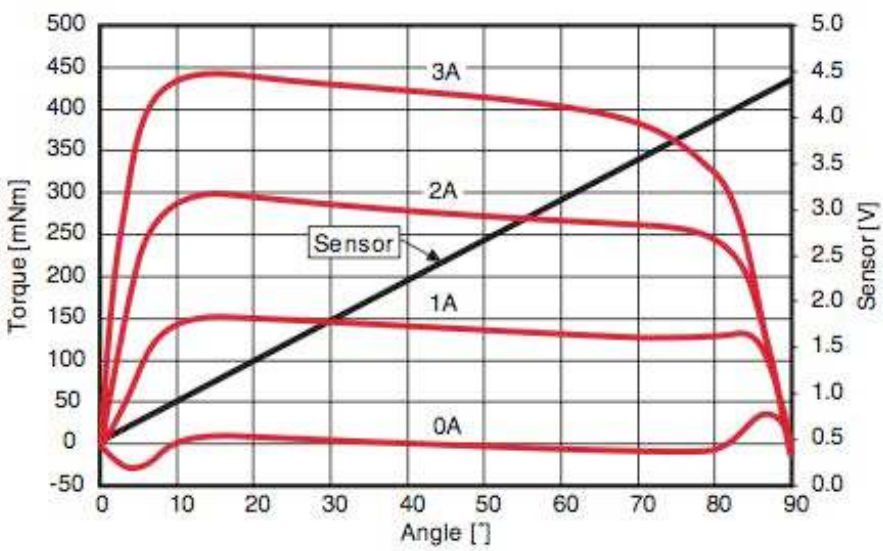


Figure 2.8. *Torque Motor Characteristics*

either as an interpolated function, or as we have used in our simulations, a lookup table based on experimental values obtained from torque measurement.

2.3 Actuator Modeling

While the flow characteristics [52] of the valve might be different (equal percentage, linear or quick opening), normally a linear characteristic is expected between the positioner motor input (supply voltage) and actuator position, such as shown in Figure 2.9.

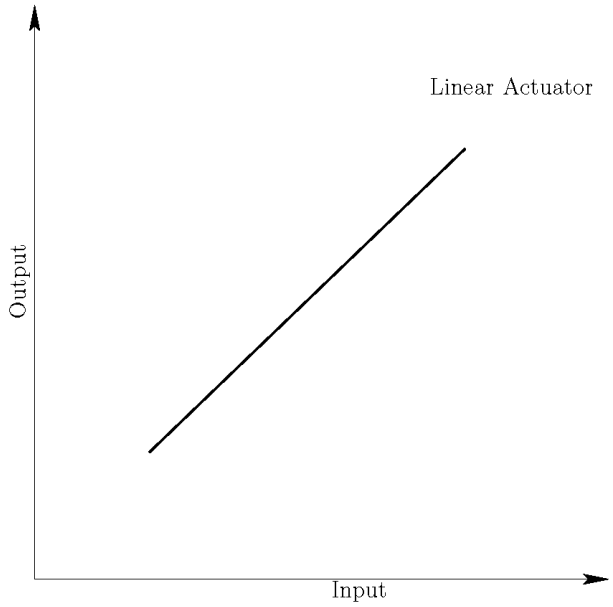
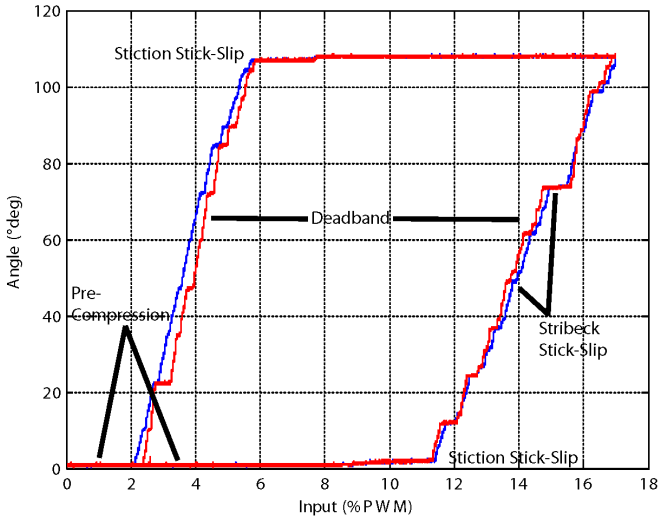


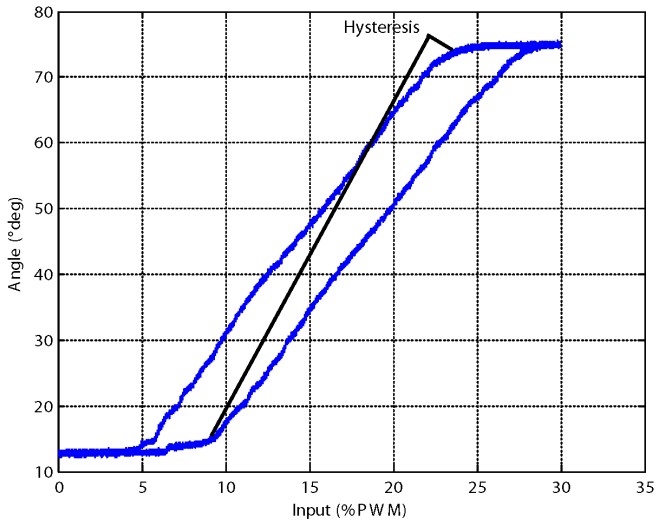
Figure 2.9. *Expected characteristic of a Single Action Mechatronic Actuator*

Unfortunately, real actuators do not possess such ideal characteristics. The experimentally obtained characteristics of two actual air-path actuators (Bosch PMDC, Valeo Torque) are shown in Figure 2.10. It is evident that the actuators have nonlinear behavior. There are three major nonlinear phenomena clearly noticeable in the characteristic curves [62]. In accordance with the work presented in [63], these phenomena are defined as follows.

Dead band:
In both the actuators, the dead band is the most noticeable feature. This phenomenon



(a) PMDC Motor based Geared Actuator



(b) Torque Motor based Direct-Drive Actuator

Figure 2.10. *Experimentally obtained characteristics of two Single Action Mechatronic Actuators*

occurs when the actuator changes direction. It is defined as *the range through which the input may be varied upon direction reversal, without any observable change resulting in the output [62].* As seen in Figure 2.11, a dead band changes the input-output relationship of an actuator for increasing and decreasing signals.

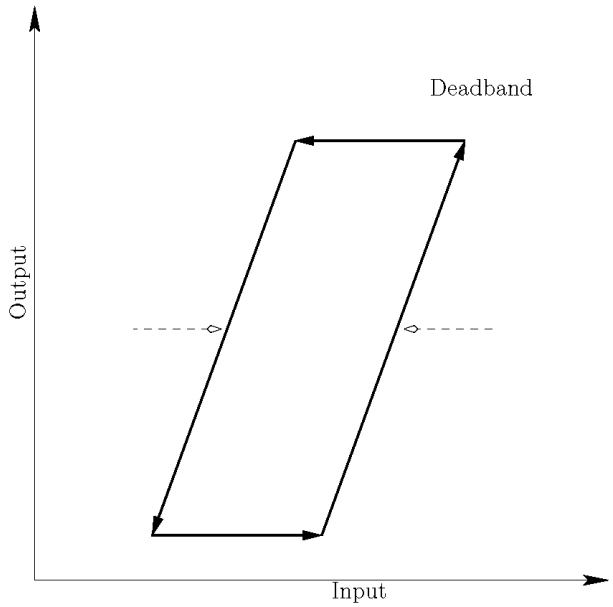


Figure 2.11. *Deadband*

Hysteresis:
Hysteresis (Figure 2.12) is defined as *the dependence of the position upon not only the present input but previous inputs as well as the direction [62].*

Dead Zone:
The dead zone is defined as *a range of input* ***irrespective of the direction of motion*** *during which the actuator position remains unchanged [62].* This phenomenon has been shown in Figure 2.13. A dead zone exists in both the actuators, seen as the shift from origin.

In this section, we address the modeling of air-path actuators based on PMDC and torque motors, taking into account this nonlinear behavior. It is shown later on, that the key factors behind this nonlinearity are friction and temperature. Therefore, various methods

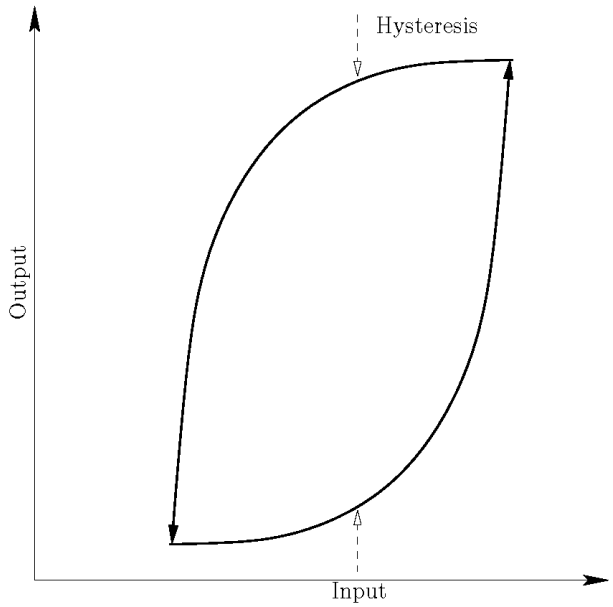


Figure 2.12. *Hysteresis*

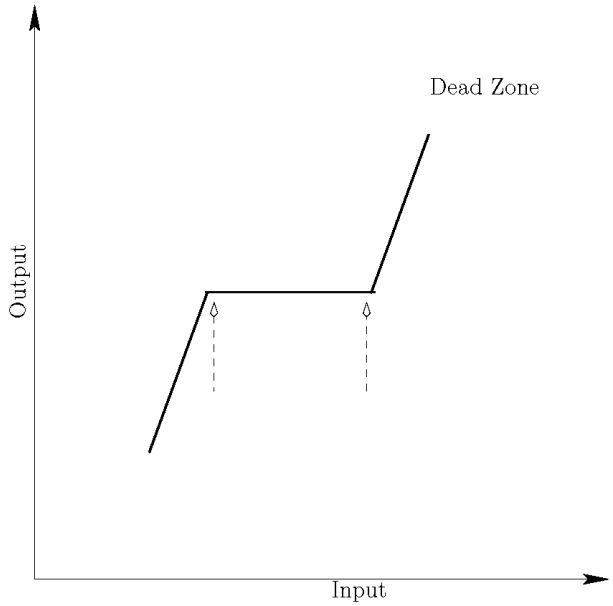


Figure 2.13. *Dead Zone*

for friction modeling have been discussed and the effect of temperature variation have also been studied. As an effective control strategy would demand compensation of nonlinearity in order to produce desired closed-loop characteristics, this chapter also serves as a basis for identification of nonlinearity and the design of predictive, robust and adaptive compensators.

NOTE: *This study has been carried out in the context of engine air-path actuators, however the contents are general and the phenomena discussed in this paper can be found in any actuator or electro-mechanical system.*

2.3.1 PMDC Motor-Spring Systems

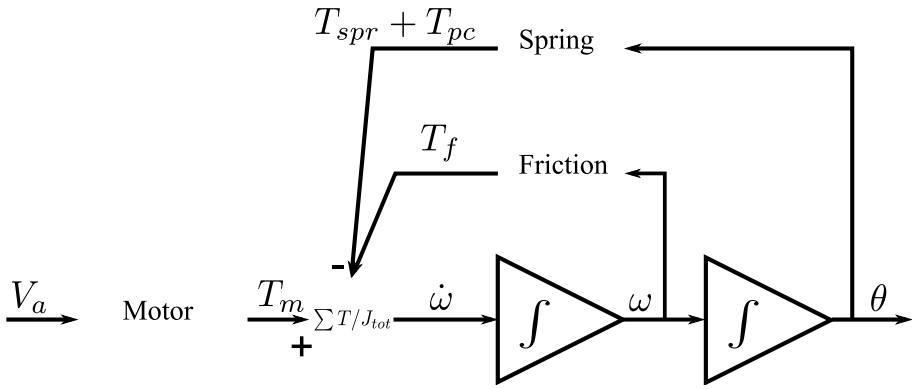


Figure 2.14. *Block diagram of Motor-Spring system*

As explained before, permanent magnet DC motors do not produce sufficient torque to be used directly to drive an actuator. Hence the actuators based on these motors require gear reduction. The motor-gear-spring system dynamics can be modeled by balancing all torques (Figure 2.14); using the following electrical and mechanical equations:

$$V_a = i_a R_a + L_a \frac{di_a}{dt} + E_a \tag{2.1}$$

$$J_{tot} \frac{d\omega}{dt} = T_m - (T_{spr} + T_{pc}) - T_f \tag{2.2}$$

In Equation (2.1), V_a is the armature voltage, i_a is the armature current, R_a is the motor coil resistance, L_a is the motor coil inductance. In general, the transitory current $L_a(di_a/dt)$ can be neglected since the mechanical time constant is generally much greater than the electrical time constant [50]. The motor back EMF E_a is defined as:

$$E_a = K_{em}\omega_m = K_{em}r\omega \tag{2.3}$$

where, K_{em} is the motor electromagnetic constant, ω_m is the angular velocity of the motor shaft, ω is the angular velocity of the output shaft of the actuator. The gear ratio r is defined by $r = \omega_m/\omega$

In Equation (2.2), J_{tot} is the total moment of inertia of the system. T_m is the electromagnetic torque, expressed from the output shaft reference as:

$$T_m = K_a i_a \tag{2.4}$$

Where $K_a = K_{em}r$ T_{spr} , the spring torque is defined by:

$$T_{spr} = K_{spr}\theta \tag{2.5}$$

T_{pc} and T_f are pre-compression and friction torques respectively. T_{pc} is constant and can be estimated through experimentation. The modeling of friction (T_f) is discussed separately. Replacing (2.3), (2.4) and (2.5) in equations (2.1):

$$K_a i_a = J_{tot}\frac{d\omega}{dt} + K_{spr}\theta + T_{pc} + T_f \tag{2.6}$$

The current, then, can be expressed from the equation (2.1) as:

$$i_a = \frac{V_a - E_a}{R_a} \tag{2.7}$$

Replacing (2.3) and (2.7) in (2.6), we get:

$$K_a\left(\frac{V_a - K_a\omega}{R_a}\right) = J_{tot}\frac{d\omega}{dt} + K_{spr}\theta + T_{pc} + T_f \tag{2.8}$$

The motor dynamics can hence be represented by the second order system with a second member:

$$\frac{K_a V_a}{R_a} = J_{tot}\frac{d^2\theta}{dt^2} + \frac{K_a^2}{R_a}\frac{d\theta}{dt} + K_{spr}\theta + (T_{pc} + T_f) \tag{2.9}$$

Let us consider a generalization of the characteristic curves in terms of duty cycle (Figure 2.15).

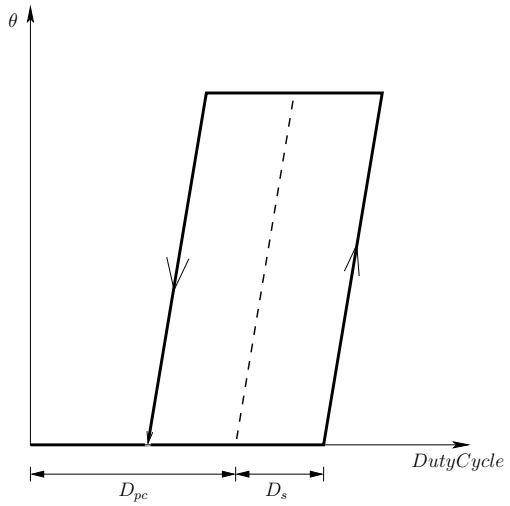


Figure 2.15. *Actuator Characteristics w.r.t. Duty Cycle*

Considering static friction to be the significant friction component, we can obtain the following variable change:

$$\overline{V_a} = V_a - V_a^*, \tag{2.10}$$

where

$$V_a^* = \frac{T_f R_a}{K_a} + \frac{T_{pc} R_a}{K_a}$$

is defined as the voltage required to overcome T_{pc} and T_f.

Let us define D as the applied duty cycle, D_a as the duty cycle at which the actuator moves, D_{pc} as the duty-cycle leading to countering the spring pre-compression and D_s as the amount countering the static friction. The value of static friction and spring pre-compression torque can directly be calculated from the graph as:

$$D_s = \frac{T_s R_a}{K_a V_s}, D_{pc} = \frac{T_{pc} R_a}{K_a V_s}$$

The effective duty-cycle and armature voltage then become:

$$D_a = D - (D_{pc} + D_s), \overline{V_a} = D_a V_s$$

for all positive values of Da and 0 for the rest.

Replacing V_a in equation (2.9), the system dynamics become:

$$\frac{K_a\overline{V_a}}{J_{tot}R_a} = \frac{d^2\theta}{dt^2} + \frac{K_a^2}{R_aJ_{tot}}\frac{d\theta}{dt} + \frac{K_{spr}}{J_{tot}}\theta$$

Considering initial conditions to be zero, the transfer function of the system can be written by performing Laplace transformation:

$$\frac{\theta(s)}{\overline{V_a}(s)} = \frac{\frac{K_a}{J_{tot}R_a}}{s^2 + \frac{K_a^2}{R_aJ_{tot}}s + \frac{K_{spr}}{J_{tot}}} \tag{2.11}$$

This transfer function can be compared to the general form of a second order system,

$$F(s) = \frac{K}{1 + \frac{2\zeta}{\omega_n}s + \frac{1}{\omega_n^2}s} \tag{2.12}$$

Where

$$\omega_n = \sqrt{\frac{K_{spr}}{J_{tot}}},\ \zeta = \frac{K_a^2}{2R_a\sqrt{J_{tot}K_{spr}}},\ K = \frac{K_a}{K_{spr}R_a}$$

2.3.2 Torque Motor

The difference between the DC motor and the Torque motor is that in its working range, the latter does not have a constant torque for a rated current [56]. The torque is a function of the rotor position as well. The system can therefore be modeled in the same manner as the DC motor, derived in the previous sub-section by defining the electromagnetic coefficient $K_em = K_a(\theta)$. The electromagnetic constant of a torque motor is a function of the rotor position and depends upon the rate of change of magnetic flux linkage with respect to position. Since the motor does not require gearing, the motor torque is the same as the output torque. The electromagnetic torque T_m can be derived from the derivative of the co-energy w_{em}:

$$T_m = \frac{\partial w_{em}}{\partial \theta} = \frac{1}{2} i^2 \frac{dL(\theta)}{d\theta} + i \frac{d\phi(\theta)}{d\theta} \tag{2.13}$$

The first term is the variable reluctant torque (with zero mean value). The second term is the synchronous electromagnetic torque which depends upon the rate of change of magnetic flux linkage ϕ with respect to position.

Inductance variation being insignificant, the reluctant term has been neglected. The electromagnetic torque becomes (let $K_a(\theta) = \frac{d\phi(i,\theta)}{d(\theta)}$)

$$T_m = K_a(\theta) i_a$$

. For simplification, let us assume that the flux ϕ is linear with respect to the current. Hence, replacing K_a with $K_a(\theta)$ in the previous model, we obtain:

$$F(s) = \frac{K}{1 + \frac{2\zeta}{\omega_n} s + \frac{1}{\omega_n^2} s} \tag{2.14}$$

Where

$$\omega_n = \sqrt{\frac{K_{spr}}{J_{tot}}},\ \zeta = \frac{K_a(\theta)^2}{2R_a\sqrt{J_{tot}K_{spr}}},\ K = \frac{K_a(\theta)}{K_{spr}R_a}$$

It can be noted that this linearized model is valid only when θ is in the region where $K_a(\theta)$ is constant.

2.3.3 Friction

Friction is a natural force that exists between two surfaces in contact, moving relative to each other [64]. The actual phenomenon is difficult to characterize since it depends upon a variety of physical conditions, however it arises essentially from surface irregularities or asperities [64, 65]. It is in fact a complex phenomenon and can be divided into two components. The first, static friction or **stiction** (T_s), has to be overcome to start the relative motion between two surfaces. The second component, dynamic friction also comprises of two further components, Coulomb and Viscous friction. Coulomb friction T_c is the minimum value to which friction can go to while the object moves, it depends upon the materials in contact. Normally, the values static and coulomb frictions are close. The

viscous friction is a linear function of velocity, and is attributed to lubricants. When a body starts from zero velocity, i.e. breaks away from static friction, the transition between static friction (or break-away force) and dynamic friction is called Stribeck effect. These effects can be understood better through Figure 2.16.

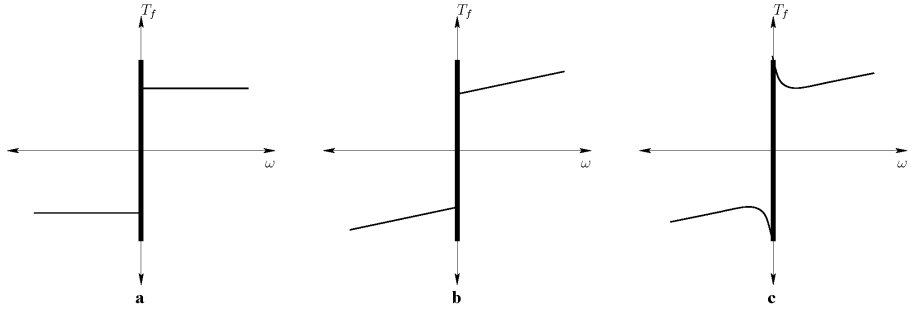


Figure 2.16. *Friction: a: Static and Coulomb b: Static, Coulomb and Viscous c: With Stribeck Effect*

Friction is the greatest contributor to the nonlinear behavior of the actuators. It can never be eliminated completely, however, lubrication (mechanical or fluid) decreases its magnitude. Other friction abatement techniques also exist, such as low amplitude vibration in the control signal. An important feature of friction is that, due to the elasticity in microscopic asperities, the phenomenon is dynamic, and requires a dynamic model (differential equation). However, in cases where this dynamic does not significantly act in the overall system performance, it can be replaced with a simple discontinuity. In this section, the modeling issue has been elaborated in detail.

2.3.3.1 Effects of friction

The control problem in mechatronic actuators arises from the presence of friction, which limits their closed-loop performance [66, 65]. Friction plays a great part in the nonlinear behavior, causing stick-slip, dead zones and part wear [65, 49, 64, 51, 67, 68].

Stiction stick-slip

Stiction, short for static friction, is the key element in the wide dead band of the actuator characteristics (as seen in Figure 2.10). As described above, it is the force that needs to be overcome before the actuator starts moving. This obstruction in movement is called ”sticking”. Once the stiction force has been overcome, the actuator starts ”slipping”

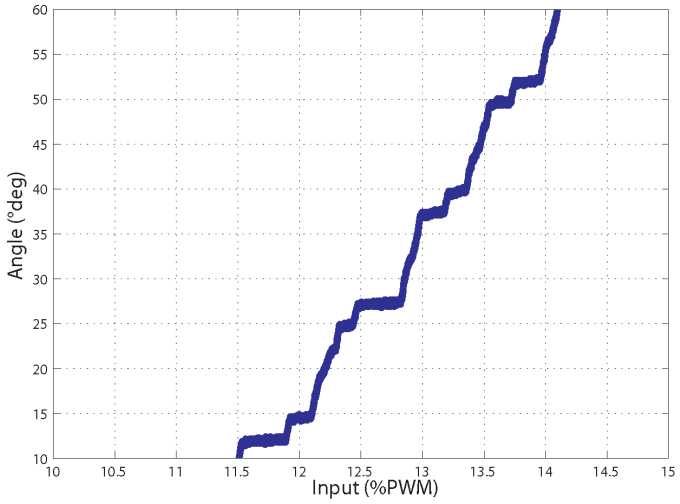
[65, 62]. If there is a significant difference between stiction and dynamic friction torque values, slipping starts with a jump, since the resistive torque decreases rapidly with velocity, creating a greater torque unbalance in the system. The jump-slip is a problem in closed-loop as the controller enters a limit cycle while trying to reach the set point or the reference [65, 69]. This happens because the actuator keeps 'jumping' about the reference, forcing the controller to change its polarity continuously.

Due to the fact that friction changes direction with direction of the velocity (since it is always in opposition to the net motion irrespective of the direction of applied force) the dead band formed is actually twice the width of the actual frictional torque. Hence if the actuators had not possessed a pre-compressed spring with sufficient torque to force valve shut-off, friction would have kept them from proper closure as it returned.

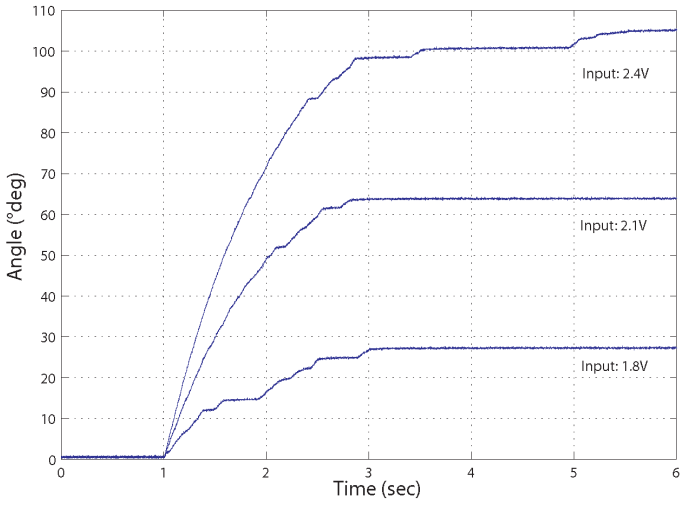
Stribeck Hysteresis:
As discussed above, the key cause of friction is the fact that surfaces have microscopic irregularities. When two surfaces are brought in contact, these irregularities or asperities mesh, locking themselves relative to each other. However, asperities are elastic in nature, hence slight movement can be seen before the actuator starts slipping. Visible clearly in the characteristic curve of the torque motor (Figure 2.10b), this slight continuous movement as the surfaces push against asperities results in a hysteresis between the sticking region and the slipping region.

Stribeck stick-slip:
Figure 2.16c shows that as velocity decreases to near zero region, the friction force increases. This greater resistive torque forces the system to come to rest earlier, creating dead zones in the path of the motion. Again, this results in a stick-slip form of motion, however, this stick-slip differs from that caused by stiction, as it occurs continuously while the actuator is moving in the same direction. Hence the resultant nonlinear phenomenon is of the dead zone type, unlike the dead band formed in stiction. This phenomenon is clearly visible in experimental results shown in Figure 2.17. Since this actuator has a gear train, the increased number of mechanical parts result in increased friction.

Hunting Effect:
The hunting effect appears in closed loop actuator position when the controller contains



(a) Stick-Slip in Static Characteristics (zoomed from figure 2.10)



(b) Stick-Slip in dynamic response (step input)

Figure 2.17. *Stribeck Stick-Slip observed in Single Action PMDC Actuator*

an integral action. In systems where F_s is much larger than F_c, friction brings the system to an abrupt stop as soon as the velocity enters the Stribeck region. Two things happen simultaneously in this case. Since the system stops before the controller could reach the reference, a static error is generated. However at this point, the control signal is too weak to overcome F_s and the actuator sticks. The integral action would continue to integrate the static error, thereby increasing the control signal against the error until it supersedes F_s. Once the control signal is strong enough, the difference between F_s and F_c leads to a slip-jump, and the actuator's position overshoots the reference.

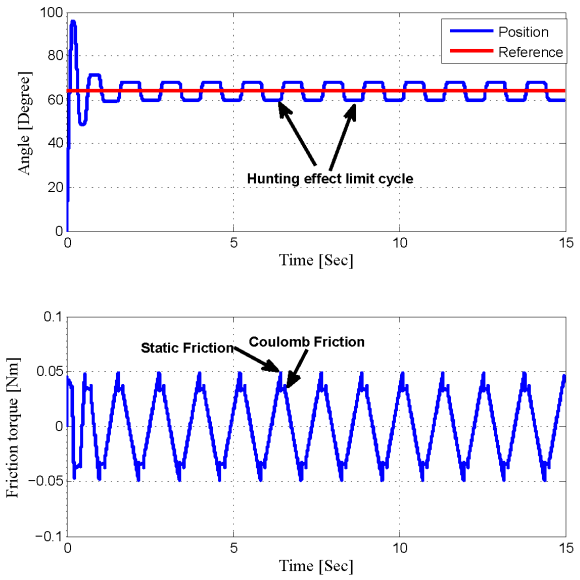


Figure 2.18. *Hunting Effect in Single Action PMDC Actuator*

The controller reverses its direction to bring the system back towards the reference. Since friction also changes direction with velocity, the stick-slip condition repeats itself in the opposite direction. Hence the actuator continues to oscillate about its reference position, "hunting" for the reference. These oscillations or limit cycles are termed as the hunting effect. They can be seen in Figure 2.18, which has been obtained during closed loop study of a PMDC Motor based single action actuator model under classical PI control.

2.3.3.2 Friction Modeling

Friction is a dynamic quantity, depending upon the elastic displacement of the microscopic asperities [65]. However, due to the complexity of an added state in systems, friction has mostly been treated as a static, discontinuous function of the system velocity [70]. However, in certain cases, systems can not be modeled without taking friction dynamics into consideration. Therefore available friction models can be divided into static and dynamic models. Dynamic models have a dynamic response to the velocity of the system. Therefore, they are continuous models, more effective in simulation, but more complex as well. In this study, we had considered many static and dynamic models for the purpose of modeling, including Coulomb model, Dahl's model, Maxwell's model etc. The models found most convenient for actuators were Karnopp model (static) and LuGre model (dynamic). These two models are described below.

Karnopp Model:

The Karnopp Friction Simulator was developed in 1985 to handle this discontinuity and to provide a friction model that can be simulated on the computer. Therefore this model was used to represent friction in the modeling of the actuator. As can be seen in Figure 2.19, the Karnopp simulator models the discontinuity by a small region between two very small values of velocity, replacing the discontinuity characteristic with a linear relationship between torque applied to the system and static friction torque [70, 71].

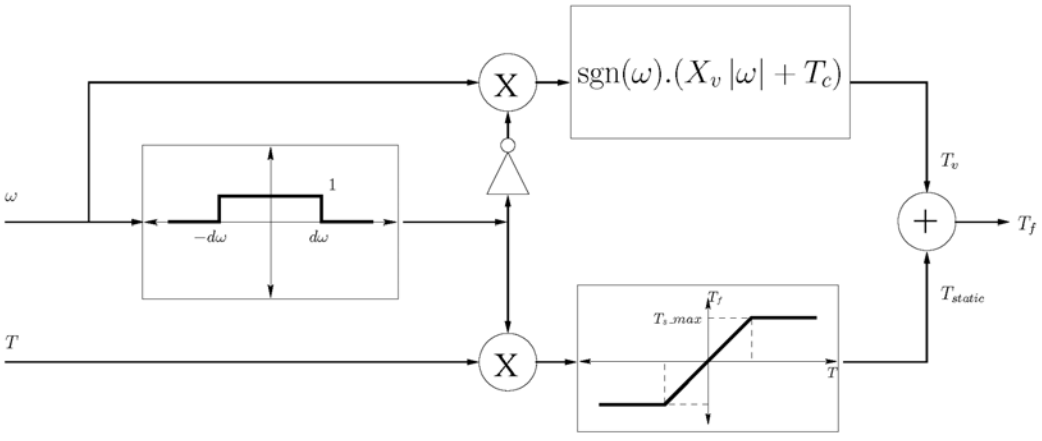


Figure 2.19. *Karnopp Model*

A small interval $[-d\omega, d\omega]$ is defined where the angular velocity is considered to be zero.

In this interval the friction torque is a function of the applied torque T, and is given by the lower part, activated by the switching function implemented in the interval test. Outside the interval $[-d\omega, d\omega]$ the dynamic torque is provided by the upper part. The Karnopp simulator follows the following mathematical relationship.

$$Tc = \begin{cases} T & \text{if} \quad |T| < T_{s-max} \text{ and } |\omega| \leq d\omega \\ \text{sgn}(T)T_{s-max} & \text{if} \quad |T| \geq T_{s-max} \text{ and } |\omega| \leq d\omega \\ \text{sgn}(\omega)T_v & \text{if} \quad |\omega| > d\omega \end{cases} \tag{2.15}$$

LuGre Model:

The LuGre Friction model is a dynamic model that treats asperities as elastic bristles. Motion, according to this model occurs when the bristles start 'slipping' [65]. It allows for the static friction to be modeled separately, and also incorporates Stribeck effect in the model [49, 64, 65]. The LuGre model considers friction as a function of the bristle displacement, bristle velocity and the system velocity

$$T_f = \begin{cases} T_f(z, \dot{z}, \omega) = \sigma_o z + \sigma_1 \dot{z} + \sigma_2 \omega \\ \dot{z} = \omega - \sigma_o \dfrac{|\omega|}{p(\omega)} z \end{cases} \tag{2.16}$$

Where z is the average deflection of the bristles before slipping, σ_o is their stiffness coefficient and σ_1 is the damping coefficient which stabilizes the dynamics in the Stribeck region [65]. σ_2 is the coefficient of viscous friction. The $p(\omega)$ function models the Stribeck effect as a function of velocity. If ω_s is the velocity at which Stribeck effect takes place (Stribeck velocity), then $p(\omega)$ can be expressed as:

$$p(\omega) = T_c + (T_s - T_c)e^{(-\omega/|\omega_s|)^\alpha} \tag{2.17}$$

α defines the shape of the function $p(\omega)$, and hence of the Stribeck phenomenon, near zero velocity. Its value is taken between 1 and 2.

2.3.3.3 Comparison

The choice of friction model depends upon how much the actual system is influenced by friction dynamics. For example, in the simple case of a robotic arm, the dynamics of friction need not be considered, since the contacts are rigid and the effect of elasticity in

surface contact is negligible. Hence Karnopp model suffices. On the other hand, in order to model vehicle dynamics and wheel traction, where the dynamic effects of friction and Stribeck effect play an important role, LuGre model is inevitable. As such, computation-wise, Karnopp model is simple but discontinuous, while LuGre model is continuous, yet complex. In the rest of this paper, the LuGre model is considered for friction modeling.

2.3.4 Temperature variation

An important aspect in the modeling of an automotive actuator is the variation of parameters due to temperature. Since the temperature conditions in an automobile can vary in a large range (-20^oC to 125^oC), it is important to analyze how the actuator would behave during various operating conditions.

As seen in Figure 2.20, more power voltage is required for the actuator to move at higher temperatures. The most important parameter that depends upon the temperature is the motor winding resistance, as the motor torque depends upon the current and current depends upon the motor resistance. As the motor gets heated the resistance increases with the temperature, which results in reduction of current at the same applied voltage.

2.3.5 Complete Model

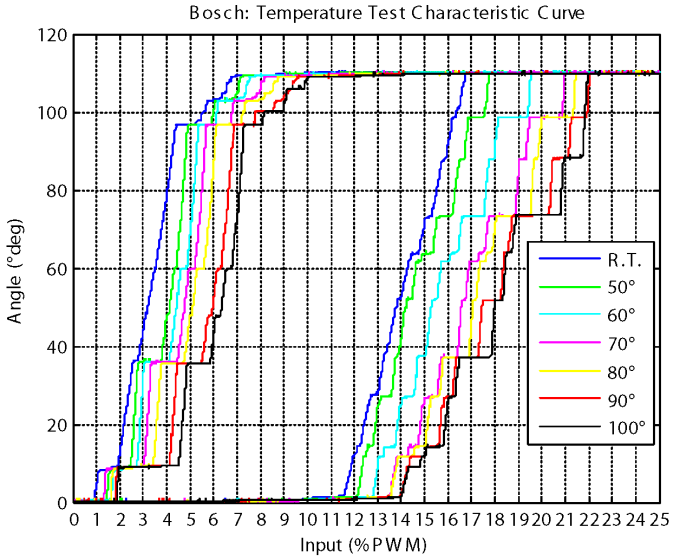
The complete system model can hence be defined in by Equations (2.12), (2.14), (2.16) and (2.17) in the following manner:

$$F(s) = \frac{K}{1 + \frac{2\zeta}{\omega_n}s + \frac{1}{\omega_n^2}s}$$

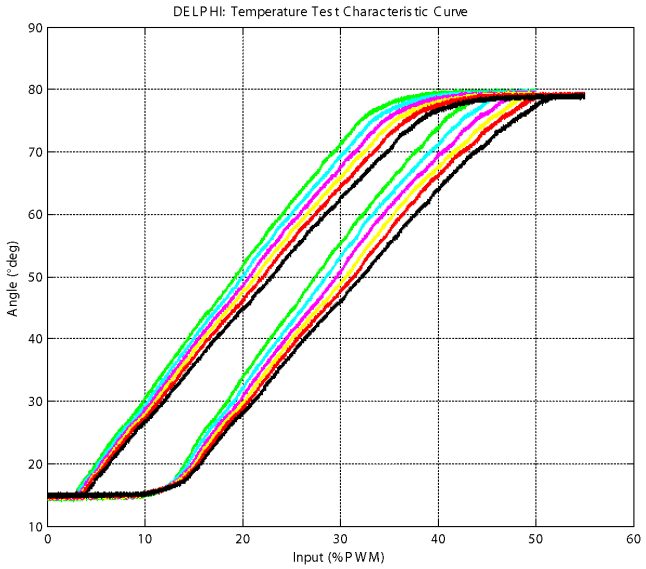
Let $x_1 = \theta$, $x_2 = \frac{d\theta}{dt}$, $u = V_a$, $J = J_{tot}$ the state space model of the system is given by

$$\begin{aligned} \dot{x}_1 &= x_2 \\ \dot{x}_2 &= -\frac{K_{spr}x_1}{J} - \frac{K_a^2 x_2}{R_a J} - \frac{T_f(x_2, z, \dot{z})}{J} - \frac{(T_{pc} + T_L)}{J} + \left(\frac{K_a}{R_a J}\right)u \\ \dot{z} &= x_2 + \frac{|x_2|}{p(x_2)}z \end{aligned} \tag{2.18}$$

$R_a = R(Temp_0) + K_t \Delta Temp.$



(a) PMDC Motor Actuator



(b) Torque Motor Actuator

Figure 2.20. *Experimentally obtained characteristics of two Single Action Mechatronic Actuators at different temperatures*

2.3.5.1 Extension to Double Action Actuators

In the case where there is no spring and the motor is the only forcing element, Equation (2.18) can be adapted to the actuator by taking $K_{spr} = 0$. In this case, K_{em} can be found directly through experimentation.

2.3.6 Actuator Implementation in AMESim

The generic physical model was implemented in AMESim. The motor and spring systems were implemented using the components of AMESim Libraries. However, sufficiently accurate friction models were not available. Therefore, the LuGre friction model was implemented as a mathematical function. The implementation of a single action actuator is shown in Figure 2.21, and a double action actuator is shown in Figure 2.22.

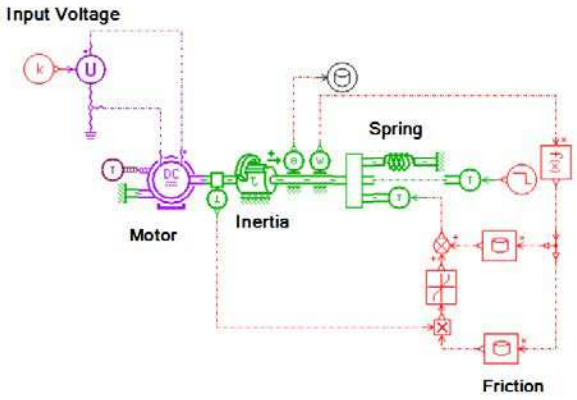


Figure 2.21. *AMESim Model of Single Action Mechatronic Actuator*

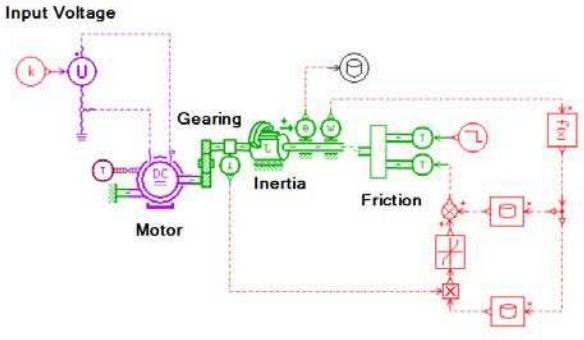


Figure 2.22. *AMESim Model of Double Action Mechatronic Actuator*

These models can be integrated directly to the EGR valve or the VGT Turbine vane port. However, its position needs to be normalized with respect to the maximum value, as both the VGT Turbine and EGR valve accept normalized positions (between 0 and 1). In the DV6TED4 Simulator, the EGR actuator was parameterized according to the Valeo Torque Motor Actuator, and the VGT Turbine was parameterized according to the Hella PMDC Actuator. The parameters of both these actuators are given in Appendix A.

2.4 Experimental Validation

The actuators were tested using a test bench. This test bench has been designed specifically for actuator characterization (Figure 2.23). It consists of a temperature controlled chamber in which the actuators are installed. This allows actuator testing at normal and high temperature conditions (up to 130^oC). The chamber has been designed in such a way that any actuator can be mounted, using an adaptor plate.



Figure 2.23. *Actuator Test Bench*

A precise dynamometer is used for torque measurement of up to 2mNm. An encoder with a 4096 slot disc provides angular measurements as small as 0.088^o. A hysteresis brake,

capable of providing a resistive torque of $35mNm$ is used to simulate loading conditions.

The test bench is interfaced with a National Instrument CompactRIO system. This system has a real-time controller for deterministic control, and an FPGA for tasks requiring speed and absolute parallelism. The CompactRIO can be configured for different input-output requirements, using different modules. The system used with the test bench has a four channel differential analog input module for measuring the dynamometer data as well as the position sensor integrated in the actuator. The hysteresis brake and the actuator are controlled through H-bridge modules which provide pulse width modulated output at switching frequencies of up to $20kHz$. The entire system can be seen in Figure 2.24

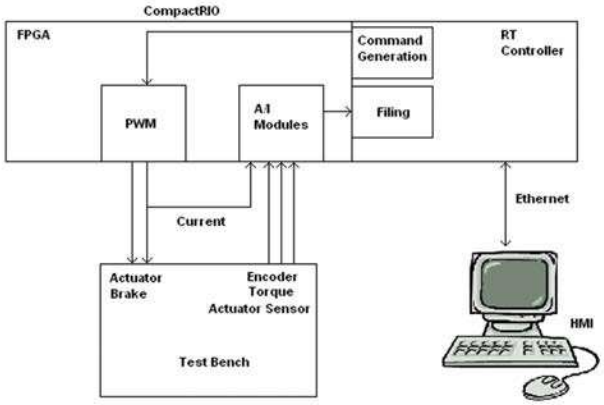


Figure 2.24. *Actuator Test Bench Block Diagram*

2.4.1 Parameter Identification

The model parameters were identified using nonlinear least squares method, supported by measurements. Using the notation

$$V_a^* = \frac{T_f R_a}{K_a} + \frac{T_{pc} R_a}{K_a},$$

we obtain from Equation (2.18)

- For DC motor : $\omega_n = \sqrt{\frac{K_{spr}}{J_{tot}}},\ \zeta = \frac{K_a^2}{2R_a\sqrt{J_{tot}K_{spr}}},\ K = \frac{K_a}{K_{spr}R_a}$
- For torque motor ($K_a(\theta) = constant$): $\omega_n = \sqrt{\frac{K_{spr}}{J_{tot}}},\ \zeta = \frac{K_a(\theta)^2}{2R_a\sqrt{J_{tot}K_{spr}}},\ K = \frac{K_a(\theta)}{K_{spr}R_a}$

The step responses show that all our actuators are over-damped ($\zeta > 1$). Hence the system response in time domain can be generalized using the following relationship.

$$\theta(t) = V\left[K + \frac{K}{2\sqrt{\zeta^2-1}}\left(\frac{1}{-\zeta+\sqrt{\zeta^2-1}}e^{-\omega_n(\zeta-\sqrt{\zeta^2-1})} + \frac{1}{\zeta+\sqrt{\zeta^2-1}}e^{-\omega_n(\zeta+\sqrt{\zeta^2-1})}\right)\right]$$

As we have seen in the modeling section, K, ζ and ω_n are all functions of K_a , K_{spr}, J_{tot} and R_a. The value of resistance R_a was measured using Ohm's law. The values of the unknown parameters (K_a , $Kspr$, J_{tot}) was found by applying the standard nonlinear least Squares procedure. An estimation vector, SS=[K_a , K_{spr}, J_{tot}] was defined for the estimation algorithm, which evaluated the model on the vector $\theta = est(V_a, \beta)$.

Where V_a represents the armature voltage values on which the model is evaluated. This model was compared to a set of measured values, θ' taken at the same armature voltages as the estimation. The estimate vector β was then obtained by solving the following least squares problem through a nonlinear minimization algorithm

$$E = \min \sum_{i=1}^{N} (\theta_i - \theta_i')^2$$

The estimated values were supported by torque measurements. The spring was characterized by turning the shaft by hand, i.e. without powering up the motor. Then, locking the rotor at certain known angles, the motor was powered up until it matched the torque of the spring. At this point, by measuring current and angle, both the electromagnetic constant, K_a and the spring constant K_{spr} were identified. The identified parameters are given in Appendix A.

2.4.2 Validation

The validation results are shown in Figures 2.25 and 2.26. The first set of graphs (Figure 2.25) shows the comparison between simulated and experimental values during static (slow input variation) tests. It can be seen that simulation results correspond to the experimentally obtained values and the effects of friction and temperature are successfully reproduced by the simulated model. The comparison of dynamic responses of the actuators and their simulated models are shown in the second set of graphs (Figure 2.26). It is clear that the model parameters obtained from the presented identification method reproduce the same dynamic response as in the real actuators.

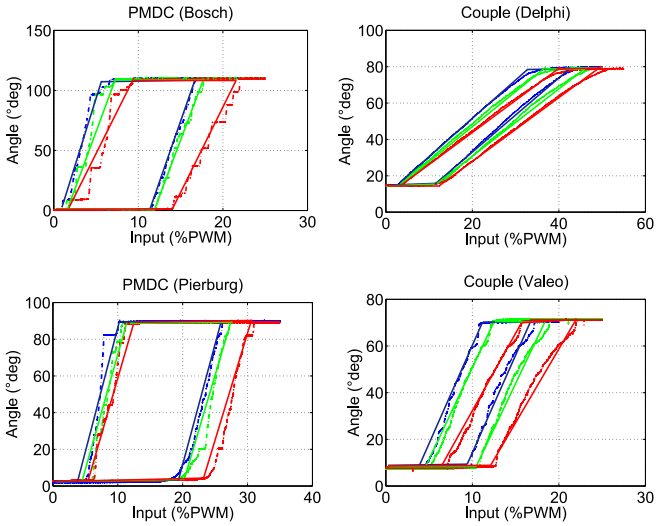


Figure 2.25. *Static Validation*

(**NB:** See Appendix B for a comparative study between the torque and friction characteristics of different mechatronic actuators. An overview of sensor technology for actuators is presented in Appendix C)

2.5 Aging

The final important part of this chapter is a discussion on the effects of aging on actuators. Certain characteristics of mechatronic actuators and the parts used in their manufacture change with time and use [44]. These changes result in variation of the overall actuator

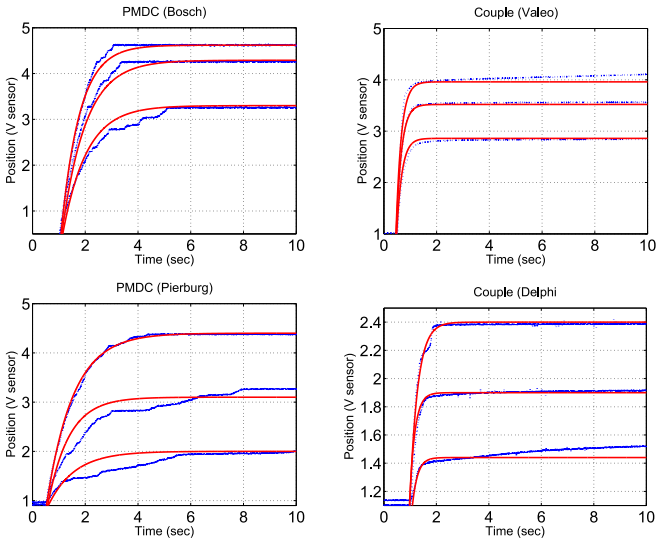


Figure 2.26. *Dynamic Validation*

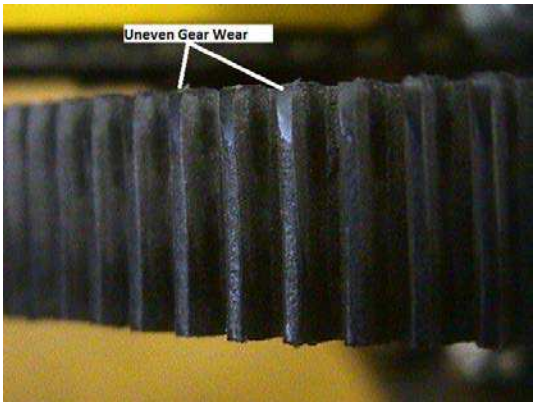
characteristics. Normally the variations due to actuator aging are adverse in nature, i.e. they deteriorate the actuator performance. The major aging effects have been discussed in this section.

2.5.1 Wear

Constant rubbing of mechanical parts results in surface degradation over time. As components wear out, more and more space is created between interconnections. During performance, the effect manifests itself as an increase in backlash, hence larger dead bands. Wear also causes structural degradation of actuator parts which, when fail, might result in actuator failure. Another important part of a control valve that is effected by wear is the packing. As the packing degrades, leakage increases and the valve flow characteristics change due to change in flow control area. Wear degradation effects on actuator gear and packing can be seen in Figure 2.27.

2.5.2 Clogging (Surface deterioration)

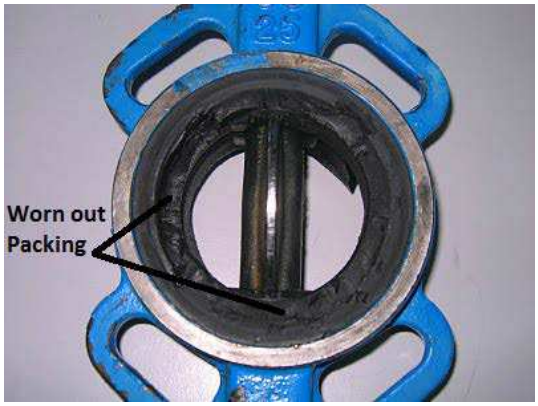
Irregular surface degradation also results in clogging. This is because the large irregularities hinder and block smooth movement and result in dead zones similar to stick slip. Irregular deterioration of gear teeth (as seen in Figure 2.27 a) can also cause gears to fail completely.



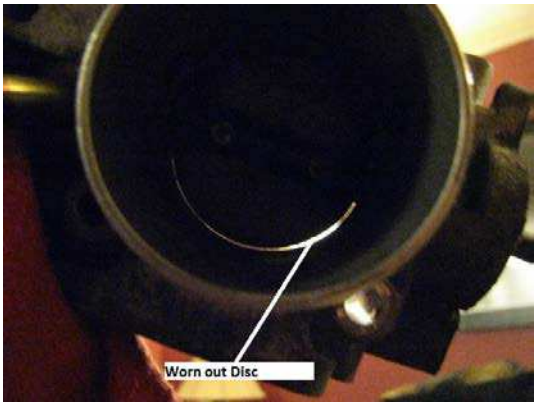
(a) Unevenly worn out gear



(b) Worn out gear (Surface damage)



(c) Worn out packing



(d) Worn out valve disc

Figure 2.27. *Worn out actuator parts*

2.5.3 Torque deterioration (Degradation of motor electrical characteristics)

While electrical and electronic devices do not wear out in the same manner as mechanical parts, parameter drift with time is a common problem[72]. In electric motors, continuous temperature variations degrade the permanent magnets, hence their net deteriorates over their lifetime [73]. Insulation failures, if not severe enough to cause motor failure, reduce the resistance and inductance of the windings, also causing torque deterioration. The deterioration of electromagnetic properties of rotor low carbon steel through heat cycles is another factor [73]. The results of an accelerated aging test performed on an actuator are given in Figure 2.28. The test was performed to determine the expected variation in torque characteristics of an actuator throughout its life. This test comprised of various

"life cycles", each cycle involving the continuous operation of the actuator through various adverse conditions, such as heat and humidity. Semiconductor devices, in form of sensors,

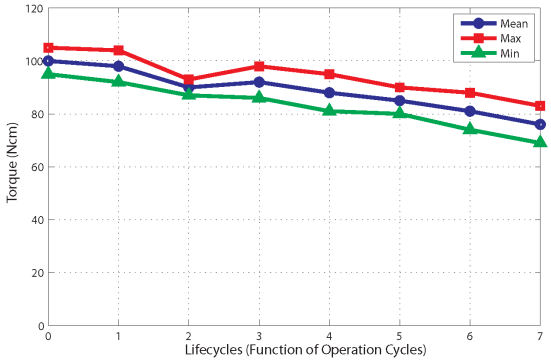


Figure 2.28. *Torque deterioration with age*

embedded controllers and power controllers suffer from physical wear as well, in form of electron migration [74]. This happens when metallic depositions (usually in the order of $> 1 micron$) on semiconductors thin out due to constant current flow.

2.6 Summary

In this chapter, we discussed the nonlinear dynamic modeling of mechatronic actuators. Two major types of actuators were identified, based on their motor technology. It was found that torque motors have certain advantages over PMDC motors due to their large size-to-torque ratio, however their limited angle rotation is a handicap. Then, the importance of friction modeling was discussed and two friction models were presented. Electromechanical modeling of both these motors was discussed, and a complete nonlinear model was obtained, which included friction and temperature effects as well. Finally, some issues related to actuator aging were discussed for consideration in long term operation and control design. It was shown that these effects can be included in the model by integrating them in the torque characteristics of the motors. They have not been included in the work presented in the rest of the thesis. As the DV6TED4 engine is used as example in this thesis, in the proceeding chapters, the actuator of interest will be the Valeo torque

motor based actuator, which is used as EGR actuator in this engine.

Chapter 3

Simulation and Validation

The most important part of modeling is experimental validation, which is required to assert the accuracy of the model. In order to validate the air-path simulator, it was parameterized according to the specifications of the DV6TED4 engine. It should be mentioned that this was made possible by the collaborative effort of the industrial project partners. The simulator was compared to the experimental results obtained on the engine. One major obstacle in this process was to reproduce the engine controller used in the experiments, in order to run the AMESim model under the same operating conditions and parameters in which the real tests had been conducted. These conditions include engine operating point in terms of speed and torque, and the corresponding pressure and mass-flow set points. To obtain these, accurate fuel injection profiles were also required for the engine model to reproduce the torque and exhaust pressure at given speeds. As the industrial test bench was controller under an open ECU system, it was possible to obtain the reference-maps and look-up tables used during engine testing, as well as the control architecture. The controller problem was solved by replicating the control system and implementing the exact maps and tables.

In this chapter, we first introduce the industrial test bench that was used to provide experimental data for comparison. The controller and its implementation in Simulink are described next, and finally, simulation results and comparative figures between the simulation output and experimental results are presented.

3.1 Industrial Test Bench

The basic premise of the project SIMBA was to rely upon concrete scientific researches on modeling and development, as well as the industrial experience of partners, which would permit to orient the developments effectively and to propose validation methods adapted to their requirements. In this regard, multiple test campaigns were conducted on a the DV6TED4 engine test bench (Figures 3.1). Located at Faurecia (Bavans, France), this test bench comprises of the engine, an EGR valve manufactured by Valeo, and a turbocharger manufactured by Honeywell-Garrett. The flow characteristics of both these systems were presented in Chapter 1 and the actuator models were presented in Chapter 2.

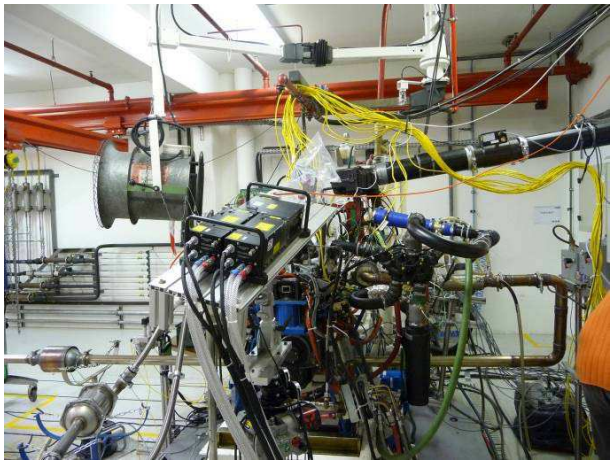


Figure 3.1. *DV6TED4 Test bench (Faurecia)*

The test bench is equipped with multiple sensors for measuring various physical quantities throughout the air-path. Of these measurements, the values of interest for us were the engine intake manifold pressure P_i, intake mass-flow $\dot{m}_i$, EGR flow $\dot{m}_{egr}$ and exhaust pressure P_e. It should be noted that the sensors were of limited bandwidth, therefore the pulsating effect of engine reciprocation could not be captured in experimental results. Therefore, validation was done through mean values of these variables, which were also obtained in the simulations.

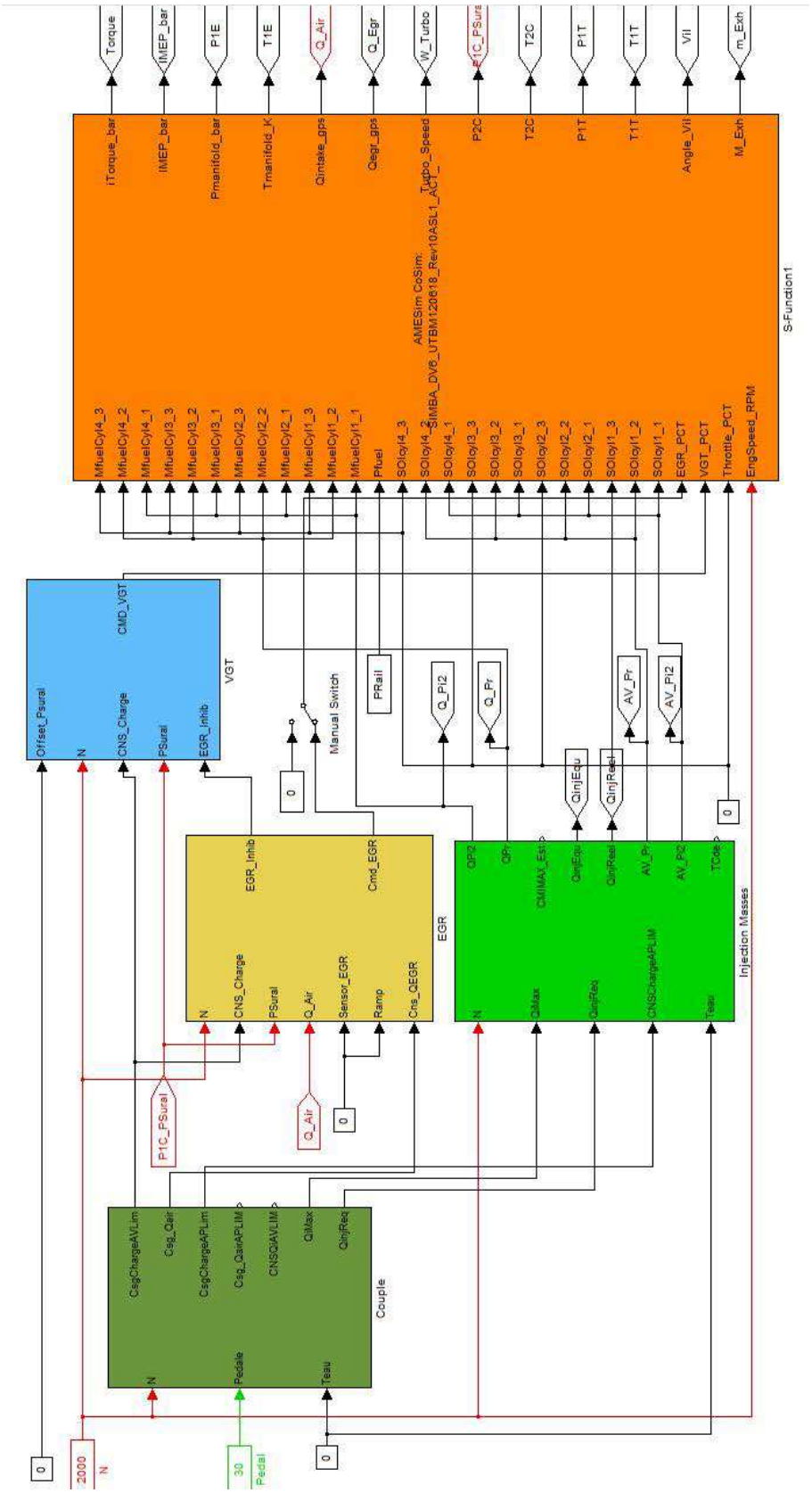


Figure 3.2. *Controller Structure*

3.2 Air-path Controller

In order to run the simulator under the same conditions as in the experiments, the open ECU control system was replicated. Simulink was chosen for this purpose because, as a leading design tool for control engineering, its programming structure was close to the controller architecture. Furthermore, as both AMESim and Simulink are compatible C++ based platforms, interfacing tools are available in both of them. Using these facilities, the controller was successfully linked with the air-path simulator.

The Simulink controller is shown in Figure 3.2. The control system was simplified by implementing only the fuel injection and air-path control units. Other operational features, such as cruise control and idle speed control served no purpose in air-path study, hence they were not included. Since the simulated engine posed no risks, safety features were also removed. Each control unit shown in Figure 3.2 is explained in the following subsections. The look-up tables and parameters were provided by Faurecia.

3.2.1 Torque Reference Unit

This is the fundamental unit, that determines the fuel-mass and air-mass required to achieve the demanded operating point. In actual application, the torque requirement is estimated from the actual engine speed and the accelerator pedal position. As shown in Figure 3.3, the required torque is estimated through a data-map, to which estimated engine losses (friction, pumping, heating etc.) are added. In addition, the maximum torque for the given speed is also determined using another map (CMImax). The torque reference is sent to another set of look-up tables (Figure 3.4), which provides the required fuel quantity and air-mass for combustion and the boost pressure required in the intake manifold in order to achieve a higher mass-flow. The pressure reference provided by this block is in percentage of the engine's maximum boost rating. The actual pressure reference point is calculated from this normalized reference in the VGT control unit.

As the experimental studies were conducted at specified torque requirements, we did not need to estimate the torque from pedal position. Therefore, a switch was added in the controller to bypass the pedal and torque maps, and to demand directly the required torque for validation. This switch is also shown in Figure 3.3.

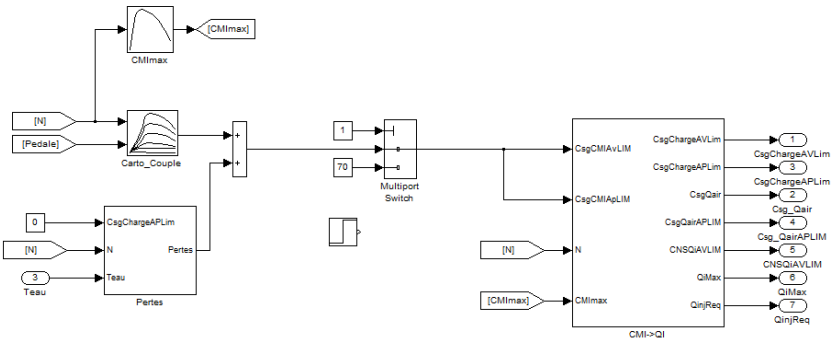


Figure 3.3. *Torque Maps*

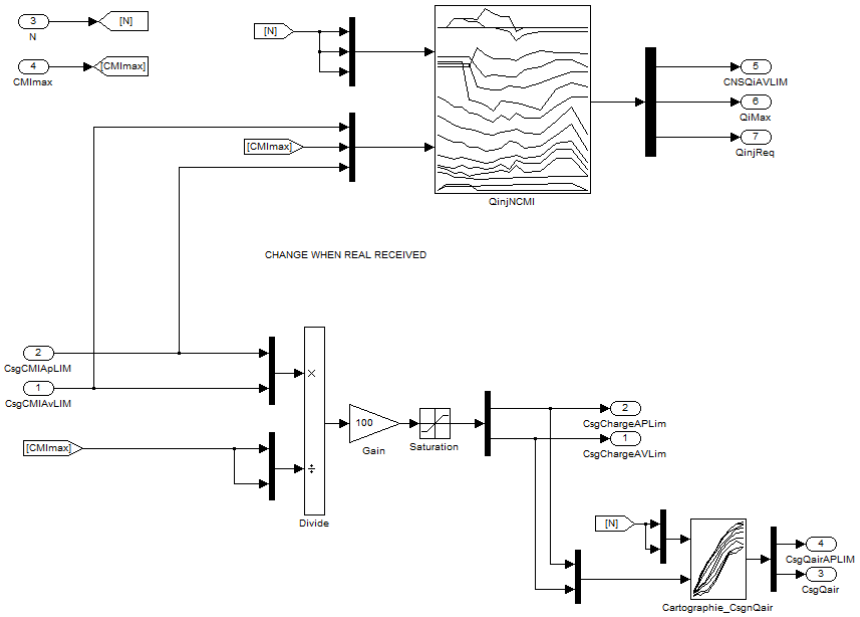


Figure 3.4. *References and constraints (CMI - Qi Block)*

3.2.2 Fuel Injection Unit

This unit receives the required fuel quantity from the torque reference unit. Based on the engine operating point, it uses a large set of look-up tables to determine the injected fuel quantity in pilot and main injection phases, and the start of injection for each phase. The start of injection is expressed in terms of the crankshaft angle. All these values are then passed to the fuel injector model in the AMESim simulator.

In real application, this unit further calculates the fuel injector opening duration required

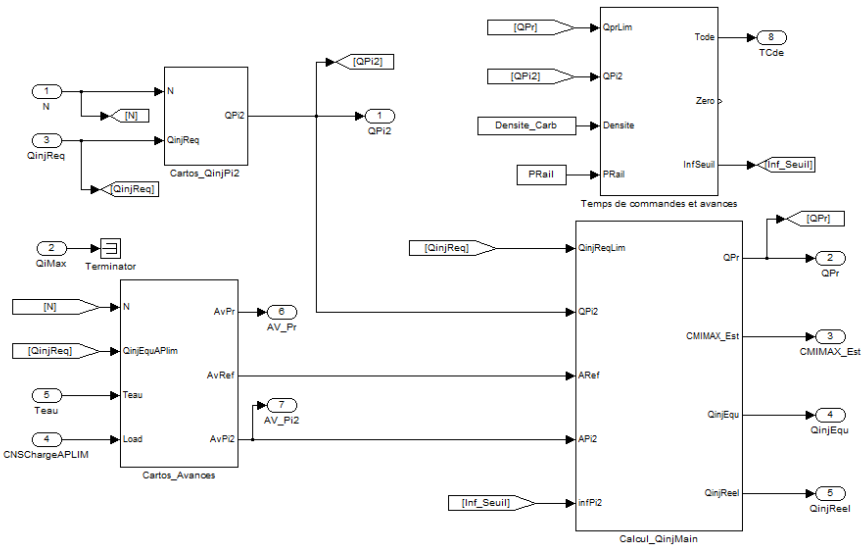


Figure 3.5. *Fuel Injection Unit*

to deliver the required fuel mass during each phase. However, the injector model used in the simulator is calibrated to guarantee the required fuel injection, as per the specifications of the DV6TED4 engine. Therefore, instead of the opening duration, the required fuel mass for each phase injection phase is passed to the cylinder. Furthermore, it is assumed that during one engine cycle, the same fuel quantity will be injected in all cylinders.

3.2.3 VGT Control Unit

The first important unit from air-path point of view is the VGT control unit. This controller is linked to the VGT actuator and regulates the VGT vane position, thereby adjusting the exhaust gas flow through the turbine and regulating its speed. As the turbine and compressor rotate at the same speed, the controller regulates the actuator until the compressor speed is sufficient to maintain the required boost pressure. As shown in Figure 3.6,

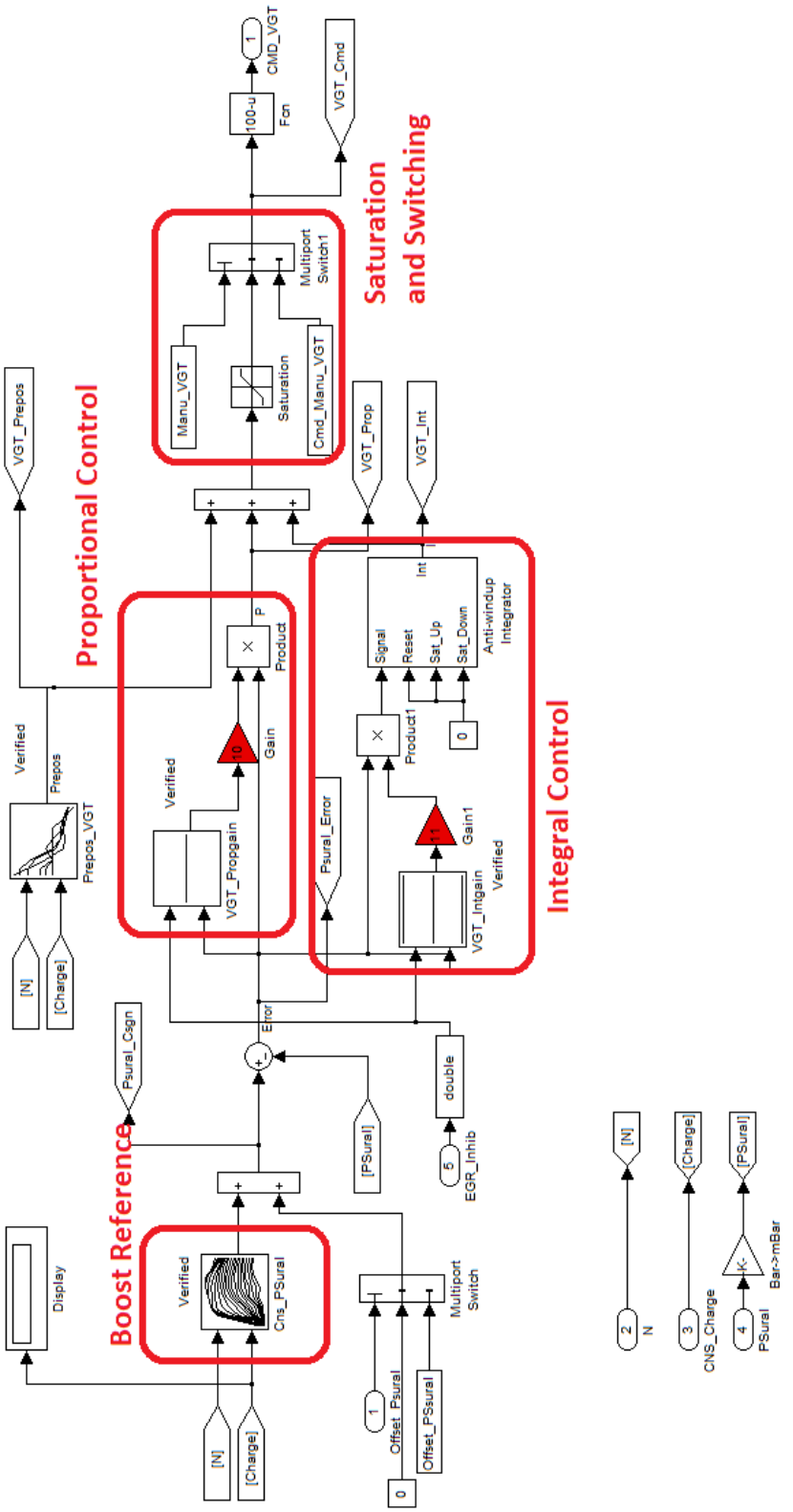


Figure 3.6. *VGT Control Unit*

a gain-scheduled PI controller was used for this purpose in the open ECU, where the gain depends upon the error as well as the availability of EGR. The output of the controller is saturated, to protect the VGT system in case of a fault. In order to avoid controller windup in such cases, an anti-windup integrator was implemented. In the Simulink version, the PI controller was implemented in the same way. As mentioned before, the torque reference unit provides a normalized boost pressure reference as input to the controller. The VGT control unit uses a look-up table to determine the actual boost pressure reference for the control.

3.2.4 EGR Control Unit

The second important unit for engine air-path control is the EGR control unit, which controls the EGR valve actuator to regulate EGR flow. This unit depends upon the actual boost pressure in the intake manifold, as well as the engine operating speed. EGR is a sensitive process because excessive exhaust gas deteriorates combustion. Therefore the controller appears complex in Figure 3.7 than that of the VGT. However, the general structure is a gain-scheduled PI as well, with certain additional features discussed below. The EGR mass-flow reference is calculated directly from the air-mass flow reference generated by the torque reference unit. Depending upon the engine speed and boost pressure, the EGR control unit determines the percentage of exhaust gas to mix with the fresh air in the intake manifold. This percentage or EGR coefficient is determined from a look-up table (Figure 3.8, and is used as reference by the controller.

It is important to take into account that EGR is not used all the time in real engines. The engine cannot tolerate EGR while idling, cruising, or at high loads. The EGR activation block (Figure 3.7) identifies whether EGR can be used or not, by comparing the engine speed and the boost pressure. When EGR is deactivated, this block forces the controller to shut the valve. In addition, an EGR inhibition block (Figure 3.8) also monitors whether EGR is active or not. When deactivated, it signals the VGT control unit, which adjusts the controller gains accordingly. In addition, the rate of change of the actuator is limited in order to avoid sudden pressure changes between the intake and exhaust paths.

In order to achieve precise control, the EGR controller is cascaded with an inner local-loop position controller, as shown in Figures 3.7 and 3.9. The outer loop provides the position

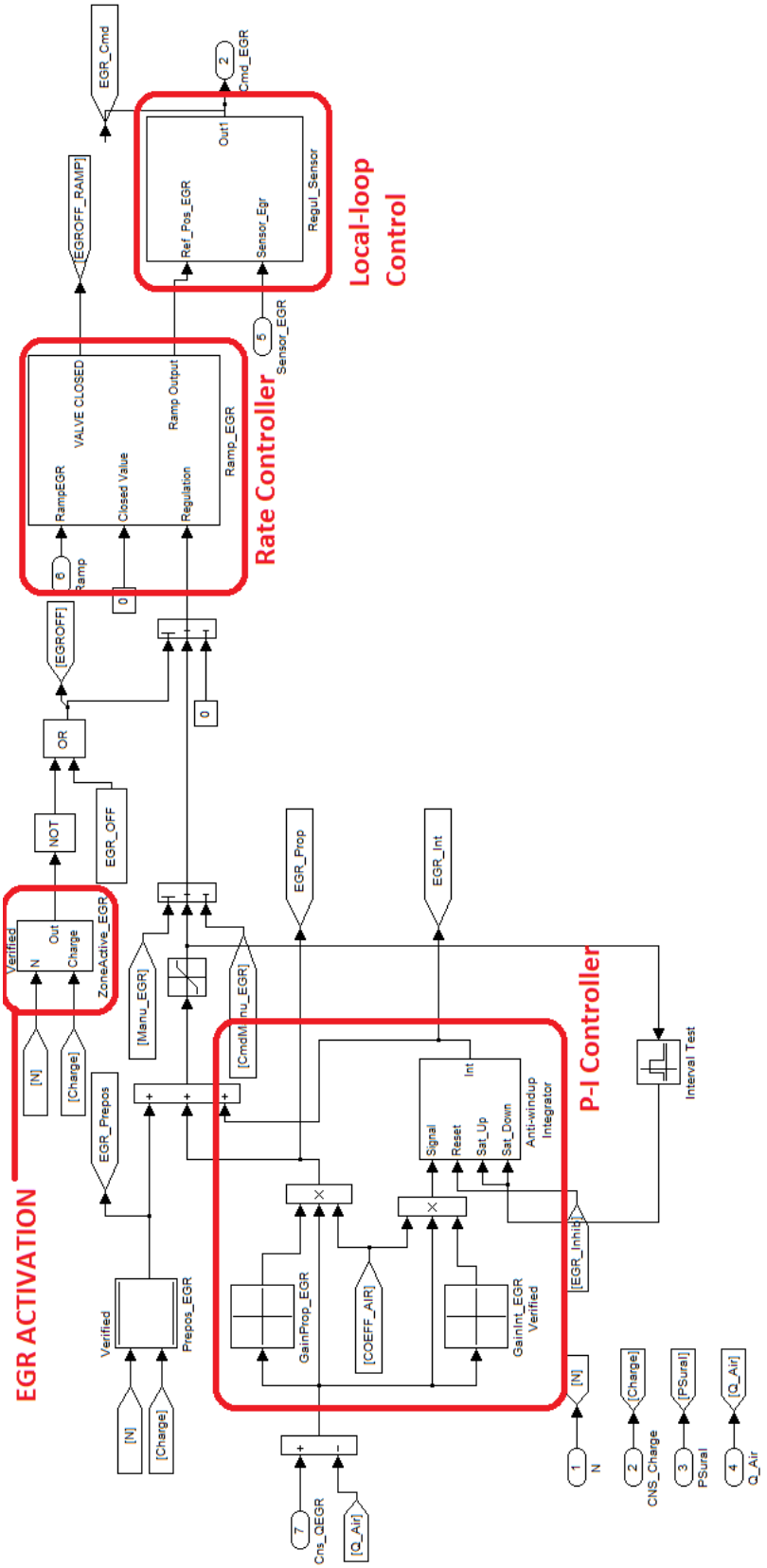


Figure 3.7. *EGR Controller*

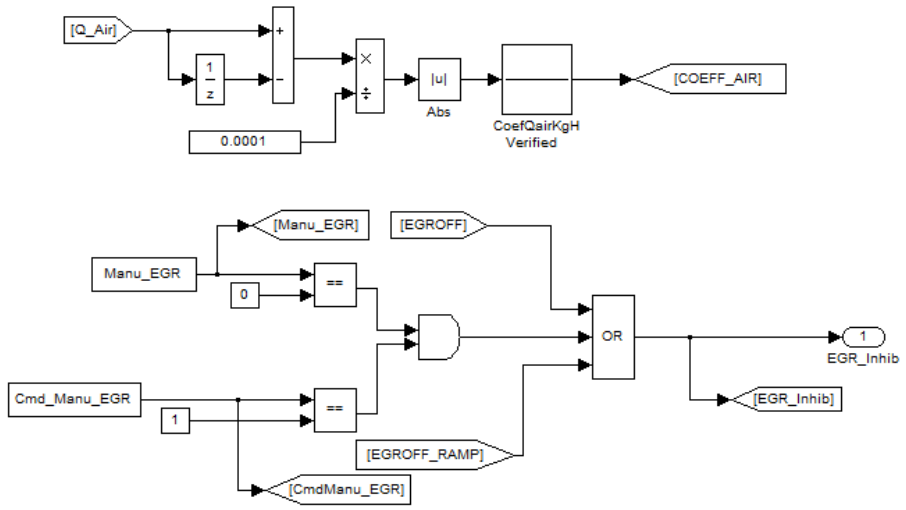


Figure 3.8. *EGR coefficient and inhibition*

reference to the inner PI loop, which then controls the position using the actuator sensor as feedback. This improves the overall response time of the EGR control loop.

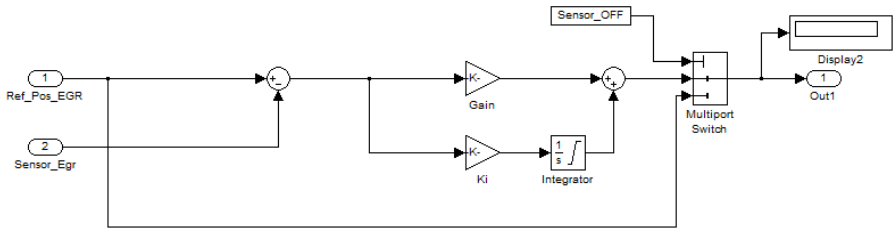


Figure 3.9. *EGR Local-Loop Controller*

3.3 Simulation and Validation Results

The model validation was conducted in two phases. First, the EGR was disabled and only the boost VGT was kept operational, in order to validate the intake and exhaust pressures and intake mass-flow characteristics. Then EGR was enabled and its characteristics were validated separately.

3.3.1 Boost Simulation

In the first phase, the simulator was evaluated without EGR. The results of intake manifold pressure, intake mass-flow and exhaust pressure are shown in Figures 3.10, 3.11 and 3.12 respectively. It can be seen that the model simulates the pulsating flow due to engine reciprocation.

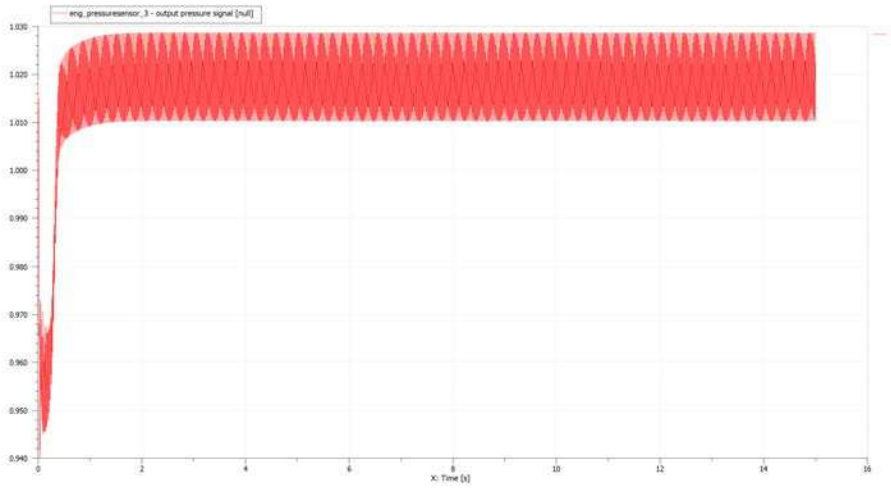


Figure 3.10. *Intake Manifold Pressure at 1500RPM, 40Nm*

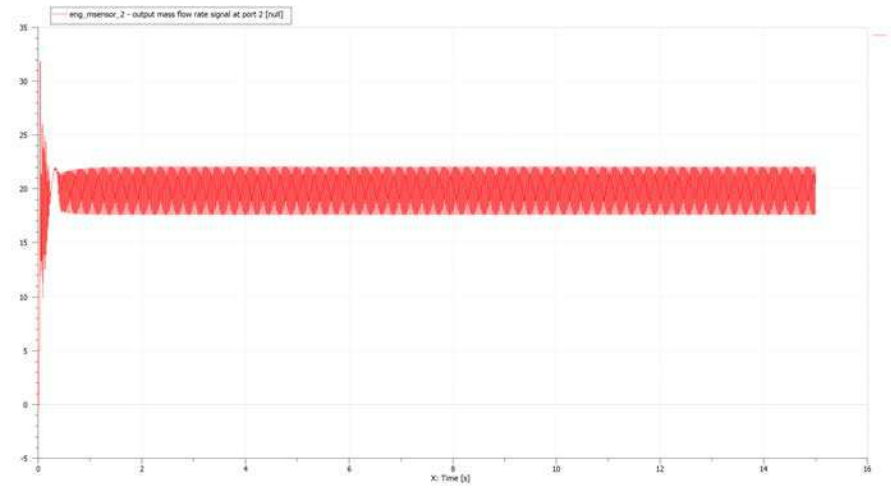


Figure 3.11. *Intake Mass Flow (g/s) at 1500RPM, 40Nm*

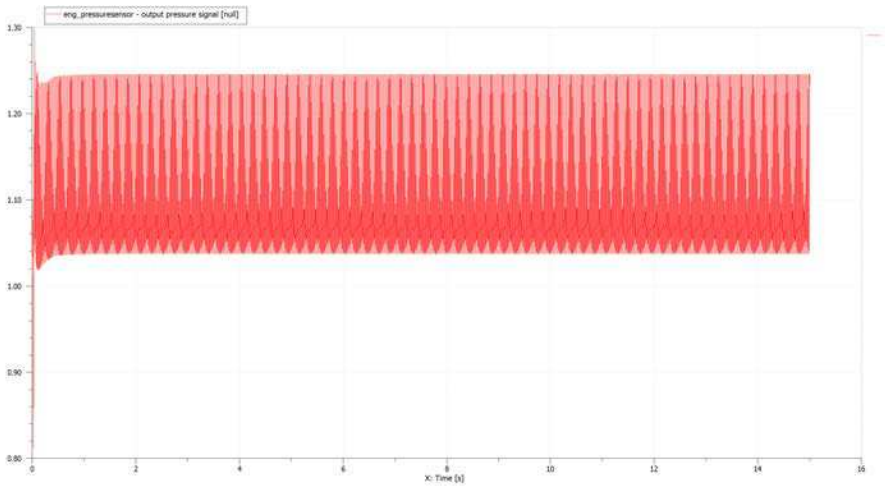


Figure 3.12. *Exhaust Manifold Pressure at 1500RPM, 40Nm*

3.3.1.1 Validation

While the objective of the study was to simulate the pulsation effect of the engine, this result does not provide much information about the validity of the simulator. Therefore, mean values of the obtained results were compared with the mean experimental results. The results are shown in Figure 3.13. It can be seen that the values obtained through simulation are very close to the experimentally obtained data. However, as certain losses were not taken into account, slight deviations exist between simulations and experiments, however they are insignificant with respect to the objectives of the simulator.

In order to evaluate the dynamic behavior of the simulator, a transitory load and speed was imposed. The engine speed was varied from 1500 RPM to 2000 RPM and the load was shifted at the same time from 40 Nm to 70 Nm. As sudden changes in an engine's operating point can be dangerous, the transition rate was controlled. The simulator's performance against the experimental data is shown in Figure 3.14. The simulated and experimental values deviate more in the transitory zone, than in the steady state zones. These deviations can be ascribed to the lack of transmission delays in the simulator. A remarkable feature during the transition phase is a sudden oscillation (between 15 and 20sec). This is due to change in functioning point in the pressure reference look-up table.

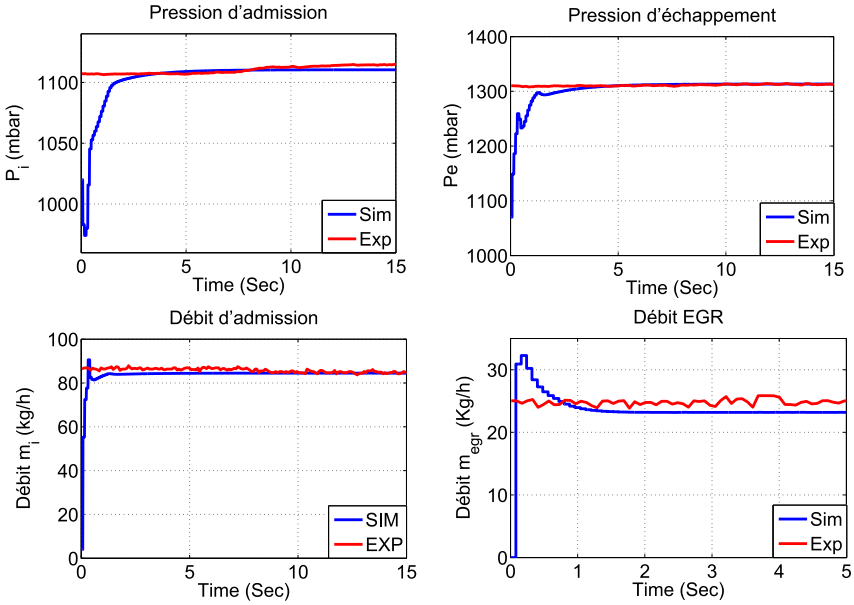


Figure 3.13. *Comparison at 1500RPM, 40Nm*

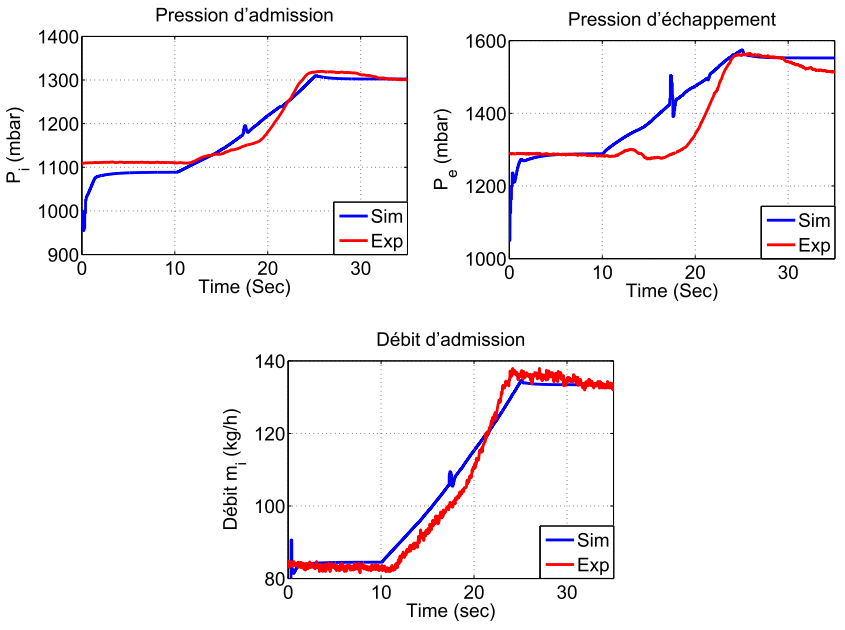


Figure 3.14. *Comparison at transition 1500RPM-2000RPM, 40Nm-70Nm*

3.3.2 EGR Simulation and Validation

The EGR was tested at 35% opening, at 1500RPM, 40Nm. The simulation result is shown in Figure 3.15. Severe pulsations in the flow are evident due to the effect of both intake and exhaust pressure pulsations. The validation result, based on mean value, is shown in Figure 3.16. Apart from the initial transition due to controller initialization, the results match satisfactorily.

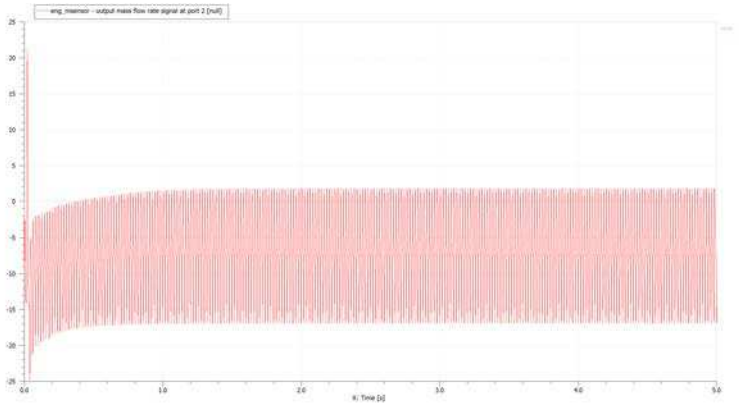


Figure 3.15. *EGR Mass Flow at 1500RPM, 40Nm*

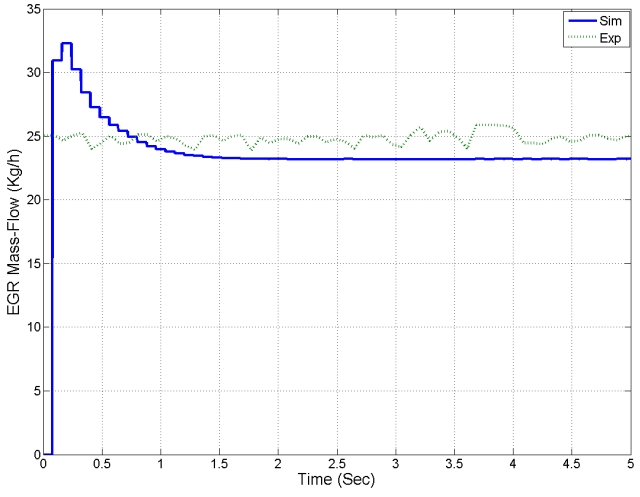


Figure 3.16. *EGR Mass Flow at 1500RPM, 40Nm*

3.4 Summary

In the chapter, the air-path simulator was validated by comparison with experimental results. An open ECU was implemented to run the simulator under the same conditions and same parameters as the real test bench. The compared variables were the intake pressure, engine mass-flow, exhaust pressure and EGR mass flow. The simulator proved to be satisfactory as its outputs were comparable with the experimental values. However, during transitions, the lack of delays due to fluid transmission caused deviation between simulation and experimental results. As these delay depend upon the physical properties of fluid flow, the need of 1D simulators cannot be ignored for better results.

This concludes the air-path modeling part of the thesis. In the following chapter, the focus is shifted to local-loop position control of air-path mechatronic actuators. Then, in the last chapter, the influence of exhaust gas flow on the VGT actuator is studied.

Chapter 4

Specialized Actuator Control

4.1 Introduction

The use of control and information processing based on microcomputers is an increasing trend in automotive vehicles and engines [44]. The combustion process and related actuators are microprocessor controlled, working under different control laws for regulation and stability of the engine [44, 47]. The driving force behind this inclination towards modern electronics in the control of engine processes is the improvement of the overall automotive performance. Drive-by-Wire (DbW) systems add to the safety of the vehicle occupants by allowing more accurate maneuvers through the use of closed-loop controlled electric drives. Also, since losses in electrical equipment are lesser as compared to mechanical systems, DbW systems contribute in increasing the car's efficiency as well [44, 47].

In the previous chapter, we examined an industrial engine and air-path test-bench control system, derived from a commercially marketed controller. In this control system, it was seen that actuators are controlled under their specific local-loop position-control laws, which receive their position reference from the global air-path control. The importance and advantage of local controllers were also discussed. On the other hand, commonly employed conventional control methods depend upon precise identification of actuator parameters, and are not robust against parametric uncertainty and external disturbance [38]. Uncertainty in friction alone can lead to tracking errors, limit cycle oscillation (hunting effect) in mechatronic actuators, and potential instability in overall control system [65].

When operating in varying environmental and operational conditions, they fail to guarantee system performance in terms of response time and disturbance rejection. For example, Figure 4.1 shows the tracking results of the an actuator under standard PID control at 100^oC. Due to heat, friction between mechanical contacts and electrical resistance of the motor increase. It can be seen that the PID controller does not maintain its robustness characteristics in this case. Hence the controller required for reliable performance of the actuators needs to be robust under parameter variations.

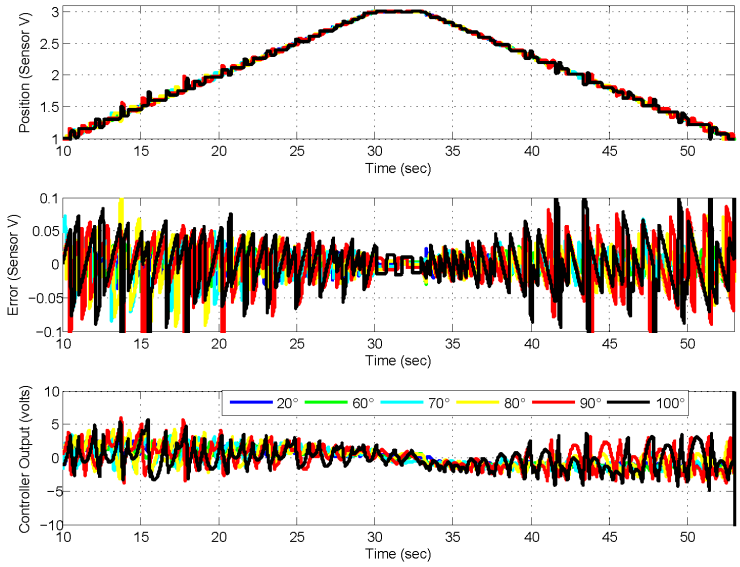


Figure 4.1. *Actuator under PID control in Temperature Variations*

This chapter is dedicated to robust local-loop control design for air-path mechatronic actuators. The objective is to study known robust control methods for uncertain systems in the context of air-path actuators, as well as to propose advanced controllers for this application, which can guarantee the desired performance irrespective of temperature and physical degradation of the actuator over its life (due to aging).

In modern control theory, a discussion on robust control of uncertain systems cannot be started without mentioning Sliding Mode Control (SMC) and Higher Order Sliding Mode Control (HOSMC). The latter is considered to be one of the most effective methods

under uncertainty conditions. In this chapter, we first present a comparative, application-oriented study of three well-known Second Order Sliding Mode Control (SOSMC) algorithms on an air-path actuator. As the theory behind these algorithms are well-known, this study is motivated from the implementation point of view. Next, an advanced adaptive backstepping controller is developed, which dynamically adapts to changes in friction parameters and load changes. As the measurements in commercial engines are limited, observers have been designed to obtain unmeasured states. Finally a comparison between SOSMC and Adaptive controllers is presented to highlight their advantages and disadvantages.

4.2 Experimental Setup

As we are interested in the local-loop position control of the actuators, the controllers discussed in this chapter have been tested on the laboratory test bench described in Chapter 2 (actuator modeling). The controllers have been implemented using LabView. The system is configured to provide the same measurement and PWM capability that would be available in a real automotive ECU, i.e. Hall effect position sensors and $1kHz$ PWM train. The temperature controlled chamber and external hysteresis brake on the test bench are used to generate actual operating conditions for the actuator. The experimental results obtained for each control method are presented in the respective section.

4.3 Sliding Mode based Robust Control

Sliding mode technique has existed since 1934 under different names, and its position as the dominant robust control method was established by Utkin [75] and Emelyanov [76]. Sliding mode control is based on defining an output function or "sliding variable", based on system state trajectories, and using a discontinuous control to converge the sliding variable onto a sliding manifold in finite time [75, 77]. When sliding mode is achieved, the system trajectories are determined by the sliding manifold, and the former are (ideally) not influenced by disturbances or parametric variations. Unfortunately, this control is usually not applicable in its basic or classic form, as high frequency discontinuous control can not always be achieved. This excites unmodeled dynamics of the system, resulting in finite amplitude, finite frequency "chattering" in the system output [75]. In order to avoid this, Higher Order sliding mode technique was proposed, and has been established

as the most successful chattering avoidance method [76, 78, 79]. In this technique, the discontinuous control is applied to some higher time derivative of the sliding manifold, and the system is controlled by an integrated control input. As this control signal is almost continuous, chattering is suppressed while the robustness properties of classical sliding mode are retained. Second order sliding mode control (SOSMC) technique is the most common method, which forces the sliding surface and its first time derivative to zero by acting on the second time derivative [79, 80, 81, 82].

In contemporary literature Sliding Mode Control (SMC) has been studied in many works on robust control of air-path control. Such controllers and observers have been proposed for mechatronic throttle valves with non-smooth nonlinearities and parameter uncertainties [83]. Detailed work has been done on Second Order SMC (SOSMC) by [79, 80, 84]. Major examples of SOSMC applied to air-path actuators are [83, 85, 86]. However, their application so far has remained conceptual, limited to prototypes. Practical implementation and performance related issues have not been detailed. These aspects are important in order to keep the actuators affordable, as actuator controllers currently used in the automobile industry have limited real time processing capabilities. In this study, we have addressed these issues and provided a comparative analysis of experimental results obtained by three SOSMC controllers applied on an engine air-path actuator. The study is partly synthesis of control techniques and partly of applied control view point. The comparison is based on differences in sliding variable as well as varying operating conditions, such as temperature and load changes. Our contribution here, is therefore of experimental interest, focused on performance validation of the SOSMC controller for our particular application. The algorithms have been tested on two sliding surfaces. The first surface is of pure output feedback type, and the second surface consists of a Hurwitz polynomial of the system error dynamics. The performance of the algorithms has been evaluated with respect to response time and chattering.

4.3.1 Actuator Model with Parametric and Load uncertainty

In Chapter 2, the actuator model had been presented and its nonlinear characteristic due to friction has also been highlighted. The shift in parameters due to temperature, and its effect on the actuator characteristics was also shown. We will recall the model here, and present a mathematical formulation of the parametric uncertainty, in order to incorporate

it in the control design.

$$\begin{aligned} \dot{x}_1 &= x_2 \\ \dot{x}_2 &= -\frac{K_{spr}x_1}{J} - \frac{K_a^2 x_2}{R_a J} - \frac{T_f(x_2, z, \dot{z})}{J} - \frac{(T_{pc} + T_L)}{J} + \left(\frac{K_a}{R_a J}\right) u \\ \dot{z} &= x_2 + \frac{|x_2|}{p(x_2)} z \end{aligned} \tag{4.1}$$

As seen in Equation (4.1), the actuator has a multitude of linear and nonlinear physical parameters associated with it. The exact evaluation of these parameters through experiments is difficult and uncertainty is expected. Following [84], let us formalize these uncertainties as

$$\begin{aligned} k_1 = k_{01} + \delta k_1 \quad &= -\frac{K_{spr}}{J} \\ k_2 = k_{02} + \delta k_2 \quad &= -\frac{K_a^2}{R_a J} \\ k_3 = k_{03}(x_2, z, \dot{z}) + \delta k_3 \quad &= -\frac{T_f(x_2, z, \dot{z})}{J} \\ k_4 = k_{04} + \delta k_4 \quad &= -\frac{(T_{pc} + T_L)}{J} \\ k_5 = k_{05} + \delta k_5 \quad &= \frac{K_a}{R_a J} \\ k_6 = k_{06}(x_2) + \delta k_6 \quad &= \frac{\sigma_o}{p(x_2)} \end{aligned} \tag{4.2}$$

Where $k_{0i} (1 \leqslant i \leqslant 6)$ is the nominal value of the parameter k_i, based on the physical parameters identified through bench tests in normal conditions. δk_i is the uncertainty related to k_i, representing parameter variations and uncertainties, such that , $|\delta k_i| \leqslant \delta k_{0i} \leqslant |k_{0i}|$, δk_{0i} being a known positive bound. Hence, system (4.1) can be re-written as:

$$\begin{cases} \dot{x}_1 = x_2 \\ \dot{x}_2 = k_1 x_1 + k_2 x_2 + k_3(x_2, z, \dot{z}) + k_4 + k_5 u \\ \dot{z} = x_2 + k_6(x_2)\,|x_2|\,z \end{cases} \tag{4.3}$$

4.3.2 Sliding Mode Control

Let us consider an uncertain nonlinear system:

$$\begin{aligned} \dot{x} &= f(x, t) + g(x, t) u \\ y &= s(x, t) \end{aligned} \tag{4.4}$$

where $x \in \mathbb{R}^n$ and $u \in \mathbb{R}$ is the input control and s(x,t) is a measured smooth output-feedback function (sliding variable). $f(x,t)$ and $g(x,t)$ are uncertain smooth functions. Assuming that

H1. The relative degree ρ of the system with respect to s is constant and known and the associated zero dynamics are stable.

The SOSMC approach allows the finite time stabilization to zero of the sliding variable s and by defining a suitable control function u. Let us consider two sliding variables, s_1 and s_2. The system (4.4) has relative degrees $\rho = 2$ and $\rho = 1$ with s_1 and s_2 respectively. We obtain the following two distinct second order dynamics.

A. $\rho = 2$

$$\begin{aligned} \dot{s}_1 &= \frac{\partial s_1}{\partial t} + \frac{\partial s_1}{\partial x}[s_1]\left[f(x) + g(x)u\right], \text{ with } \frac{\partial}{\partial x} s_1(x,t) g(x) u = 0 \\ \ddot{s}_1 &= \frac{\partial^2 s_1}{\partial t^2} + \frac{\partial}{\partial x}\dot{s}_1(x,t) f(x) + \frac{\partial}{\partial x}\dot{s}_1(x,t) g(x) u \\ &= \phi_A(x,t) + \gamma_A(x,t) u \end{aligned} \tag{4.5}$$

B. $\rho = 1$

$$\begin{aligned} \dot{s}_2 &= \frac{\partial s_2}{\partial t} + \frac{\partial s_2}{\partial x}[s_2]\left[f(x) + g(x)u\right], \text{ with } \frac{\partial}{\partial x} s(x,t) g(x) u \neq 0 \\ \ddot{s}_2 &= \frac{\partial^2}{\partial t^2} s_2(x,t,u) + \frac{\partial}{\partial x}\dot{s}_2(x,t,u)\left[f(x) + g(x)u\right] + \frac{\partial}{\partial x}\dot{s}_2((x,t,u)\dot{u}(t) \\ &= \phi_B(x,t,u) + \gamma_B(x,t,u)\dot{u} \end{aligned} \tag{4.6}$$

Let us assume that

H2. Functions $\phi(.)$ and $\gamma(.)$ are bounded uncertain functions and the sign of control gain γ is strictly positive. There exist $K_m \in \mathbb{R}^+$, $K_M \in \mathbb{R}^+$, $C \in \mathbb{R}^+$ such that:

$$0 < K_m < \gamma < K_M, \quad |\phi| \leq C \tag{4.7}$$

The second-order sliding-mode problem may be expressed in terms of the finite time stabilization problem of the following uncertain second-order system.

$$\begin{aligned} \dot{\xi}_1 &= \xi_2 \\ \dot{\xi}_2 &= \phi(.) + \gamma(.)\upsilon \end{aligned}$$

where, for the two surfaces defined above:

$$A: \begin{cases} \phi(.) = \phi_A(x,t) \\ \gamma(.) = \gamma_A(x,t) \\ v(t) = u(t) \end{cases} \qquad B: \begin{cases} \phi(.) = \phi_B(x,t,u) \\ \gamma(.) = \gamma_B(x,t,u) \\ v(t) = \dot{u}(t) \end{cases}$$

where

$$A:\ \xi_1 = s_1,\ \ \xi_2 = \dot{s}_1,\ \ v(t) = u(t)$$
$$B:\ \xi_1 = s_2,\ \ \xi_2 = \dot{s}_2,\ \ v(t) = \dot{u}(t)$$

Hence the second order sliding mode control problem is to find a discontinuous control v that would bring the system trajectories to the sliding surface or variable (s_1 and s_2), and then would exactly keep them on the trajectory under parametric variations bounded by K_m, K_M and C. Such a control algorithm would ensure $s = \dot{s} = 0$. Under the constraints imposed in (4.7), let us now review the control algorithms used in the study.

4.3.2.1 Twisting Algorithm

The twisting algorithm is one of the earliest SOSMC algorithms developed to guarantee finite time convergence of the sliding variable dynamics to zero [76]. The twisting algorithm is based on adequate commutation of the control between two different gains, that allow the trajectories to converge towards origin in finite time [76, 78, 84]. This control algorithm is defined as:

$$v = \begin{cases} -v & if\ |v| > v_{\max} \\ -\alpha_m sgn(\xi_1) & if\ \xi_1\xi_2 \le 0\ \ and\ \ |v| \le v_{\max} \\ -\alpha_M sgn(\xi_1) & if\ \xi_1\xi_2 > 0\ \ and\ \ |v| \le v_{\max} \end{cases}$$

Here v_{max} is the maximum limit value of control (in our case, input voltage) that can be physically applied, while α_M and α_m are strictly positive constants. The parameterization is based on the knowledge of the bounds K_m, K_M and C. The following conditions are sufficient to ensure finite time convergence and keeping to zero of the sliding variable [78].

$$\begin{cases} 0 < \alpha_m < \alpha_M, & \alpha_m > \dfrac{C}{K_m} \\ K_m\alpha_M - C > K_M\alpha_m + C \end{cases}$$

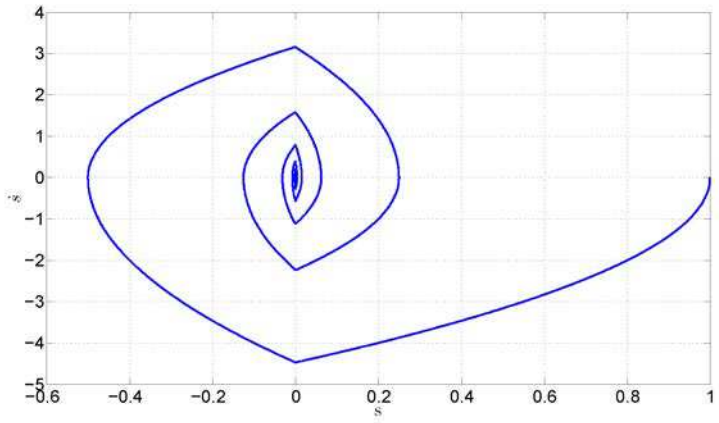


Figure 4.2. *Convergence of the sliding variable under Twisting algorithm*

The stabilization of the sliding variable in the phase plane is shown in Figure 4.2
The twisting algorithm is one of the initial higher order sliding mode algorithms, and is notable for its use of switched gains to achieve finite time convergence. However its disadvantage is that the controller depends upon the derivative of the sliding variable. The calculation of signal derivatives in real time is a well known problem in controller implementation [87].

4.3.2.2 Super twisting Algorithm

The super twisting algorithm [86, 88, 78, 83, 85] is limited to systems with relative degree 1 with the sliding variable. The control signal is continuous, in which the discontinuity is *hidden* behind an added virtual state. The algorithm is given as follows:

$$\dot{v}_1 = \begin{cases} -v & if\ |v| > v_{\max} \\ -\alpha sgn(\xi_1) & if\ |v| \leq v_{\max} \end{cases}$$
$$v_2 = -\varphi\sqrt{|\xi_1|}sgn(\xi_1)$$
$$v = v_1 + v_2$$

Where α and φ are strictly positive constants. The sufficient conditions for convergence of the closed loop system in presence of parametric uncertainty in the system have been presented in [78]. These conditions are based on the knowledge of bounds on the sliding variable and its derivatives. In order to facilitate control design, a generalized set of

conditions has been presented in [89]. These conditions have been used in our study, given as follows:

$$\alpha > \frac{C}{K_m}, \quad \varphi^2 \geq \frac{4CK_M(\alpha + C)}{K_m^3(\alpha - C)}$$

The stabilization of the sliding variable is shown in Figure 4.3

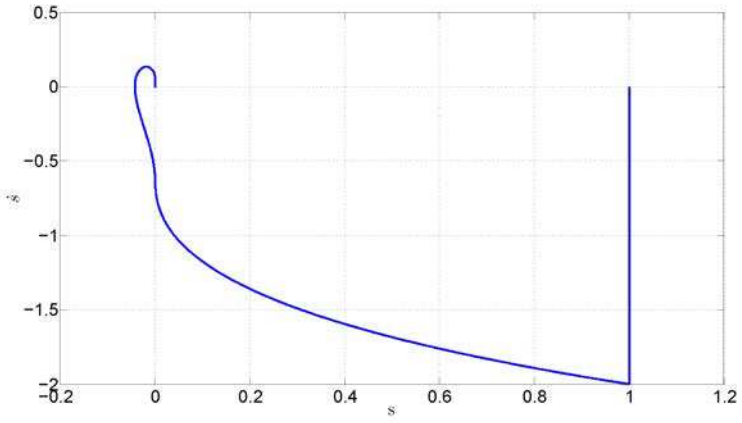


Figure 4.3. *Convergence of the sliding variable under Super Twisting algorithm*

The greatest advantage of super twisting algorithm is that it does not depend upon the derivative of the sliding variable. Also, since the control signal is almost continuous, the chattering is remarkably less than other algorithms. However the limitation of its applicability on variables with relative degree 1 restricts its use, as for systems where the control variable appears in the third or fourth derivative of the output for example, the designer is obliged to calculate multiple derivatives of the output variable, in order to construct the sliding variable itself.

4.3.2.3 Quasi-Continuous Algorithm

The quasi-continuous second order sliding mode controller [87] is a feedback function of ξ_1 and ξ_2 which is continuous everywhere except on the sliding manifold. It has the following form:

$$u = -\alpha \frac{\xi_2 + \sqrt{|\xi_1|}\,\mathrm{sgn}(\xi_1)}{|\xi_2| + \sqrt{|\xi_1|}}$$

Where α is a strictly positive constant. The advantage of this controller is that using the homogeneity reasoning for finite time controllers [82], the improved transient response is achieved as compared to many other higher order SMC, such as [90, 91]. The important disadvantage however, is that there are no formal conditions to parameterize this controller, and while there is only one parameter to tune, its adjustment is empirical. Also, like the twisting algorithm, it requires the derivative of sliding surface as well.

Remark: The tuning of parameters with respect to imposed constraints is important because very high controller gains result in unwanted oscillations and chattering.

4.3.2.4 Robust Differentiator

It can be seen in the previous subsections that two of the three control algorithms under consideration depend upon the time derivative of the sliding variable. Differentiation of signals in real time is a well-known obstacle in practical implementation of controllers [90]. Levant has proposed an arbitrary order exact finite time convergent differentiator [87, 90, 92] to combine with the feedback controller. For a given function s with approximately known Lipschitz constant L (or continuous Lipschitz function $L(t)$), the first order differentiator has the following form [92]:

$$\dot{i}_o = -\lambda_2 L^{1/2} |i_o - s|^{1/2} \operatorname{sgn}(i_o - s) + i_1$$
$$\dot{i}_1 = -\lambda_1 L \operatorname{sgn}(i_1 - i_o)$$

where i_o and i_1 are the estimates of s and $\dot{s}$ respectively. The choice of parameters λ_1 and λ_2 is empirical, and in [87], the values 1.1 and 1.5 respectively have been considered sufficient. In this case, the differentiator depends only upon the knowledge of the Lipschitz constant. Since this constant serves as a gain in the differentiator, in cases where it is not exactly known, a large enough approximation is sufficient. However its order must be comparable to that of the actual value, as taking too large a value would result in larger errors and in extreme cases, oscillations in the derivative output. Due to this dependence on the Lipschitz constant, the differentiator must be be adapted to each application (or adaptive gains may be used). In our study, the applicable value of L was tuned through simulation by evaluating the differentiator using the following function:

$$f(t) = 0.5 \sin(0.5t) + 0.5 \cos(t)$$

Figure 4.4 shows the simulation results ($f(\dot{t})$) based on the differentiator $L = 260$. It can be seen that the derivative calculated by the robust differentiator follows the actual derivative very closely, with a phase shift corresponding to an error of $-8 \times 10_{-3}$.

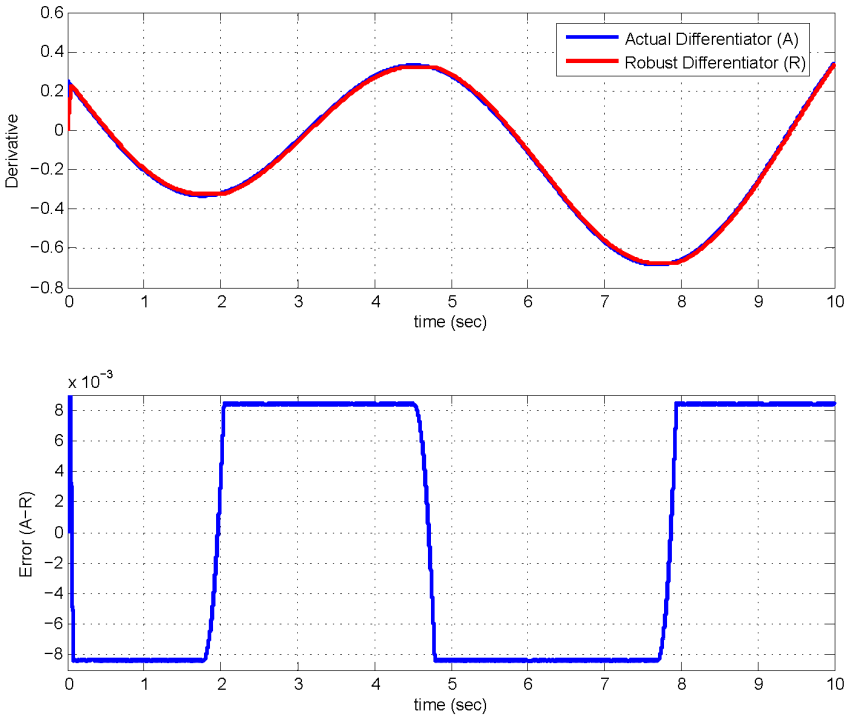


Figure 4.4. *Differentiator Simulation*

4.3.3 Control Design

The control objective is to design a robust control for the actuator represented by (4.3), which guarantees that the actuator output $x_1 = \theta$ tracks a reference trajectory x_{ref} under parameter and load variations. As can be understood in the previous section, the second-order sliding-mode approach requires two steps. The first step is to select a sliding surface or variable suitable for the control task, the second step is to design a control algorithm that would make the variable and its first derivative converge to the sliding manifold. In order to achieve the control objective, two sliding variables have been studied in this paper (defined by s_1 and s_2) along with three control algorithms. The algorithms and their parameterization constraints have been defined in the previous section. In this section, the

sliding variables will be defined and the constraints with respect to (4.3) will be evaluated in order to parameterize the algorithms.

4.3.3.1 Sliding Variables

Sliding variable s_1:
The first sliding variable has the following form

$$s_1 = x_1 - x_{ref}$$

The system has a relative degree $\rho = 2$ with respect to this variable. The time derivatives of this surface are as follows:

$$\ddot{s}_1 = k_1 x_1 + k_2 x_2 + k_3(x_2, z, \dot{z}) + k_4 + k_5 u - \ddot{x}_{ref} \ddot{s}_1 = A_1 + B_1 u \tag{4.8}$$

where

$$A_1 = k_1 x_1 + k_2 x_2 + k_3(x_2, z, \dot{z}) + k_4 - \ddot{x}_{ref} \quad =: A_{o1} + \delta A_1$$
$$B_1 = k_5 \quad =: B_{o1} + \delta B_1$$

where

$$A_{o1} = k_{01} x_1 + k_{02} x_2 + k_{03}(x_2, z, \dot{z}) + + k_{04} - \ddot{x}_{ref}$$
$$\delta A_1 = \delta k_1 x_1 + \delta k_2 x_2 + \delta k_3(x_2, z, \dot{z}) + \delta k_4$$
$$B_{o1} = k_{05}, \;\; \delta B_1 = \delta k_5$$

Here, A_{o1} and B_{o1} are known nominal expressions (based on k_{0i}) while δA and δB contain all uncertainties due to parameter and load variations (based on δk_i). The disturbance δ is uncertain but bounded. The problem of second-order SMC now is equivalent to the stabilization of (4.8) to zero in finite time.

Sliding variable s_2:
The sliding variable has been chosen as the following Hurwitz polynomial

$$s_2 = \dot{e} + \lambda e, \;\; where \; e = x_1 - x_{ref}$$

The system has a relative degree $\rho = 1$ with respect to the sliding variable. Consider the time derivatives of s_2

$$\begin{aligned} \dot{s}_2 &= k_1 x_1 + k_2 x_2 + k_3(x_2, z, \dot{z}) + k_4 + k_5 u + \lambda(x_2 - \dot{x}_{ref}) - \ddot{x}_{ref} \\ \ddot{s}_2 &= A_2 + B_2 \dot{u} \end{aligned} \tag{4.9}$$

where

$$\begin{aligned} A_2 &= k_1 x_2 + k_2 [k_1 x_1 + k_2 x_2 + k_3(x_2, z, \dot{z}) + k_4 + k_5 u] + k_3(x_2, z, \dot{z}) \\ &\quad + \lambda [k_1 x_1 + k_2 x_2 + k_3(x_2, z, \dot{z}) + k_4 + k_5 u] - (\lambda \ddot{x}_{ref} + \dddot{x}_{ref}) \\ &:= A_{o2} + \delta A_2 \\ B_2 &= k_5 =: B_{o2} + \delta B_2 \end{aligned}$$

where

$$\begin{aligned} A_{o2} &= k_{01} x_2 + k_{01} k_{02} x_1 + k_{02}^2 x_2 + k_{02} k_{03} + k_{02} k_{04} + k_{02} k_{05} u + k_3 \\ &\quad + \lambda(k_{01} + k_{02} + k_{03} + k_{04} + k_{05} u) \\ \delta A_2 &= \delta k_1 x_2 + k_{01} \delta k_2 x_1 + k_{02} \delta k_1 x_1 + \delta k_1 \delta k_2 x_1 + 2 k_{02} \delta k_2 x_2 + \delta k_2^2 x_2 \\ &\quad + k_{02} \delta k_3 + k_{03} \delta k_2 + \delta k_2 \delta k_3 + k_{02} \delta k_4 + k_{04} \delta k_2 + \delta k_2 \delta k_4 \\ &\quad + k_{02} \delta k_5 u + k_{03} \delta k_5 u + \delta k_2 \delta k_5 u + \lambda(\delta k_1 + \delta k_2 + \delta k_3 + \delta k_4 + \delta k_5 u) \\ B_{o2} &= k_{05} \,, \; \delta B_2 = \delta k_5 \end{aligned}$$

where, A_{o2}, B_{o2}, δA_2, δB_2 have the same significance as in the case of s_1.

4.3.3.2 Feedback Linearization

The control problem is equivalent to the finite time stabilization of equations (4.8) and (4.9). In order to simplify, we have chosen the notations A and B for both surfaces, since the same generalization has been followed. However the actual expressions for A and B are unique to each surface, as derived in the above sections. In the complete system model, if we consider feedback linearization, applying control to cancel all known nonlinearities, we would get:
For s_1

$$u = B_{o1}^{-1}(-A_{o1} + v)$$

For s_2

$$\dot{u} = B_{o2}^{-1}(-A_{o2} + v)$$

Applied to Equations (4.8) and (4.9), we get for both cases

$$\ddot{s}_i = \hat{A}_i + \hat{B}_i v$$

where

$$\hat{A}_i = \delta A_i - \frac{\delta B_i}{B_{oi}}\ ,\ \hat{B}_i = \left(1 + \frac{\delta B_i}{B_{oi}}\right) \tag{4.10}$$

where $i = 1,2$ refers to the surface. In fact, the control laws u and $\dot{u}$ are functions which would permit feedback linearization if the system had been modeled perfectly, without uncertainties, i.e. $(\delta A = \delta B = 0)$. As δA and δB are not equal to zero, the system remains nonlinear. Nevertheless, this feedback allows narrow bounds on the parameters $\hat{A}$ and $\hat{B}$ as compared to A and B.

4.3.3.3 Controller Parameters

Let us recall hypothesis **H2**, which states that there exist positive constants C, K_m, K_M, such that:

$$\left|\hat{A}_i\right| \leq C_i\ (c1) \qquad 0 < K_{mi} < \hat{B}_i < K_{Mi}\ (c2)$$

As seen in the previous section, the parameters of the control algorithm are determined respecting these constraints. The problem of second order sliding mode control now is equivalent to the stabilization of $\ddot{s}_1$ and $\ddot{s}_2$ to zero in finite time. The disturbance δ is uncertain but bounded. It is hence left to be compensated by the controller parameters. In this section, the parameters of the three control algorithms discussed in the previous section, would be determined to satisfy the binding conditions.

The parametric variations have been evaluated by open loop testing of the actuator, under various temperature and load changes. Based on the results, a variation of ±30% was measured in the resistance R_a and ±10% in the torque coefficient K_a. These variations were distributed amongst the parameters of equation (4.3) as ±1% with respect to k_{01}, ±30% with respect to k_{02}, ±10% with respect to k_{03}, ±10% with respect to k_{04}, and ±30% with respect to k_{05}. The changes in parameter k_{06} were considered to have been incorporated in the friction torque; the nominal value of the latter was taken as the static friction value. The distribution of these variable is based on the physical characteristics of the actuator, and has been validated based on simulation and experimental results.

The controller parameters are evaluated using the condition sets (c1) and (c2) given in sections 3 and 4. $\hat{B}$ has two values, corresponding to the upper and lower uncertainty bounds. The values for $\hat{A}$ and $\hat{B}$ and the respective bounding parameters are given in the

following sections.

For Variable s_1:

The values for $\hat{A}$ and $\hat{B}$ for this variable were calculated to be:

$$\hat{A}_1 = 19.152 \times 10^3, \ \hat{B}_1 = 0.7, 1.3$$

For these values, the following positive constant parameters were chosen to evaluate controller parameters

$K_{m1} = 0.6, \ K_{M1} = 1.4, \ C_1 = 19.560 \times 10^3$

For Variable s_2:

For the sliding variable parameter $\lambda = 100$ the following values were found for $\hat{A}$ and $\hat{B}$

$$\hat{A}_2 = 2.134 \ , \ \hat{B}_2 = 0.7, 1.3$$

A significant difference can be seen between the values of $\hat{A}$ in the two variables. $\hat{B}$ is not effected by the choice of surface and remains the same as in the case of s_1. For these values, the following positive constant parameters were chosen to evaluate controller parameters

$K_{m2} = 0.6, \ K_{M2} = 1.4, \ C_2 = 2.65$

The controller parameters were evaluated following these bounding conditions, as expressed in the algorithms. As mentioned before, if parameters are chosen very large, they result in unwanted oscillations and chattering. The parameters of twisting algorithm were adjusted so that they would satisfy the conditions of both the surfaces. Since no stability conditions are present for the quasi-continuous algorithm, its value was determined empirically, through simulations, which have been presented in the next section. These parameters are given in Appendix A.

4.3.4 Simulation

In order to choose the control parameters, the three algorithms used in our study were simulated using the actuator model given in Equation (4.1). As this study is focused on experimental results, simulations have been carried out for determination of parameters only. Performance and robustness issues have been presented in experimentation.

4.3.4.1 Test Trajectory

The primary control problems used with control valves are that of regulation and tracking. Therefore the reference trajectory (shown in Figure 4.5) has been designed to tune and test the controllers according to their performance with a step and a linear tracking problem. This trajectory is an industrial bench mark, in fact used by a certain manufacturer of EGR valves for the performance evaluation of their systems. The said manufacturer uses this trajectory at a sampling rate of $1kHz$. In compliance, the simulations were carried out at $1msec$.

The first part of the test, a step input is used to characterize the time response of the actuator, after a low-to-high step and a high-to-low step. This part of the tests allows to measure the time response (settling time), overshoots and positioning characteristics (steady state error, chattering). The second part, the ramp is for evaluating the tracking efficiency of the control law. The different slopes characterize any changes in the system with change in direction. The stationary region between the ramps, provides a zero-velocity region between the two ramps and also helps in comparing positioning characteristics with tracking characteristics (tracking error, chattering while in motion).

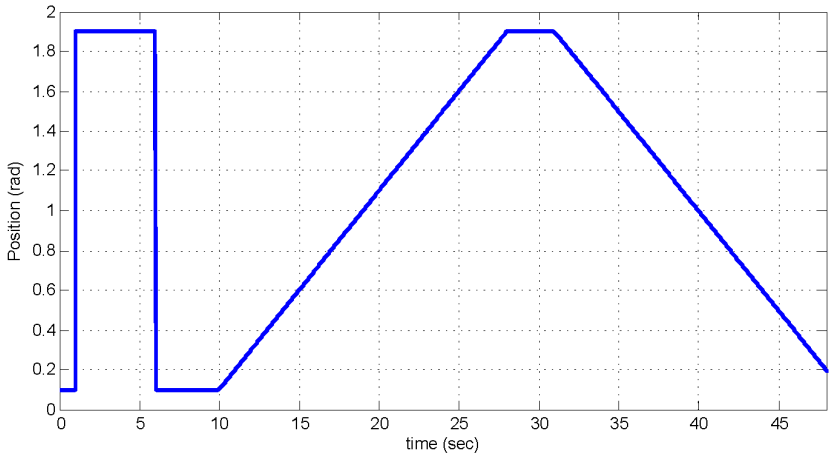
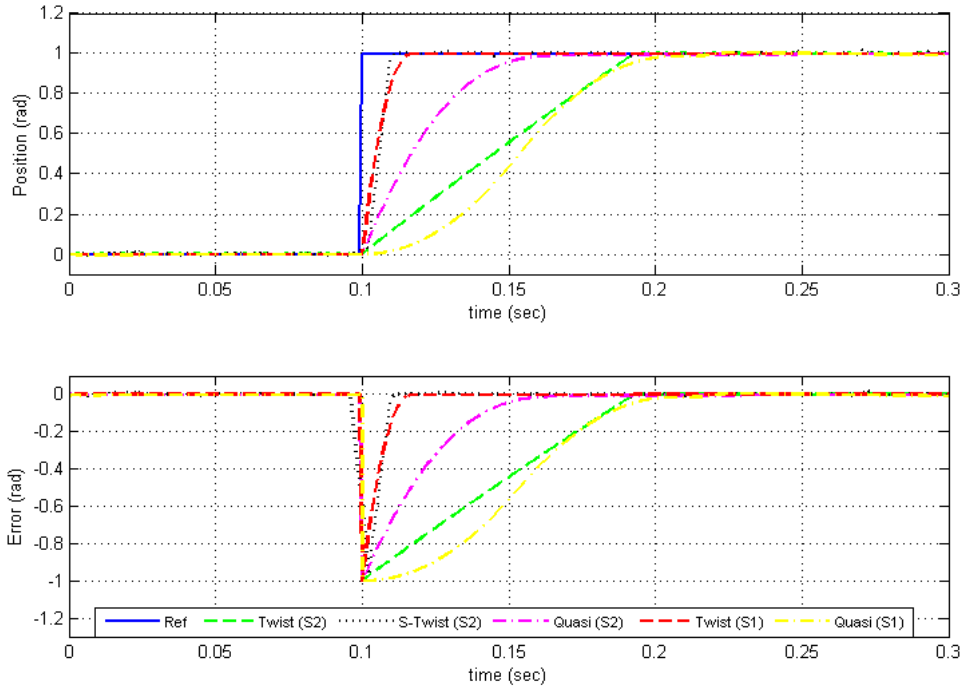


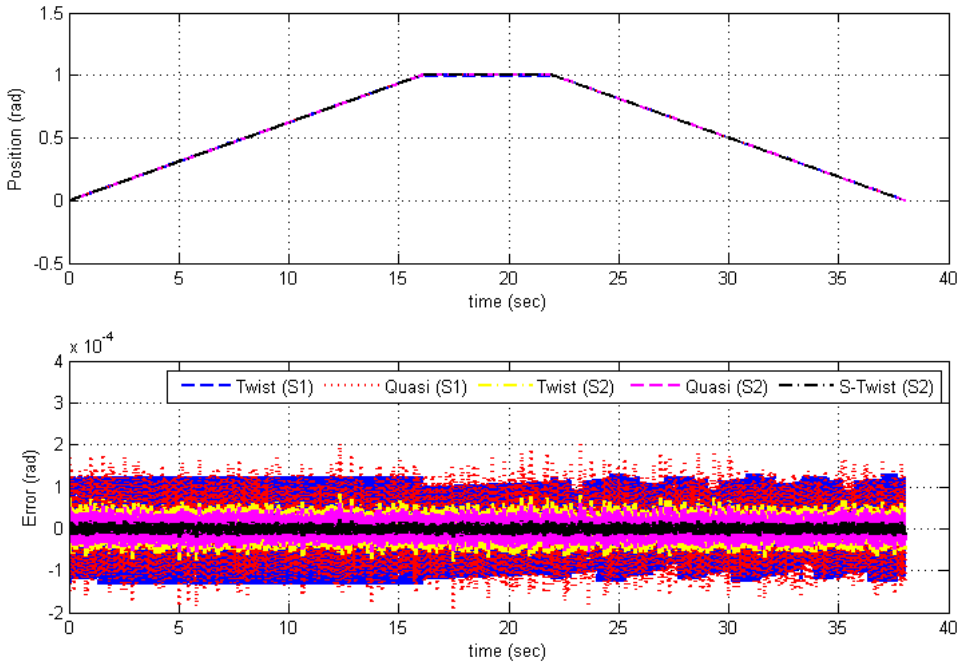
Figure 4.5. *Reference Trajectory*

4.3.4.2 Simulation Results

The performances of all the control algorithms have been shown in Figure 4.6.



(a) Step Response



(b) Tracking Response

Figure 4.6. *Simulation Results*

It can be seen that in simulations, the Super Twisting algorithm has provided the lowest level of chattering. In terms of time response, Twisting Algorithm is the fastest. The Quasi-Continuous controller could not achieve a time response better than $180msec$. However it is important to consider that its parameter have to be determined empirically as there are no bounding conditions applicable to this algorithm.

4.3.5 Experimental results

All the controllers except the super-twisting were tested on both sliding variables. The super-twisting algorithm was implemented only on variable s_2 since it is the only one with respect to which, the system has relative degree of 1. The same reference trajectory was applied on the controllers, as used in simulations. The performance criteria set to judge the controllers were steady state error, settling time and chattering level. Tests were conducted in two stages. In the first stage, all controllers were tested in nominal conditions (room temperature), to determine their performance according to the performance criteria. In the next step the controllers whose performance was satisfactory, were tested in high temperature to verify their robustness. In this stage, they were expected to maintain their performance throughout the temperature range.

4.3.5.1 Nominal Conditions

In the first stage of tests, all controllers were tested at no load and room temperature. These results are shown in Figure 4.7. There is only one result for super twisting controller since it can only be applied to s_2. It is clear that in terms of steady state error, all sliding mode controllers bring the system error to zero, validating the finite time stabilization claim.

Sliding variable s_1:

The performance of the controllers on s_1 shows that this surface is prone to chattering (Figure 4.7). The twisting algorithm showed a good settling time of $100msec$, and no steady state error was present. However significant chattering oscillation was present, of the magnitude of $0.1rad$. This chattering level is not acceptable since oscillations are large enough to disrupt air flow through the actuator. The performance of the quasi continuous algorithm was worse on s_1. Like the twisting algorithm, no static error existed. Its settling time was $300msec$. Chattering was slightly less than twisting, but still significant enough

to rule this controller out for application.

Sliding variable s_2:

The performance of all the controllers was improved on s_2, with respect to chattering. As can be seen in Figure 4.7, the chattering in the twisting algorithm was reduced drastically with the use of this surface, from $0.1rad$ to $0.03rad$. This chattering level however is still visible and noticeable and hence higher than acceptable. The settling time of the twisting algorithm deteriorated, increasing from $100msec$ to $210msec$.

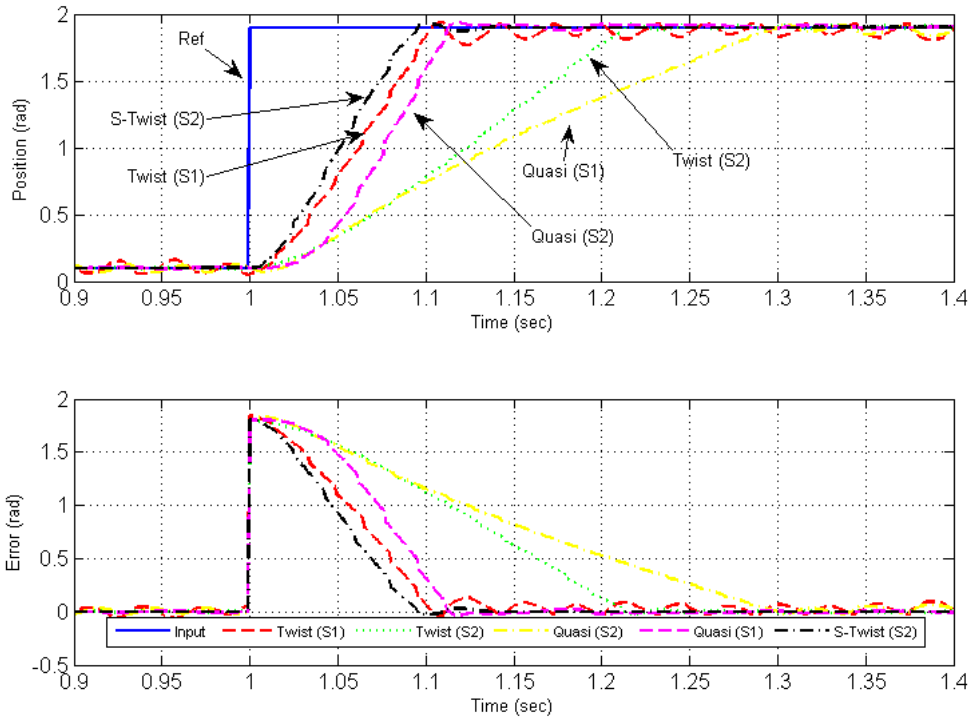
Improvement was seen in the performance of the quasi-continuous controller, with respect to both chattering level and settling time (Figure 4.7). On s_2, the quasi-continuous algorithm achieved $120msec$ and the chattering level was also reduced to $0.01rad$. Hence the quasi-continuous controller qualified as a viable option for practical application of our actuator.

The super-twisting algorithm was tested for the first time on s_2. Its performance was better than both the previous algorithms, achieving a time response of $110msec$ with a chattering level in the order of $5mrad$ (Figure 4.7). This controller hence qualified for the next stage of experiments.

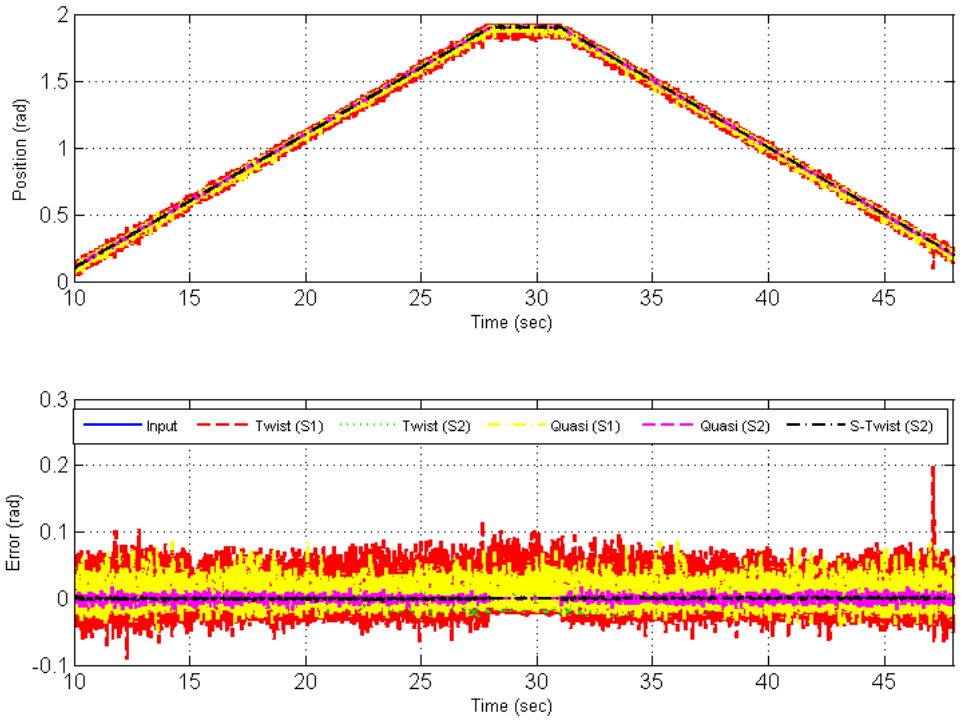
4.3.5.2 Temperature tests

In the previous section, we saw that two controllers proved themselves as viable options for practical application on the actuator under consideration. The quasi-continuous controller (on s_2) and the super twisting controller were then tested for robustness under parametric drift due to temperature. The actuator was heated at temperatures from 20^oC to 100^oC. Given the imposed conditions of uncertainty bounds, the controllers were expected to maintain their performance level (time response, chattering level)throughout the temperature range as the controllers would compensate for the parametric variations.

In Figures 4.8 and 4.9, it can be seen that both the controllers maintained their performance at high temperatures. The quasi-continuous controller maintained its time response at $120msec$ and chattering level to $0.01rad$. The super twisting controller maintained its time response at $110msec$ and chattering level to $5mrad$. Hence these controllers are

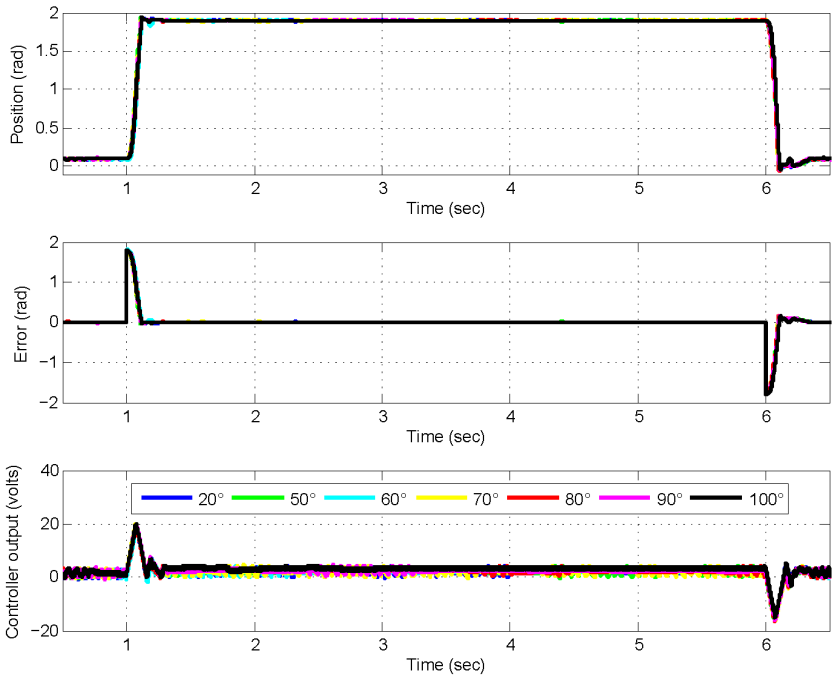


(a) Step Response

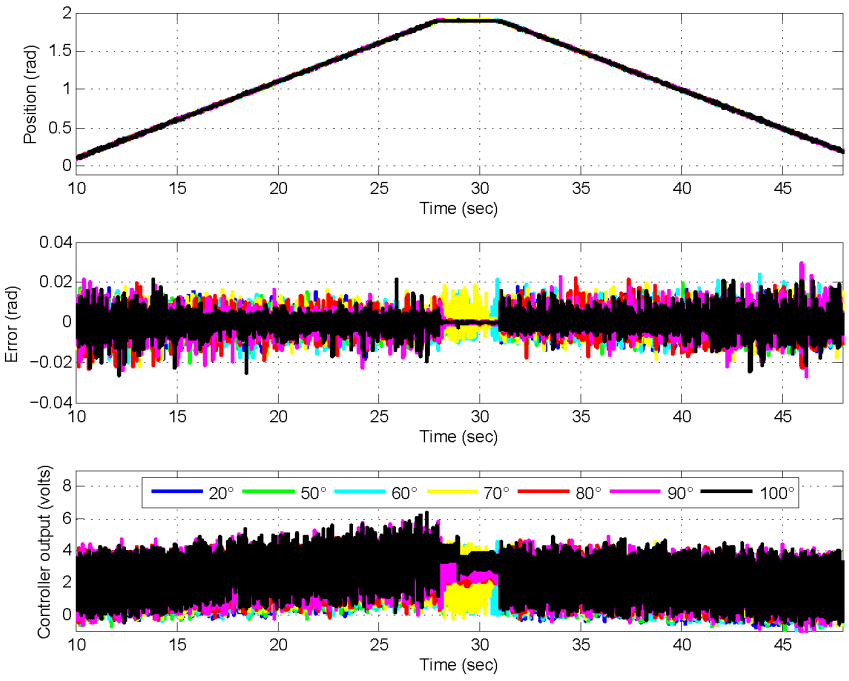


(b) Tracking Response

Figure 4.7. *Comparison: Desired and Actual Trajectories (Nominal Conditions)*

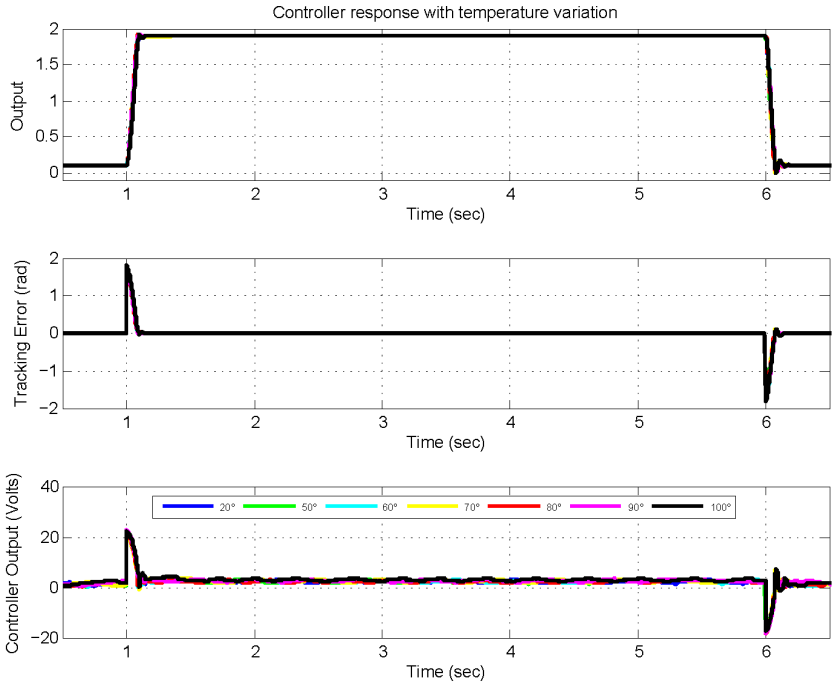


(a) Step Response

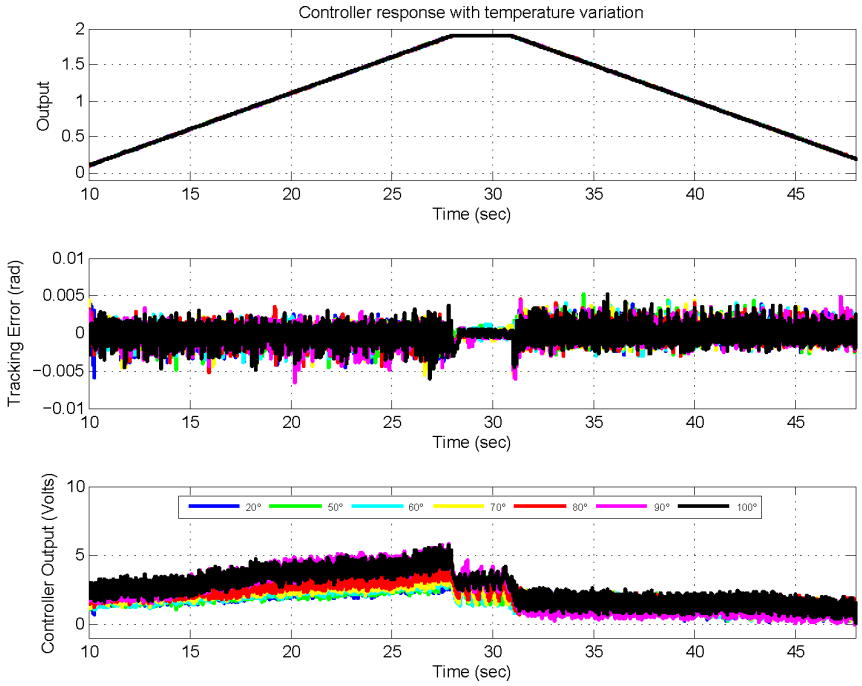


(b) Tracking Response

Figure 4.8. *Quasi Continuous Controller under Temperature Variation*



(a) Step Response



(b) Tracking Response

Figure 4.9. *Super Twisting Controller under Temperature Variation*

robust for application in temperature varying environments.

4.3.5.3 Sinusoid tests

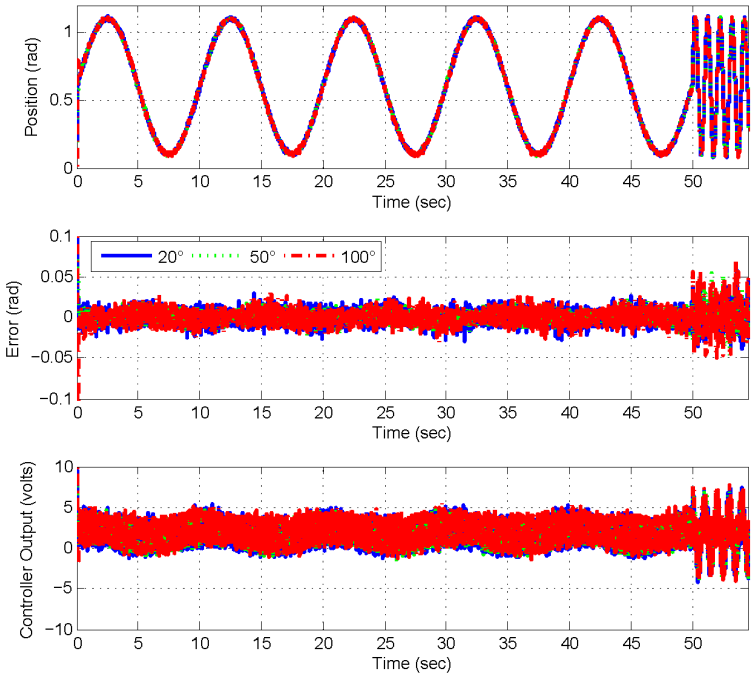
In addition to trapezoidal tracking, a sinusoidal trajectory has also been used in experimental performance evaluation of the actuators. The sinusoidal trajectory permits to evaluate the controller performance of mechanical systems during movement or velocity direction inversion, as it demonstrates the effects of friction and backlash on the controller [93]. In our study, two frequencies were used, $0.1Hz$ and $1Hz$.
The results in Figure 4.10 show how the controllers change their output to compensate for the increased velocity. It can be seen that the controllers are robust against nonlinear changes on a continuously varying trajectory. However as the frequency increases, the tracking error increases due to the demand of smaller response time which the controller fails to provide. This is inherently due to the inertial constraints of the actuator itself, which limit the acceleration.

4.3.6 Conclusion on sliding mode controllers

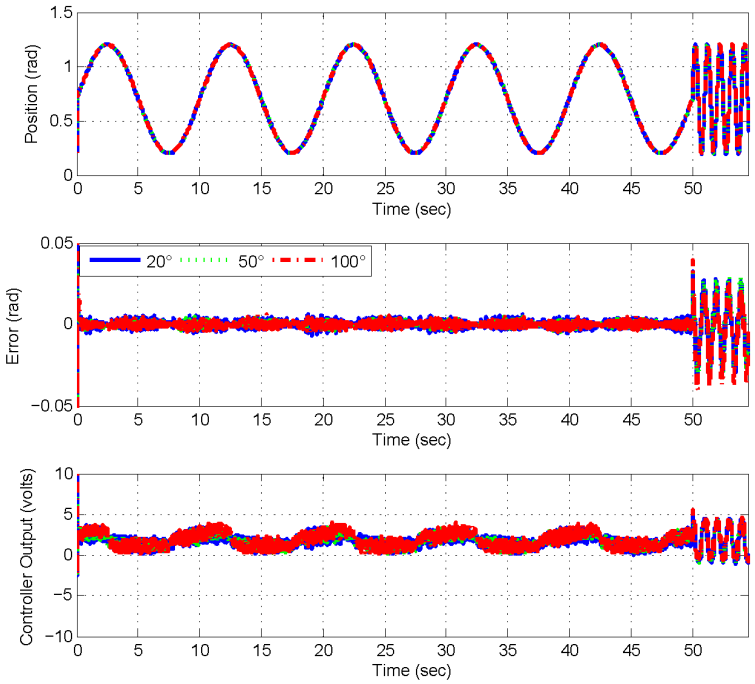
While all controllers performed well in tracking, chattering proved to be a nuisance in their application. The closed loop system performed better in terms of response time and chattering when a surface of relative degree 1 was used. Among control algorithms, the chattering phenomenon was reduced significantly using the quasi-continuous controller and was almost negligible when the super-twisting algorithm was applied. Both these controllers proved their worth in terms of robustness as well. Hence sliding mode control proved to be an effective control strategy in the presence of uncertainties.

4.4 Backstepping Based Adaptive Output Feedback Controller

In the previous section, the effectiveness of Second Order Sliding Mode Control was shown for air-path actuator control. Essentially, sliding mode control gains are tuned such that the control input is very large, as compared to the system uncertainty limits. In practice, this approach is acceptable if the gains are properly tuned. However if the uncertainty bounds are wrongly estimated, this can also result in unnecessarily large control inputs,



(a) Quasi-Continuous Controller



(b) Supertwisting Controller

Figure 4.10. *Tracking a sinusoidal trajectory*

which in turn, can damage the actuator itself. In application, it is preferable that the control input calculated by the controller be just sufficiently large to compensate friction and uncertainty [94]. Also, in certain cases, the internal dynamics of the control cannot be neglected, i.e. the dynamics of current are not ignorable [95]. This case has two important consequences; stability using sliding mode control needs to be proved and control design using the LuGre model is not applicable because its derivative is discontinuous. It is therefore important to replace it with an approximation.

In this section, we propose an advanced backstepping based adaptive output feedback controller for position control and friction compensation of air-path actuators. In order to overcome the problem stated above, the current dynamics are also taken into account. Dynamic adaptive laws compensate friction and load variations, making the controller robust. The main contribution of our controller with respect to the contemporary works cited above, is that it requires the measurement of position only, while velocity, current and friction state are obtained using estimation and observation. It is based on velocity estimation through fixed time differentiation and observers for friction and current states. The robustness of the controller is augmented using projection operator, which bounds the output of nonlinear adaptive controllers while conforming to Lyapunov stability rules. This is necessary in order to avoid system instability. It also forces estimated parameters to remain bounded [96]. The controller is designed using adaptive backstepping method and Lyapunov-based proof is presented to demonstrate the convergence of the closed loop controller-observer system. It shows that the controller ensures asymptotic convergence of feedback and state observer errors to zero.

4.4.1 Problem Formulation

Let us rewrite the actuator model presented in Chapter 2, and include the current dynamics:

$$\begin{aligned} \dot{\theta} &= \omega, \\ J\dot{\omega} &= K_I I - F - T_l, \\ \dot{I} &= \frac{v}{L} - \frac{K_I}{L}\omega - \frac{R_a}{L} I, \end{aligned} \tag{4.11}$$

where the additional parameter L represents the motor inductance. The rest of the definitions are same as in Chapter 2. In this formulation, the current I acts as the input force on the mechanical system. Current dynamics are driven by the input voltage v. The load

torque T_l acts as an external perturbation to the system, since it varies with the operating conditions of the system, i.e. air mass flow through the servo valve and valve plate orientation. As the geometric characteristics of valves are fixed, and the mass flow is bounded, T_l is treated as an unknown external perturbation that varies slowly, its derivative being negligible.

The friction force F is modeled by a continuous extension of the LuGre model, because this model contains discontinuous terms in its original form, which cannot be resolved for certain classes of systems or controllers that require the time derivative of the estimated friction force. The continuous extension of the LuGre model proposed in [95] model solves this problem by introducing continuous and differentiable approximations of the discontinuous terms, such that the passivity and boundedness of the internal states are not affected. This model is represented by the following equations,

$$\begin{aligned} \dot{z} &= S_1\omega - \alpha(\omega)S_2 z, \\ F &= \sigma_o z + \sigma_1 \dot{z} + \sigma_2 \omega, \\ \alpha(\omega) &= \frac{1}{F_C + (F_S - F_C)\, e^{-\left(\frac{\omega}{x_s}\right)^2}}, \end{aligned} \tag{4.12}$$

The functions S_1 and S_2 are given by

$$\begin{aligned} S_1 &= \left(\tanh(C\omega)^2\right) \\ S_2 &= \omega \tanh(C\omega). \end{aligned}$$

4.4.1.1 Control problem formulation

For the purpose of backstepping control design, let us rewrite the system equations (4.11) into a general form. Defining

$$\begin{aligned} x_1 &= \theta, & x_2 &= \omega, & X_3 &= I, \\ \beta_o &= \frac{\sigma_o}{J}, & \beta_1 &= \frac{\sigma_1 + \sigma_2}{J}, & \beta_2 &= \frac{\sigma_1}{J}, \\ k_I &= \frac{K_I}{J}, & k_2 &= \frac{K_I}{L}, & k_3 &= \frac{R_a}{L}, \\ T_L &= \frac{T_l}{J} & u &= \frac{v}{L}. \end{aligned}$$

Using these notations, the equations (4.11) and (4.12) can be rewritten as

$$\begin{aligned} \dot{x}_1 &= x_2, \\ \dot{x}_2 &= k_I z - \beta_0 z - \beta_1 S_1 x_2 + \beta_2 \alpha(x_2) S_2 z - T_L, \\ \dot{x}_3 &= u - k_2 x_2 - k_3 x_3, \\ \dot{z} &= S_1 x_2 - \alpha(x_2) S_2 z. \end{aligned} \tag{4.13}$$

Assumption 1: Friction is bounded ($F \leq F_{max}$) and the variation limits of β_0, β_1 and β_2 are known, i.e. for $i = 0, 1, 2$,

$$\beta_{i_{min}} \leq \beta_i \leq \beta_{i_{max}},$$

where $\beta_{i_{min}}$ and $\beta_{i_{max}}$ are known positive constants.
This leads to the following result:
Lemma 1: *Under Assumption 1, if $|\sigma_0 z(0)| \leq F_{max}$ then $|\sigma_0 z(t)| \leq F_{max}$ $\forall t \geq 0$.*

Proof of this lemma can be found in [95]. In the following, we assume that $|z| \leq z_{max} := \frac{JF_{max}}{\beta_{0_{min}}}$.

The control objective is to force x_1 to track a smooth and bounded reference trajectory x_{1d}, i.e. converging the following feedback error asymptotically to the zero.

$$e_1 = x_1 - x_{1d}. \tag{4.14}$$

As actuators and control valves are equipped with a position sensor only, the output feedback problem requires that the other states be observed. In the following sections, we will first present the observers used for state observation. The velocity is estimated from the position, using exact finite time differentiator. The advantage of this method is that after the convergence of the differentiator, the estimated value is considered as the actual velocity and used as the basis of the current and friction observers. Based on these observed values, the controller will be designed, and the convergence of the complete controller-observer closed loop system will be demonstrated.

4.4.2 State Estimation

Advances in semiconductor technology have made available accurate magnetic position sensors in small packages and at a low cost. Therefore manufacturers prefer integrating these sensors into servo valves that require position control. For precise control however,

the measurement of output variable only is not sufficient, and the knowledge of other internal states is required. In our problem, the state variables x_2 and x_3 are observed from the measured state x_1, as presented in this section. The dynamics of friction state observer are presented later on, during Lyapunov Analysis.

4.4.2.1 Velocity Estimator

The velocity is estimated using the uniform robust exact differentiator (URED) described in [97]. This differentiator is similar to Levant's exact differentiator [87], with higher degree terms added to provide uniform convergence with respect to the initial condition. This means that the URED converges in fixed time T_0 from any initial condition, after which the derivative value can be considered equal to the actual velocity. The URED has the following structure:

$$\begin{aligned} \dot{\hat{x}}_1 &= -K_1\mu_1(\tilde{x}_1), \\ \dot{\hat{x}}_2 &= -K_2\mu_2(\tilde{x}_1), \end{aligned} \tag{4.15}$$

where $\hat{x}_1$ and $\hat{x}_2$ are the estimates of x_1 and x_2 respectively and $\tilde{x}_1 = x_1 - \hat{x}_1$. The gains K_1 and K_2 are positive constants to be tuned. The functions μ_1 and μ_2 are given as

$$\begin{aligned} \mu_1(x_1) &= \phi_1 |\tilde{x}_1|^{\frac{1}{2}} sign(\tilde{x}_1) + \phi_2 |\tilde{x}_1|^{\frac{3}{2}} sign(\tilde{x}_1), \\ \mu_2(x_1) &= \frac{\phi_1^2}{2} sign(\tilde{x}_1) + 2\phi_1\phi_2\tilde{x}_1 + \frac{3}{2}\phi_2^2 |\tilde{x}_1|^2 sign(\tilde{x}_1). \end{aligned} \tag{4.16}$$

The terms $\phi_1, \phi_2 \geq 0$ are scalars. All the parameters are chosen using the assumption that the second derivative of the input signal is bounded, i.e. $|\ddot{x}_1| \leq L$ is bounded. Using $L \leq 100$, the parameters used in this paper are $(K_1, K_2) = (50, 80)$, $(\phi_1, \phi_2) = (1, 1)$. Using these parameters, the upper limit of the convergence time is determined according to [97] as $T_0 = 500\ msec$ (claculation given in Appendix E).

Remark 1: *As the URED converges in fixed time, $\hat{x}_2$ will be considered equal to x_2 in all further calculations. As in [87], it is assumed that in practical implementation, the controller is activated after the convergence of the URED.*

4.4.2.2 Current observer

This observer requires the correction factor μ_2 of Equation (4.15) as well as the estimated value of x_2. From Equations (4.13) and (4.15), the error in velocity estimation is found as follows:

$$\begin{aligned} \dot{\tilde{x}}_1 &= \dot{x}_1 - \dot{\hat{x}}_1 = x_2 + K_1\mu_1(\tilde{x}_1), \\ \dot{\tilde{x}}_2 &= \dot{x}_2 - \dot{\hat{x}}_2 = k_I x_3 - \beta_0 z - \beta_1 S_1 x_2 + \beta_2 \alpha(x_2) S_2 z - T_L - K_2\mu_2(\tilde{x}_1). \end{aligned} \tag{4.17}$$

Defining $\mu_2 = \mu_2(\tilde{x}_1)$, it can be found that after $\tilde{x}_2 = x_2 - \hat{x}_2 = 0$. Then the output injection principle gives us

$$K_2\mu_2 = k_I x_3 - \beta_0 z - \beta_1 S_1 x_2 + \beta_2 \alpha(x_2) S_2 z - T_L.$$

From (4.13), the current observer has been constructed as follows

$$\begin{aligned} \dot{\hat{x}}_3 &= -k_2 x_2 - k_3 \hat{x}_3 + u \\ &\quad + \hat{k}\left[K_2\mu_2 - k_I \hat{x}_3 + \hat{\beta}_0 \hat{z}_0 + \hat{\beta}_1 S_1 x_2 - \hat{\beta}_2 \alpha(x_2) S_2 \hat{z}_1 + \hat{T}_L.\right], \end{aligned} \tag{4.18}$$

where $\hat{k}$ is a positive function, defined later on. The terms $\hat{z}_0$ and $\hat{z}_1$ are observed values of the friction state z, where the dynamics of $\hat{z}_0$ and $\hat{z}_1$ are obtained later. As β_0, β_1 and β_2 are unknown, the dynamic adaptive terms $\hat{\beta}_0$, $\hat{\beta}_1$ and $\hat{\beta}_2$ are introduced to compensate friction. The dynamics of the current observer error $\tilde{x}_3 = x_3 - \hat{x}_3$ are given as

$$\begin{aligned} \dot{\tilde{x}}_3 &= -x_3 \tilde{x}_3 - \hat{k}\left[K_2\mu_2 - k_I \hat{x}_3 + \hat{\beta}_0 \hat{z}_0 + \hat{\beta}_1 S_1 x_2 - \hat{\beta}_2 \alpha(x_2) S_2 \hat{z}_1 - \tilde{T}_L.\right]. \\ &= -k_3 \tilde{x}_3 - \hat{k}\left(k_I \tilde{x}_3 - \beta_0 z + \hat{\beta}_0 \hat{z}_0 - \tilde{\beta}_1 S_1 x_2 + \beta_2 \alpha(x_2) S_2 z - \hat{\beta}_2 \alpha(x_2) S_2 \hat{z}_1 - \tilde{T}_L\right) \\ &= -\left(k_3 + \hat{k} k_I\right) \tilde{x}_3 - \hat{k}\left(-\beta_0 z + \hat{\beta}_0 \hat{z}_0 - \tilde{\beta}_1 S_1 x_2 + \beta_2 \alpha(x_2) S_2 z - \hat{\beta}_2 \alpha(x_2) S_2 \hat{z}_1 - \tilde{T}_L\right). \end{aligned} \tag{4.19}$$

The dynamics of the adaptive terms will be chosen during the Lyapunov analysis, such that they would ensure the exact convergence of $\tilde{x}_3$ to zero.

4.4.3 Controller Design

We will now use adaptive backstepping design method for developing the position controller of the actuator. From Equation (4.14), the following relationships are obtained:

$$e_1 = x_1 - x_{1d}\ ,\ \dot{e}_1 = \dot{x}_1 - \dot{x}_{1d}. \tag{4.20}$$

For the error e_1, a virtual controller x_2^* is defined as

$$x_2^* = -C_1 e_1 + \dot{x}_{1d}, \tag{4.21}$$

where C_1 is a positive constant. The necessary conditions for fixing its value will be presented later. Using (4.20) and (4.21), the dynamics of e_1 become

$$\begin{aligned} \dot{e}_1 &= \left(x_2 - x_2^*\right) + x_2^* - \dot{x}_{1d} \\ &= \left(x_2 - x_2^*\right) - C_1 e_1 + \dot{x}_{1d} - \dot{x}_{1d} \\ &= -C_1 e_1 + e_2, \end{aligned} \tag{4.22}$$

with $e_2 = x_2 - x_2^*$.

The dynamics of e_2 are given as follows:

$$\begin{aligned}\dot{e}_2 &= \dot{x}_2 - \dot{x}_2^* \\ &= k_I x_3 - \beta_0 z - \beta_1 S_1 x_2 + \beta_2 \alpha(x_2) S_2 z - T_L + C_1 \dot{e}_1 - \ddot{x}_{1d} \\ &= k_I x_3 - \beta_0 z - \beta_1 S_1 x_2 + \beta_2 \alpha(x_2) S_2 z - T_L + C_1 (x_2 - \dot{x}_{1d}) - \ddot{x}_{1d}.\end{aligned}$$

A second virtual controller x_3^* is introduced as

$$k_I x_3^* = \hat{\beta}_0 \hat{z}_0 + \hat{\beta}_1 S_1 \hat{x}_2 - \hat{\beta}_2 \alpha(x_2) S_2 \hat{z}_1 - C_1 (x_2 - \dot{x}_{1d}) + \ddot{x}_{1d} - C_2 e_2 + \hat{T}_L. \tag{4.23}$$

Under (4.23), the dynamics of e_2 can be rewritten as

$$\begin{aligned}\dot{e}_2 &= k_I \left(x_3 - x_3^*\right) + k_I x_3^* - \beta_0 z - \beta_1 S_1 x_2 + \beta_2 \alpha(x_2) S_2 z + C_1 (x_2 - \dot{x}_{1d}) - \ddot{x}_{1d} - T_L \\ &= k_I e_3 - C_2 e_2 - \beta_0 z - \beta_1 S_1 x_2 + \beta_2 \alpha(x_2) S_2 z + \hat{\beta}_0 \hat{z}_0 + \hat{\beta}_1 S_1 x_2 - \hat{\beta}_2 \alpha(x_2) S_2 \hat{z}_1 - \tilde{T}_L.\end{aligned} \tag{4.24}$$

Let us introduce a simple rearrangement;

$$\begin{aligned}-\beta_0 z + \hat{\beta}_0 \hat{z}_0 &= -\tilde{\beta}_0 \hat{z}_0 - \beta_0 \tilde{z}_0, \\ -\beta_2 z + \hat{\beta}_2 \hat{z}_1 &= -\tilde{\beta}_2 \hat{z}_1 - \beta_2 \tilde{z}_1,\end{aligned}$$

where $\tilde{\beta}_i = \beta_i - \hat{\beta}_i$ and $\tilde{z}_i = z - \hat{z}_i$. The dynamics of e_2 then become

$$\dot{e}_2 = -C_2 e_2 + k_I e_3 - \tilde{\beta}_0 \hat{z}_0 - \beta_0 \tilde{z}_0 + \tilde{\beta}_2 \alpha(x_2) S_2 \hat{z}_1 + \beta_2 \alpha(x_2) S_2 \tilde{z}_1 - \tilde{\beta}_1 S_1 x_2 - \tilde{T}_L, \tag{4.25}$$

where e_3 is a third error term, defined as

$$e_3 = x_3 - x_3^*. \tag{4.26}$$

The dynamics of e_3 are

$$\begin{aligned}\dot{e}_3 &= \dot{x}_3 - \dot{x}_3^* \\ &= u - k_2 x_2 - k_3 x_3 - \dot{x}_3^*.\end{aligned} \tag{4.27}$$

Let us now compute $\dot{x}_3^*$, by replacing e_2 in (4.23) with $e_2 = x_2 - x_2^*$, where x_2^* is given by (4.21) and $\hat{x}_2 = x_2$. Then Equation (4.23) can be rewritten as

$$k_I x_3^* = -C_1 C_2 e_1 + (C_1 + C_2) \dot{x}_{1d} + \ddot{x}_{1d} + \hat{\beta}_0 \hat{z}_0 - \hat{\beta}_2 \alpha(x_2) S_2 \hat{z}_1 + \left(\hat{\beta}_1 S_1 - C_1 - C_2\right) x_2 + \hat{T}_L, \tag{4.28}$$

and the dynamics of e_3 presented in Equation (4.27) become

$$\dot{e}_3 = u - k_2 x_2 - k_3 x_3 - \frac{1}{k_I} \Psi - \frac{\partial x_3^*}{\partial x_2} \dot{x}_2, \tag{4.29}$$

where term Ψ is defined by,

$$\begin{aligned}\Psi &= -C_1C_2\dot{e}_1 + (C_1+C_2)\,\ddot{x}_{1d} + x_{1d}^{(3)} + \dot{\hat{\beta}}_0\hat{z}_0 + \hat{\beta}_0\dot{\hat{z}}_0 \\ &\quad -\dot{\hat{\beta}}_2\alpha(x_2)S_2\hat{z}_1 - \hat{\beta}_2\alpha(x_2)S_2\dot{\hat{z}}_1 + \dot{\hat{\beta}}_1S_1x_2 + \dot{\hat{T}}_L.\end{aligned} \tag{4.30}$$

The term $\dfrac{\partial x_3^*}{\partial x_2}$ is a function based upon known variables, the expression of which can be obtained by simple calculations

$$\begin{aligned}\frac{\partial x_3^*}{\partial x_2} &= \frac{1}{k_I}\left[-C_1 - C_2 + \hat{\beta}_2\hat{z}_1\frac{\partial\left[\alpha(x_2)S_2\right]}{\partial x_2} + \hat{\beta}_1\frac{\partial\left[S_1x_2\right]}{\partial x_2}\right] \\ &= \frac{1}{k_I}\left[-C_1 - C_2 + \tilde{F}\right].\end{aligned} \tag{4.31}$$

We will see later that $\hat{\beta}_i$ and $\hat{z}_1$ will be bounded by the same bounds of β_i and z given in Assumption 1 and Lemma 1. Therefore the function $\tilde{F}$ is also bounded by a known term $\bar{F}$.

The feedback control law is now defined, using the aforementioned virtual controllers:

$$\begin{aligned}u &= k_2x_2 + \left(k_3 + \frac{\partial x_3^*}{\partial x_2}k_I\right)\hat{x}_3 + \frac{\partial x_3^*}{\partial x_2}\left(-\hat{\beta}_0\hat{z}_0 - \hat{\beta}_1S_1x_2 + \hat{\beta}_2\alpha(x_2)S_2\hat{z}_1 - \hat{T}_L\right) \\ &\quad -C_3\left(\hat{x}_3 - x_3^*\right) + \frac{1}{k_I}\Psi.\end{aligned} \tag{4.32}$$

The dynamics of e_3 in terms of u can then be expressed as

$$\begin{aligned}\dot{e}_3 &= -C_3\left(\hat{x}_3 - x_3^*\right) - \left(k_3 + \frac{\partial x_3^*}{\partial x_2}k_I\right)\tilde{x}_3 \\ &\quad + \frac{\partial x_3^*}{\partial x_2}\left(\beta_0 z - \hat{\beta}_0\hat{z}_0 + \beta_1S_1x_2 - \hat{\beta}_1S_1x_2 - \beta_2\alpha(x_2)S_2z + \hat{\beta}_2\alpha(x_2)S_2\hat{z}_1 + \tilde{T}_L\right),\end{aligned} \tag{4.33}$$

where C_3 is a *function* to be defined later. This step gives us

$$\begin{aligned}\dot{e}_3 &= -C_3\left(\hat{x}_3 - x_3^*\right) - \left(k_3 + \frac{\partial x_3^*}{\partial x_2}k_I\right)\tilde{x}_3 \\ &\quad + \frac{\partial x_3^*}{\partial x_2}\left(\tilde{\beta}_0\hat{z}_0 + \beta_0\tilde{z}_0 + \tilde{\beta}_1S_1x_2 + \left(\beta_2\tilde{z}_1 - \tilde{\beta}_2\hat{z}_1\right)\alpha(x_2)S_2 + \tilde{T}_L\right).\end{aligned} \tag{4.34}$$

4.4.4 Lyapunov Analysis

The proof of convergence of the system (4.13) under adaptive feedback law (4.32) is developed using a Lyapunov-based argument and the LaSalle-Yoshizawa theorem [98](see Appendix D). The dynamic terms left undefined in the previous section, will also be defined here. The velocity estimate is allowed to converge before the controller comes into

action. The Lyapunov candidate function used to prove the stability and convergence of the closed loop system is as follows,

$$V = \frac{1}{2}e_1^2+\frac{1}{2}e_2^2+\frac{1}{2}e_3^2+\frac{1}{2}\tilde{x}_3^2+\frac{1}{2\gamma_0}\tilde{\beta}_0^2+\frac{1}{2\gamma_1}\tilde{\beta}_1^2+\frac{1}{2\gamma_2}\tilde{\beta}_2^2+\frac{1}{2\eta_2}\tilde{T}_L^2+\frac{1}{2\eta_0}\beta_0\tilde{z}_0^2+\frac{1}{2\eta_1}\beta_2\tilde{z}_1^2, \tag{4.35}$$

where γ_0, γ_1, γ_2, η_0 and η_2 are arbitrary positive constants, η_1 is a sufficiently small positive constant defined later on in this section. This function can be written in the following form:

$$V = \frac{1}{2}E^TE+\frac{1}{2}\tilde{\Theta}^T\Gamma^{-1}\tilde{\Theta}+\frac{1}{2\eta_0}\beta_0\tilde{z}_0^2+\frac{1}{2\eta_1}\beta_2\tilde{z}_1^2, \tag{4.36}$$

where $E=[e_1,e_2,e_3,\tilde{x}_3]^T$, $\tilde{\Theta}=\left[\tilde{\beta}_0,\tilde{\beta}_1,\tilde{\beta}_2,\tilde{T}_L\right]$ and $\Gamma=diag\left(\gamma_0,\gamma_1,\gamma_2,\eta_2\right)$. The time derivative of V is given as

$$\begin{aligned}\dot{V} = {} & e_1\dot{e}_1+e_2\dot{e}_2+e_3\dot{e}_3+\tilde{x}_3\dot{\tilde{x}}_3-\frac{1}{\gamma_0}\tilde{\beta}_0\dot{\tilde{\beta}}_0-\frac{1}{\gamma_1}\tilde{\beta}_1\dot{\tilde{\beta}}_1-\frac{1}{\gamma_2}\tilde{\beta}_2\dot{\tilde{\beta}}_2\\ & +\frac{1}{\eta_2}\tilde{T}_L\dot{\tilde{T}}_L+\frac{1}{\eta_0}\beta_0\tilde{z}_0\dot{\tilde{z}}_0+\frac{1}{\eta_1}\beta_2\tilde{z}_1\dot{\tilde{z}}_1.\end{aligned} \tag{4.37}$$

For simplicity and facility in analysis, e_3 is formulated as follows

$$e_3=x_3-x_3^*=x_3-\hat{x}_3+\hat{x}_3-x_3^*=\tilde{x}_3-\bar{x}_3.$$

The advantage of this reformulation is that $\bar{x}_3$ does not depend upon any values external to the controller. Therefore the only remaining unknown element is $\tilde{x}_3$. From the expressions (4.19), (4.22), (4.24) and (4.34), presented in the previous section, the derivative (4.37) can be written as

$$\begin{aligned}\dot{V} = {} & -C_1e_1^2-C_2e_2^2-C_3e_3^2-\left(k_3+\hat{k}k_I\right)\tilde{x}_3^2+e_1e_2+k_Ie_2e_3+\left(C_3-k_3+\frac{\partial x_3^*}{\partial x_2}k_I\right)\tilde{x}_3e_3\\ & -\frac{1}{\eta_0}\beta_0\alpha(x_2)S_2\tilde{z}_0^2-\frac{1}{\eta_1}\beta_2\alpha(x_2)S_2\tilde{z}_1^2-\tilde{\beta}_0\left(e_2\hat{z}_0+\frac{\partial x_3^*}{\partial x_2}\hat{z}_0\bar{x}_3+\frac{1}{\gamma_0}\dot{\tilde{\beta}}_0\right)\\ & -\tilde{\beta}_1\left(e_2S_1x_2+\frac{\partial x_3^*}{\partial x_2}x_2S_1\bar{x}_3+\frac{1}{\gamma_1}\dot{\tilde{\beta}}_1\right)-\tilde{\beta}_2\left(-e_2\alpha(x_2)S_2\hat{z}_1-\frac{\partial x_3^*}{\partial x_2}\hat{z}_1\bar{x}_3\alpha(x_2)S_2+\frac{1}{\gamma_2}\dot{\tilde{\beta}}_2\right)\\ & -\tilde{T}_L\left(e_2+\frac{\partial x_3^*}{\partial x_2}\bar{x}_3+\frac{1}{\eta_2}\dot{\tilde{T}}_L\right)-\beta_0\tilde{z}_0\left(e_2+\frac{\partial x_3^*}{\partial x_2}\bar{x}_3+\frac{1}{\eta_0}\left(\dot{\hat{z}}_0+\alpha(x_2)S_2\hat{z}_0-S_1x_2\right)\right)\\ & +\beta_2\tilde{z}_1\left(\alpha(x_2)S_2e_2+\frac{\partial x_3^*}{\partial x_2}\bar{x}_3\alpha(x_2)S_2-\frac{1}{\eta_1}\left(\dot{\hat{z}}_1+\alpha(x_2)S_2\hat{z}_1-S_1x_2\right)\right)\\ & +\tilde{x}_3\left(\hat{k}+\frac{\partial x_3^*}{\partial x_2}\right)\left(\tilde{\beta}_0\hat{z}_0+\tilde{\beta}_1S_1x_2-\tilde{\beta}_2\alpha(x_2)S_2\hat{z}_1+\beta_0\tilde{z}_0-\beta_2\alpha(x_2)S_2\tilde{z}_1+\tilde{T}_L\right).\end{aligned} \tag{4.38}$$

We define $\hat{k}$ and C_3 as

$$\begin{aligned}\hat{k} &= -\frac{\partial x_3^*}{\partial x_2},\\ C_3 &= k_3-\frac{\partial x_3^*}{\partial x_2}k_I,\end{aligned} \tag{4.39}$$

and we impose the following,

$$\begin{aligned} C_1 &> \max\left(\frac{1}{2}, \left|k_3 + \bar{F}\right|\right) \\ C_2 &> \frac{k_I + 1}{2}. \end{aligned} \tag{4.40}$$

From Equations (4.40) and (4.31), we get

$$\begin{aligned} C_3 &= k_3 + \hat{k} k_I, \\ &= k_3 + C_1 + C_2 - \tilde{F}, \\ &\geq k_3 + C_1 + C_2 - \bar{F} \quad \geq \quad 2k_3 + \frac{1}{2} + \frac{k_I}{2} \quad > \quad \frac{k_I}{2}. \end{aligned} \tag{4.41}$$

Let us define

$$\bar{c} = \min\left[\left(C_1 - \frac{1}{2}\right), \left(C_2 - \frac{k_I + 1}{2}\right), \left(C_3 - \frac{k_I}{2}\right)\right].$$

In this case,

$$\begin{aligned} \dot{V} \leq\ & -\bar{c} E^T E - \frac{1}{\eta_0}\beta_0 \alpha(x_2) S_2 \tilde{z}_0^2 - \frac{1}{\eta_1}\beta_2 \alpha(x_2) S_2 \tilde{z}_1^2 \\ & -\tilde{\beta}_0 \frac{1}{\gamma_0}\left[\dot{\hat{\beta}}_0 + \gamma_0 \hat{z}_0 \left(e_2 + \frac{\partial x_3^*}{\partial x_2}\bar{x}_3\right)\right] - \tilde{\beta}_1 \frac{1}{\gamma_1}\left[\dot{\hat{\beta}}_0 + \gamma_1 S_1 x_2 \left(e_2 + \frac{\partial x_3^*}{\partial x_2}\bar{x}_3\right)\right] \\ & -\tilde{\beta}_2 \frac{1}{\gamma_2}\left[\dot{\hat{\beta}}_2 + \gamma_2 S_2 \hat{z}_1 \left(e_2 + \frac{\partial x_3^*}{\partial x_2}\bar{x}_3\right)\right] - \tilde{T}_L \frac{1}{\eta_2}\left[\dot{\hat{T}}_L - \eta_2 \left(e_2 + \frac{\partial x_3^*}{\partial x_2}\bar{x}_3\right)\right] \\ & -\tilde{z}_0 \frac{1}{\eta_0/\beta_0}\left[\dot{\hat{z}}_0 + \alpha(x_2) S_2 \hat{z}_0 - S_1 x_2 + \eta_0 \left(e_2 + \frac{\partial x_3^*}{\partial x_2}\bar{x}_3\right)\right] \\ & -\tilde{z}_1 \frac{1}{\eta_1/\beta_2}\left[\dot{\hat{z}}_1 + \alpha(x_2) S_2 \hat{z}_1 - S_1 x_2 + \eta_1 \alpha(x_2) S_2 \left(e_2 + \frac{\partial x_3^*}{\partial x_2}\bar{x}_3\right)\right. \end{aligned} \tag{4.42}$$

Consider the following dual observer of z:

$$\begin{aligned} \dot{\hat{z}}_0 &= -\alpha(x_2) S_2 \hat{z}_0 + S_1 x_2 - \eta_0 \left(e_2 + \frac{\partial x_3^*}{\partial x_2}\bar{x}_3\right), \\ \dot{\hat{z}}_1 &= -\alpha(x_2) S_2 \hat{z}_1 + S_1 x_2 + \\ & \quad \begin{cases} -\eta_1 \alpha(x_2) S_2 \left(e_2 + \frac{\partial x_3^*}{\partial x_2}\bar{x}_3\right) & , |\hat{z}_1| < z_{max}, \\ 0 & , |\hat{z}_1| \geq z_{max}. \end{cases} \end{aligned} \tag{4.43}$$

The dynamics of $\hat{z}_1$ is chosen such that $\hat{z}_1$ is bounded. In fact for $|\hat{z}_1| \geq z_{max}$, we get

$$\dot{\tilde{z}}_1 = -\alpha(x_2) S_2 \tilde{z}_1,$$

with $\alpha(x_2) S_2 \geq 0$, which implies that $|\tilde{z} - 1|$ is decreasing and then $\hat{z}_1$ remains bounded as z is bounded. Let $\hat{\Theta}^T = \left[\hat{\beta}_0, \hat{\beta}_1, \hat{\beta}_2, \hat{T}_L\right]$, and $D^T = \left(e_2 + \frac{\partial x_3^*}{\partial x_2}\bar{x}_3\right)\left[\gamma_0 \hat{z}_0, \gamma_1 S_1 x_2, \gamma_2 S_2 \hat{z}_1, \eta_2\right]$, then

$\dot{V}$ satisfies,

$$\begin{aligned}\dot{V} &\leq -\bar{c}E^TE - \frac{1}{\eta_0}\beta_0\alpha(x_2)S_2\tilde{z}_0^2 - \frac{1}{\eta_1}\beta_2\alpha(x_2)S_2\tilde{z}_1^2 - \tilde{\Theta}\Gamma^{-1}\left[\dot{\hat{\Theta}} + D\right] \\ &\quad + \frac{1}{\eta_1}\beta_2\alpha(x_2)S_2\left|\tilde{z}_1\eta_1\left(e_2 + \frac{\partial x_3^*}{\partial x_2}\bar{x}_3\right)\right|, \\ &\leq -\bar{c}E^TE - \frac{1}{\eta_0}\beta_0\alpha(x_2)S_2\tilde{z}_0^2 - \frac{1}{2\eta_1}\beta_2\alpha(x_2)S_2\tilde{z}_1^2 \\ &\quad -\tilde{\Theta}\Gamma^{-1}\left[\dot{\hat{\Theta}} + D\right] + \frac{\eta_1}{2}\beta_2\alpha(x_2)S_2\left(e_2 + \frac{\partial x_3^*}{\partial x_2}\bar{x}_3\right)^2.\end{aligned} \tag{4.44}$$

Let $M = \beta_{2_{max}} \max\left\{1, \left(\frac{C_1 + C_2 + \bar{F}}{k_I}\right)^2\right\} \max\{\alpha(x_2)S_2\}$, then

$$\dot{V} \leq -(\bar{c} - \eta_1 M)E^TE - \tilde{\Theta}\Gamma^{-1}\left[\dot{\hat{\Theta}} + D\right] \tag{4.45}$$

we take $0 < \eta < \frac{\bar{c}}{M} =: \tilde{c}$ and $\dot{\hat{\Theta}} = -Proj_{\hat{\Theta}}(D)$ [96]. Then we obtain

$$\dot{V} \leq -\tilde{c}E^TE - \frac{1}{\eta_0}\beta_0\alpha(x_2)S_2\tilde{z}_0^2 - \frac{1}{2\eta_1}\beta_2\alpha(x_2)S_2\tilde{z}_1^2 + \tilde{\Theta}\Gamma^{-1}\left[Proj_{\hat{\Theta}}(D) - D\right] \tag{4.46}$$

According to the properties of projection operation, we get

$$\dot{V} \leq -\bar{c}E^TE - \frac{1}{\eta_0}\beta_0\alpha(x_2)S_2\tilde{z}_0^2 - \frac{1}{2\eta_1}\beta_2\alpha(x_2)S_2\tilde{z}_1^2. \tag{4.47}$$

The fact that $\dot{V}$ is negative semi-definite is not sufficient for knowing the asymptotic behavior of our system, since the adaptive parameters render the system non-autonomous (time-varying). Therefore, we need to proceed with the help of Barbalat's lemma [99, 100]. As $\dot{V} \leq 0$, it can be concluded that V is bounded by its initial condition $V(0)$. This means that all the terms of V, i.e. e_1, e_2, e_3, $\tilde{x}_3$, along with $\tilde{\beta}_0$, $\tilde{\beta}_1$, $\tilde{\beta}_2$, $\tilde{z}_0$, $\tilde{z}_1$ and $\tilde{T}_L$ are bounded as well. In particular, for $i = 1,2,3$, we have $e_i, \tilde{x}_3 \in \mathcal{L}_\infty$.

We will now demonstrate that $\dot{e}_i, \dot{\tilde{x}}_3 \in \mathcal{L}_\infty$. The terms $\hat{\beta}_i$ and $\hat{T}_L$ are also bounded, as this is the main property of projection operator. According to (4.22), $\dot{e}_1$ is bounded since e_1 and e_2 are bounded. Also, from Equations (4.20) and (4.21), it can be concluded that x_1, and therefore x_2^* are also bounded. Then $e_2 = x_2 - x_2^*$ means that x_2 is also bounded. From the dynamics of z in (4.13), as x_2 is bounded and $\alpha(x_2)|x_2|$ is positive, z is also bounded. As z and $\tilde{z}_i$ are bounded, $\hat{z}_0$ and $\hat{z}_1$ are also bounded. In this way, all the terms of the dynamic equations (4.23) and (4.24) are bounded, therefore x_3^*, $\dot{e}_2$ are bounded. From (4.31), $\frac{\partial x_3^*}{\partial x_2}$ is bounded, which means that $\hat{k}$ and from (4.19), $\dot{\tilde{x}}_3$ are bounded. Now, (4.27)

implies that since e_3 and x_3^* are bounded, x_3 is bounded as well, which means that $\hat{x}_3$ is also bounded. Therefore, $\dot{e}_3$ in (4.34) is bounded. To sum it up, this discussion results in $\dot{e}_i, \dot{\tilde{x}}_3 \in \mathcal{L}_\infty$. To be noted that we are working locally, this mean that the state x_i are bounded in addition to z which is bounded according to Lemma 1.

By integrating both sides of (4.42) between 0 and ∞, we obtain

$$\begin{aligned} 0 &\leq \int_0^{+\infty} e_1^2 d\tau + \int_0^{+\infty} e_2^2 d\tau + \int_0^{+\infty} e_3^2 d\tau + \int_0^{+\infty} \tilde{x}_3^2 d\tau \\ &\leq \frac{V(0) - V(\infty)}{\bar{c}} \leq +\infty. \end{aligned} \tag{4.48}$$

This means that $e_i, \tilde{x}_3 \in \mathcal{L}_2$. As we have also demonstrated that $e_i, \tilde{x}_3, \dot{e}_i, \dot{\tilde{x}}_3 \in \mathcal{L}_\infty$, in this case, $e_i, \tilde{x}_3 \to 0$ asymptotically, according to Barbalat's Lemma [100]. Thus the control objective is achieved and the position converges to the reference. We note that the proof can be obtained by applying Lasalle-Yoshisawa Theorem on (4.47).

4.4.5 Simulation and Experiments

As friction is a function of velocity, continuous sinusoidal trajectories are preferred for testing controllers with friction compensation. These trajectories effectively highlight the abrupt nonlinear change in friction force with directional changes [101]. The two trajectories used in simulations and experiments are given in Equation (4.49) The first trajectory is a smooth low frequency sinusoid and the second trajectory is a high frequency modulated sinusoid. As the increase in frequency translates into increase in mechanical speed of the servo valve, the trajectories will be referred to as low-speed and high-speed in the rest of this paper.

$$\begin{aligned} x_{ref1} &= sin(2\pi t), \\ x_{ref2} &= sin(10\pi t)\, sin(0.2\pi t). \end{aligned} \tag{4.49}$$

The controller parameters have been evaluated based on the model of the Hella VGT Actuator. The physical parameters of this actuator and the controller gains are given in (Appendix A).

4.4.5.1 Simulation results

As all states are available in simulation, a comparison of simulated and observed values is easily possible. The values of $\hat{\beta}_0$, $\hat{\beta}_1$ and $\hat{\beta}_2$ start from an arbitrary initial condition,

and they adapt dynamically to minimize the output feedback error. It should be kept in mind that the parameters do not converge to their actual values, but act simply as adaptive parameters. Figures 4.11 and 4.12 show the convergence of x_1 to x_{ref}. Although error is larger for high-speed perturbed trajectory as compared to low-speed trajectory, it is clear in the second modulation cycle that as time progresses, the error continues to diminish. From Figures 4.13, 4.14, 4.15, 4.16, 4.17 and 4.18, it can be seen that the performances of velocity, current and friction observers improve in the same way as that of the controller. Figures 4.19 and 4.20 show the adaptation of $\hat{\beta}_0$, $\hat{\beta}_1$ and $\hat{\beta}_2$. As can be seen, the parameters quickly attain steady state values with the low-speed constant amplitude trajectory. On the high-speed perturbed trajectory, the values continue to adjust with variations in amplitude. As seen in controller and observer outputs, the overall errors continue to diminish with each cycle.

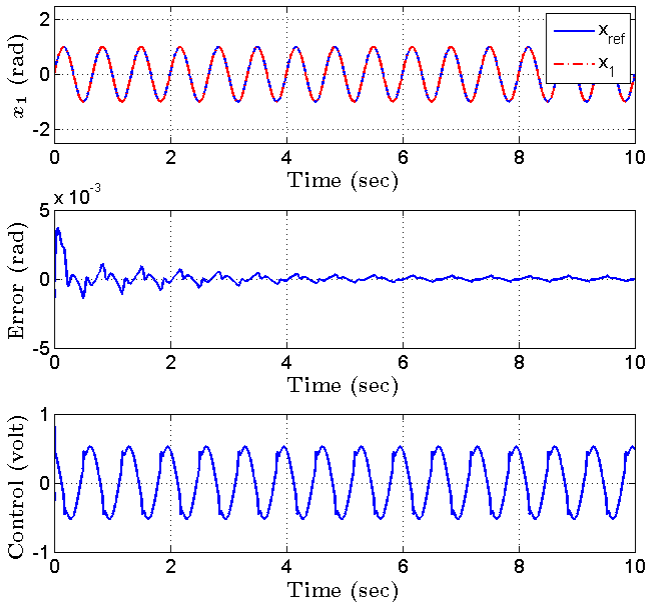


Figure 4.11. *Position Convergence, low-speed (Simulation)*

4.4.5.2 Experimental results

The controller has been implemented using LabView. The design is complete output feedback, which means that only the position of the servo valve has been measured. The

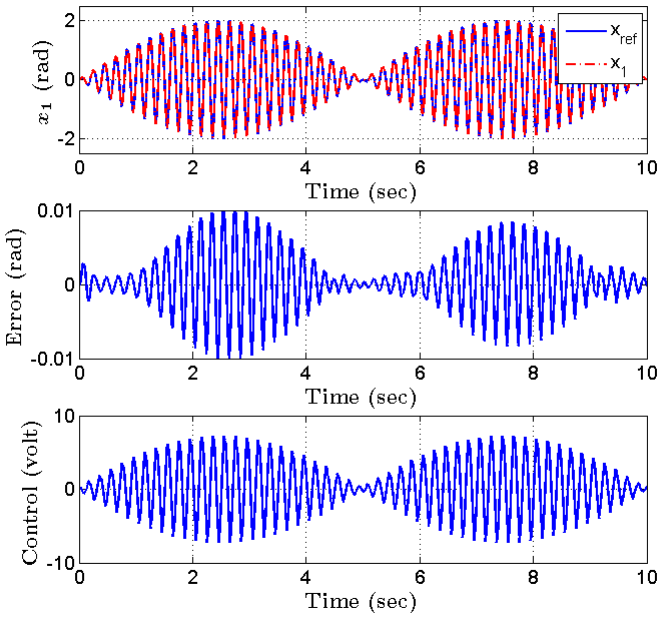


Figure 4.12. *Position Convergence, high-speed (Simulation)*

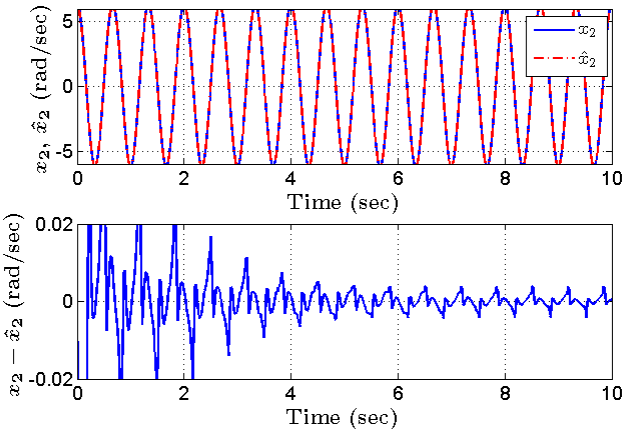


Figure 4.13. *Velocity Observer low-speed (Simulation)*

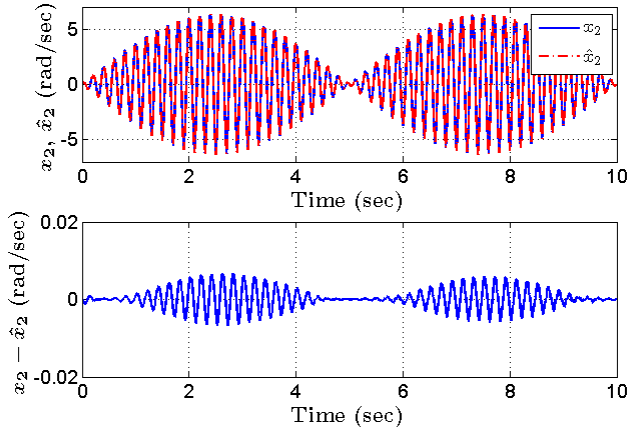


Figure 4.14. *Velocity Observer high-speed (Simulation)*

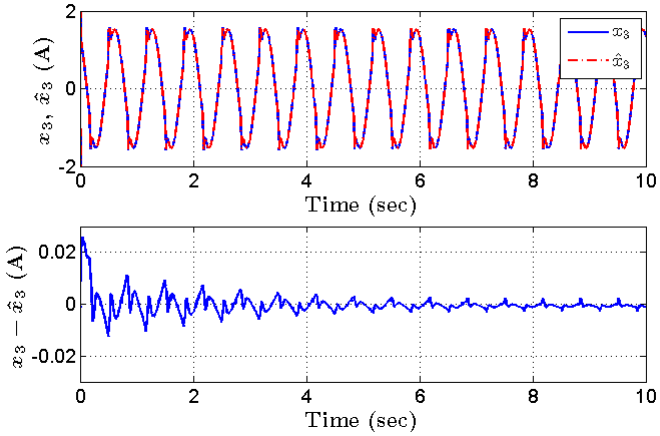


Figure 4.15. *Current Observer low-speed (Simulation)*

experiments were conducted using the same reference trajectories and controller parameters as in simulations. The results have been presented in the following figures. The adaptive controller works without any information of the friction parameters. Starting from arbitrary values, the results show that the adaptive controller maintains the closed loop performance very close to that obtained in simulations (Figures 4.21 and 4.22). It can be seen that the position error is not significant in either the low-speed or the high-speed trajectory. Figures 4.23 and 4.24 show the observed values $\hat{x}_1$ and $\hat{x}_2$. The observed velocity is comparable to the simulation results. The current observer results can be seen in Figures 4.25 and 4.26. As the test bench is equipped with current measurement, comparative results could be provided. It can be seen that the observed current $\hat{x}_3$ closely

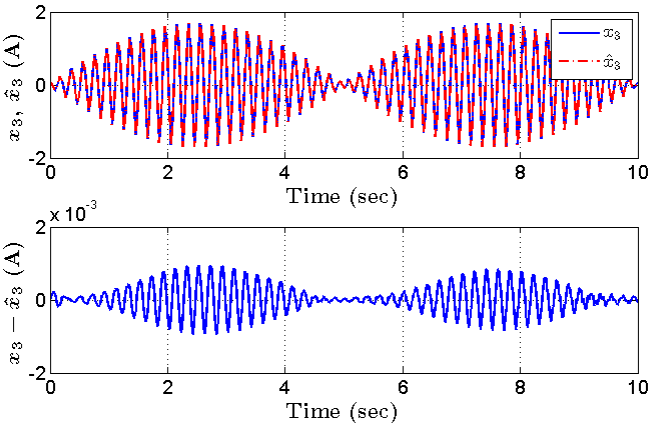


Figure 4.16. *Current Observer high-speed (Simulation)*

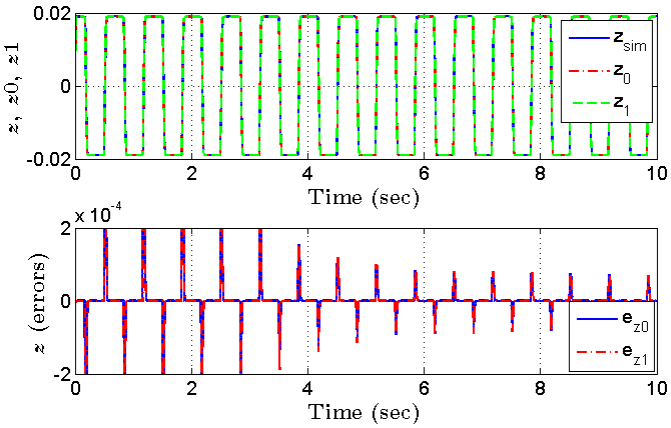


Figure 4.17. *Friction State Observer low-speed (Simulation)*

follows measured current x_3. There exists some error in current observation due to PWM frequency limitations and hardware imperfections. However, this error remains within a 5% margin. The observed values of z are shown in Figures 4.27 and 4.28. These values are also comparable to simulations. As in simulations, the controller during experimentation maintains the expected performance level as would be obtained with nominal parameter values.

External perturbations and load variation have significant adverse effects upon controller performance. By adding an adaptation term for T_L, we have overcome this problem. This has been verified by creating worst case flow conditions on the test bench, as per

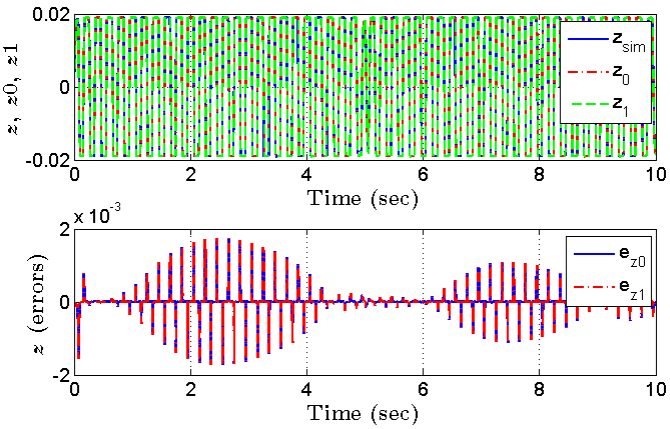


Figure 4.18. *Friction State Observer high-speed (Simulation)*

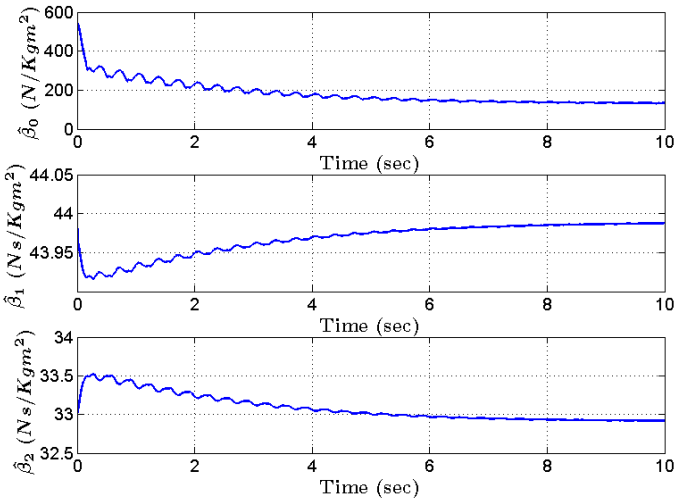


Figure 4.19. *Parameter Adaptation low-speed (Simulation)*

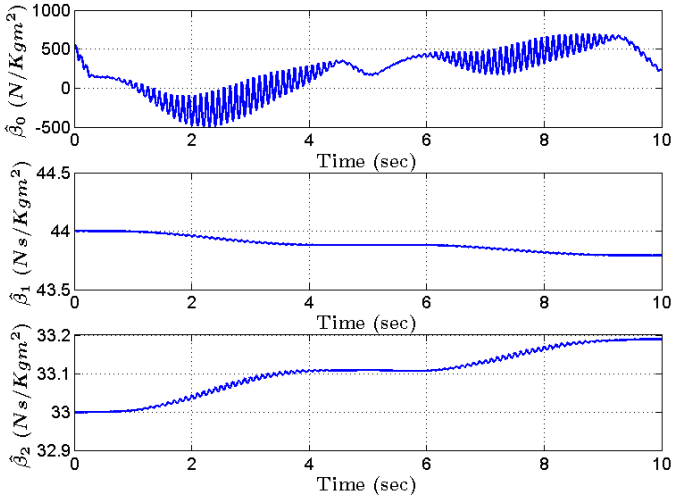


Figure 4.20. *Parameter Adaptation high-speed (Simulation)*

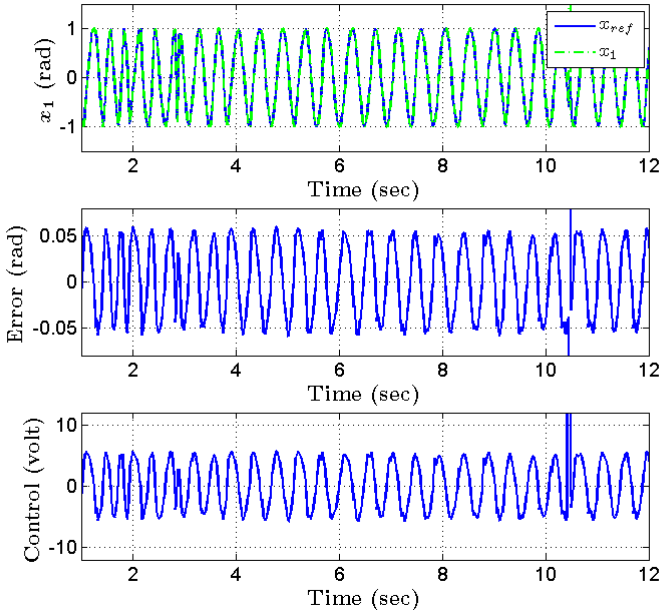


Figure 4.21. *Position Convergence, low-speed (Experimental)*

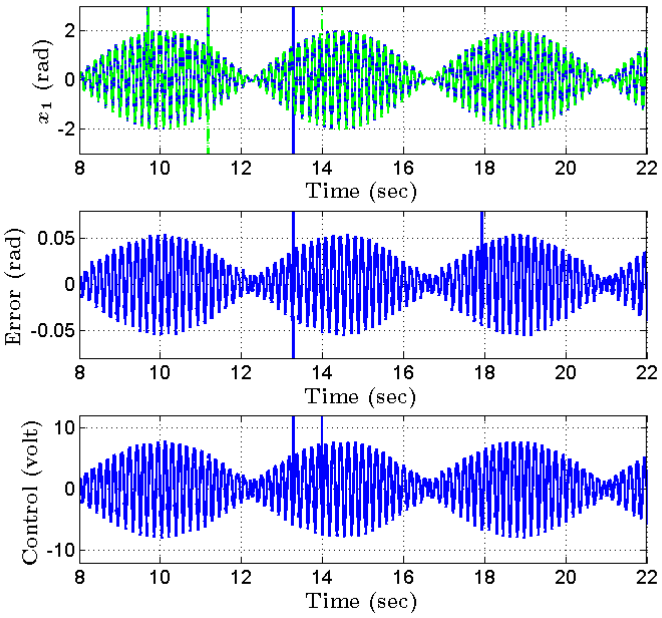


Figure 4.22. *Position Convergence, high-speed (Experimental)*

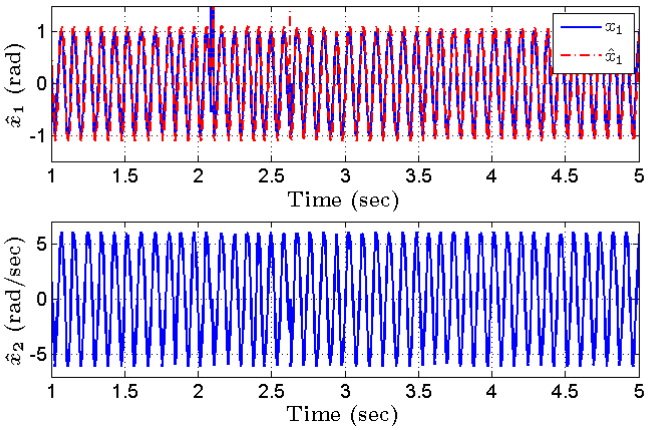


Figure 4.23. *Observer Convergence (x_1), low-speed (Experimental)*

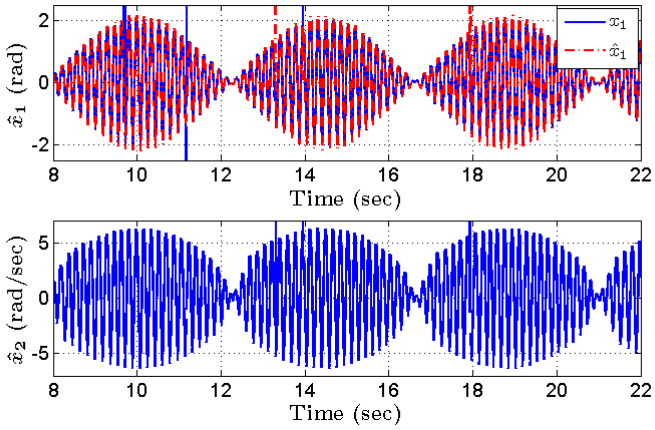


Figure 4.24. *Observer Convergence (x_1), high-speed (Experimental)*

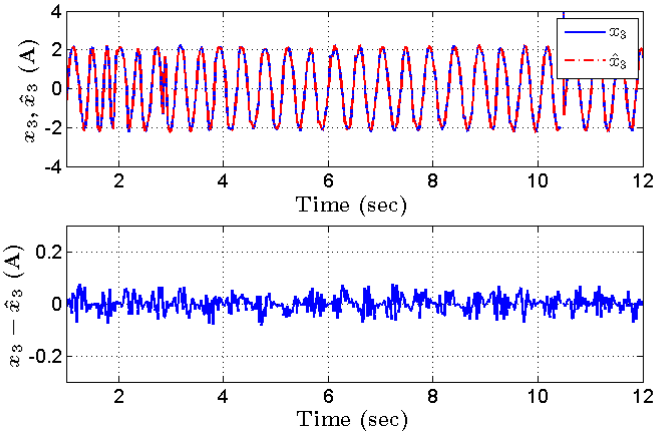


Figure 4.25. *Observed Velocity and Current, low-speed (Experimental)*

the specifications of the manufacturer. The actuator specification indicates a maximum continuous load torque equal to $600mN.m$. As seen in Figure 4.29 that even in this extreme condition, the controller adapts and the error does not exceed the performance margins.

Furthermore, the effect of temperature variation was also verified experimentally. It can be seen in Figure 4.30 that the controller adapts to parametric changes due to temperature variation and no significant deviation occurs in the error characteristics.

Finally, the controller was implemented on an industrial engine test bench to compare its performance with the conventional PI controller usually programmed in modern Engine Control Units (ECUs). The test bench consists of a commercial four cylinder turbocharged

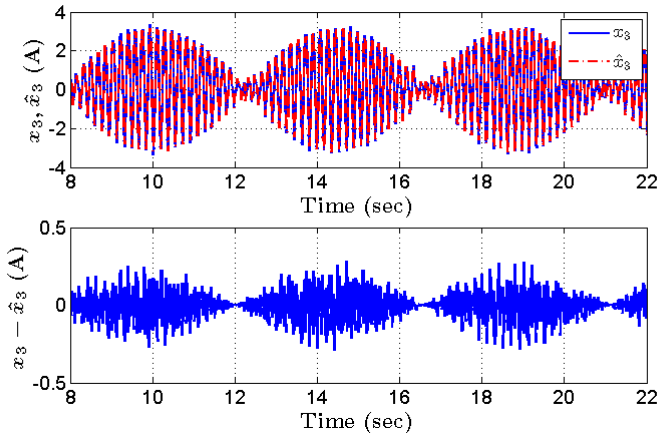


Figure 4.26. *Observed Velocity and Current, high-speed (Experimental)*

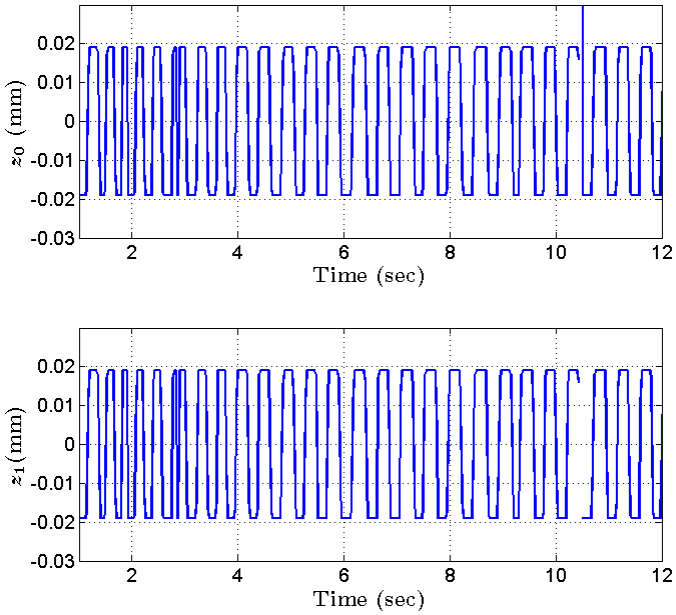


Figure 4.27. *Observed Friction State, low-speed (Experimental)*

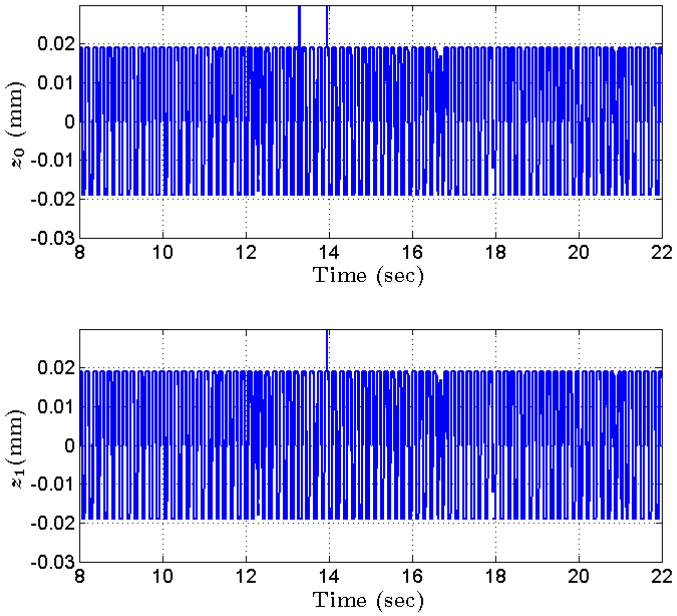


Figure 4.28. *Observed Friction State, high-speed (Experimental)*

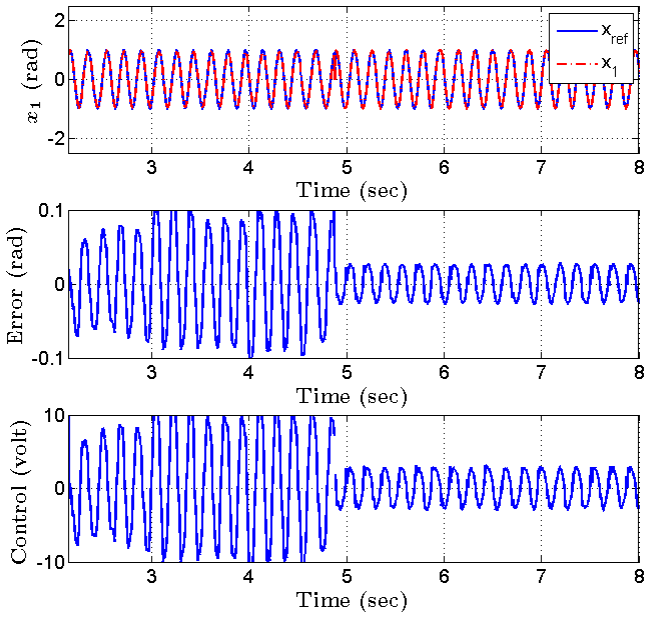


Figure 4.29. *Worst case condition (600mN.m Load Torque)*

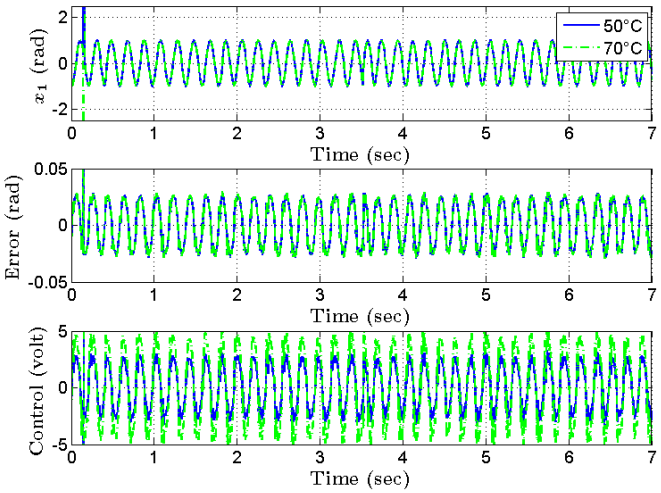


Figure 4.30. *Temperature Variation*

diesel engine with EGR, running under an open ECU. The adaptive controller was implemented in a secondary controller, forming a primary position control loop. The reference trajectory was two part industrial benchmark, used by a commercial automotive valve manufacturer. First, a step test to evaluates the positioning characteristics of valves and their controllers. This test highlights the response time and overshoots of the system. Then a linear tracking test evaluates the tracking characteristics, which are more close to actual automotive application, since rates are limited in real engine operations to prevent sudden changes which may damage the engine. The tests were carried out under two net exhaust pressure levels of 2 bar (light load) and 3 bar (heavy load).The actual pressure across the valve was pulsating. The effect of these pulsations on the valve is reduced by mechanical damping, however the pulses cause significant load variation on the actuator. The test results are presented in the following figures, for both light and heavy load conditions. Figure 4.31 highlights that the presented adaptive controller provides a slight improvement in the response time of the actuator, during the positioning test under light load. The more significant aspect is that there are no overshoots and the position stabilizes immediately upon reaching the desired position. The tracking test in Figure 4.32 shows that under light load, the adaptive controller follows the trajectory more accurately as compared to the PI controller, with an important reduction in the tracking error. Under heavy load, the better performance of the adaptive controller is more clear, as seen in Figure 4.33. The difference between the response time of the two controllers is more

significant, as the PI controller needs more time to stabilize. The overshoots also increase in the PI controller as the loading pressure changes, while the adaptive controller shows no overshoots in this case as well. Tracking under heavy load is also more smooth with the adaptive controller, as shown in Figure 4.34. Together, these tests demonstrate that the adaptive controller is suitable for industrial applications.

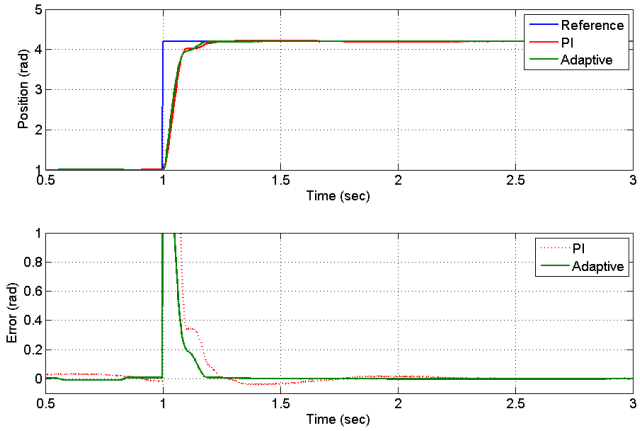


Figure 4.31. *Positioning Response (Exhaust Pressure:* 2 *bar)*

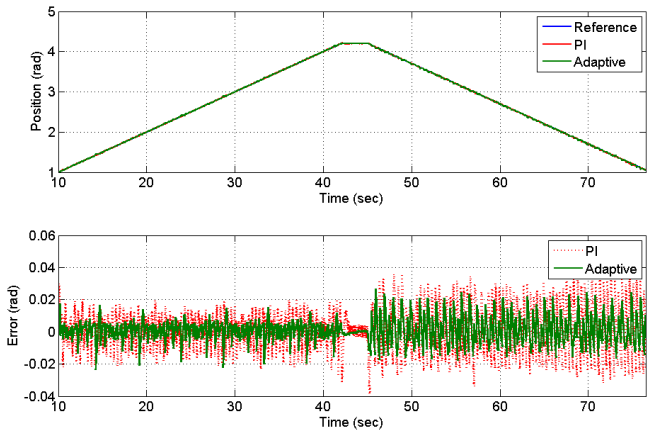


Figure 4.32. *Tracking Response (Exhaust Pressure:* 2 *bar)*

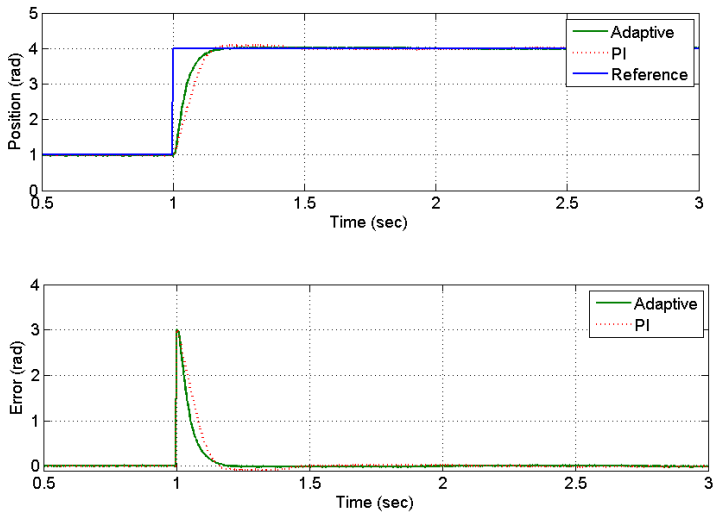


Figure 4.33. *Positioning Response (Exhaust Pressure:* 3 *bar)*

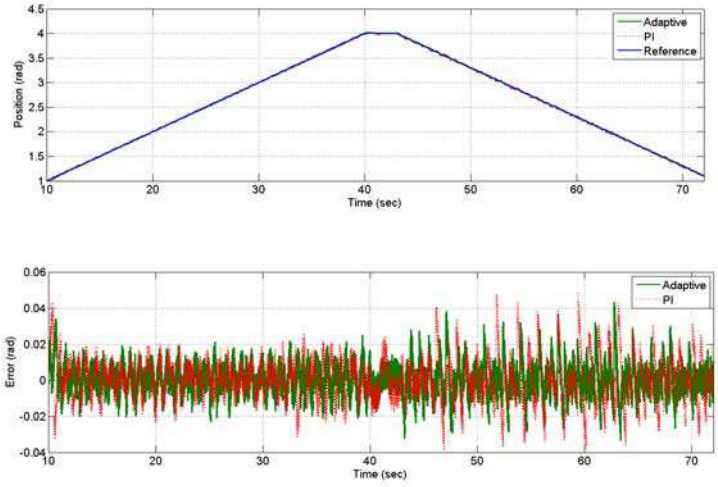


Figure 4.34. *Tracking Response (Exhaust Pressure:* 3 *bar)*

4.5 Summary

In this chapter, actuator control methods were discussed. First, three SOSMC algorithms were studied, in order to evaluate their performance in presence of parametric uncertainty. The control problem was to ensure reliable actuator operation in uncertainties. Different sliding surfaces were used to control a mechatronic swirl actuator, along with different second order sliding mode algorithms. The actuator was modeled and friction nonlinearities were incorporated in the physical model. Controller parameters were determined through simulations. Differences were noticeable in simulation and experimental response in terms of magnitude, but the performances matched qualitatively. While all controllers performed well in tracking, chattering proved to be a nuisance in their application. The closed loop system performed better in terms of response time and chattering when a surface of relative degree 1 was used. Among control algorithms, the chattering phenomenon was reduced significantly using the quasi-continuous controller and was almost negligible when the super-twisting algorithm was applied. Both these controllers proved their worth in terms of robustness as well. Hence sliding mode control proved to be an effective control strategy in the presence of uncertainties.

Then, an adaptive backstepping based output feedback controller was presented for actuator control, which is also applicable in cases where current dynamics cannot be ignored. Dynamic adaptive laws compensate friction and load variations. The velocity is obtained through uniform exact differentiation, which guarantees convergence in fixed time. Current and friction states are obtained from observers. The convergence of the closed loop system has been proven using a Lyapunov function based argument, which shows the local asymptotic convergence of the system and observers. The controller has been tested on a automotive servo valve in simulation and experiments using different position trajectories. The results have shown the effectiveness of the adaptive controller in absence of any information on friction parameters. The controller is capable of dealing with high-speed variations in positioning reference. Robustness property of the controller has been verified by subjecting the actuator to temperature and external load variation. The results show that the controller is indeed robust to these variations.

Both, types of controllers, sliding mode and adaptive, show better performance in robustness tests, as compared to PI Controllers. Specially, they maintain their performance at

varying temperatures. The adaptive control law is more calculation-extensive as compared to sliding mode control, which is a problem in its implementation in commercial ECUs of limited computational power. However, with the advent of DSP controllers, its advantages may be exploited in the near future.

Chapter 5

VGT Aerodynamic Force Modeling

We now proceed to the next major part of this report: the estimation of aerodynamic force on the VGT actuator. The working of a VGT was explained in Chapter 1; and it was mentioned that this force is exerted on the VGT vanes by the exhaust gas flow [102]. This force has a significant magnitude, which adds to the load on the VGT actuator. Hence the effect of the aerodynamic force on the dynamics of the actuator and the air-path can not be neglected. It needs to be taken into account in order to develop robust schemes for VGT position control and air-path boost pressure control.

The estimation of this force as a function of turbine flow is difficult, as the actual flow is three dimensional. However, in literature, compressor and turbine flow models are mostly analytical and lumped volume (0D) models that depend on their characteristic maps [103]. These models are simple but not accurate, and their application is limited to estimation of exhaust pressure by considering engine dynamics, i.e. engine speed and load or turbocharger speed [104, 105]. For the purpose of aerodynamic force estimation, these models are not applicable since they do not consider the directional components of exhaust gas flow. On the other hand, 2D or 3D models are too complex to be solved by numerical analysis [106, 107]. Therefore, for a reasonably accurate estimation of the aerodynamic force, 1D models of the turbine air-flow are essential to capture the directional force components. The existing 1D models are limited to fixed geometry turbochargers [108, 109].

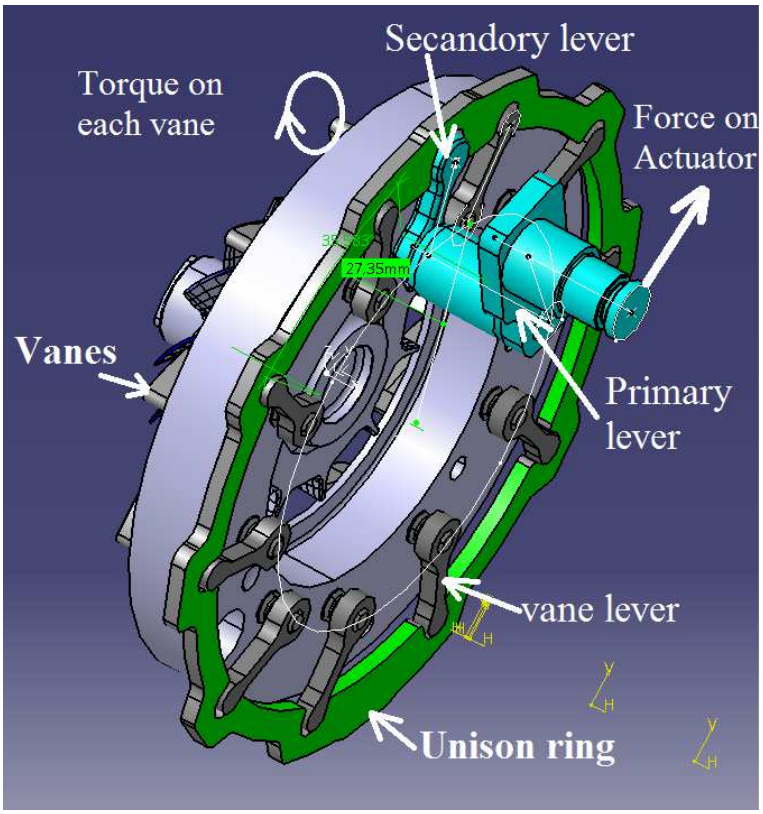


Figure 5.1. *VGT with vane actuation mechanism*

In this chapter, a tool is developed for the estimation of the aerodynamic force, based on 1D analysis and modeling of the turbine air-flow through a VGT. The flow characteristics are modeled using 1D Navier Stokes equations and their numerical approximation are also discussed. The force exerted on the vanes is estimated through finite element modeling of the vane geometry and the net force is found as a function of number of vanes. The transfer of the resultant net force to the actuator is then calculated by vectorial decomposition of the force along the mechanical linkages between the actuator and the vanes.

5.1 Mechanism and Notations

The aerodynamic force depends on the exhaust gas flow characteristics inside the turbine. However, in practice we only know the gas properties before it enters the turbine. Therefore, in order to determine the pressure, density and temperature inside the turbine, the gas flow through the turbine inlet vanes needs to be modeled. Once these variables are

found, the torque acting on the turbine vanes can be calculated and the net force acting on the actuator can be derived from force transfer analysis through the mechanical linkages. To be precise, the torque on the vanes is transferred to the crank and actuator via two levers. The primary lever is connected to the actuator crank and the secondary lever is connected to all the vanes through a unison ring. In Figure 5.1 an isometric view of the turbine and linkage is shown. In order to facilitate the reading of this chapter, the notations used to derive the one dimension flow model are tabulated as follows

Notations

α	fluid inlet and outlet angle	h^0	total specific enthalpy
β	blade inlet and outlet angle	k	blade clearance
β_{metal}	camber line angle	m	arc length
$\delta\beta$	stagger angle	M	Mach number
δi	incidence	o	length of blade opening
ρ	fluid density	p	pressure
ζ	pressure loses	p^0	total pressure
ζ_p	pressure loses due to profile	Q	source terms
ζ_t	pressure loses due to play	Q_{ext}	external forces
ζ_s	pressure loses due to secondary effects	r	radius
$\overrightarrow{\overrightarrow{\sigma}}$	tenser of constraints	R	perfect gas constant
$\overrightarrow{\overrightarrow{\tau_f}}$	tenser of viscous constraints	R_e	Reynolds number
a	velocity of sound	R_{eref}	reference Reynolds number
A_n	channel cross section	S	cross sectional area.
A_s	channel cross section at start	s	distance between vanes
A_o	channel cross section at exit	Δs	variation in entropy
c	vane comber length	T	static temperature
C_L	lift coefficient	T^0	total temperature
C_D	drag coefficient	Δt	time interval
C_p	specific heat at constant pressure	$\overrightarrow{u}$	normal to $\overrightarrow{m}$
e	specific energy	$\overrightarrow{V}$	velocity vector
ep	maximum thicknesses of the blade	V_m	meridional velocity
e^0	total specific energy	V_u	tangential velocity
E_c	kinetic energy	$\overrightarrow{W}$	velocity vector in reference frame
$\overrightarrow{F}$	external force on the fluid	v	volume
h	specific enthalpy	Ω	radius of curvature

5.2 One dimensional CFD model

Let us review the geometry of VGT system. In Figure 5.2 the VGT vanes are shown in both their open and closed positions. These vanes are actuated by a linear actuator

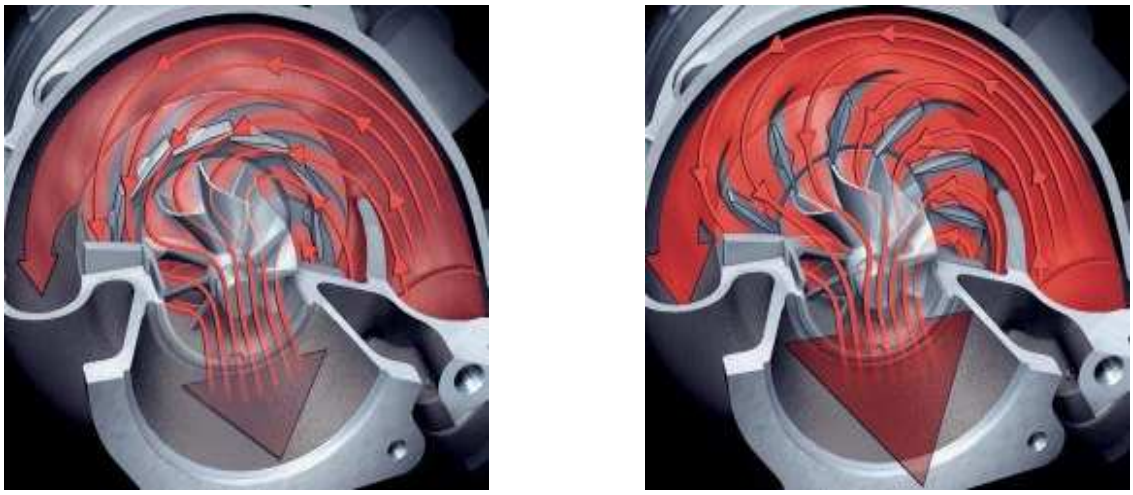


Figure 5.2. *VGT Vanes, closed and open*

which is connected to them via a crank and unison ring. The unison ring is a mechanical assembly which moves all these vanes together i.e. all vanes can be opened and closed together through this assembly. In Figure 5.3 a turbocharger is shown along with the moving mechanism.

5.2.1 Hypothesis and problem formulation with Navier-Stokes equations

The Navier-Stokes equations can be used to model the aerodynamic force exerted by the exhaust gases coming from the exhaust manifold and passing through the turbocharger. These equations are derived from the generalized Euler equation and they represent the conservation laws for mass, energy and momentum of the fluid in all directions. The Navier-Stokes equations can be reformed to obtain 1D model of the fluid with some assumptions on the fluid's direction of flow. The velocity vector for fluid is $\overrightarrow{V} = [V_m\, V_u\, V_l]^T$ with condition that the velocity of the fluid in the vertical direction is zero $V_l = 0$. Henceforth, we get the following equation

$$\iiint dv = \int S dm \tag{5.1}$$

The term S is the cross section of the channel through which the gas passes, and $dv = dm\, du\, dl$ is an elementary volume. m, u and l represent respectively, the meridional,

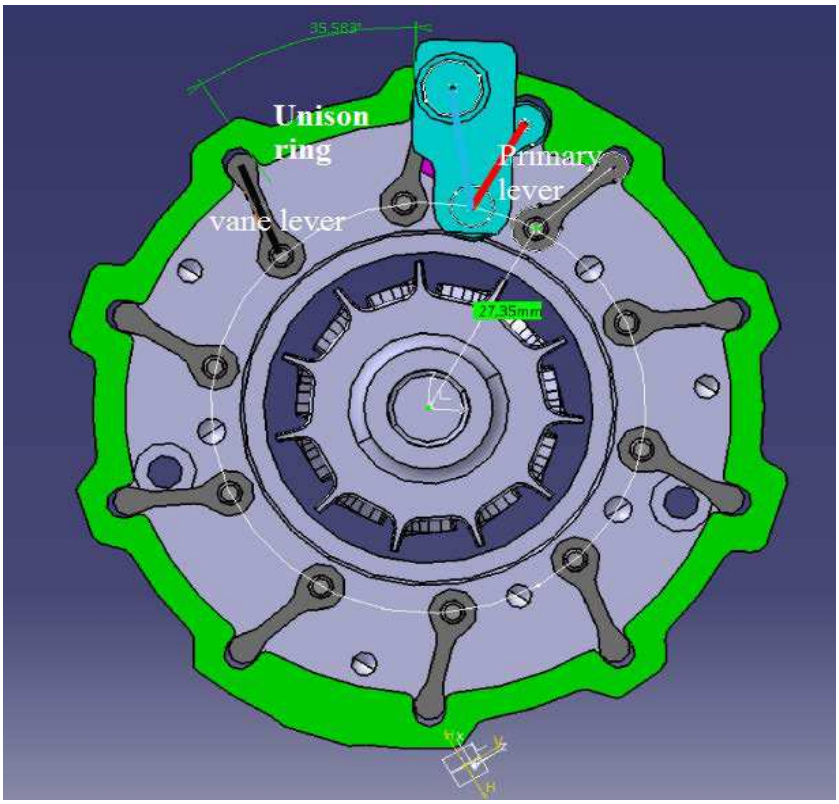


Figure 5.3. *VGT mechanical diagram*

tangential and vertical axes of the fluid flow, as explained in Figure (5.4).

For the perfect gas the tensor for the viscous forces can be consider as equal to zero

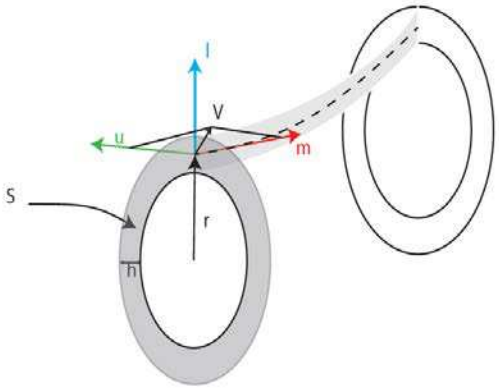


Figure 5.4. *Velocity components of air-flow through a vane*

i.e. $\overrightarrow{\overrightarrow{\tau_f}} = \overrightarrow{\overrightarrow{0}}$. Additionally, for initial development of Navier-Stokes equations, it is consider

that external source terms are zero. They will be introduced in the model later on. Under these assumptions, the following mathematical properties are established for an arbitrary function x, velocity $\vec{V}$ and :

$$\begin{aligned}
div(\vec{V}) &= \frac{1}{S}\frac{\partial SV_m}{\partial m} \\
\overrightarrow{grad}(x) &= \begin{bmatrix} \frac{\partial x}{\partial m} \\ 0 \\ 0 \end{bmatrix} \\
\overrightarrow{rot}(\vec{V}) \wedge \vec{V} &= \begin{bmatrix} -\frac{V_u}{r}\frac{\partial rV_u}{\partial m} \\ \frac{V_m}{r}\frac{\partial rV_u}{\partial m} \\ 0 \end{bmatrix} \\
\overrightarrow{grad}(\frac{V^2}{2}) &= \begin{bmatrix} V_u\frac{\partial V_u}{\partial m} + V_m\frac{\partial V_m}{\partial m} \\ 0 \\ 0 \end{bmatrix} \\
\frac{dx}{dt} &= \frac{\partial x}{\partial t} + \vec{V}\cdot\overrightarrow{grad}(x) \\
\frac{d\vec{V}}{dt} &= \frac{\partial \vec{V}}{\partial t} + rot(\vec{V}) \wedge \vec{V} + \overrightarrow{grad}\left(\frac{V^2}{2}\right)
\end{aligned} \tag{5.2}$$

5.2.2 Model derivation

A physical interpretation of 1D flow models is the study of fluid flow in a thin tube or a narrow channel. This permits us to analyze the properties of the fluid; velocity, density and energy change only along the tube or the channel. The law of conservation of mass for a fluid can be derived from the Navier-Stokes equation. The equation is also known as the continuity equation and it is given below [110]

$$\iiint \left(\frac{\partial \rho}{\partial t} + div\left(\rho\vec{V}\right)\right) dv = 0 \tag{5.3}$$

By using Equation (5.1), we get

$$\int \left(\frac{\partial S\rho}{\partial t} + Sdiv\left(\rho\vec{V}\right)\right) dm = 0 \tag{5.4}$$

In the differential form, this equation becomes

$$\frac{\partial S\rho}{\partial t} + \frac{\partial S\rho V_m}{\partial m} = 0 \tag{5.5}$$

The terms ρ and V_m are the density and meridional velocity of the fluid, respectively. The momentum equation is based on the principle of conservation of momentum, as follows:

$$\iiint \frac{d\rho\vec{V}}{dt} dv = \iiint \rho\vec{F}\, dv + \iiint \frac{1}{\rho}\overrightarrow{grad}(p) + \frac{1}{\rho} div(\vec{\vec{\tau}_f}) dv \tag{5.6}$$

Let us rewrite this equation in one dimensional form, by using Equation (5.1).

$$\int \frac{d\rho S\vec{V}}{dt} dm = \int S\rho\vec{F}\, dm - \int \overrightarrow{grad}(Sp) dm \tag{5.7}$$

which implies:

$$\frac{\partial S\rho\vec{V}}{\partial t} = -S\rho.rot(\vec{V}) \wedge \vec{V} - \rho S.\overrightarrow{grad}\left(\frac{V^2}{2}\right) - S.\overrightarrow{grad}(p) - \vec{V}\frac{\partial S\rho}{\partial t} \tag{5.8}$$

In the derivation, we assume that $V_l = 0$, i.e. the fluid has only tangential V_u and meridional V_m velocity components. Therefore, the momentum equation (5.8) obtained by the equivalent meridian velocity (velocity of fluid in the direction of fluid flow) is given as

$$\frac{\partial S\rho V_m}{\partial t} + \frac{\partial S\rho\left(p/\rho + V_m^2\right)}{\partial m} = S\rho\frac{V_u^2}{r}\frac{\partial r}{\partial m} + p\frac{\partial S}{\partial m} \tag{5.9}$$

The momentum equation (5.8) for the tangential component of the velocity is given as

$$\frac{\partial S\rho V_u}{\partial t} + \frac{\partial S\rho V_m V_u}{\partial m} = -S\rho\frac{V_m V_u}{r}\frac{\partial r}{\partial m} \tag{5.10}$$

Figure 5.5 shows the direction of fluid through a variable geometry turbocharger. Cartesian components of the velocity are also shown in this figure. The direction of air flow at the turbine outlet is perpendicular to the flow at inlet. In this figure, m is the meridian coordinate and r is the radius of the fluid channel. The conservation of energy, like conservation of mass and momentum, represents that total energy in a fluid remain constant. The total energy of the fluid can be obtained by integrating it in all directions

$$\iiint \rho\frac{de^0}{dt} dv = \iiint \rho\vec{F}.\vec{V}\, dv + \iiint -div\left(p\vec{V}\right) - \overrightarrow{grad}(p).\vec{V} + div(\vec{\vec{\tau}_f}).\vec{V} + \vec{\vec{\tau}_f}.\overrightarrow{\overrightarrow{grad}}(\vec{V}) dv + Q_{ext} \tag{5.11}$$

The energy balance equation can be obtained by using Equation (5.1):

$$\int \rho S\frac{\partial e^0}{\partial t} dm = \int \rho S\vec{F}.\vec{V}\, dm - \int S.div\left(p\vec{V}\right) + S\overrightarrow{grad}(p).\vec{V}\, dm - \int \rho S\overrightarrow{grad}(e^0).\vec{V}\, dm \tag{5.12}$$

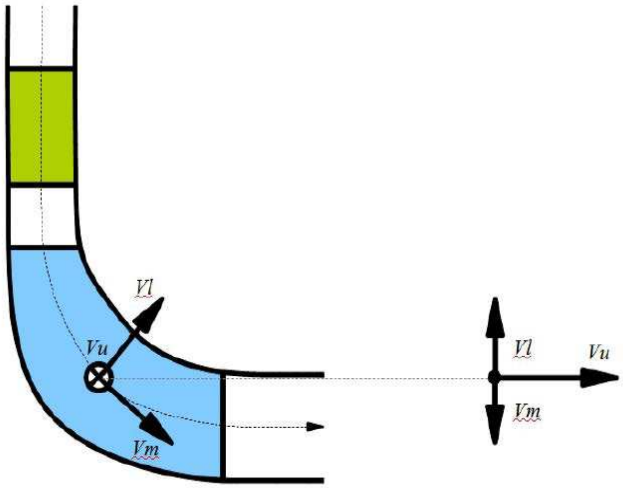


Figure 5.5. *Exhaust gas flow through VGT*

Let us rewrite this equation in the differential form by using the mathematical derivations given in equation set (5.2).

$$\frac{\partial}{\partial t}\left(S\rho e^0\right) + S\rho V_m \frac{\partial e^0}{\partial m} + e^0 \frac{\partial S\rho V_m}{\partial m} + V_m S \frac{\partial p}{\partial m} + S\frac{\partial p V_m}{\partial m} = 0 \tag{5.13}$$

With further simplifications, we obtain

$$\frac{\partial}{\partial t}\left(S\rho e^0\right) + \frac{\partial S\rho V_m\left(\frac{p}{\rho} + e^0\right)}{\partial m} = 0 \tag{5.14}$$

Finally, we get the following equation for energy of the fluid

$$\frac{\partial S e^0 \rho}{\partial t} + \frac{\partial S\rho V_m h^0}{\partial m} = -S\rho\Omega \frac{V_m V_u \partial r}{\partial m} \tag{5.15}$$

where e^0 and h^0 are the total energy and enthalpy of the fluid. Equations (5.5), (5.9), (5.10) and (5.15) can be combined together and can be written in the non-dimensional vector form

$$\frac{\partial U}{\partial t} + \frac{\partial E}{\partial m} = Q \tag{5.16}$$

where U, E and Q are conservative variable vector, flux vector and the source term vector respectively. In the vector from these terms are given as

$$U = \begin{bmatrix} \rho S \\ \rho V_m S \\ \rho V_u S \\ \rho e^0 S \end{bmatrix}, \quad E = \begin{bmatrix} \rho V_m S \\ \left(p + \rho V_m^2\right) S \\ \rho V_m V_u S \\ \rho V_m h^0 S \end{bmatrix}, \quad \mathrm{Q} = \begin{bmatrix} 0 \\ S\rho \dfrac{V_u W_u}{r}\dfrac{\partial r}{\partial m} + p\dfrac{\partial S}{\partial m} \\ -S\rho \dfrac{V_m V_u}{r}\dfrac{\partial r}{\partial m} \\ -S\rho V_m V_u \Omega \dfrac{\partial r}{\partial m} \end{bmatrix} \tag{5.17}$$

Let $U = [U_0\, U_1\, U_2\, U_3]^T$, then the conservative flux vector E can be written as a function of components of the vector U. By rewriting the flux vector, we get

$$\begin{aligned} E_0 &= U_1 \\ E_1 &= (\gamma - 1)\left(U_3 - \frac{1}{2}\left(\frac{U_1^2}{U_0} + \frac{U_2^2}{U_0}\right)\right) + \frac{U_1^2}{U_0} \\ E_2 &= \frac{U_1 U_2}{U_0} \end{aligned} \tag{5.18}$$

Next, we develop E_3, the last term of vector E. The total enthalpy h^0 of the fluid can be written as a function of its total kinetic energy at that particular point

$$h^0 = e^0 + \frac{p}{\rho} \tag{5.19}$$

with total energy e^0

$$e^0 = C_v T + \frac{1}{2} V^2 \tag{5.20}$$

where C_v, t and V are the specific heat at constant volume, temperature of the gas and the sum of its meridional and tangential velocities, respectively. By using the perfect gas equation $\frac{p}{\rho} = rT$ and $C_v = \frac{r}{\gamma - 1}$, with γ and r are specific heat ratio and universal gas constant

$$e^0 = \frac{1}{(\gamma - 1)} \frac{p}{\rho} + \frac{1}{2}(V_m^2 + V_u^2). \tag{5.21}$$

By introducing the expression related to the sound velocity, $a^2 = \frac{\gamma p}{\rho}$, in equation (5.21), the total energy will become

$$e^0 = \frac{a^2}{\gamma(\gamma - 1)} + \frac{1}{2}(V_m^2 + V_u^2). \tag{5.22}$$

The total kinetic energy of the fluid for the both tangential and meridional components of velocities is given by

$$\frac{1}{2}(V_m^2 + V_u^2) = \frac{1}{2}\left(\left(\frac{U_1}{U_0}\right)^2 + \left(\frac{U_2}{U_0}\right)^2\right). \tag{5.23}$$

With $h^0 = e^0 + \frac{p}{\rho}$, we get

$$p = (\gamma - 1)\left(U_3 - \frac{1}{2}\left(\frac{U_1^2}{U_0} + \frac{U_2^2}{U_0}\right)\right) \tag{5.24}$$

Finally the conservative flux vector E can be represented as a function of U by the following expression

$$E = \begin{bmatrix} U_1 \\ (\gamma-1)\left(U_3 - \frac{1}{2}\left(\frac{U_1^2}{U_0} + \frac{U_2^2}{U_0}\right)\right) + \frac{U_1^2}{U_0} \\ \frac{U_1 U_2}{U_0} \\ \left(\gamma U_3 - \frac{\gamma-1}{2}\left(\frac{U_1^2}{U_0} + \frac{U_2^2}{U_0}\right)\right)\frac{U_1}{U_0} \end{bmatrix} \tag{5.25}$$

In order to find a numerical solution of equation (5.16), the Jacobian flux vector A needs to be calculated. For this, the flux vector E needs to be written as a function of U. The Jacobian vector is obtained by taking the partial derivatives of E with respect to U [106], i.e $A = \frac{\partial E}{\partial U}$, we get

$$A = \begin{bmatrix} 0 & 1 & 0 & 0 \\ \frac{(\gamma-3)V_m^2 + (\gamma-1)V_u^2}{2} & -(\gamma-3)V_m & -(\gamma-1)V_u & \gamma-1 \\ -V_m V_u & V_u & V_m & 0 \\ \left(\frac{\gamma-2}{2}(V_m^2+V_u^2) - \frac{a^2}{\gamma-1}\right)V_m & \frac{a^2}{\gamma-1} - \frac{2\gamma-3}{2}V_m^2 - \frac{V_u^2}{2} & -(\gamma-1)V_m V_u & \gamma V_m \end{bmatrix} \tag{5.26}$$

5.2.3 Source terms

The source terms in the Euler equations are used to represent the influence of the blade rows and the flow-path on the fluid. The source terms vector Q is the vector of all contributions which were initially neglected in the derivation. It may be further divided into four distinct categories by their physical meanings

$$Q = Q_g + Q_b + Q_f + Q_c \tag{5.27}$$

where Q_c is the cooling source term and it is neglected in this derivation i.e. $Q_c = 0$. The other terms, for example Q_g, Q_b and Q_f are the source terms due to the geometry of the volute, impeller blade force and viscous friction, respectively. These terms are described below.

5.2.3.1 Geometry of the flow-path

The source term Q_g, represents the variation in fluid velocities and pressure drop across the exhaust air flow-path. The air flow direction through the vein between the exhaust

manifold and the turbocharger is shown in Figure 5.5, where r represents the mean-line radius. This term can be obtained by considering the right hand side of equations (5.5), (5.9), (5.10) and (5.15). The final form of geometrical source term is given by

$$Q_g = \begin{bmatrix} 0 \\ S\rho\dfrac{V_u V_u}{r}\dfrac{\partial r}{\partial m} + p\dfrac{\partial S}{\partial m} \\ -S\rho\dfrac{V_m V_u}{r}\dfrac{\partial r}{\partial m} \\ 0 \end{bmatrix} \tag{5.28}$$

5.2.3.2 Evaluation of the output angle

The turbine impeller and the VGT vanes, both modify the fluid angle by directing it from their leading edge to the trailing edge, as seen in Figure 5.7. Fluids angles α and β are defined as follows: The rotating blades of the impeller change the angle β, while the VGT

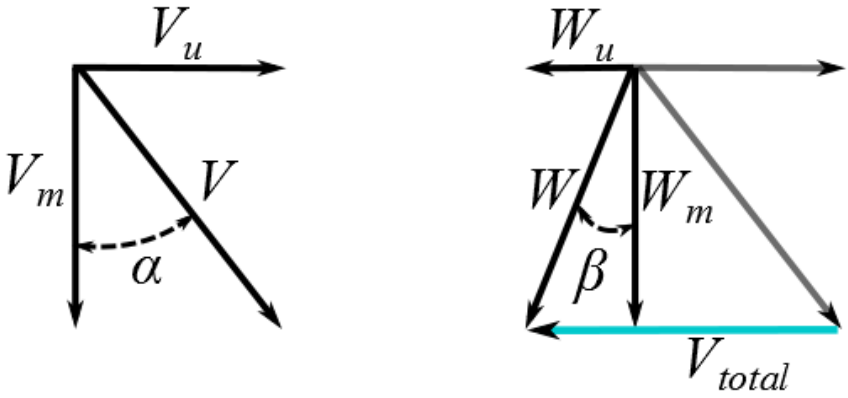


Figure 5.6. *Velocity triangle*

vanes change the angle α. Representing the flow velocity ate the output in terms of mach as M_2, the following model has been proposed in [111] for evaluating the output angle of the fluid:

- For $M_2 < 0.5$: the output angle is determined by the nomogram 5.8.

- For $0.5 < M_2 < 1$, a linear transition is carried out.

- For $M_2 = 1$ we get: $\alpha_2 = -cos^{-1}\left(\frac{A_s}{A_o}\right)$.

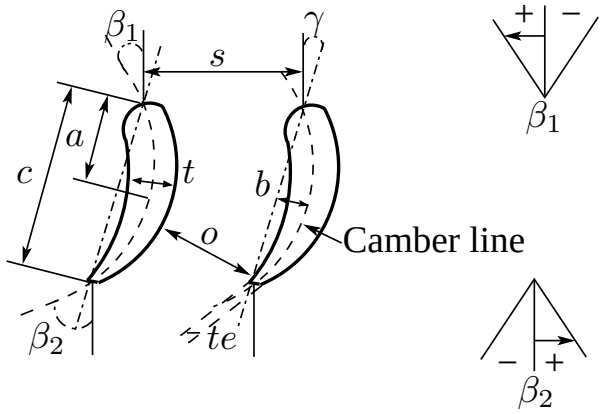


Figure 5.7. *Blade geometry*

Figure 5.7 notations for VGT Vane

a	tip to maximum camber distance	b	maximum camber
c	chord length	γ	Mach number
s	maximum inter-vane distance	o	opening inter-vane distance
t	maximum width	t_e	width at exit
β_1	angle of attack	β_2	angle of attack at exit

5.2.3.3 Blade source terms

This term is implemented to represent the isentropic influence of blade rows. The force applied by the blades onto the fluid can be deduced from the knowledge of the velocity triangles, see Figure 5.6. An angular momentum balance over the blade row provides the tangential component of the blade force. Here we have used the tangential velocities along the blade deflection induced by the given component for $\tilde{V}_{u\ i}$.

$$\tilde{V}_{ui} = \frac{V_{mi}}{tan(\alpha_i)}, \tag{5.29}$$

where α_i is the angle of the fluid with respect to blade comber line. The index $_i$ comes from the discretization of the blade in finite number of elements, as presented in Figure 5.9 . By writing the Euler equation and the equation of variation in energy, we get

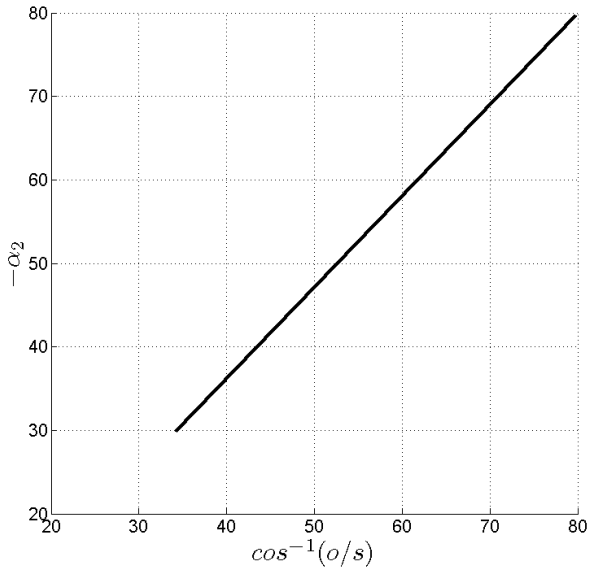


Figure 5.8. *Gas outlet angles vs.* $cos^{-1}(o/s)$ *(straight back blades operating at low mach numbers)*

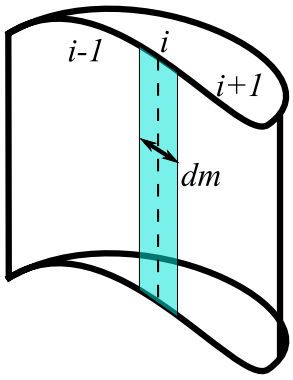


Figure 5.9. *Finite element division of VGT vane*

$$r_i F_{bui}\Omega = \left(r_i \Omega \widetilde{V}_{ui} - r_{i-1}\Omega V_{ui-1}\right)\frac{q_m}{S_i(m_i - m_{i-1})}, \tag{5.30}$$

where Ω is the angular velocity of the blades and F_{bui} is the blade force in the tangential direction, given by

$$F_{bui} = \left(r_{i1}\widetilde{V}_{ui} - r_{i-1}V_{ui-1}\right)\frac{q_m}{S_i r_i(m_{i+1} - m_{i-1})}. \tag{5.31}$$

The forces acting on the blade are perpendicular to the referential velocity $\overrightarrow{W}$. Henceforth, it can be assumed that the axial and tangential forces do not generate losses

$$F_{bmi}W_{mi} + F_{bui}W_{ui} = 0, \tag{5.32}$$

where W_m is the relative velocity vector. By analyzing the velocity triangles for the fluid through the single stage turbocharger, it can be deduced that in the meridional direction relative meridional velocity is equal to the absolute velocity, thence $W_{m\ i} = V_{m\ i}$. Therefore, the blade force in the meridional direction is given by

$$F_{bmi} = -F_{bui}\frac{W_{ui}}{V_{mi}}. \tag{5.33}$$

The source term related to the action of impeller blade on the turbocharger vanes is given below

$$Q_{bi} = \begin{bmatrix} 0 \\ F_{bmi}S_i \\ F_{bui}S_i \\ r_i \Omega F_{bui}S_i \end{bmatrix}. \tag{5.34}$$

5.2.3.4 Pressure losses

As described previously, the source term obtained from friction depends upon the pressure losses in the turbocharger. These losses are mainly due to the turbine geometry, play in its components and some secondary effects. In [111], two different methods are presented to determine these losses. These methods are described below

Interpolation based method

The pressure losses in the vanes increase with the increase in tip clearance in a blade row of a turbine, which results in a decrease of turbine efficiency. The gas mass flow and

the power output corresponding to a fixed turbine speed and pressure ratio also change. Typical profile losses on conventional blades intermediate between nozzle and impulse blades may be interpolated in the following manner

$$\zeta_p = \left(Y_{p(\beta_1=0)} + \left(\frac{\beta_1}{\alpha_2}\right)^2 \left(Y_{p(\beta_1=-\alpha 2)} - Y_{p(\beta_1=0)}\right)\right)\left(\frac{ep}{0.2c}\right), \tag{5.35}$$

where ep is the pitch to chord ratio. The term Y_p represents the profile losses at different inlet angles for blades. These losses are determined through the mapping between inlet and outlet angles for both the blade and fluid: and the profile. Stodola quoted a simplified method to determine the losses associated with the tip clearance. The formula to determine clearance losses is given by

$$\zeta_t = 6.26\frac{k^{1.4}}{h_c}, \tag{5.36}$$

where h_c is the blade hight and k is the radial clearance. In this approach the secondary losses are neglected, therefore we considered that

$$\zeta_s = 0. \tag{5.37}$$

Angle ratio based method

In this method, the profile losses are determined with more sophisticated and more precise model. It depends upon the ratio of angles α_2 and β_1 presented in Section (5.2.3.2), as explained in [108] and [111].

$$\zeta_{p(\delta i=0)} = \left(Y_{p(\beta_1=0)} + \left(\frac{\beta_1}{\alpha_2}\right)^2 \left(Y_{p(\beta_1=-\alpha 2)} - Y_{p(\beta_1=0)}\right)\right)\left(\frac{ep}{0.2c}\right)^{-\frac{\beta_1}{\alpha_2}} \tag{5.38}$$

with $Y_{p(\beta_1=0)}$ and $Y_{p(\beta_1=-\alpha_2)}$ are obtained from the maps between pitch to chord ratio and profile loss coefficient. The pressure losses due to blade tip clearance ζ_t is given by the following equation

$$\zeta_t = 0.5\frac{k}{h_c}\left(\frac{C_L}{\frac{s}{c}}\right)^2 \frac{cos(\alpha_2)^2}{cos(\alpha_m)^3} \tag{5.39}$$

where C_L is the lift coefficient. The term α_m is the mean gas angle. Its expression for this angle is given in [110]

$$\zeta_s = \lambda\left(\frac{C_L}{\frac{s}{c}}\right)^2 \frac{cos(\alpha_2)^2}{cos(\alpha_m)^3} \tag{5.40}$$

with $\lambda = f\left(\frac{\left(\frac{A_2}{A_1}\right)^2}{1+\frac{I.D}{O.D}}\right)$ is the ratio of drag and lift coefficient. It can also be mapped by the ratio of inlet and outlet flow area

Here $I.D = r - \frac{h_c}{2}$ and $O.D = r + \frac{h_c}{2}$. The inlet and outlet flow area depends on the blade inlet and the fluid outlet angle

$$\begin{aligned} A_1 &= A_{n0} cos(\beta_1) \\ A_2 &= A_{n2} cos(\alpha_2) \end{aligned} \tag{5.41}$$

The ratio $\frac{C_L}{\frac{s}{c}}$ can also be represented as a function of fluid inlet, outlet and mean angle. So, its expression in equation (5.40) can be replaced by following equation

$$\frac{C_L}{\frac{s}{c}} = 2\,(tan(\alpha_1) - tan(\alpha_2))\, cos(\alpha_m) \tag{5.42}$$

5.2.3.5 Friction source terms

In the Euler equations, the entropy production is due to a separate distributed friction force F_f in the momentum equations. This force causes the loss in fluid pressure when it moves through the channel. The pressure drop due to this friction may cause the variation in momentum and energy loss in the fluid. This friction force is aligned with the relative velocity by the following expression. The negative sign indicate that it has the opposite direction

$$\vec{F_f} = -\left|\vec{F_f}\right| \frac{\vec{W}}{\left|\vec{W}\right|} \tag{5.43}$$

The change in entropy of the fluid can be represented by the following formula

$$\Delta s = -R\, ln\,(1-\zeta) \tag{5.44}$$

where R is the gas constant and ζ represents the pressure losses due to profile, play in the turbine geometry and secondary effects. The force related to these losses can be evaluated from the Gibbs relation, which is given below

$$\left|\vec{F_f}\right| = \rho T \frac{\Delta s}{\Delta m} \tag{5.45}$$

To obtain the source term that contains the momentum and energy equations can be determined from the axial and tangential components of the friction force.

$$F_{fm} = \rho T \frac{R\,ln\,(1-\zeta)}{\Delta m} \frac{V_m}{\sqrt{V_m^2 + (V_u - r\Omega)^2}} \tag{5.46}$$

where Δm is the small step size in the meridional direction. The tangential component of the force is given by

$$F_{fu} = \rho T \frac{R\,ln\,(1-\zeta)}{\Delta m} \frac{V_u - r\Omega}{\sqrt{V_m^2 + (V_u - r\Omega)^2}} \tag{5.47}$$

The source term related to friction forces is given by the following expression

$$Q_{fi} = \begin{bmatrix} 0 \\ F_{fmi} S_i \\ F_{fui} S_i \\ r_i \Omega F_{fui} S_i \end{bmatrix} \tag{5.48}$$

5.3 Numeric resolution of 1D Navier Stokes Equations

The objective of this solver is to calculate the point force exerted by the gas on the vanes, and then to find out the total force experienced by the actuator. Let us recall equation (5.16), which represents fluid flow in matrix form

$$\frac{\partial U}{\partial t} + \frac{\partial E}{\partial m} = Q,$$

which can be written as

$$\frac{\partial U}{\partial t} + A\frac{\partial U}{\partial m} = Q, \tag{5.49}$$

where $A = \dfrac{\partial E}{\partial U}$ is the Jacobian of E. This equation will be discretized in order to solve it numerically.

As explained in [110, 108], in order to guarantee the convergence of the solver, the positive and negative components of the vector flow A need to be separated. This is achieved by separating the jacobian of E in two matrices, one composed of positive eigenvalues A^+ and the other composed of negative eigenvalues A^-.

Starting first by the diagonalization of A, we suppose that there exists a matrix X and a diagonal matrix D such that $AX = XD$, with

$$D = \begin{bmatrix} V_m & & & & \\ & V_m & & & \\ & & a+V_m & & \\ & & & -a+V_m & \end{bmatrix}, \tag{5.50}$$

where a is the velocity of sound. Let D^+ and D^- be the matrices composed respectively of positive and negative eigenvalues of A. In our case, the flow is subsonic, i.e. $V_m < a$. Therefore we get

$$D^+ = \begin{bmatrix} V_m & & & \\ & V_m & & \\ & & a+V_m & \\ & & & 0 \end{bmatrix}, \quad D^- = \begin{bmatrix} 0 & & & \\ & 0 & & \\ & & 0 & \\ & & & -a+V_m \end{bmatrix}. \tag{5.51}$$

Let A^+, A^-, E^+, E^- given as

$$\begin{aligned} A^+ &= XD^+X^{-1}, \\ A^- &= XD^-X^{-1}, \\ E^+ &= A^+U, \\ E^- &= A^-U, \end{aligned} \tag{5.52}$$

The explicit value of E^+ and $E^-$are given as follows

$$\begin{aligned} E^+ &= \begin{bmatrix} \frac{\rho}{2\gamma}(-a+V_m) \\ \frac{\rho}{2\gamma}(-a+V_m)^2 \\ \frac{\rho}{2\gamma}(-a+V_m) \\ \frac{\rho}{4\gamma}\left(V_m^3 - 3V_m^2 a + 2\frac{\gamma a^2 V_m}{\gamma-1} + V_u^2(-a+V_m) - 2\frac{a^3}{\gamma-1}\right) \end{bmatrix}, \\ E^- &= \begin{bmatrix} \rho V_m + \frac{\rho}{2\gamma}(-a+V_m) \\ \left(\rho - \frac{\rho}{2\gamma g}\right)V_m^2 + \frac{a\rho V_m}{\gamma g} + \frac{\rho a^2}{2\gamma g} \\ \left(\rho - \frac{\rho}{2\gamma g}\right)V_u V_m + \frac{\rho V_u a}{2\gamma g} \\ \frac{\rho}{4\gamma}\left((2\gamma g-1)V_m^3 + \left((2\gamma g-1)V_u^2 + 2\frac{\gamma g a^2}{\gamma g-1}\right)V_m + \cdots \right. \\ \left. \cdots + V_u^2 a + 2\frac{\gamma a^2 V_m}{\gamma-1} + V_u^2(-a+V_m) - 2\frac{a^3}{\gamma-1}\right) \end{bmatrix}, \end{aligned} \tag{5.53}$$

It is clear that in the supersonic case, i.e. $V_m > a$, we have $D^+ = D$ et $D^- = 0$. This implies that

$$A^+ = A, \quad A^- = 0, \quad E^+ = E, \quad E^- = 0.$$

5.3.1 Numerical Resolution

Once the matrices have been calculated, we need to determine an appropriate numeric solver for the partial differential equation. This requires discretization of time as well as space. In each iteration, the vector U will be calculated at all discrete *nodes* of each vane. The nodes together form a finite element mesh representing a vane.

The operator $\frac{\partial U}{\partial t}$ is estimated by

$$\frac{\partial U}{\partial t} \approx \frac{\Delta U}{\Delta t} = \frac{U^{(n+1)} - U^{(n)}}{\Delta t},$$

where Δt is the discretization time, and $U^{(n)}$ is the value of the vector U calculated at the time $n\Delta t$. As mentioned before, E is expressed in the form $E = E^+ + E^-$, in order to ensure solver convergence. This implies that

$$\frac{\Delta U}{\Delta t} = -\frac{\partial}{\partial m}\left(E^+ + E^-\right) + Q, \tag{5.54}$$

where the approximation of $\frac{\partial E^+}{\partial m}$ backward difference and the approximation of $\frac{\partial E^-}{\partial m}$ requites forward difference, explained in Table (5.1).

These methods can be formulated by explicit and implicit formulations [112]. In explicit methods, the vector $U^{(n+1)}$ is estimated from precedent values only, i.e. U^n, Q^n, E^n, as shown in the following equation

$$\frac{U^{(n+1)} - U^{(n)}}{\Delta t} = -\left(\frac{\partial E}{\partial m}\right)^{(n)} + Q^{(n)}. \tag{5.55}$$

On the other hand, implicit methods estimate the vectors U, Q, E together, for the instance $n+1$, using the value of U calculated in the preceding iteration. These methods, as shown in the following equation, are more complicated, yet more precise than explicit methods

$$\frac{U^{(n+1)} - U^{(n)}}{\Delta t} = -\left(\frac{\partial E}{\partial m}\right)^{(n+1)} + Q^{(n+1)} \tag{5.56}$$

Method	Notation	
First order forward difference	$FOFD(X_i)$	$\frac{\partial X_i}{\partial m} = \frac{X_{i+1} - X_i}{m_{i+1} - m_i}$
First order backward difference	$FOBD(X_i)$	$\frac{\partial X_i}{\partial m} = \frac{X_i - X_{i-1}}{m_i - m_{i-1}}$
Second order forward difference	$SOFD(X_i)$	$\frac{\partial X_i}{\partial m} = \frac{-\alpha(\alpha+2)X_i + (\alpha+1)^2 X_{i+1} - \alpha(\alpha+1)X_{i+2}}{-\alpha(\alpha+1)(m_{i+1} - m_i)}$, $\alpha = \frac{m_{i+2} - m_{i+1}}{mi+1 - m_i}$
Second order backward difference	$SOBD(X_i)$	$\frac{\partial X_i}{\partial m} = \frac{\alpha(\alpha+2)X_i - (\alpha-1)^2 X_{i+1} + \alpha(\alpha+1)X_{i-2}}{-\alpha(\alpha+1)(m_{i+1} - m_i)}$, $\alpha = \frac{m_{i-1} - m_{i-2}}{mi - m_{i-1}}$

TABLE 5.1: *Numerical differentiation algorithms*

5.3.1.1 Explicit method

Consider Equation (5.55), and let I_{max}, the last node of the vane mesh (0 being the index of the first node), the problem can be resolved using either first or second order numerical estimation:

$$\begin{aligned} U_i^{(n+1)} &= U_i^{(n)} + \Delta t\left(Q_i^{(n)} - FOBD(E_i^{+(n)}) - FOFD(E_i^{-(n)})\right), \\ &\quad i = 1, \cdots, I_{max} - 1, \\ U_i^{(n+1)} &= U_i^{(n)} + \Delta t\left(Q_i^{(n)} - SOBD(E_i^{+(n)}) - SOFD(E_i^{-(n)})\right), \\ &\quad i = 1, \cdots, I_{max} - 1, \end{aligned} \tag{5.57}$$

5.3.1.2 Implicit method

Using Taylor expansion, Equation ((5.56) is simplified as

$$\frac{\Delta U}{\Delta t} + \frac{\partial}{\partial m}\left(E^{(n)} + \frac{\partial E^{(n)}}{\partial U}\Delta U\right) - \left(Q^{(n)} + \frac{\partial Q^{(n)}}{\partial U}\Delta U\right) = 0 \tag{5.58}$$

where $\Delta U = U^{(n+1)} - U^{(n)}$.
Considering the Jacobian of Q, $B = \frac{\partial Q}{\partial U}$, we obtain the following implicit form:

$$\left(I + \Delta t\left(\frac{\partial A^{(n)}}{\partial m} - B^{(n)}\right)\right)\Delta U = \Delta t\left(\frac{\partial E^{(n)}}{\partial m} - Q^{(n)}\right) \tag{5.59}$$

The index $^{(n)}$ is no longer explicit and ΔU will be expressed in terms of elements calculated

in previous iteration. Rewriting this equation in form of matrix sums,

$$\left(I+\Delta t\left(\frac{\partial}{\partial m}\left(A^{+}+A^{-}\right)-B\right)\right)\Delta U=\Delta t\left(\frac{\partial}{\partial m}\left(E^{+}+E^{-}\right)-Q\right). \tag{5.60}$$

Using first order backward difference for A^{+} and E^{+}, and first order forward difference for A^{-} et E^{-}, we obtain for $i=1,\cdots,I_{max}$

$$\left(I+\Delta t\left(\frac{A_i^{+}-A_{i-1}^{+}}{m_i-m_{i-1}}+\frac{A_{i+1}^{+}-A_i^{+}}{m_{i+1}-m_i}-B_i\right)\right)\Delta U=\Delta t\left(\frac{E_i^{+}-E_{i-1}^{+}}{m_i-m_{i-1}}+\frac{E_{i+1}^{+}-E_i^{+}}{m_{i+1}-m_i}-Q_i\right). \tag{5.61}$$

We have considered: $\Delta m^{+}=m_i-m_{i-1}$ and $\Delta m^{-}=m_{i+1}-m_i$. This implies that

$$\begin{aligned}&-\left(\frac{\Delta t}{\Delta m^{+}}A_{i-1}^{+}\right)\Delta U_{i-1}+\left(I+\Delta t\left(\frac{A_i^{+}}{\Delta m^{+}}-\frac{A_i^{-}}{\Delta m^{-}}-B_i\right)\right)\Delta U_{i-1}\\&+\left(\frac{\Delta t}{\Delta m^{-}}A_{i+1}^{-}\right)\Delta U_{i+1}=\Delta t\left(\frac{E_i^{+}-E_{i-1}^{+}}{m_i-m_{i-1}}+\frac{E_{i+1}^{+}-E_i^{+}}{m_{i+1}-m_i}-Q_i\right).\end{aligned} \tag{5.62}$$

Let us define

$$\begin{aligned}AM_i &= -\frac{\Delta t}{\Delta m^{+}}A_{i-1}^{+},\\AA_i &= I+\Delta t\left(\frac{A_i^{+}}{\Delta m^{+}}-\frac{A_i^{-}}{\Delta m^{-}}-B_i\right),\\AP_i &= \frac{\Delta t}{\Delta m^{-}}A_{i+1}^{-},\\RHS_i &= \frac{E_i^{+}-E_{i-1}^{+}}{m_i-m_{i-1}}+\frac{E_{i+1}^{+}-E_i^{+}}{m_{i+1}-m_i}-Q_i.\end{aligned} \tag{5.63}$$

The equation (5.61) can be rewritten in the following compact form:

$$AM_i\Delta U_{i-1}+AA_i\Delta U_i+AP_i\Delta U_{i+1}=RHS_i$$

From here, the problem is reduced to calculating I_{max} linear equations with I_{max} unknowns, i.e.

$$\begin{bmatrix} AA_0 & AP_0 & & & & \\ AM_1 & AA_1 & \ddots & & & \\ & \ddots & \ddots & \ddots & & \\ & & \ddots & \ddots & \ddots & \\ & & & \ddots & AA_{I_{max}-1} & AP_{I_{max}-1} \\ & & & & AM_{I_{max}} & AA_{I_{max}} \end{bmatrix}\cdot\Delta U=\begin{bmatrix} RSH_0-AM_0 \\ RSH_1 \\ \vdots \\ \vdots \\ RSH_{I_{max}-1}RSH_{I_{max}}-AP_{I_{max}}. \end{bmatrix} \tag{5.64}$$

This system can be solved easily for ΔU, and then for $U^{(n+1)}$, we get:

$$U^{(n+1)} = U^{(n)} + \Delta U.$$

It can be seen that AM_0 and AP_n of Equation (5.64) are the boundary conditions, hence known. According to the stability theory presented in [108], for subsonic flow, static density needs to be imposed on the upstream, static pressure on the downstream and static fluid speed in both sides. The other variables can be interpolated:

$$\begin{cases} \rho_0 \text{ imposed} \\ V_{m\ 0} \text{ imposed} \\ V_{u\ 0} \text{ imposed} \\ p_0 = 2p_1 - p_2 \end{cases}$$

$$\begin{cases} \rho_{imax} = 2\rho_{imax-1} - \rho_{imax-2} \\ V_{m\ imax} = V_{m\ imax-1} V_{m\ imax-2} \\ V_{u\ imax} = V_{u\ imax-1} V_{u\ imax-2} \\ p_{imax} \text{ imposed} \end{cases}$$

The calculation ends when the residual of $\dfrac{\partial U}{\partial t}$ becomes inferior to a certain threshold. As their exist many definitions for this residual, we consider the maximum and average residuals:

$$\begin{aligned} res_{max} &= \max\left(\left|\frac{U_{i,j}^{(n+1)} - U_{i,j}^{(n)}}{U_{i,j}^{(n)}}\right|\right), \\ res_{avg} &= \frac{1}{4I_{max}} \sum_{i=0}^{I_{max}} \sum_{j=0}^{3} \left(\left|\frac{U_{i,j}^{(n+1)} - U_{i,j}^{(n)}}{U_{i,j}^{(n)}}\right|\right). \end{aligned} \tag{5.65}$$

5.4 Calculation of aerodynamic force on the actuator

Once the calculation is terminated; the resultant vector U allows us to calculate the physical quantities, like V_u, V_m, ρ, on the blades. The meridian and tangential forces on the finite elements of the vanes are then calculated as follows

$$\begin{aligned} dF_u(m) &= \rho(m) V_m(m) hs(m) \frac{\partial V_u}{\partial m} dm, \\ dF_m(m) &= \rho(m) V_m(m) hs(m) \frac{\partial V_m}{\partial m} dm, \end{aligned} \tag{5.66}$$

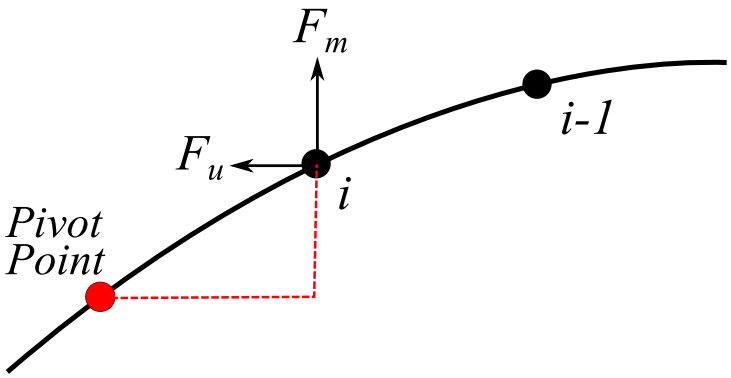


Figure 5.10. *Forces on the vane*

where h et s are the height and distance between two vanes.

The total torque acting on the vanes is then obtained by integrating the force on each finite element. The resultant net torque is the sum of the torques on each vane, i.e. the cross product between the displacement $\vec{r}$ and vector sum of the meridian and tangential forces $\vec{F}$

$$\vec{\tau} = \sum_{i=1}^{n} \vec{r}_i \Lambda \vec{F}_i. \tag{5.67}$$

This torque is transferred to the actuator shaft through the mechanical linkages. In order to find a mathematical relationship for this transfer as a function of the actuator position, let us consider a unit net torque (1N.m) to obtain a generalized expression.

5.4.1 Relation between crank handle angle and actuator position

Let A be the position of the rotation axis of the crank handle (in 2D, with the direction Y oriented along the crank handle axis towards the center of the turbine). We measure:

$$x(A) = 1.433 \quad \text{and} \quad y(A) = -27.308.$$

Let B be the position of the point where the actuator shaft enters the actuator, and where the actuator allows small rotations in the shaft to accommodate the crank handle rotation.

$$x(B) = -100.212 \quad \text{and} \quad y(B) = 4.602,$$

Also, let C be the point of connection between the crank handle and actuator shaft. We take

$$L = \|\vec{BC}\|, \quad L_1 = \|\vec{AC}\|,$$

In Figure 5.11 geometrical position of the actuator and the crank are shown to determine the relationship between crank handle angle and the actuator position.

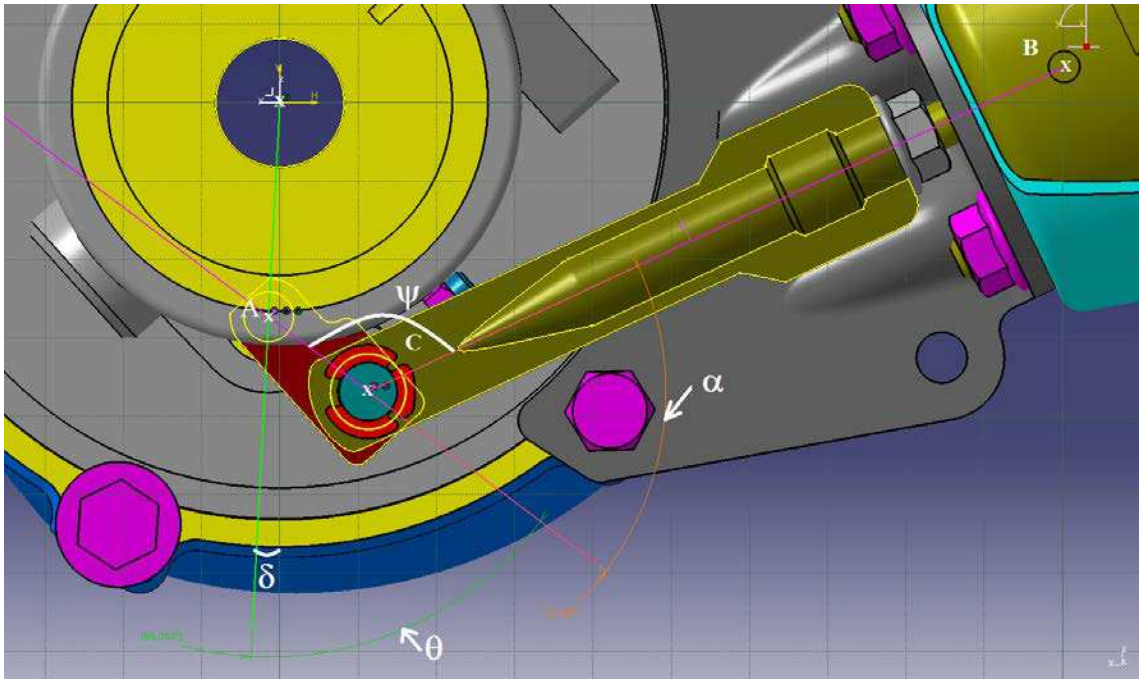


Figure 5.11. *Physical positions of primary lever pivot point (A), crank rotation axis (C) actuator position (B)*

$$\sqrt{x'(C)^2 + y'(C)^2} = L_1 = 15.895,$$
$$L = \sqrt{x''(C)^2 + y''(C)^2},$$
$$\tan(\delta) = \frac{x'(C)}{y'(C)}$$

with

$$x'(C) = x(C) - x(A), \quad y'(C) = y(C) - y(A),$$
$$x''(C) = x(C) - x(B), \quad y''(C) = y(C) - y(B),$$

and

$$\delta = \gamma + arctan\left(\frac{1.433}{-27.308}\right),$$

where γ is the angle of the crank handle measured when the vanes are closed.

5.4.2 Relation between crank handle angle and lever direction

Let θ be the crank handle angle, and β be the angle of vane levers. These are shifted, and vary equally:

$$\beta = \theta - b_3,$$

where b_3 is the direction of levers, measured when the vanes are closed. In our case, the aerodynamic force tends to open the vanes:

$$\beta = \theta - 7.456.$$

5.4.3 Relation between the levers and unison ring

Let us define r_2 as the radial position of the point of contact between the unison ring and the "secondary lever" of the crank handle, and r_3 as the radial position of the point of contact between the unison ring and any vane lever. The maximum values of r_2 and r_3 are r_{20} and r_{30} respectively, both obtained when the direction of the secondary lever is purely radial to the unison ring. We obtain the following relationships:

$$r_2 = r_{20} - 2r_{20}\tan(\frac{\beta}{2})sin(\frac{\beta}{2}),$$
$$r_3 = r_{30} - 2r_{30}\tan(\frac{\beta}{2})sin(\frac{\beta}{2}).$$

5.4.3.1 Total torque on the rim

The total torque on the rim of the unison ring can be found by

$$T_{rim} = n\frac{r_3}{L_3}cos(\varphi_3 - \alpha + \theta),$$

with:

n: number of vanes

α: displacement angle of the crank handle, same as levers

L_3: length of vane levers

φ_3:angle of contact between levers and unison ring.

In Figure 5.12, different dimensions of the turbocharger are shown to determine the angle of each part associated with actuator.

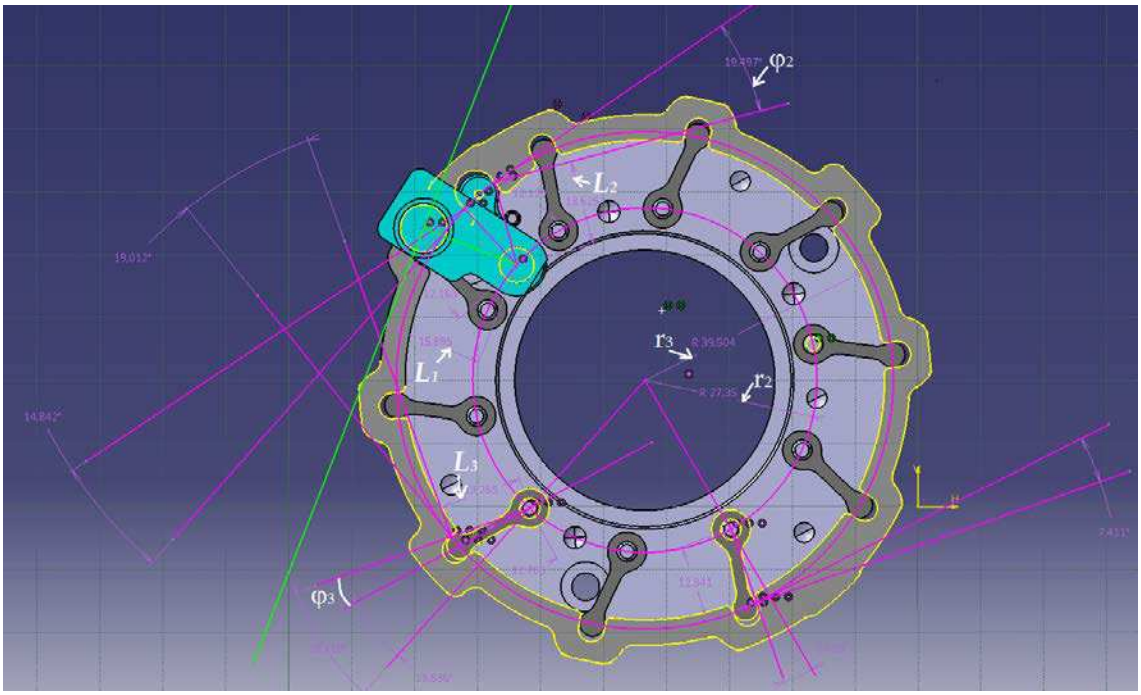


Figure 5.12. *Turbocharger geometry with all dimensions*

5.4.3.2 Net torque on the crank handle

The net torque on the crank handle can be found by

$$T_{crank} = T_{rim}\frac{L_2}{L_3}cos(\varphi_2 - \alpha + \theta),$$

where L_2 is the length of the "secondary lever" of the crank handle and φ_2 is the angle between the secondary lever and the unison ring.

5.4.4 Angle between the Crank Handle and Actuator Shaft

Let ξ be the direction of the Shaft:

$$\xi = arctan(\frac{x''(C)}{y''(C)}).$$

Let ψ be the angle between the shaft and the "primary lever" of the crank handle, i.e. between segments BC and AC :

$$\psi = \delta - \xi, \delta = \arctan(\frac{x'(C)}{y'(C)}).$$

Force on actuator:
Finally, the force acting on the actuator is obtained as

$$L_{rod} = \frac{1000 T_{crank}}{L_1} \left| \frac{\cos(a_0 - \alpha + \theta)}{\sin(\psi)} \right|.$$

where a_0 is the angle between the axis of the actuator shaft and the normal of the primary lever, when the vanes are open.

5.5 Model validation

The engine testing was carried at the "R&D moteurs" facilities with the DV6TED4 engine, equipped with GT1544V turbocharger from Honeywell GARRETT with a force sensor installed on the actuator shaft. Data acquisition was done in two modes: slow acquisition (sampling frequency of 10 hz) and medium acquisition (sampling frequency of 1000 Hz) on an AVL system. The aerodynamic force estimate was obtained by implementing the calculations discussed in this chapter in Solver 1D. In this section, comparative results between the estimated and measured force are discussed, along with the turbine inlet pressure measured in the engine and estimated through the 1D Model.

A simulation tool was developed in QtCreator, in which, the 1D flow model was implemented in form of C++ class libraries. The graphical user interface of this tool is shown in Figure 5.13. It is used to configure the initial conditions of the model, i.e. the initial temperature and pressure at the turbine inlet, its speed and vane opening position.

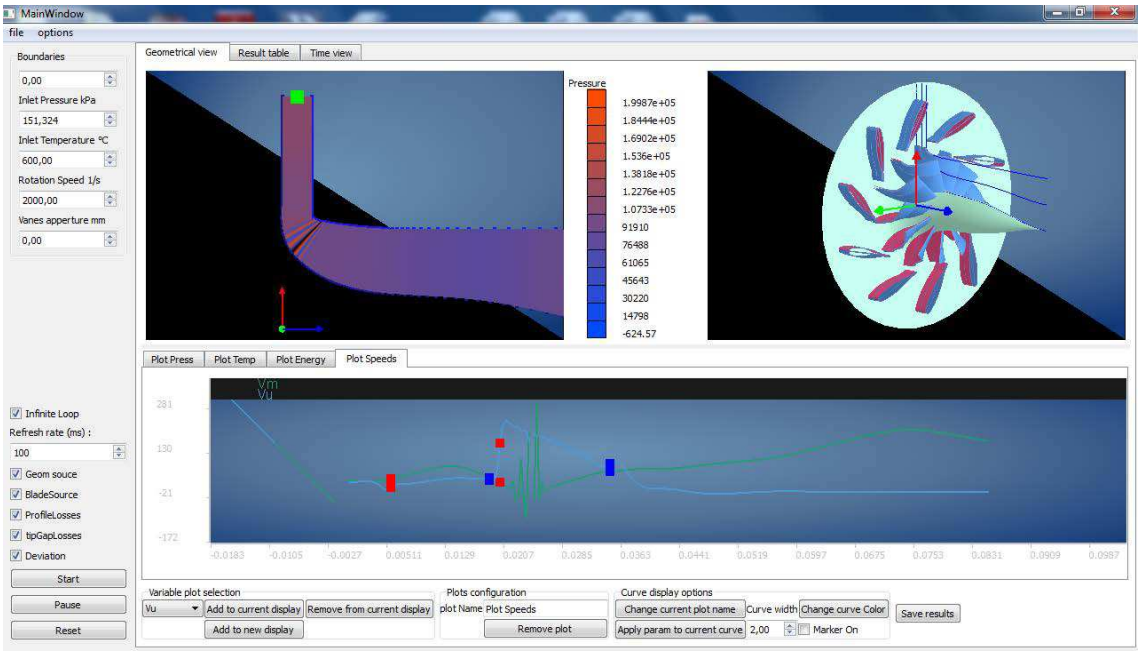


Figure 5.13. *A Simulator based on C compiler code to solve 1D flow equations*

In Figure 5.14 different outputs of the code are shown in the graphical form. The outputs of the simulator are tangential and meridional components of velocities and forces, torque on the vanes, the pressure in the turbine and force acting on the actuator due to turbine pressure etc.

The comparison results between estimated and measured turbine inlet pressure are shown in Figures 5.15 and 5.16. The error is around 20% when losses are not included in the calculations and less than 10% when they are included. It can be seen that the results deviate at larger actuator displacements. This is because when the vane is nearly closed, the small throat area causes high turbulence in the actual airflow, which is not taken into account in the calculations.

Figures 5.17 and 5.18 show the comparison of the actuator force at different engine loads. It can be seen that the pressure losses play an important part in the estimation of aerodynamic force. The addition of losses improves the correlation between the estimated result and the experimental result. The minor deviation in these results can be attributed to the distribution of mechanical tolerances between the mechanisms.

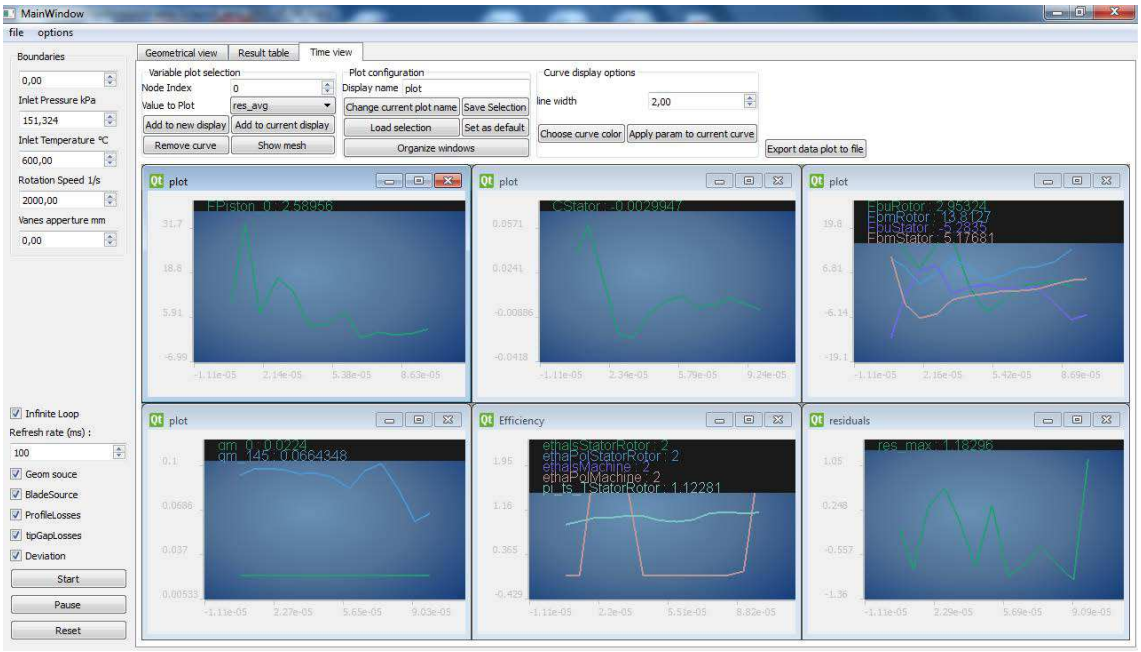


Figure 5.14. *Output results of the QtCreator simulator*

5.6 Summary

A 1D turbine airflow model was developed in order to estimate the aerodynamic force exerted by the exhaust gas flow on the VGT vanes. The model was discretized in order to facilitate its implementation, and numerical approximation of its partial derivatives was also discussed. Then, the aerodynamic force was estimated on the VGT vanes and transferred to the actuator shaft, in order to obtain its influence on the actuator. The model was used to develop a simulation tool for prediction of the aerodynamic force as well as the internal mass-flow states of the turbine. Experimental validation shows that the tool predicts the aerodynamic force accurately. However, the estimation of turbine inlet pressure requires detailed modeling of turbulent air-flow at narrow apertures. The transition response of the simulator has not been studied yet. This simulation tool can be used to study the effect of the aerodynamic force on the air-path control and to develop robust controllers that can successfully counteract it.

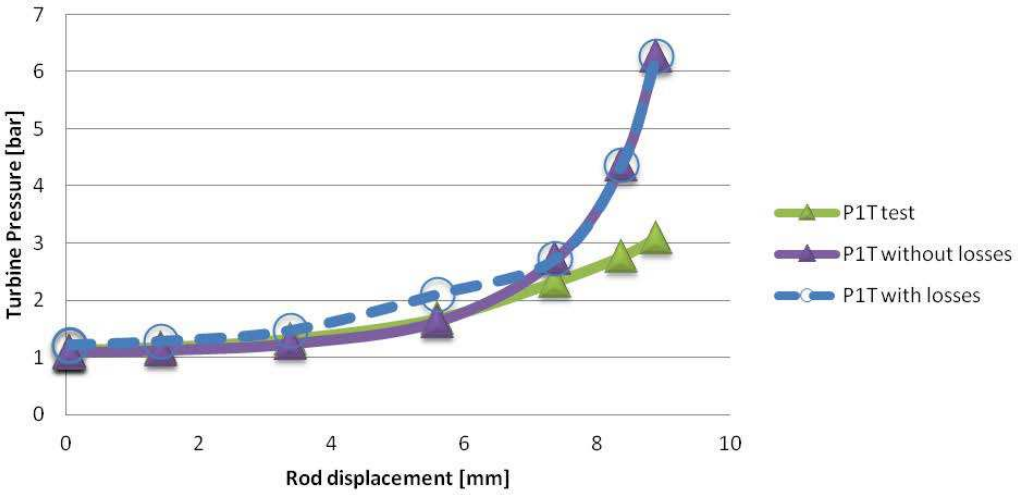


Figure 5.15. *Comparison of turbine inlet pressure, Engine: 2000RPM, 100Nm*

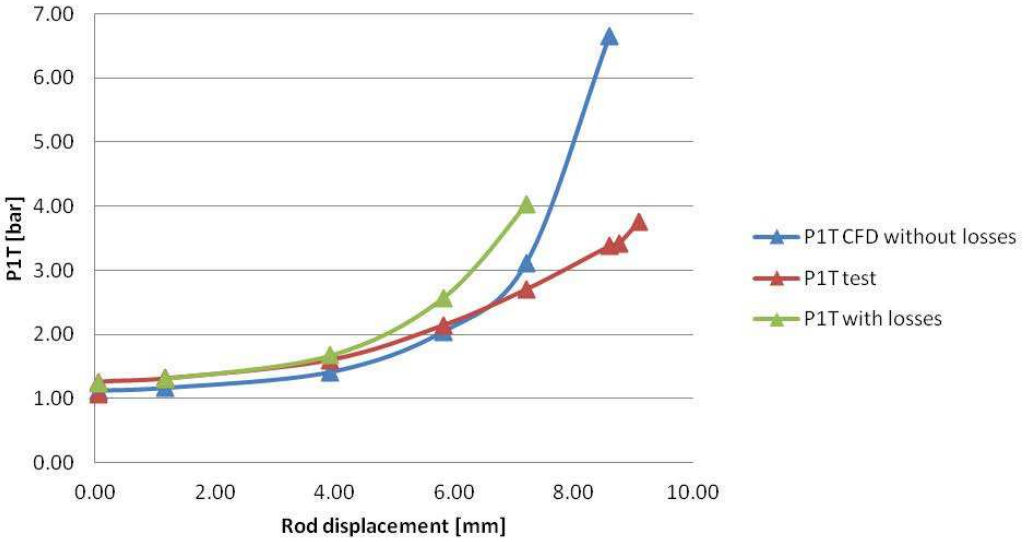


Figure 5.16. *Comparison of turbine inlet pressure, Engine: 2000RPM, 150Nm*

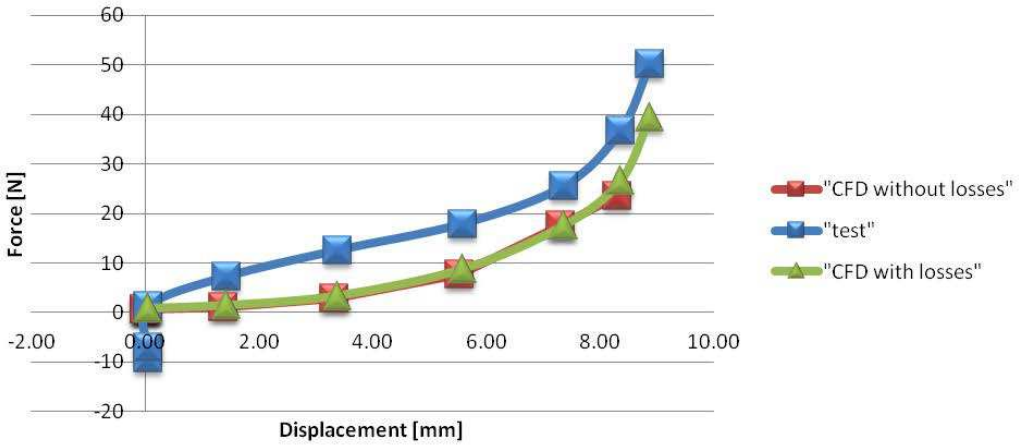


Figure 5.17. *Comparison of aerodynamic force on actuator, Engine: 2000RPM, 100Nm*

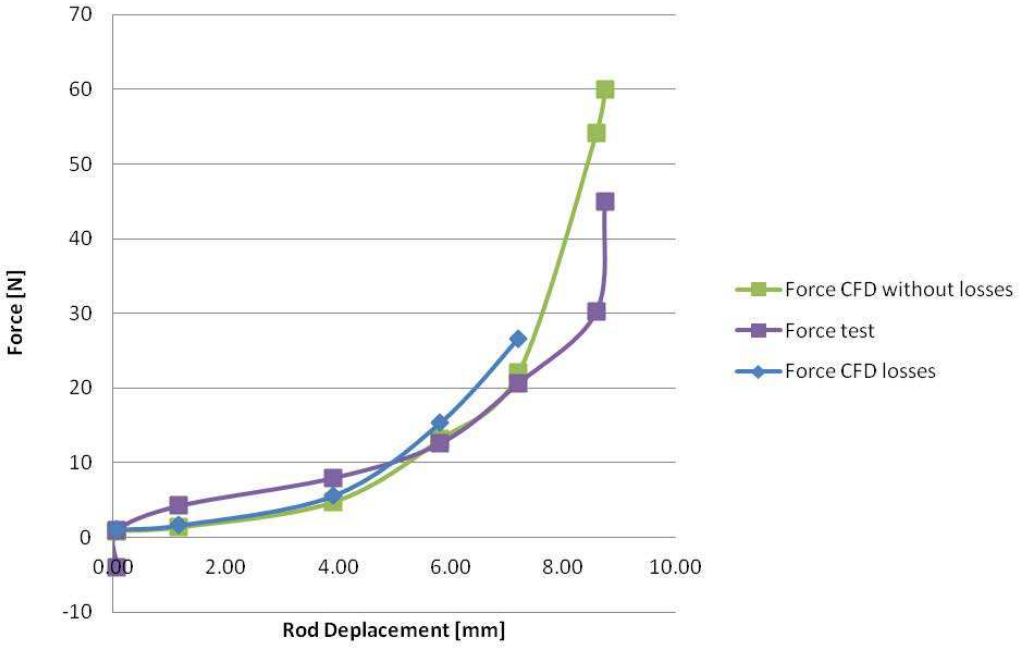


Figure 5.18. *Comparison of aerodynamic force on actuator, Engine: 2000RPM, 150Nm*

Conclusion and Perspectives

Overview

The need of system modeling and simulation tools has increased in the automobile industry, due to intense competition and strict quality regulations. These simulation tools need to maintain the physical structure of the overall system represent the interaction between their subsystems as well as that with other systems. This thesis addressed the issues related with modeling and simulation of the engine air-path, which is responsible for the management of the intake and exhaust air quality and quantity.

The study was focused on diesel engine air-paths, as they are more complex than their SI engine counterparts. The structure of a typical engine air-path was presented, and its key subsystems were introduced. It was shown that the reciprocating process of diesel engines and its resultant pulsations in the air-path need to be modeled. A suitable discrete event model was identified for inclusion in air-path simulation. Then, the mass-flow characteristics in different sections and between different subsystems, specially VGT and EGR, were described. Finally, using these developments, an air-path simulator was developed in AMESim.

In the next part of this thesis, the importance of modeling of actuation systems was discussed. These actuation systems are used in precise control of different air-path subsystems, such as VGT and EGR. This study was focused on mechatronic actuators. Based on experimental results of commercial actuators, a generic nonlinear dynamic model was developed that could be parameterized to fit specific mechatronic actuator. Friction and temperature effects were taken into account. A parameter identification method was

demonstrated and the model was validated experimentally. The model was implemented in AMESim, parameterized according to the actuators used in DV6TED4, and integrated in the air-path simulator.

Validation of the simulator was addressed after its completion. Experimental results on the DV6TED4 engine test bench, obtained during the testing phase of SIMBA, were used for this purpose. This obliged us to reproduce the engine controller used in the test campaigns. The open ECU was implemented in Simulink and interfaced with the AMESim simulator. The model was simulated under different testing conditions. It provided satisfactory results, which were comparable to the experimental values.

The final part of this thesis was targeted on actuators. First, local-loop actuator control was studied. The importance of robust control was highlighted and various existing robust control methods were tested in simulation and in experimentation on an air-path actuator. Then, an advanced controller was developed using backstepping technique, which adapts dynamically to changes in friction and external load. After this, the aerodynamic force on VGT actuators was studied. A 1D turbine flow model was developed and it was resolved numerically in order to estimate this force. Based on this model, a simulation tool was developed and validated experimentally.

Concluding Remarks

The scope of this thesis required multidisciplinary research work, involving fluid mechanics, thermodynamics, modeling and simulation, industrial electronics and automation and control. The objectives and goals were achieved successfully. Many important physical aspects were considered in the development of the simulator, which had so far remained ignored in the global structure of the air-path. The results of this work provide a working platform for air-path design, as well as a basis for further research in virtual design and development tools for the automotive industry.

Future Research

There are a number of directions in which research can be continued for improving the air-path simulator, some of which are as follows:

- Transmission delays need to be taken into account in the simulator. The geometry of some parts of the air-path (e.g. swirl) also affects the flow dynamics. Therefore simulator needs to be extended, from 0D to 1D.

- The aerodynamic force estimation tool should be adapted for integration in the air-path simulator. Controllers would perform more reliably if this force is taken in to account during control design.

- Turbulence models are required in the turbocharger exhaust flow model, to cover the effects of narrow apertures at small openings.

- VGT turbines are characterized on a flow bench with steady flow, whereas the turbines on the engine experiences strong pressure pulsations. Unsteady turbine flow models should be developed to reflect the turbocharger behavior more accurately.

- Better, high performance implementation platforms need to be explored for ECU processors, in order to implement mathematically intensive controllers for engine and air-path control.

- Advanced robust control methods should be developed, both for the local-loop control of actuators and the global control of the air-path, in order to achieve better performance in terms of engine efficiency and pollution control. In this regard, the controllers studied and developed in this report should be integrated and tested on the air-path simulator.

We aim to address these issues in the future, specially those pertaining to control.

Appendices

Appendices

A Tables

Actuator	**Gear Ratio**	**Motor Constant**	**Winding Resistance**	**Spring Constant**	**Pre compression Torque**	**Static Friction Torque**	**Tř constant**
Bosch GPA-S (DC)	27.5	13.82	3.35	60.88	119.4	51.2	0.0105
Pierburg (DC)	37.3	27.9	3.63	133.68	91.6	53.2	0.0114
Valeo (T)	-	109.1	3.75	45.97	37.9	12.633	0.0121
Delphi (T)	-	120	2.79	114.28	45.16	12.9	0.0085
Dellorto (DC)	-	63.03	2.06	217.6	86.32	68.8	0.012
HELLA (DC)	60	12.21	3.84	-	-	-	0.012

TABLE A.1: *Chapter 1: Identified parameters of different commercial actuators*

Algorithm	Parameter	Value
Twisting	α_m	400000
	α_M	1000000
Quasi-continuous	α	250
Super twisting	α	5
	φ	15
Differentiator	λ_1	1.1
	λ_2	1.5
	L	260

TABLE A.2: *Chapter 4: Parameters for sliding mode controllers*

Parameter	Value
C_1	11500
C_2	50
C_3	100
γ_0	10
γ_1	0.001
γ_2	0.01
κ_0	1E-11
κ_1	1E-13

TABLE A.3: *Chapter 4: Parameters for adaptive controller an observers*

B Torque and friction characteristics comparison

In Figure B.1, the electromagnetic coefficients of different actuator motors are presented. It can be seen that the PMDC motor based actuators are much lower on the scale than the torque motor based actuators. This result is comparable to the comparison between static friction values of the actuators, shown in Figure B.2. As PMDC motors have lower torque values, they require gearing, which results in added friction. Torque motors on the other hand, produce sufficient torque due to their high electromagnetic coefficients, and can therefore be connected directly to the load. A special case is the Dellorto actuator, which contains a variant of PMDC motor. Due to the modified Poki Poki windings (introduced by Mitsubishi), they produce higher torque as compared to conventional PMDC motors. However, they are larger in size, and the torque is still not sufficient for air-path applications. This is why they need additional gearing, and are therefore at a high position on the friction chart.

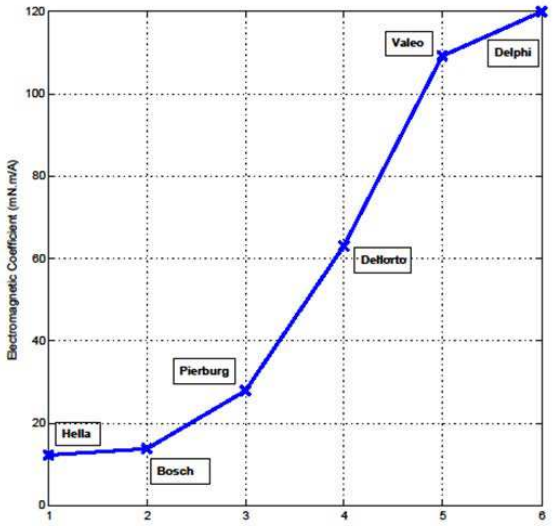


Figure B.1. *Electromagnetic coefficients of different actuators*

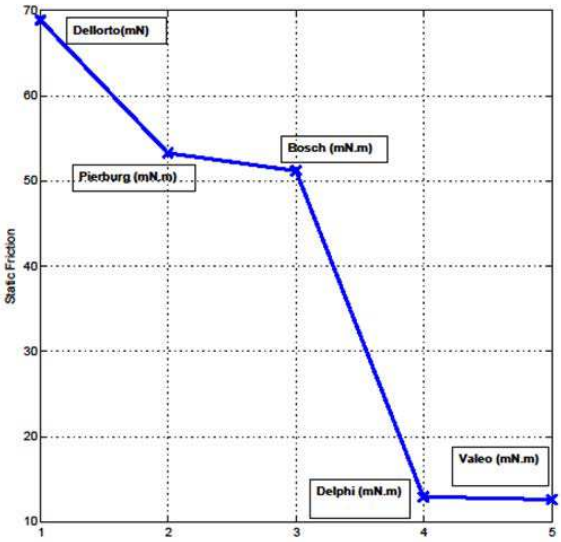


Figure B.2. *Static friction values of different actuators*

C Sensors and transmission protocol in actuators

Hall Effect Sensors

Hall effect sensors are active sensors, i.e. they require a power supply in order to function. More precisely, the sensor is a cubic structure of magnetic material and a current is passed through the transverse section. As the sensor experiences a magnetic field on a plane orthogonal to the current flow, the deflection in current leads to a voltage appearing on the third plane. The voltage is proportional to the angle between the current plane and the magnetic field. In accuracy and range, they compete well with optical sensors. Their output to rotary motion is sinusoidal, however it can be linearized using electronic signal processing or the configuration described in [53]. The popularity of Hall effect sensors can be judged by the fact that all but one actuator presented in this study have Hall effect sensors for position feedback.

Inductive Sensors

Inductive sensors, while accurate and robust, have been avoided in the past due to their size and manufacturing complexities [14]. With advances in microelectronics and PCB miniaturization however, this technology too is making its way into the automobile industry. In addition to the advantages of magnetic sensors, the inductive sensors are also less sensitive to temperature since there are no materials with temperature-dependent permeability. Hence such sensors are used where failure cost has to be minimum

Protocols

Apart from sensor technology, new protocols are arising in the sensor signal transmission as well. Manufacturers are integrating signal processing and digital converters into the actuators. These actuators transmit digitally coded signal which can be read directly by the ECU. One such example is the Single Edge Nibble Transmission (SENT), an asynchronous protocol which codes data in the form of pulse width.

SENT Transmission Protocol

To keep the operation as close to the real life application of the actuator, the position sensor integrated in the actuator was used for feedback. The SENT Protocol, intended for use in applications where high-resolution sensor data needs to be communicated from a sensor to an engine control unit (ECU). It is intended as a replacement for the lower resolution methods of 10-bit ADCs and PWM and as a simpler low-cost alternative to CAN or LIN data buses. Designated by the SAE task force as J2716, SENT is a unidirectional communications scheme from sensor/ transmitting device to controller/ receiving device. The protocol has been so designed that no coordination signal is required from the controller/receiving device. The sensor signal is transmitted as a series of pulses with data measured as falling to falling edge times.

The SENT protocol data packet (figure C.3) transmits a sequence of 9 pulses repeatedly. Following a 3μ sec timing (this period shall henceforth be referred to as ticks, 3 ţsec=1 tick), the width of each pulse determines the nibble value coded in it. The pulse width is measured from one falling edge to the other falling edge. Each pulse has a low time of about, but no less than 4 ticks. The rest of the pulse time is high. The transmission sequence is as follows:

- Calibration Pulse (no data)
- Status/Serial Pulse (4 bit)
- Channel 1: Nibble 1 (4bit)
- Channel 1: Nibble 2 (4bit)
- Channel 1: Nibble 3 (4bit)
- Channel 2: Nibble 1 (4bit)
- Channel 2: Nibble 2 (4bit)
- Channel 2: Nibble 3 (4bit)
- Cyclic Redundancy Check CRC (4 bit)

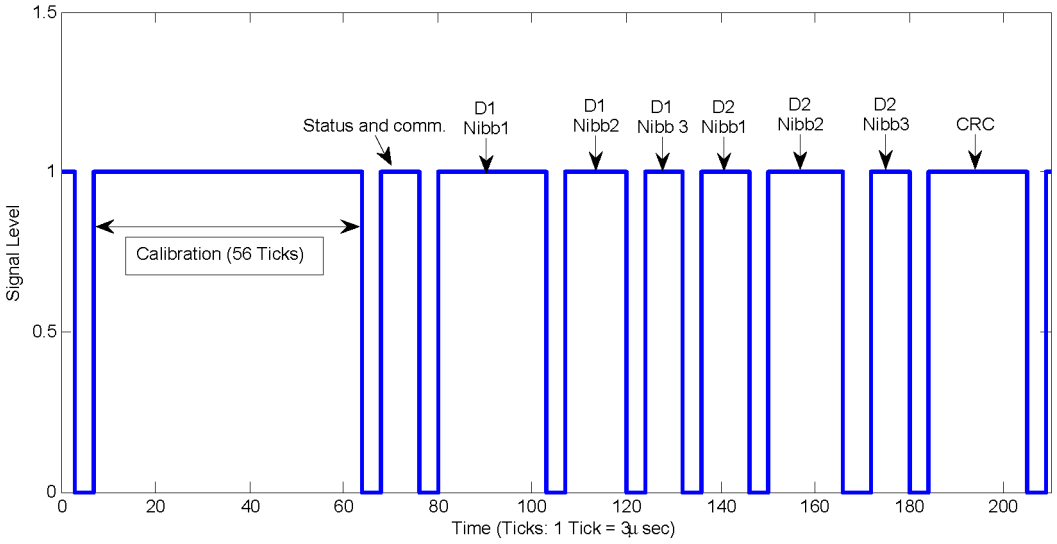


Figure C.3. *SENT Transmission Packet*

D LaSalle Yoshizawa Theorem

The LaSalle Yoshizawa Theorem [98] is stated as follows:

Consider the general time-varying system:

$$\dot{x} = f(x,t) \tag{68}$$

where $x \in \mathbb{R}^n$ and $f : \mathbb{R}^n \times \mathbb{R}_+ \to \mathbb{R}^n$ is locally Lipschitz in x uniformly in t. Let $x = 0$ be an equilibrium point of the system and $V : \mathbb{R}^n \times \mathbb{R}_+ \to \mathbb{R}_+$ be a continuously differentiable function such that $\forall\, t \geqslant 0$, $\forall\, x \geqslant \mathbb{R}^n$,

$$\begin{aligned} \gamma_1(|x|) &\leqslant V(x,t) \leqslant \gamma_2(|x|), \\ \dot{V} &= \frac{\partial V}{\partial t} + \frac{\partial V}{\partial x} f(x,t) \leqslant -W(x) \leqslant 0, \end{aligned}$$

where γ_1 and γ_2 are class k_∞ functions and W is a continuous function. Then, all solutions of (68) are globally uniformly bounded and satisfy

$$\lim_{t\to\infty} W(x(t)) \leqslant 0.$$

In addition, if $W(x)$ is positive definite, then the equilibrium $x = 0$ is globally uniformly asymptotically stable.

E Calculation of upper time bound of URED

The upper time bound is calculated following the method described in [97]. As the details are explained in the reference, we will not define the constants here, the reader can refer to the original article for details. We recall the equations of the Uniform Robust Exact Differentiator from Section III-A.

$$\begin{aligned}
\dot{\hat{x}}_1 &= -K_1\mu_1(x_1), \\
\dot{\hat{x}}_2 &= -K_2\mu_2(x_1), \\
\mu_1(x_1) &= \phi_1|x_1|^{\frac{1}{2}}sign(x_1) + \phi_2|x_1|^{\frac{3}{2}}sign(x_1), \\
\mu_2(x_1) &= \frac{\phi_1^2}{2}sign(x_1) + 2\phi_1\phi_2 x_1 + \frac{3}{2}\phi_2^2|x_1|^2 sign(x_1).
\end{aligned} \tag{69}$$

The parameters to be tuned are K_1, K_2, ϕ_1 and ϕ_2. It can be noticed that the differentiator is composed of a term with homogeneity of positive degree, and one with negative degree. The first term guarantees convergence from infinity to a fixed neighborhood of the derivative, in fixed time. Therefore, from a fixed point in the domain, the time taken to converge to the neighborhood is bounded by the time period required from infinity. The second term then guarantees convergence from the neighborhood to the exact value of the derivative in finite time. In this way, after the two time durations have elapsed, it can be said with certainty that the derivative has converged. We suppose that the second derivative of the input signal (acceleration) is bounded by $L = 100$, such that $|\dot{x}_2| \leq 100$. Then for a particular choice of ϕ_1 and ϕ_2, the parameters K_1 and K_2 can be chosen as

$$\begin{aligned}
K_2 &> \frac{2L}{\phi_1^2}, \\
K_1^2\left(K_2 - 0.25K_1^2\right) &> \frac{4L^2}{\phi_1^4}.
\end{aligned} \tag{70}$$

From these relationships, the values of differentiator parameters are chosen as $(K_1, K_2) = (50, 80)$, $(\phi_1, \phi_2) = (1, 1)$. Once these parameters have been chosen, the upper time bound

can be found out through the equations of Lyapunov Analysis, presented in [97]. We choose

$$\gamma_1 = \left(\frac{24\tilde{k}_1}{7}\right)^{\frac{4}{7}}, \quad \gamma_2 = \left(\frac{32\tilde{k}_2}{7}\right)^{\frac{1}{7}}, \quad \gamma_3 = \left(\frac{\tilde{k}_2}{28}\right)^{\frac{2}{9}},$$
$$\gamma_4 = (K_1)^{\frac{1}{5}}, \quad \gamma_5 = \left(\phi_1^2 K_2^{\frac{1}{5}}\right)^{\frac{1}{3}}, \quad \gamma_6 = \left(\frac{3\phi_2 K_1}{2}\right)^{\frac{2}{5}},$$
$$\gamma_7 = \left(\frac{3\phi_2 K_1}{2\delta}\right)^{\frac{2}{5}},$$
$$\delta = \frac{3}{7\tilde{k}_2}\left(\frac{24\tilde{k}_1}{7}\right)^{\frac{4}{3}} + \frac{8}{7\tilde{k}_2}\left(\frac{32\tilde{k}_1 2}{7}\right)^{\frac{1}{6}} + 0.05,$$

where $\tilde{k}_1 = \phi_1 K_1$ and $\tilde{k}_2 = \frac{3}{2}\phi_2^2 K_2$. The upper time bound is defined by

$$T_0 = \frac{2}{\gamma_1}\epsilon_1^{\frac{1}{2}} + \frac{12C_4}{C_1}(2C_4)^{\frac{7}{6}}\left(\frac{1}{\epsilon_2}\right), \tag{71}$$

where ϵ_1, ϵ_2, C_1 and C_4 are constants, defined in terms of γ_i and δ. From the calculations presented in [97], we find $C_1 = 50$, $C_4 = 1.1$, $\epsilon_1 = 9$ and $\epsilon_2 = 1000$. From these values, the upper time limit is obtained as $T_0 = 509$ msec.

Bibliography

[1] Euro VI Automotive. Euro vi - emissions from heavy duty vehicles. *www.ec.europa.eu*, 2013. [cited at p. 1]

[2] J. Heywood. *Internal Combustion Engine Fundamentals*. Publishers McGraw-Hill, ISBN-13: 978-0070286375, 1988. [cited at p. 3, 5]

[3] B. Challen and R. Baranescu. *Diesel Engine Reference Book - (2^{nd} Edition)*. Butterworth-Heinemann, Oxford, 1999. [cited at p. 4, 5, 15]

[4] G. H. Abd-Alla. Using exhaust gas recirculation in internal combustion engines: A review. *Energy Conversion and Management*, 43:1027–1042, 2002. [cited at p. 4, 6]

[5] A. Maiboom, X. Tauzia, and J. F. Hétet. Experimental study of various effects of exhaust gas recirculation (egr) on combustion and emissions of an automotive direct injection diesel engine. *Energy*, 33:22–24, 2008. [cited at p. 4, 6]

[6] H. Hiereth and P. Prenninger. *Charging the Internal Combustion Engine*. Publishers Springer-Verlag, ISBN-13: 978-3211330333, 2007. [cited at p. 4]

[7] W. W. Pulkrabek. *Engineering Fundamentals of the Internal Combustion Engine*. Publishers Prentice Hall (2 edition), ISBN-13: 978-0131405707, 2003. [cited at p. 5]

[8] M. Muller, E. Hendricks, and S. C. Sorenson. Mean value modelling of turbocharged spark ignition engines. *SAE technical paper*, (980784):125–145, 1998. [cited at p. 5]

[9] L. Guzzella and C. H. Onder. *Introduction to modeling and control of internal combustion engine system*. Publishers Springer, ISBN-13: 978-3540222743, 2004. [cited at p. 5, 6, 15, 16, 17, 19, 21]

[10] M. Zheng, G. T. Reader, and J. G. Hawley. Diesel engine exhaust gas recirculation - a review on advanced and novel concepts. *Energy Conversion and Management*, 45:883–900, 2004. [cited at p. 5]

[11] T. Jacobs, D. Assanis, and Z. Filipi. The impact of exhaust gas recirculation on performance and emissions of a heavy duty diesel engines. *Journal Society of Automotive Engineers Inc.*, (SAE Paper 2003-01-1068), 2003. [cited at p. 6]

[12] R. D. Kopa and H. Kimura. Exhaust gas recirculation as a method of nitrogen oxides control in an internal combustion engine. *APCA 53rd Annual Meeting, Cincinnati, Ohio*, 1960. [cited at p. 6]

[13] J. Galindo, H. Climent, C. Guardiola, and J. Doménech. Modeling the vacuum circuit of a pneumatic valve system. *Journal of Dynamic systems, measurement and Control ASME*, 131, 2009. [cited at p. 6, 9, 35]

[14] H. T. Doriben and K. Durkopp. Mechatronics and drive-by-wire systems advanced non-contacting position sensors. *Control Engineering Practice*, 11:191–197, 2003. [cited at p. 6, 36, 176]

[15] F. S. Ahmed, S. Laghrouche, and M. El Bagdouri. An experimental comparative study of different second order sliding mode algorithms on a mechatronic actuator. *In Proc. IEEE american control conference ACC, San Francisco*, pages 5286–5291, 2011. [cited at p. 8]

[16] A. Albrecht, O. Grondin, F. LeBerr, and G G. Le Solliec. Towards a stronger simulation support for engine control design: a methodological point of view. *Oil and Gas Science and Technology-Revue de l'IFP*, 62(4):437–456, 2007. [cited at p. 15, 17]

[17] L. Guzzella and A. Amstutz. Control of diesel engine. *IEEE control system magazine*, 18(5):53–71, 1998. [cited at p. 15]

[18] B. K. Powell and J. A. Cook. Nonlinear low frequency phenomenological engine modeling and analysis. *IEEE American Control Conference*, 1987. [cited at p. 16]

[19] L. Eriksson. Modeling and control of trubocharged si and di engines. *Oil and Gas Science and Technology*, 62(4):523–538, 2007. [cited at p. 16]

[20] V. Utkin, H. Chang, I. Kolmanovsky, and J. A. Cook. Sliding mode control for variable geometry turbocharged diesel engines, 2000. [cited at p. 16]

[21] A. G. Stefanopoulou, I. Kolmanovsky, and J. S. Freudenberg. Control of variable geometry turbocharged diesel engines for reduced emissions. *Control Systems Technology, IEEE Transactions on*, 8(4):733–745, 2000. [cited at p. 16]

[22] A. Albrecht, O. Grondin, P. Moulin, and G. Corde. Hcci diesel engine control design using advanced simulation with real time capabilities. *Oil and Gas Science and Technology-Revue de l'IFP*, 63(4):535–551, 2008. [cited at p. 16, 17]

[23] J. Chauvin, G. Corde, N. Petit, and P. Rouchon. Motion planning for experimental airpath control of a diesel homogeneous charge-compression ignition engine. *Control Engineering Practice*, 16(9):1081–1091, 2008. [cited at p. 16]

[24] J. Chauvin, P. Moulin, B. Youssef, and O. Grondin. Global airpath control for a turbocharged diesel hcci engine. *Oil and Gas Science and Technology-Revue de l'IFP*, 63(4):553–561, 2008. [cited at p. 16]

[25] M. Kao and J. J. Moskwa. Turbocharged diesel engine modeling for nonlinear engine control and state estimation. *Journal of dynamic systems, measurement, and control*, 117(1):20–30, 1995. [cited at p. 17]

[26] P. A. Lakshminarayanan and Y. V. Aghav. *Modelling Diesel Combustion*. Springer, Heidelberg, 2010. [cited at p. 19]

[27] A. E. W. Austen and W. T. Lyn. Relation between fuel injection and heat release in a direct injection engine and the nature of the combustion process. *Proceedings of the Institution of Mechanical Engineers: Automobile Division*, 14:47–62, 1960. [cited at p. 19]

[28] W. Cartillieri and R. J. R. Johns. Multidimensional modelling of engine processes: Progress and prospects. *15th CIMAC Congress, Paris*, 1983. [cited at p. 19]

[29] A. D. Gosman, Y. Y. Tsui, and A. P. Watkins. Calculation of unsteady three-dimensional flow in a model motored reciprocating engine and comparison with experiment. *Fifth International Turbulent Shear Flow Meeting, Cornell University, USA.*, 1985. [cited at p. 19]

[30] J. Rife and J. Heywood. Photographic and performance studies of diesel combustion with a rapid compression machine. *SAE Technical Paper 740948*, 1974. [cited at p. 19]

[31] J. C. Dent and P. S. Mehta. Phenomenological combustion model for a quiescent chamber diesel engine. *SAE Technical Paper 811235*, 1981. [cited at p. 19]

[32] D. A. Kouremenos, C. D. Rakopoulos, and D. Hountalas. Thermodynamic analysis of indirect injection diesel engines by two-zone modeling of combustion. *Journal of engineering for gas turbines and power*, 112(1):138–149, 1990. [cited at p. 20]

[33] C. Barba, C. Burkhardt, K. Boulouchos, and M. Bargende. A phenomenological combustion model for heat release rate prediction in high-speed di diesel engines with common rail injection. *SAE Technical Paper 2000-01-2933*, 2000. [cited at p. 20]

[34] R. Lebas, G. Mauviot, and F. LeBerr. A phenomenological approach to model diesel engine combustion and in-cylinder pollutant emissions adapted to control strategy. *IFAC Workshop on Engine and Powertrain Control, Simulation and Modeling, France*, 2009. [cited at p. 20, 27]

[35] Z. D. Husain. *Theoretical Uncertainty of Orifice Flow Measurement.* Daniel Flow Products, Incorporated, 1995. [cited at p. 22]

[36] Parcol inc Inc. *Handbook of Control Valve Sizing.* Parcol S.p.A. Italy, 2007. [cited at p. 22]

[37] A. Mehmood, S. Laghrouche, and M. El Bagdouri. Modeling and identifcation of electro-pneumatic vnt actuator for simulation and control. *In Proc. 8th IFAC Symposium on Nonlinear Control Systems, Bologna*, 2010. [cited at p. 23]

[38] R. Buratti, A. Carlo, E. Lanfranco, and A. Pisoni. Di diesel engine with variable geometry turbocharger (vgt): a model based boost pressure control strategy. *Meccanica*, 32(5):409–421, 1997. [cited at p. 23, 85]

[39] G. Decombes, J. F. Pichouron, F. Maroteaux, N. Moreno, and J. Jullien. Simulation of the performance of a variable geometry turbocharger for diesel engine road propulsion. *International Journal of Thermodynamics*, 5(3):139–149, 2010. [cited at p. 23]

[40] S. Brown and J. Estill. The turbomustangs.com complete turbocharging guide. *Sources: Garrett, turbodriven.com*, 2003. [cited at p. 24]

[41] P. Moraal and I. Kolmanovsky. Turbocharger modeling for automotive control applications. *SAE Technical Paper 1999-01-0908*, 1999. [cited at p. 25, 26]

[42] F. T. Brown. *Engineering System Dynamics, a Unified Graph-Centered Approach.* CRC Press, USA., 2006. [cited at p. 27]

[43] R. Lebas, M. Fremovici, G. Font, F. LeBerr, and a. Albrecht. A phenomenological combustion model including in-cylinder pollutants to support engine control optimisation under transient conditions. *SAE Technical Paper 2011-01-1837*, 2011. [cited at p. 27]

[44] R. Isermann, R. Schwarz, and S. Stolzl. Fault-tolerant drive by wire systems. *Control System Magazine*, 22:22–24, 2002. [cited at p. 33, 64, 85]

[45] R. Hoseinnezhad and A. Bab-Hadiashar. Missing data compensation for safety-critical components in a drive-by-wire system. *", IEEE Trans. Vehicular Technology*, 54, 2005. [cited at p. 33, 35]

[46] M. Bertoluzzo, G. Buja, and J. R. Pimentel. Design of a safety-critical drive-by-wire system using flexcan. *SAE International*, 2005. [cited at p. 33]

[47] J. B. Song and K. S. Byun. Throttle actuator control system for vehicle traction control. *Mechatronics*, 9:477–495, 1999. [cited at p. 33, 85]

[48] P. Mercorelli. Robust feedback linearization using an adaptive pd regulator for a sensorless control of a throttle valve. *Mechatronics*, 2009. [cited at p. 33, 35, 37]

[49] F. Contreras, I. P. Quiroz, and C. C. deWit. Further results on modeling and identification of an electronic throttle body. In *Proc. 10th Mediterranean Conf. on Control and Automation-MED*, 2002. [cited at p. 33, 52, 57]

[50] R. Scattolini, C. Siviero, M. Mazzucco, S. Ricci, L. Poggio, and C. Rossi. Modeling and identification of an electromechanical internal combustion engine throttle body. *Control Engineering Practice*, 5:1253–1259, 1997. [cited at p. 33, 35, 37, 47]

[51] C. Rossi, A. Tilli, and A. Tonielli. "robust control of a throttle body for drive by wire operation of automotive engines. *IEEE Trans. Control Systems Technology*, 8, 2000. [cited at p. 33, 52]

[52] H. D. Baumann. *Control Valve Primer- A User's Guide - (4^{th} Edition)*. ISA, USA, 2009. [cited at p. 34, 43]

[53] J. P. Yonnet, A. Foggia, and S. Adenot. A differential magnetic position sensor. *Sensors and Actuators A: Physical*, 81:340 – 342, 2000. [cited at p. 36, 176]

[54] C. Tsai, S. Lin, H. Huang, and Y. Cheng. Design and control of a brushless dc limited-angle torque motor with its application to fuel control of small-scale gas turbine engines. *Mechatronics*, 19:29–41, 2009. [cited at p. 37]

[55] L. Walha, T. Fakhfar, and M. Haddar. Nonlinear dynamics of a two-stage gear system with mesh stiffness fluctuation, bearing flexibility and backlash. *Mechanisms and Machine theory*, 44:1058–1069, 2009. [cited at p. 37]

[56] R. K. Jurgen and C. Menard. A new multipurpose servo valve for fast applications. *Actuators SAE*, 1997. [cited at p. 37, 38, 39, 50]

[57] F. S. Ahmed, S. Laghrouche, and M. El Bagdouri. Nonlinear modeling of pancake dc limited angle torque motor based on lugre friction model. *Vehicle Power and Propulsion Conference (VPPC 10), France*, 2010. [cited at p. 37]

[58] M. C. Leu and R. A. Aubrecht. Feasible and optimal designs of variable air gap torque motors. *Journal of Engineering for Industry, ASME*, 1991. [cited at p. 38]

[59] A. G. Mikerov. Adaptive control of automotive electronic throttle. *EUROCON'09 IEEE*, 2009. [cited at p. 38]

[60] Y. Zhang. Ph.d. thesis: High performance dsp based servo drive control for a limited angle torque motor. *Loughsborough University, England*, 1997. [cited at p. 38]

[61] D. Chunyang, L. Tiecai, and C. Zhengcai. Accurate tracking control of a limited angle torque motor. *Industry Applications Conference, IEEE*, 2003. [cited at p. 38]

[62] M. A. A. S. Chaudhry, N. F. Thornhill, and S. L. Shah. Modelling valve stiction. *Control Engineering Practice*, 13:641–658, 2005. [cited at p. 43, 45, 53]

[63] J. Gerry and M. Ruer. How to measure and combat valve stiction online. *Instrumentation, systems and automated society*, 2002. [cited at p. 43]

[64] H. Olsson, K.J. Astrom, C. Canudas de Wit, M. Gäfvert, and P. Lischinsky. Friction models and friction compensation. *European Journal of Control*, 4, 1997. [cited at p. 51, 52, 57]

[65] C. C. de Witt, H. Olsson, K. J. Astrom, and P. Lischinsky. A new model for control of systems with friction. *IEEE Trans. on Automatic Control*, 40(3), 1995. [cited at p. 51, 52, 53, 56, 57, 85]

[66] R. Isermann. *Mechatronic Systems Fundamentals*. Springer Verlag, Heidelberg, DE, 2005. [cited at p. 52]

[67] L. Marton and B. Lantos. Modeling, identification and compensation of stick-slip friction. *IEEE Trans. on Industrial Electronics*, 54(1), 2007. [cited at p. 52]

[68] D. Pavkovic, J. Deur, M. Jansznn, and N. Peric. Adaptive control of automotive electronic throttle. *Control Engineering Practice*, 14:121–136, 2006. [cited at p. 52]

[69] L. Desborough and R. Miller. Increasing customer value of industrial control performance monitoringŮhoneywellŠs experience. *AIChE Symposium Series 2001*, 326:172Ű192, 2001. [cited at p. 53]

[70] D. Karnopp. Computer simulation of stick-slip friction in mechanical dynamic systems. *ASME Journal of Dynamic Systems, Measurement and Control*, 107:100–103, 1985. [cited at p. 56]

[71] C. Garcia. Comparison of friction models applied to a control valve. *Control Engineering Practice*, 16, 2008. [cited at p. 56]

[72] L. Nashelsky R. L. Boylestad. *Electronic Devices and Circuits - (8^{th} Edition)*. Pearson Education, 2010. [cited at p. 66]

[73] Montgomery. Wormgear with backlash-adaptable toothing. *Offprint: Antriebstechnik*, 30(4), 1991. [cited at p. 66]

[74] J. P. Uyemura. *Introduction to VLSI Circuits and Systems*. Wiley, 2001. [cited at p. 67]

[75] V. I. Utkin. *Sliding Modes in Optimization and Control Problem*. Springer Verlag, New York, 1992. [cited at p. 87]

[76] S.V Emelyanove, S.K Korovin, and A Levant. Higher-order sliding modes in control systems. *Differential Equations*, 29:1627–1647, 1993. [cited at p. 87, 88, 91]

[77] A.F Filippov. *Differential Equations with Discontinuous Right-Hand Side*. Kluwer, Dordrecht, the Netherlands, 1988. [cited at p. 87]

[78] A. Levant. Sliding order and sliding accuracy in sliding mode control. *International Journal of Control*, 58(06), 1993. [cited at p. 88, 91, 92]

[79] G. Bartolini, A. Ferrara, E. Usai, and V. I. Utkin. On multi-input chattering-free second-order sliding-mode control. *IEEE Trans. on Automatic Control*, 45(9), 2000. [cited at p. 88]

[80] A. Levant. Quasi-continuous high-order sliding-mode controllers. *IEEE Trans. on Automatic control*, 50(11), 2005. [cited at p. 88]

[81] G. Bartolini, E. Punta, and T. Zolezzi. Regular simplex method and chattering elimination for nonlinear sliding mode control of uncertain systems. *Proc. 46th IEEE Conf. Decision and Control*, 2007. [cited at p. 88]

[82] A. Levant. Homogeneity approach to higher-order slidng-mode design. *Automatica*, 41:823–830, 2005. [cited at p. 88, 94]

[83] Y. Pan, U. Ozguner, and O. H. Dagci. Variable-structure control of electronic throttle valve. *IEEE Trans. on Indusrial Electronics*, 55(11), 2008. [cited at p. 88, 92]

[84] S. Laghrouche, F. Plestan, A. Glumineau, and R. Boisliveau. Robust second order sliding mode control of a permanent magnet synchronous motor. *Proc. American Control Conference*, 2003. [cited at p. 88, 89, 91]

[85] M. Reichhartinger and M. Horn. Application of higher order sliding-mode concepts to a throttle actuator for gasoline engines. *IEEE Trans. on Industrial Electronics*, 56(9), 2009. [cited at p. 88, 92]

[86] M. Horn, A. Hofer, and M. Reichhartinger. Control of an electronic throttle valve based on concepts of sliding-mode control. *17th IEEE International Conf. Control Applications*, 2008. [cited at p. 88, 92]

[87] A. Levant. Higher-order sliding modes, differentiation and output-feedback control. *International Journal of Control*, 46(09), 2001. [cited at p. 92, 93, 94, 112]

[88] S. V. Emelyanov, S. K. Korovin, and L. V. Levantovskii. A new class of second order sliding algorithms (russian). *Mathematical Modeling*, 2:89–100, 1990. [cited at p. 92]

[89] W. Perruquetti and J.P.Barbot, editors. *Sliding Mode Control in Engineering*. Marcel Dekker Inc., New York-Basel, 2002. [cited at p. 93]

[90] A. Levant. Robust exact differentiation via sliding mode technique. *Automatica*, 34(03):379–384, 1998. [cited at p. 94]

[91] A. Levant. Universal siso sliding mode controllers with finite time convergence. *IEEE Trans. Automatic Control*, 46(09), 2001. [cited at p. 94]

[92] A. Levant. Exact differentiation of signals with unbounded higher derivatives. *IEEE Trans. Automatic Control*, 99, 2011. [cited at p. 94]

[93] P. L. Andrighetto, A. C. Valdiero, and D. Bavaresco. Dead zone compensation in pneumatic servo systems. *ABCM Symposium Series in Mechatronics*, 3:501–509, 2008. [cited at p. 107]

[94] F. Plestan, Y. Shtessel, V. Bregeault, and A. Poznyak. Sliding mode control with gain adaptation: Application to an electropneumatic actuator. *Control Engineering Practice, DOI: j.conengprac.2012.04.012*, 2012. [cited at p. 109]

[95] M. R. Sobcyzk, E. A. Perondi, and M. A. B. Cunha. A continuous extension of the lugre friction model with application to the control of a pneumatic servo positioner. *51st IEEE Conference on Decision and Control, Maui, Hawaii, USA.*, 2012. [cited at p. 109, 110, 111]

[96] G. V. Larchev, S. F. Campbell, and J. T. Kaneshige. Projection operator: A step towards certification of adaptive controllers. *National Technical Information Service, Alexandria, VA 22312 USA*, 2010. [cited at p. 109, 118]

[97] E. C. Zavala, J. A. Moreno, and L. Fridman. Uniform robust exact differentiator. *Proc. 49th CDC Conference, GA, USA*, pages 102–107, 2010. [cited at p. 112, 179, 180]

[98] J. Zhou and C. Wen. *Adaptive Backstepping Control of Uncertain Systems*. Springer-Verlag, Berlin-Heidelberg, 2008. [cited at p. 115, 178]

[99] J. E. Slotline and W. Li. *Applied Nonlinear Control*. Prentice Hall, New Jersey, USA, 1991. [cited at p. 118]

[100] H. K. Khalil. *Nonlinear Systems (3^{rd} ed.)*. Prentice Hall, New Jersey, USA, 2002. [cited at p. 118, 119]

[101] C. C. de Witt and P. Lischinsky. Adaptive friction compensation with partially known dynamic friction model. *International Journal of Adaptive Control and Signal Processing*, 11(1):65–80, 1997. [cited at p. 119]

[102] A. Mehmood, S. Laghrouche, and M. El Bagdouri. Modeling identifcation and simulation of pneumatic actuator for vgt system. *Sensors and actuators: A Physical*, 165:367–378, 2011. [cited at p. 135]

[103] J. R. Serrano, F. J. Arnau, V. Dolz, A. Tiseira, and C. Cervello. A model of turbocharger radial turbines appropriate to be used in zero- and one-dimensional gas dynamics codes for internal combustion engines modelling. *Energy Conversion and Management*, 49:3729–3745, 2008. [cited at p. 135]

[104] G. Hoge. Exhast pressure modeling for feedforward active control of internal combustion engine exhaust noise. *Journal of automobile engineering part D*, 213:109–117, 1998. [cited at p. 135]

[105] V. Macian, J. M. Lujan, V. Bermudez, and C. Guardiola. Exhaust pressure pulsation observation from turbocharger instantaneous speed measurement. *Journal of measurement science and technology*, 15:1185–1194, 2004. [cited at p. 135]

[106] O. Leonard and O. Adam. A quasi one dimensional cfd model for multistage turbomachines. *Journal of thermal science*, 16(2):1–15, 2007. [cited at p. 135, 144]

[107] W. Du and O. Leonard. Numerical simulation of surge in axial compressor. *International journal of rotating machinery*, 12:1–10, 2012. [cited at p. 135]

[108] H. C. Yee. *Numerical approximation of boundary conditions with applications to inviscid equations of gas dynamics.* NASA Technical Memorandum 81265, Ames Research Center, Moffett Field, California, 1981. [cited at p. 135, 149, 151, 156]

[109] A. C. Love, G. Agnew, and B. Szczyrba. Adaptive variable geometry turbocharger strategy. *patent number: US 2009/0123272 A1*, 2009. [cited at p. 135]

[110] K. A. Hoffman and S. T. Chiang. *Computational fluid dynamics, volume 1.* Engineering Education System, ISBN-13: 978-0962373107, 2000. [cited at p. 140, 149, 151]

[111] D. G. Ainley and G. C. R. Mathieson. *An examination of the flow and pressure losses in blade rows of axial flow turbines.* Ministry of supply technical memorandum no. 2891, Aeronautical Research Council, London, 1951. [cited at p. 145, 148, 149]

[112] K. W. Morton and D. F. Mayers. *Numerical Solution of Partial Differential Equations: An Introduction.* Cambridge University Press, ISBN-13: 978-0521607933, 2005. [cited at p. 153]

Résumé :

Dans l'environnement concurrentiel d'aujourd'hui, la mondialisation des marchés et les enjeux socio- écologiques du développement durable représentent des défis majeurs pour l'industrie automobile. Afin de relever ces défis, les entreprises doivent investir dans des outils de développent plus performants. Pour améliorer la performance d'un moteur thermique en termes de consommation et d'émissions une compréhension enrichie de la boucle d'air autour du moteur et de l'interaction entre ses composants est indispensable.

Cette thèse suit deux axes de recherche dans ce contexte. Dans un premier temps, les problèmes liés à la modélisation d'une boucle d'air globale sont traités. En particulier, sont modélisés le débit d'air entre les différents sous-systèmes, la combustion en fonction du degré vilebrequin, la pulsation du débit et de la pression et l'estimation de la force aérodynamique sur les vannes des turbocompresseurs à géométrie variable (TGV). Cette étude de modélisation détaillée à été utilisée pour mettre en place un simulateur de la boucle d'air, qui prend en compte ces interactions et qui peut prédire l'influence des sous-systèmes sur la boucle globale. En suite, l'effort de notre recherche a été consacré à la modélisation des actionneurs mécatroniques de la boucle d'air et de leur comportement non linéaire dû au frottement, aux variations de la température, etc. Un modèle dynamique non linéaire à été développé et intégré dans le simulateur. Ce modèle peut être adapté aux plusieurs types d'actionneurs commerciaux. Le simulateur complet à été implémenté sous AMESim pour les modèles du moteur et de la boucle d'air, et sous Simulink pour le contrôle. Les modèles ont été paramétrées selon les spécifications d'un moteur commercial et le simulateur à été validé expérimentalement.

Finalement, des lois de commande robustes ont été étudiées pour le contrôle en position (contrôle locale) des actionneurs. Un contrôleur adaptatif à été développé pour garantir la performance des actionneurs malgré la variation des frottements et du couple de charge. La performance de toutes les méthodes étudiées, a été validée expérimentalement.

Mots clés : Boucle d'air du moteur diesel, force aérodynamique, actionneurs mécatroniques, modélisation non linéaires, commande avancé des actionneurs.

Abstract:

Today's globally competitive market and its associated environmental and social issues of sustainable development are major challenges for the automobile industry. To meet them, the industry needs to invest in high performance development tools. For improving engine performance in terms of consumption and emission, the interactions between the subsystems of the engine air-path need to be understood.

This thesis followed two major axes of research in this context. First, the problems related to the modeling of the global air-path system were studied, which include the airflow characteristics between the different subsystems of the air-path, high frequency combustion modeling and pulsating airflow, and estimation of the exhaust aerodynamic force on the vanes of variable geometry turbochargers (VGT). The detailed modeling study was used for developing an engine air-path simulator, which takes into account these interactions and predicts the influence of subsystems on the global air-path. The second axis of research was focused on modeling of mechatronic actuators of the air-path, taking into account their nonlinear behavior due to friction and changes in operating conditions. A generic nonlinear dynamic model was developed and included in the simulator. This model can be adapted to most commercial actuators. The complete simulator has been implemented using AMESim for engine and air-path modeling, and Simulink for control. It has been parameterized according to the specifications of a commercial diesel engine and validated against experimental data.

Finally, robust local controllers were studied for actuator position control, aimed at guaranteeing the performance of the actuators under parametric uncertainty and external disturbances. An advanced controller was developed, which adapts to changes in friction characteristics of the actuator and external load changes. The performance of all controllers has been demonstrated experimentally.

Keywords: Diesel Engine Air-path, Aerodynamic Force, Mechatronic Actuators, Nonlinear Modeling, Advanced Actuator Control.

SPIM

■ École doctorale SPIM - Université de Technologie Belfort-Montbéliard
F - 90010 Belfort Cedex ■ tél. +33 (0)3 84 58 31 39
■ ed-spim@univ-fcomte.fr ■ www.ed-spim.univ-fcomte.fr

utbm
université de technologie Belfort-Montbéliard